ABSTRACT

Title of Dissertation: SPECTROSCOPY OF TWO LEVEL DEFECTS &

QUASIPARTICLES IN SUPERCONDUCTING RESONATORS

Timothy P. Kohler, Doctor of Philosophy, 2021

Thesis directed by: Dr./Prof. Kevin D. Osborn

Laboratory of Physical Science and Joint Quantum Institute

Superconducting films are inherently limited by losses due to two-level system (TLS) defects within the amorphous oxide layers surrounding them and from quasiparticles in the film. In this thesis I will discuss novel theoretical and experimental methods toward understanding superconducting resonator loss from deleterious surface TLS defects as well as a loss transition from non-equilibrium quasiparticles in granular TiN. I will show using finite element solver software that a resonator with submicron linewidth and linespacing can be used to better characterize and simulate surface TLS as part of a circuit QED system. I have observed individual surface TLS and found coupling values in the range of $g/2\pi$ =50 kHz -280 kHz with a maximum dipole moment

$p_{z,max}$ = 4.5 Debye (.93 eÅ). I have found in in simulation of experiment that over 80% of the strongly coupled TLS reside within 50 nm of the corner between the Metal-Substrate (MS) and Substrate-Air (SA) interface. Additionally I have studied a loss transition from non-equilibrium quasiparticles in TiN films. These films exhibit an anomalous loss dependence on substrate treatment and film thickness. The films of interest are ones grown thin on oxidized substrates, which exhibit an order of magnitude decrease in internal quality factor (Q_i) relative to either thicker films or films grown without the oxidized substrate. These films additionally exhibit a grain size on average of 7.5 nm, a higher inhomogeneous gap, a transition to lower stress and a preference for the [111] crystal growth. The temperature dependence of the conductivity is fit and a factor of two difference in quasiparticle lifetime is found between the two films where the thinner film has a shorter lifetime. A two gap quasiparticle trapping model is fit to the temperature dependent loss data. The data is consistent with a model where non-equilibrium quasiparticles are trapped in low gapped grains on the inside of the films. From these works and others presented in my thesis the understanding of TLSs on surfaces and non-equilibrium quasiparticles in TiN has improved. This will help illuminate some of the most important absorption mechanisms plaguing superconducting qubits and resonators.

SPECTROSCOPY OF TWO LEVEL DEFECTS & QUASIPARTICLES IN SUPERCONDUCTING RESONATORS

by

Timothy P. Kohler

Dissertation submitted to the Faculty of the Graduate School of the

University of Maryland, College Park in partial fulfillment

of the requirements for the degree of

Doctor of Philosophy

2021

Advisory Committee:
Professor Steven Anlage, Chair
Professor Kevin D. Osborn, Chair
Professor Julius Goldhar
Professor Christopher Monroe
Professor Ichiro Takeuchi

Preface

I have made substantial contributions to the relevant aspects of the jointly authored works included in the dissertation, [57],[63].

Dedication

To my family and fiancée for their love and support

Acknowledgments

I would like acknowledge all the people that have helped me along the way. It has been a long road and I appreciate everyone that helped me in any way.

Foremost, I would like to thank my advisor Dr. Kevin Osborn. I consider myself very lucky to have been a part of his group. Kevin was a very supportive and encouraging advisor who mixed a cheerful demeanor with a hardworking attitude. His doors were always open and provided thoughtful guidance and invaluable suggestions along the way.

I would like to thank my other committee members Professor Steven Anlage, Professor Goldhar, Professor Takeuchi, and Professor Monroe for their time and effort, especially Professor Steven Anlage who was my ECE advisor. Professor Anlage was always very encouraging and welcoming throughout my years and always appreciated his guidance.

I would like to thank Fred Wellstood who's invaluable insight helped improve my understanding a number of times throughout my PhD.

I would like to thank Dr. Ben Palmer, Dr. Michael Dryer, and Dr. Chris Richardson for their knowledge and making themselves available when I needed help. Ben and Michael especially provided invaluable insight into managing and maintaining our Leiden system.

I would like to thank the LPS staff, research and cleanroom members – Steve Brown, Toby Oliver, Curt Walsh, Jim Fogleboch, Paul Hannah, Dan Hinkel, Doug Ketchum, Warren Berk, Debtanu Basu, Dave Bowen, Jonas Wood, Niquinn Fowler, Althia Kirlew and Cynthia Evans. I would like to thank the machinists at LPS – Donald Crouse, who was one of the first people I worked with and who's cheerful and positive demeanor was always a pleasure to talk to, Ruben Brun, John Sugrue and Bill Donaldson. I thank Greg Latini and Mark Thornton, for their helps with issues on electronics or computers.

I would like to thank my collaborators Leonardo Civale at LANL, Jenny Lock at NRL & Pops at SUNYPOLY .

I would like to thank all the other scientists, researchers and friends that have helped me during my PhD, Dr. Cody Ballard, Dr. Sudeep Dutta, Ashish Alexander, Margaret Samuels, Dr. Jen-Hao Yeh and Dr. Shavi Premaratne, Dr. Joyce Coppock, Dr. Wan-Ting Liao, Luke Robertson.

I would like to thank my predecessors in the group, Dr. Bahman Sarabi, Dr. Yaniv Rosen, who continues to be a supportive mentor, and Dr. Aruna Ramanayaka. I would not have been as successful without them teaching me the ropes when I was starting out and for answering all my questions.

I would like to thank my current and past group members, Dr. Peng Xu, Dr. Neda Forouzani, Dr. Liuqi Yu, Dr. Stephen Gil, Dr. Samaresh Guchhait, Dr. Ekta Bhatia and Chih-Chiao Hung. I really have learned so much from all of you and really appreciate all your help and time. Neda and Liuqi were incredibly kind and supportive during my last years at LPS and

I would like to thank my friends & family in Maryland and around the country who know how long I've been working in school. Thank you to Benjamin "Benjammin" Bulson, Gino Crecco, Kyle & Katerina Gruber, Geoff & Ariel Winkley, Kiren Arjawat, Adam Zander, Alex Contreras, Cougar & Marlaena Garcia, Dan Antinori, Evans Gritton, Quinn & Kayla Matthew, Mark Rutecki, Andrew Knauss, Sophie Schwartz, Katie Farnum, Amulya Khajuri, Maria Sullivan, Emily Briskin, Chris & Joy Diffley, Griffin Godbey, Mike McHale, the future Gabe & Lana Ziegler, and Mike Trepanier.

I have to especially thank my family. My mom, Susan Kelleher-Kohler, dad, Peter Kohler, my grandmothers Catherine Kelleher, and Ilse Kohler, and brothers, Mike Kohler, Dan Kohler and Rich Kohler have been incredibly supportive. I've enjoyed them asking questions, giving advice and keeping me in good spirits. I get a laugh every time my mom or dad talk about superconducting circuits or send me the latest article they had read about qubits. I'm also so proud of my little brothers who have each grown up and become such persevering and persistent adults. I also want to thank my future family-in-law, Dr. Praveen Chawla, Anju Chawla, and especially Neha Chawla a.k.a Shorty, a.k.a "Holla for Chawla". They have been very welcoming, supportive and patient through out the years.

And I have to absolutely thank my fiancée, Priya Chawla, whose love and support has inspired me and who continues to be the wind beneath my wings.

Contents

List of Figures

1 Introduction

Feynman once said, "Nature uses only the longest threads to weave her patterns, so each small piece of her fabric reveals the organization of the entire tapestry." Feynman was describing how all of nature is intertwined. By understanding "small pieces" or problems one can illuminate the whole idea. As a graduate student in the field of superconducting quantum computing, one can attempt to bring new ideas to light and to understand the smallest pieces of the quantum fabric. Quantum computing has become one of the most popular researched areas. With the ability to harness quantum information comes the ability to perform computations not possible with current classical computers. Shor's algorithm [1] has shown that a quantum computer can be used to factor numbers exponentially faster than classical algorithms, allowing one to break standard encryption. Grover's algorithm provides a quadratic speed up in searching for information. But these algorithms are only the beginning. In addition, complex optimization problems may be solved in the short term which is of interest for quantum chemistry and pharmaceuticals. Realizing this potential starts by understanding and manipulating small sets of superconducting qubits and resonators, where the latter are used to interface and readout the former, and where a qubit is an abbreviation for quantum bit. Ideally, it is a quantum two level system as shown in Figure 1, which has the ability to be in any superposition of its ground and excited states.

While there are multiple ways to construct a qubit, including trapped ion qubits, spin qubits and semiconductor qubits, superconducting qubits provide

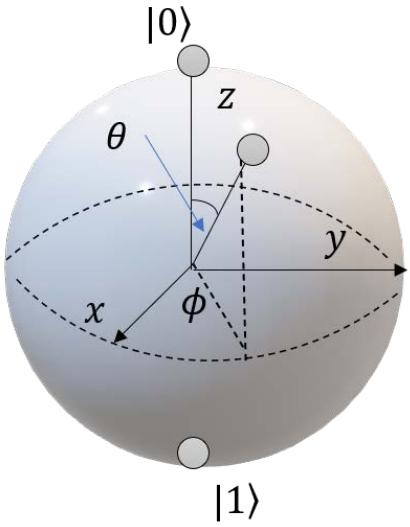

Figure 1: The block sphere represents the state space of the two level qubit. It shows how it can be in the $|0\rangle$ state, represented as the most-positive z state, the $|1\rangle$ state which is the most-negative, or any superposition of the two states. ϕ represents the phase difference between these two states.

a very promising path forward. Superconducting qubits have many advantages. These qubits are made up of ordinary circuit elements such as capacitors and inductors. These devices can be fabricated using standard photo lithography and e-beam lithography. Because they are simple circuits they can be controlled using basic RF and DC lines. At this temperature the electrons form Cooper pairs and group into a single quantum wave function allowing for quantum phenomena to be seen macroscopically. The low temperatures are made possible using a dilution refrigerator where the process of moving Helium-3 through the phase boundary of a Helium-3 and Helium-4 isotope mixture is endothermic and absorbs heat. Right at that boundary between Helium-3 and Helium-4 the lowest temperature stage in a dilution refrigerator exists. This cooling power is needed to obtain a base temperature of ~10 mK. This low temperature is important to stay in the quantum regime with thermal energy much less than the qubit transition frequency, k_b T$\ll\hbar\omega$. Superconducting qubits are formed with Josephson tunnel junctions, which are made from two

layers of superconducting film with a tunneling barrier in between. This junction provides a low loss, non-linear circuit element. While other qubits make use of microscopic quantum phenomena such as spins or atoms which have trouble coupling to each other, superconducting qubits can have high coupling rates. High coupling means it will be easier to couple multiple qubits. The downside is that each qubit also couples highly to the environment which can cause loss or a decrease in coherence time. When the qubit decays from excited state to ground state, this process is associated with the T_1 coherence time or relaxation time (θ in Figure 1). On the other hand, fluctuations in qubit frequency (and ϕ in Figure 1) only affect the phase coherence time T_ϕ. The total coherence is $T_2 = (2T_1^{-1} + T_\phi^{-1})^{-1}$. The need for a higher coherence time and a better understanding of coherence motivates a substantial amount of modern research in superconducting quantum computing. Understanding the causes of decoherence such as two level system defects, vortices, radiation, thermal noise, and quasiparticles are very important.

The coherence of superconducting qubits has grown over five orders of magnitude over the last two decades [2], but the size of the current high-performance qubits are on the order of 1 millimeter, which poses challenges for qubit-qubit isolation. When made more compact, qubits generally couple more strongly to two-level system (TLS) defects, causing added decoherence. However, a microscopic (or small) volume of the electrical mode will also allow discreteness to be observed in the TLS spectrum, due to sampling of their sparse random energies. I am studying a resonator design with surface TLSs

near the edges of the resonator, in regions with high participation energy ratios. Understanding the loss in superconducting resonators, which have noise from TLS as do qubits, is crucial for improving coherence times and the maturation of superconducting qubits in general.

Another way to advance superconducting qubits is to explore different superconductors. High-quality superconducting films of TiN and related NbTiN are of recent interest in the field of quantum information science and astronomical detection. Titanium nitride (TiN) has a higher critical temperature than aluminum, lower loss on the silicon surface than many other superconductors, and an ability for high kinetic inductance. While aluminum oxide is known to contain a large density of TLS defects certain growth directions of TiN have been found to be less lossy when exposed to oxygen [7][3]. TiN has a very low carrier concentration which leads to a high kinetic inductance. Large inductances leads to large impedances which are useful in resonators. High inductance gives better sensitivity to high-frequency photons in microwave kinetic inductance detectors (MKIDs). Microwave kinetic inductance detectors are used for detecting photon energies above a specific superconducting gap[51]. The sensitivity and accuracy of this detection is dependent upon the materials used. In qubits TiN allows for tunable coupling due to its fast frequency tunability[4]. Additionally it has shown to yield high quality factor resonators[3]. I will discuss a loss transition in TiN resonators and then cover the design, fabrication and results of a tuned surface TLS study. The following section introduces superconducting qubits and the different loss mechanisms

present. I then describe the important theory behind two level system defects and quasiparticles.

1.1 Quantum Computing Background

Feynman was one of the first to propose that quantum mechanics could be used to create a new form of computing. He said, "if you want to make a simulation of nature, you'd better make it a quantum mechanical." During the rise of quantum information he has inspired the fields of superconducting qubits where tremendous progress has been made. Some of the first theoretical proofs showing the power of quantum computing came from David Deutsch and Richard Jozsa. They showed that a quantum algorithm could out-perform its classical counterpart. Further quantum algorithms emerged from Peter Shor[1]and Grover that a quantum computer could factor number exponentially faster and could give a $\sqrt{N}$ improvement in the time needed to search a database respectively. Modern classical computers rely on classical binary logic where information is stored in an off state (0) or on state (1). These 2 states are the only possible states that exist classically. Physically these states manifest themselves as a high (1) and low potential (0), as in the transistors in your phone and computer, or as classical up (1) or down (0) magnetic moments on a hard drive. Quantum mechanics gives the possibility to be in a superposition of states. Thus a qubit or quantum bit can be in the 1 and 0 state at the same time. So for example, in an n qubit register placed in superposition or can store all the numbers between 0 and 2^{n-1} at the

same time. If an operation is performed on this system then it acts on all the numbers stored by the qubits in one operation. This parallelism is a concept that enables efficient quantum computing.

1.2 Introduction to Superconductivity

Heike Kamerlingh Onnes was a dutch physicist, and the first to liquify helium and discovered key properties of superconductivity . It was unclear at the time in the 1900s if the conductivity or the movement of electrons would be completely stopped at low enough temperatures. In 1911 Onnes discovered something very puzzling[89]. After bringing the refrigerant liquid helium to 4.19K, Kamerlingh tested the conductivity of mercury and reported a disappearance of resistance as the temperature was lowered. Onnes had discovered the world's first superconductor. Decades later more characteristics about superconductors were revealed. In 1933 Meissner discovered that superconductors can act as diamagnetic substances and expelled magnetic fields. Superconductivity wasn't microscopically described until later in the 1950s by a theory proposed by Bardeen, Cooper, and Schrieffer (BCS). They discovered that a weak attractive interaction between electrons mediated by phonons can cause the formation of bound pairs of electrons with equal and opposite momentum and spin. These paired electrons are called Cooper pairs. They predicted that the minimum energy to break this pair is E_g=2Δ=3.528 $k_B T_C$. The breaking of Cooper pairs will create quasiparticles. The length scale of the Cooper pair in the superconductor is named the superconducting coherence

length, ξ_0. This length can be as large as $1\mu m$ in high quality crystals. Due to scattering at defects or grain boundaries, the coherence length is reduced to the effective coherence length is $\xi_{eff} = (\frac{1}{\xi_0} + \frac{1}{l})^{-1}$where l is the mean free path.

Additionally superconductors are either of type I or type II, depending on the relation between their London penetration depth, λ_L, and the coherence length. Aluminum is a type I superconductor where the bulk material cannot be penetrated by magnetic fields. This phenomena is called the Meissner effect. In type II superconductors such as TiN, and films of most materials including aluminum, the coherence length is less than the penetration depth, which allows magnetic fields to penetrate the material in quantized bundles named vortices. In TiN, the typical coherence lengths are close to 20 nm but penetration depths can be much larger. $\lambda_L = \sqrt{\frac{m}{\mu_0 n q^2}}$where m is the charge carrier mass, n is the number density and q is the elementary charge [88]. A superconductor often acts as an inductance, where a large penetration depth leads to increased inductance. This inductance type is called kinetic inductance and will be discussed in later sections.

1.3 Quasi-classical electron transport

In 1900 Paul Drude proposed a model to describe the conduction of electrons in materials. He assumed that a sea of electrons with a number density, n, continuously collided at positive scattering centers thus keeping the overall charge of the solid neutral. The number density of this sea of electrons is

equal to

$$n = N_A Z \rho_m / A \tag{1.1}$$

where N_A is Avogadro's number, Z is the atomic mass number and ρ_m is the concentration of the ions. Mathematically we can find the equations of motion for an electron over time

$$\frac{d}{dt}\langle p(t)\rangle = qE - \frac{\langle p(t)\rangle}{\tau} \tag{1.2}$$

where p is the momentum, q is the elementary charge, and E is the electric field which is assumed to be homogeneous and uniform. τ is the time between collisions or the inverse of the scattering rate. The solution for this differential equation is

$$\langle p(t)\rangle = q\tau E(1 - e^{t/\tau}) + p(0)e^{t/\tau} \tag{1.3}$$

If you look at the steady state solution $dp/dt = 0$ then the equation simplifies to

$$\langle p\rangle = q\tau E \tag{1.4}$$

We can then relate momentum to the current density, J using

$$\langle p\rangle = m\langle v\rangle \tag{1.5}$$

and

$$J = nq\langle v \rangle \tag{1.6}$$

From Ohm's law, $J = \sigma_0 E$ and thus the DC conductivity from the Drude model is

$$\sigma_0 = \frac{nq^2\tau}{m} \tag{1.7}$$

For AC fields, the general formula is

$$\sigma(\omega) = \frac{\sigma_0}{1 - i\omega T} \tag{1.8}$$

Landau then demonstrated that despite the Coulomb interaction between individual free electrons, electrons in general acts as groups or a cloud that screens the Coulomb interaction. Landau referred to this system as a Landau-Fermi-liquid where the moving cloud can be thought of as a quasiparticle with an effective mass[35]. These quasiparticles can scatter whether due to impurities or thermally through phonons. The scattering rate is thus $\tau^{-1} = \tau_{th}^{-1} + \tau_{im}^{-1}$. Furthermore while the phonon scattering rate increases with temperature the impurity scattering rate due to disorder is temperature independent.

Quantum mechanically, electrons behaves like waves with a wavelength $\lambda = 2\pi/k$, where k is the wave vector. By solving the Schrodinger equation for a free electron in a cube the accessible energy levels are given by $E = \hbar^2 k^2/2m$ where m is the mass. Because the Pauli exclusion principle, they cannot occupy

the same state and will fill up all available energy states up to the Fermi Energy, E_F. Only electrons near the Fermi energy will be a part of the current with a Fermi velocity, $v_F = \hbar k_F/m$. Additionally, a mean free path can then be defined as $l = v_F\tau$ which is the average distance between scattering events. For a 3 dimensional system we can also relate the carrier density to the Fermi wave vector, $n = k_F^3/(3\pi^2)$ and then equation 1.7 can be rewritten as

$$\sigma_{3D} = \frac{e^2}{3\pi^2\hbar}k_F^2 l \tag{1.9}$$

When a crystal is very disordered the atomic distance of the lattice is on the order of the mean free path and there will be a large increase in the scattering rate. This will not allow it to travel a full wavelength and thus sets a disorder limit known as the Ioffe-Regel criterion,

$$k_F l >> 1 \tag{1.10}$$

In my TiN experiments I get close to this criteria and due to the high resistivity, grain size and quasiparticle scattering in the film I see a very interesting consequence in the loss of my resonators.

Two Fluid Model

Many properties of superconductors can be described in terms of a two-fluid model that consists a normal electrons or quasiparticles combined with superconducting cooper pairs. The two fluids coexist in the superconductor[88].

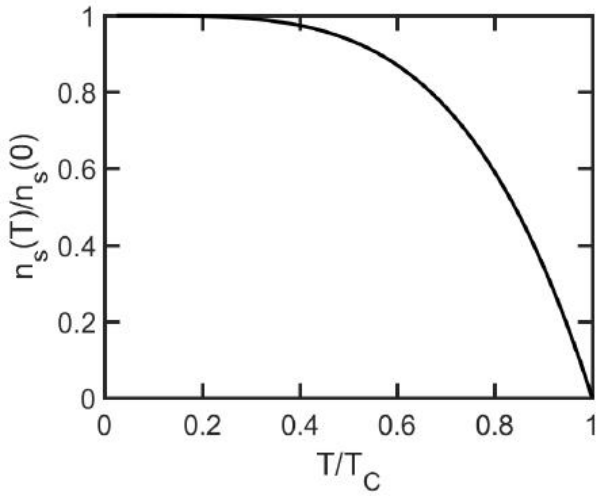

Figure 2: Superconducting charge carriers, n_s versus temperature. With normal electron carriers, n_n they sum to a total carrier concentration n as a function of normalized temperature. Ideally all charge carriers are superconducting at zero temperature.

When a superconductor is cooled below Tc, normal electrons begin to transform to the super electron state. The densities of the normal and the super electrons, n_n and n_s, respectively, are temperature dependent, and sum to the total density n of the conduction electrons,

$$n = n_s(T) + n_n(T) \tag{1.11}$$

We can then define a temperature dependent penetration depth

$$\lambda(T) = \sqrt{\frac{m}{\mu_0 n_s(T) q^2}} \tag{1.12}$$

Temperature dependence of the density of superconducting electrons is

$$\frac{n_s}{n} = \frac{\lambda(0)^2}{\lambda(T)^2} \tag{1.13}$$

which becomes

$$n_s = n(1 - (T/T_C)^4) \tag{1.14}$$

Mattis Bardeen Theory

The conductivity of a superconductor can be thought as being complex where $\sigma = \sigma_1 + i\sigma_2$where σ_1 describes the normal (quasiparticle) conductivity and σ_2 describes the equation for superconducting condensate conductivity. Mattis Bardeen Theory describes the response of the superconducting cooper pairs and normal metal electrons to non-local electromagnetic waves. In normal metals, a local relationship can be established between the current and electric field where

$$\overrightarrow{J}_n = \frac{\sigma_0}{1 - i\omega T} \overrightarrow{E}(\overrightarrow{r}) \tag{1.15}$$

In superconductors where the mean free path can be high at low temperatures a non local relationship is needed. Thus in 1958 Mattis and Bardeen developed a non local relation between the current density and vector potential, $\overrightarrow{A}$.

$$\overrightarrow{J}(\overrightarrow{r}) = \frac{3\Delta_0}{4\pi\xi_0\lambda_L^2} \int_V d\overrightarrow{r}' \frac{\overrightarrow{R}\,\overrightarrow{R} \cdot \overrightarrow{A}(\overrightarrow{r}) I(\omega, R, T) e^{-R/l}}{R^4} \tag{1.16}$$

where the kernel $I(\omega, R, T)$

$I(\omega, R, T) = i\pi \int_{\Delta-\hbar\omega}^{\Delta} dE(1-2f(E+\hbar\omega))(g(E)\cos\alpha\Delta_2 - i\sin\alpha\Delta_2)e^{-i\alpha\Delta_1}$

$-i\pi \int_{\Delta}^{\infty} dE(1-2f(E+\hbar\omega))(g(E)\cos\alpha\Delta_2 - i\sin\alpha\Delta_2)e^{-i\alpha\Delta_1}$

$+i\pi \int_{\Delta}^{\infty} dE(1-2f(E+\hbar\omega))(g(E)\cos\alpha\Delta_1 - i\sin\alpha\Delta_1)e^{-i\alpha\Delta_2}$

where

$\Delta_1 = \left\{ \begin{array}{ll} \sqrt{E^2-\Delta^2}, & |E| > \Delta \\ J\sqrt{\Delta^2-E^2} & ,|E| < \Delta \end{array} \right\}, \Delta_2 = \sqrt{(E+\hbar\omega)^2-\Delta^2}, g(E) = \frac{E^2+\Delta^2+\hbar\omega E}{\Delta_1\Delta_2}, \alpha = R/\hbar v_0$

and where Δ is the gap parameter and f(E) is the Fermi distribution function,

$$f(E) = \frac{1}{1+e^{E/kT}} \tag{1.17}$$

Furthermore, the conductivities are

$$\sigma_1/\sigma_n = \frac{2}{\hbar\omega}\int_{\Delta}^{\infty} \frac{(E(E+\hbar\omega)+\Delta^2(f(E)-f(E+\hbar\omega)))}{((E^2-\Delta^2)(1/2)((E+\hbar\omega)^2-\Delta^2)(1/2))}dE+$$

$$\frac{1}{\hbar\omega}\int_{\Delta-\hbar\omega}^{-\Delta} \frac{(E(E+\hbar\omega)+\Delta^2(1-2f(E+\hbar\omega)))}{((E^2-\Delta^2)(1/2)((E+\hbar\omega)^2-\Delta^2)(1/2))}dE \tag{1.18}$$

$$\sigma_2/\sigma_n = \frac{1}{\hbar\omega}\int_{\Delta\text{-}\hbar\omega}^{\Delta} \frac{(E(E+\hbar\omega)+\Delta^2(f(E)-f(E+\hbar\omega)))}{((E^2-\Delta^2)(1/2)((E+\hbar\omega)^2-\Delta^2)(1/2))}dE \tag{1.19}$$

While Mattis Bardeen theory can be used to predict the loss from thermal quasiparticles, it is often the case that excess or non-equilibrium quasiparticles

can plague a resonator as well. To incorporate non equilibrium excess quasiparticles it is convention to use an effective potential in the Fermi energy[65]. This changes the quasiparticle concentration to

$$n_{qp} = 4N_0 \int_0^\infty \frac{1}{1 + e^{\frac{E-u}{kT}}} d\epsilon \tag{1.20}$$

where , $\epsilon = \sqrt{E^2 - \Delta^2}$, N_0 is the single spin density of states, and u is the chemical potential.

In this section I have described quasi-classical electron transport, from the Drude model, two-fluid model and Mattis Bardeen theory. I will use the two-fluid model to analyze the quasiparticle lifetimes in my TiN loss results and frequency shifts. Additionally I will also use a modified version of the Mattis Bardeen formula to account for non-equilibrium quasiparticles[16]. So far I have discussed the theory behind conduction in superconductors. Next I will discuss the actual quantum hardware or circuit that dictates the conduction of superconducting and normal charge carriers.

1.4 Superconducting Quantum Devices

Superconducting devices are becoming widespread with applications for low power digital systems[103, 104], in space, and for superconducting quantum information. Because they are superconducting they can achieve very high Q factors and do not have to suffer from the skin effect and AC crowding as normal conducting resonators do. High quality factors in resonators allow

for the study of smaller effects in the E&M response and the study of the underlying physics. Specifically superconducting resonators are used to read out qubits [24]and as Microwave Kinetic Inductance Detectors[51] for incoming photons from space. Recently resonators have been modified to make traveling wave amplifiers [114].

The total quality factor of a resonator Q is equal to

$$Q = \omega_r \frac{E_s}{P_l} \tag{1.21}$$

where E_s is the energy stored, P_l is the power lost, and ω_r is the resonant frequency. Thus the quality factor is a measure of how well the resonator retains the energy stored. A resonator can lose energy in two general ways due to internal losses or external losses. Internal quality factor can be a representation of the internal loss mechanisms that the resonator suffers from such as dielectric loss, quasiparticle loss, radiation loss, vortices and magnetic fields. External quality factor mainly measures a resonator's ability to couple to external structures such as transmission lines, other resonators, or qubits. The total loss is

$$Q^{-1} = \sum_n Q_{i,n}^{-1} + Q_e^{-1} \tag{1.22}$$

Quality factors as high as $10^6 - 10^7$have been achieved on thin film resonators[54] [44]. These high quality factors typically occur on high resistivity low-loss substrates with careful fabrication and at high power where dielectric loss is

saturated. Losses due to quasiparticles and dielectric loss will be described in greater detail in later chapters. Next, I will discuss the co-planar waveguide resonator and lumped element resonators.

1.4.1 Coplanar Waveguides Resonators

There are a number of superconducting devices that will be used in a superconducting quantum computer. The main components will be resonators and qubits. The types of resonators available are 3D cavity resonators, 2D co-planar waveguide resonators, and lumped element resonators. Each type provides particular advantages over the other.

A general transmission line equation can be used to describe the impedance from small sections [20]

$$Z_0 = \frac{\sqrt{R_l + i\omega L_l}}{\sqrt{G_l + i\omega C_l}} \tag{1.23}$$

where $R_l$is the per length resistance, L_l the per length inductance, G_l the per length conductance, and C_l the per length capacitance. A signal propagates down the line with a complex propagation coefficient $\gamma = \sqrt{(R_l + i\omega L_l)(G_l + i\omega C_l)}$ and this implies a phase velocity, $v = \omega/\beta$, where the wavenumber $\beta = \frac{2\pi}{\lambda}$. If the loss is low the impedance and phase velocity reduce to $Z_0 = \sqrt{\frac{L_l}{C_l}}$ and $v = \frac{1}{\sqrt{L_l C_l}}$.

Furthermore, the input impedance seen from an unknown load at a distance l in the transmission line can be viewed as

$$Z_{in} = Z_0 \left(\frac{Z_L + i \tanh(\gamma l)}{1 + i Z_L \tanh(\gamma l)} \right) \tag{1.24}$$

For my designs in this thesis I have used co-planar waveguides where the length is either $l = \lambda/2$ or $l = \lambda/4$ which resonates at f_r as determined by the equation

$$v_p = \frac{c}{\sqrt{\epsilon_{eff}}} = f_r \lambda \tag{1.25}$$

The capacitance and inductance per length, C_l, L_l gives the resonant frequency $\omega_r = \frac{1}{\sqrt{C_l L_l}}$. c is the speed of light and is equal to $2.99792 \times 10^8 m/s$. The effective permittivity is equal to $\epsilon_{eff} = \sum_n \epsilon_{r,n} \frac{1}{n}$. f is the resonator frequency, $v_p$is the phase velocity, and λ is the wavelength. These resonators are considered to be distributed meaning that we can model them with an infinitesimal capacitance and inductance in series per unit length l. How the resonator is terminated at each end creates a particular standing wave. For example in Figure 3 the resonator is open at the bottom and grounded at the top. These boundary conditions create a standing wave with a wavelength $\lambda/4 = l$ and fundamental frequency $f_r = v_p 4l$. The open end is capacitively coupled to a feedline and is a voltage anti-node while the grounded end is a voltage node. Additionally one can have a resonator that is open at both ends creating a $\lambda/2 = l$ resonance.

CPW resonators have the benefit of being able to be fabricated in a single layer or 1 step. This allows for quick and for reproducible resonators. Ad-

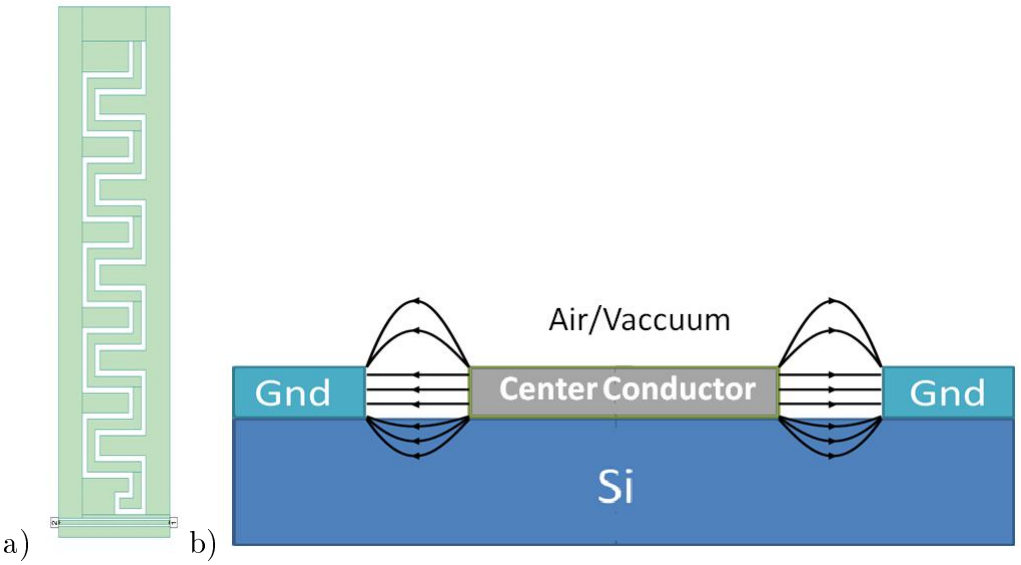

Figure 3: a) Quarter wave co-planar waveguide (CPW) resonator in Microwave Office. The open end of the resonator is a voltage anti-node while the grounded end is a voltage node. The resonant frequency is determined by the length and permittivity of the substrate. 3b shows a cross-section of a CPW with a silicon substrate. The CPW has a center conductor width w and a distance to ground of s.

ditionally multiple $\lambda/4$ resonators can measured at the same time in a single feedline. The disadvantage is that each resonator has a higher order mode and typically qubits are sensitive enough to these higher frequency modes and can lose energy to these modes called the Purcell effect [12].

The resonator is capacitively coupled to the transmission line. Figure 3 shows an example of the the quarterwave co-planar waveguide that is measured. At the top end of the Figure are the two ports, 1 and 2.

Additionally the feed line used to measure the resonators is also a CPW. It is important for the feed through line to be at the right geometry to get

an impedance close to 50 ohms. Often there is kinetic inductance that also needs to be taken into account as well. The impedance can be solved for analytically,[66] following for a semi-infinite dielectric [9]

$$Z0 = \frac{30\pi}{\sqrt{(1+\epsilon)/2}} \frac{K(k_0')}{K(k_0)} \tag{1.26}$$

where

$$k_0 = w/2(s + w/2) \tag{1.27}$$

$$k_0' = \sqrt{1 - k_0^2} \tag{1.28}$$

where s is the width of the center strip, w is the width of the slots in the ground plane, and $K(k_0)$ is the elliptic integral with geometric factor k_0. In the next section I will discuss lumped element resonators.

1.4.2 Lumped element Resonators

Lumped element (LE) resonators will resonate only at a single frequency where the electric and magnetic energy are captured or lumped in a certain area whether in the capacitor or inductor. Additionally the LE is different than the CPW resonator in that the size of the capacitor and inductance components is much smaller than the wavelength. Lumped element resonators like CPWs use thin film technology with the standard photolithography process, however, they typically involve multiple layers. They can be comprised of interdigitated or parallel plate capacitors with a meandering or spiral inductor, where the

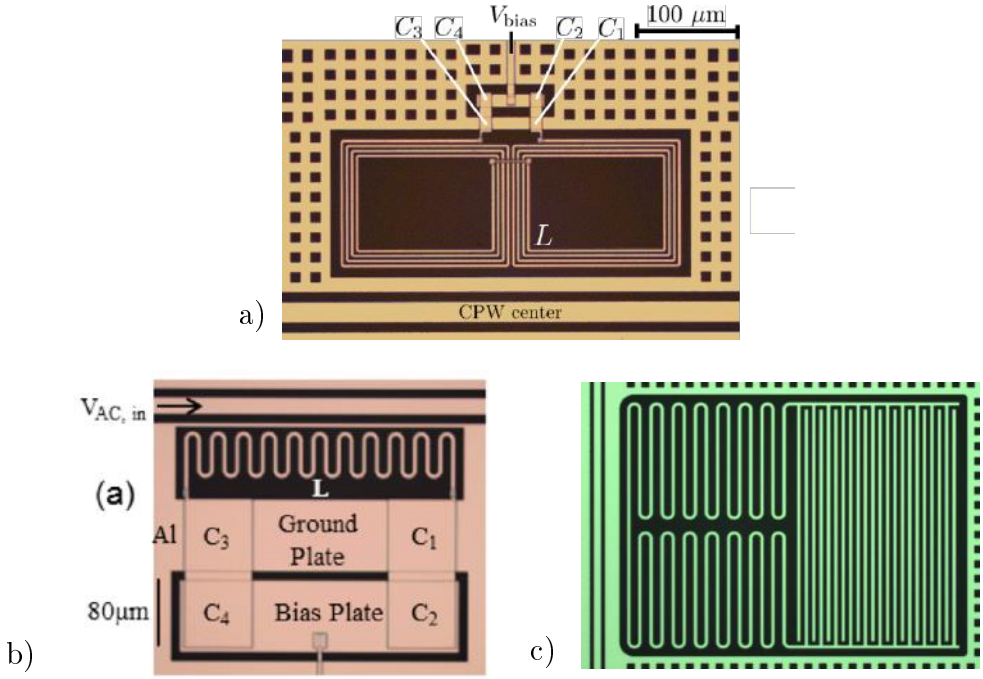

Figure 4: Examples of lumped element resonators that have previously been designed in the Osborn group. a) A lumped element resonator with large spiral inductor and small parallel plate capacitor b) is a smaller meander inductor with larger parallel plate capacitors c) A meander inductor with an interdigitated capacitor (IDC).

latter require multiple layers. The quality factor for an LCR resonator is $Q = \omega RC$. The resistance R take the form of the many different loss mechanisms a superconducting resonator is exposed to. As the name implies, one advantage of LE resonators is that the energy is from relatively small sized components. This ability to make compact designs can allow one to focus on the study of specific losses in a particular volume. In other words For example, a resonator designed with a parallel plate capacitor has the advantage of being compact and the advantage of testing a single dielectric but the disadvantage of having a high dielectric loss. However this concentration of loss to one area makes studying dielectric loss a useful tool in research.

We have examined the quasi-classical transport and the quantum hardware that is typical for superconducting quantum computing. Now I will treat the

fields in a fully quantum mechanical way starting with an LC resonator which is an important concept for superconducting qubit technology.

1.5 Quantization of LC Circuit

In order to better understand how to treat the electromagnetic field as a quantum system let's start with quantization of the LC circuit. In my thesis I will discuss the characteristics of resonators and qubits which act as harmonic oscillators in the case of resonators and anharmonic oscillators in the case of many qubits. Since a resonator and qubit system have a coupling related to LC circuits, one can understand them by first examining the equations of motion for one simple LC circuit [17]. Looking at the Lagrangian for a LC circuit

$$\mathcal{L} = T - U \tag{1.29}$$

Where T and U are the kinetic energy and potential energy of the system.

$$\mathcal{L} = C\dot{\Phi}^2/2 - \Phi^2/2L \tag{1.30}$$

The equation of motion is then

$$\frac{d}{dt}\frac{\partial \mathcal{L}}{\partial \dot{q}} - \frac{\partial \mathcal{L}}{\partial q} = 0 \tag{1.31}$$

Substituting equation 30 into equation 31 reveals the familiar harmonic oscillator:

$$L\ddot{q} + q/C = 0 \tag{1.32}$$

or

$$\ddot{q} + \omega^2 q = 0 \tag{1.33}$$

Where $\omega^2 = 1/LC$ and the solution of that differential equation is $q(t) = q_0 cos(\omega t)$. Recalling that the charge and flux operators do not commute $[\hat{\phi}, \hat{q}] = i\hbar$ one will identify ϕ as the canonical momentum where one will define the Hamiltonian

$$H = \partial\mathcal{L}/(\partial\dot{q}) = \mathcal{L}\dot{q}H = q\partial\mathcal{L}/(\partial\dot{q}) - \mathcal{L} \tag{1.34}$$

And finally substituting the expression for L

$$H = \Phi^2/2L + (L\omega^2 q^2)/2 \tag{1.35}$$

One can notice this is similar to the classical mechanical spring-mass system where one could substitute p→Q,x→ϕ,m→C,$m\omega^2$→1/L to regain

$$H = p^2/2m + m\omega^2 x^2/2 \tag{1.36}$$

To quantize this system one can again recall the non-commuting operators:

$[\hat{\phi}, q] = i\hbar$ or their classical mechanical equivalent $[\hat{x}, \hat{p}] = i\hbar$ If one defines the operator $\hat{X} = \sqrt{m\omega x}$ and $\hat{P} = \hat{p}/\sqrt{m\omega}$ then:

$$H = (P^2/2 + X^2/2)\omega \tag{1.37}$$

Then one can define the annihilation and creation operators,

$$\hat{a} = \sqrt{1/(2\hbar Z_r)}(\hat{\Phi} + iZ_r\hat{Q}) \tag{1.38}$$

$$\hat{a}^\dagger = \sqrt{1/(2\hbar Z_r)}(\hat{\Phi} - iZ_r\hat{Q}) \tag{1.39}$$

where, $Z_r = \sqrt{(L/C)}$ is the characteristic impedance of the resonator. The Hamiltonian becomes:

$$H = \hbar\omega(a^\dagger a + 1/2) \tag{1.40}$$

The Hamiltonian of the system is now the familiar harmonic oscillator:

$$H|\psi_n >= \hbar\omega(\widehat{N} + 1/2)|\psi_n >= \hbar\omega(n + 1/2)|\psi_n > \tag{1.41}$$

where

$$E_n = (n + 1/2)\hbar\omega \tag{1.42}$$

and where operator N tells the number of photons and $|n\rangle$is the photon number state

$$\widehat{N} = a^\dagger a \tag{1.43}$$

The operators $\hat{a}$ and $\hat{a}^\dagger$result in the emission or absorption of a photon to the field mode such that

$$\hat{a}|n\rangle = \sqrt{n}|n-1\rangle \tag{1.44}$$

and

$$\hat{a}^\dagger|n\rangle = \sqrt{n+1}|n+1\rangle \tag{1.45}$$

1.6 Cavity Quantum Electrodynamics

Cavity Quantum Electrodynamics or CQED examines atom or two-level system coupled to a cavity. For this, I will show derivations that culminate in the Jaynes-Cummings model, which will be used in subsequent sections. As stated, CQED deals with matter interacting with light generally, and looking at the Hamiltonians of each,

$$H = H_{atom} + H_{vac} + H_{int} \tag{1.46}$$

In the previous section, I showed how a LC resonator is equivalent to a harmonic oscillator. I will next show how we ultimately find the other Hamiltonians which govern most of the interactions seen from my devices in this thesis

$$H = \frac{1}{2}\hbar\omega_0\sigma_z + \sum_k \hbar\omega a_k^+ a_k + \hbar\sum_k (g_k\sigma^+ a_k + h.c.) \tag{1.47}$$

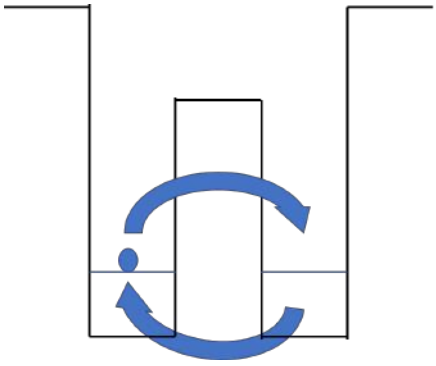

Figure 5: Double well potential is an example of a two level system where the particle can tunnel between the lowest energy levels in each well. A two level system defect is in a similar double well potential with asymmetric lowest energy levels.

Let's examine in general how a two level system couples to another environment to find the Rabi model. Two level systems can generally be spin 1/2 particles, such as a two level atom perhaps being probed by a laser at one of the atomic transition frequency. The most relevant case for us in this thesis however is the case of a particle in a double well potential. Consider something simple like below where the particle can only tunnel at some rate, $\Delta_0/\hbar$ between the lowest energy levels of two potential wells.

Now if we look at a system with two quantum energy levels and a Hamiltonian H_0. The eigenstate show

$$H_0|1\rangle = \hbar\omega_1|1\rangle \tag{1.48}$$

$$H_0|2\rangle = \hbar\omega_2|2\rangle \tag{1.49}$$

and thus

$$H_0 = \hbar\omega_1|1\rangle\langle 1| + \hbar\omega_2|2\rangle\langle 2| \tag{1.50}$$

and in matrix form

$$H_0 = \begin{bmatrix} \hbar\omega_1 & 0 \\ 0 & \hbar\omega_2 \end{bmatrix} \tag{1.51}$$

$$H_0 = \frac{\hbar}{2}\begin{bmatrix} \omega_2+\omega_1 & 0 \\ 0 & \omega_2+\omega_1 \end{bmatrix} + \frac{\hbar}{2}\begin{bmatrix} \omega_2-\omega_1 & 0 \\ 0 & -(\omega_2-\omega_1) \end{bmatrix} \tag{1.52}$$

$$= \frac{1}{2}\hbar(\omega_1+\omega_2)\hat{I} + \frac{1}{2}\hbar(\omega_2-\omega_1)\sigma_z$$

where $\sigma_z$is the Pauli operator

$$\sigma_z = \begin{bmatrix} 1 & 0 \\ 0 & -1 \end{bmatrix} \tag{1.53}$$

We can then create an atomic like Hamiltonian by defining $\hbar\omega_0 = \hbar\omega_2 - \hbar\omega_1$and setting $\frac{1}{2}\hbar(\omega_1+\omega_2) = 0$ we get that an atomic two level system Hamiltonian of

$$H_a = \frac{1}{2}\hbar\omega_0\sigma_z \tag{1.54}$$

The time evolution of the system is then

$$|\psi(t)\rangle = |1\rangle e^{-i\omega_1 t}\langle 1|\psi(0)\rangle + |2\rangle e^{-i\omega_2 t}\langle 2|\psi(0)\rangle \tag{1.55}$$

One can add a perturbation such as an external field so that $H = H_0 + W$

$$H = \begin{bmatrix} \hbar\omega_1 + W_{11} & W_{12} \\ W_{12}^* & \hbar\omega_2 + W_{22} \end{bmatrix} \tag{1.56}$$

If we choose a zero energy

$$E_0 = -\frac{1}{2}(\hbar\omega_1 + W_{11} + \hbar\omega_2 + W_{22}) \tag{1.57}$$

$$H = \begin{bmatrix} \frac{1}{2}(\hbar\omega_1 + W_{11} - \hbar\omega_2 - W_{22}) & W_{12} \\ W_{12}^* & -\frac{1}{2}(\hbar\omega_1 + W_{11} - \hbar\omega_2 - W_{22}) \end{bmatrix} \tag{1.58}$$

we can then define the detuning and Rabi frequency

$$\Delta = \omega_2 + W_{22}/\hbar - \omega_1 - W_{11}/\hbar \tag{1.59}$$

$$\Omega = 2W_{21}/\hbar \tag{1.60}$$

The detuning is the energy separation between the two energy levels and Ω represents the vacuum Rabi splitting or coupling between them. Below is called the two level Rabi model and we will use this in later sections to describe the

nanoscale TLS defect Hamiltonian.

$$H_0 = \frac{\hbar}{2}\begin{bmatrix} -\Delta & \Omega^* \\ \Omega & \Delta \end{bmatrix} \tag{1.61}$$

In a double well potential $\Delta = (E_L - E_R)/\hbar$ where $E_L$and $E_R$are the energy of the left and right wells.The eigenvalues are then

$$\omega_\pm = \pm\frac{1}{2\hbar}\sqrt{\Delta^2 + \Omega^2} \tag{1.62}$$

If there is coupling the degeneracy is lifted between the two eigenmodes and at $\Delta = 0$ the $E_{gap} = \hbar\Omega$

1.6.1 Interaction Hamiltonian

For this thesis the coupling of the qubit-resonator or TLS-resonator system is considered dipole coupling to an electric field. One can assume that the electric field is uniform across the TLS or qubit since the wavelength is much larger than the dipole length. Thus one can write the interaction of coupling Hamiltonian as

$$\hat{H}_{int} = -\hat{p} \cdot \hat{E} \tag{1.63}$$

where $\hat{p}$ is the electric dipole operator. The interactions works on the off diagonal terms and thus the diagonal dipole matrix elements vanish as a result of parity,

$$\langle e|\hat{p}|e\rangle = \langle g|\hat{p}|g\rangle = 0 \tag{1.64}$$

$\hat{p}$ can be composed as

$$\hat{p} = \hat{p}\hat{\sigma_+} + \hat{p}\hat{\sigma_-} = \hat{p}(\hat{\sigma_+} + \hat{\sigma_-}) \tag{1.65}$$

where $\hat{\sigma_+}$and $\hat{\sigma_-}$are the raising and lowering operators

$$\hat{\sigma}_+ = \begin{pmatrix} 0 & 1 \\ 0 & 0 \end{pmatrix} = |e\rangle\langle g|, \hat{\sigma}_+|g\rangle = |e\rangle, \hat{\sigma}_+|e\rangle = 0 \tag{1.66}$$

$$\hat{\sigma}_- = \begin{pmatrix} 0 & 0 \\ 1 & 0 \end{pmatrix} = |g\rangle\langle e|, \hat{\sigma}_-|e\rangle = |g\rangle, \hat{\sigma}_-|g\rangle = 0 \tag{1.67}$$

The quantized electric field $\hat{E}$ can be written as

$$\hat{E} = iu(r)\sqrt{\frac{2\pi\hbar\omega}{V}}(\hat{a} - \hat{a}^\dagger) \tag{1.68}$$

Combining the above equations gives

$$\hat{H}_{int} = i\hbar p \cdot u(r)\sqrt{\frac{2\pi\hbar\omega}{V}}(\hat{\sigma}_+ + \hat{\sigma}_-)(\hat{a} - \hat{a}^\dagger) \tag{1.69}$$

Then one can define a coupling term

$$g = p \cdot u(r)\sqrt{\frac{2\pi\hbar\omega}{V}} \tag{1.70}$$

where g demonstrates the atom-field coupling strength and the Hamiltonian becomes

$$\hat{H}_{int} = -i\hbar g(\hat{\sigma}_+ + \hat{\sigma}_-)(\hat{a} - \hat{a}^\dagger) \tag{1.71}$$

These operators will have a time dependence

$\hat{a}^\dagger(t) = \hat{a}^\dagger e^{i\omega t}$,$\hat{a}(t) = \hat{a}e^{i\omega t}$, $\hat{\sigma}_-(t) = \hat{\sigma}_- e^{-i\omega_0 t}$, $\hat{\sigma}_+(t) = \hat{\sigma}_+ e^{i\omega_0 t}$

and thus

$$\hat{H}_{int} = -i\hbar g(\hat{\sigma}_+\hat{a}e^{-i(\omega-\omega_0)t} + \hat{\sigma}_-\hat{a}e^{-i(\omega+\omega_0)t} + \hat{\sigma}_+\hat{a}^\dagger e^{i(\omega+\omega_0)t} + \hat{\sigma}_-\hat{a}^\dagger e^{i(\omega-\omega_0)t} \tag{1.72}$$

Near resonance ($\omega \simeq \omega_0$), the $e^{\pm i(\omega-\omega_0)t}$ terms vary slowly and allows those terms to accumulate effects from the atom-cavity interaction. The rapidly varying terms $e^{\pm i(\omega+\omega_0)t}$ will vanish since they are far from resonance. By using this rotating wave approximation (RWA), the interactions Hamiltonian reduces to

$$\hat{H}_{int} = -i\hbar g(\hat{\sigma}_+\hat{a} + \hat{\sigma}_-\hat{a}^\dagger) \tag{1.73}$$

Thus we see an intuitive picture which describes the conversion of atomic-like excitations to photonic excitations and vice versa. This is the fully derived Jaynes-Cummings Hamiltonian [46] when you add the atom-like term and the cavity term to the interaction terms

$$H_{JC} = \hbar\omega_r(a^\dagger a + 1/2) + \frac{1}{2}\hbar\omega_a\sigma_z + \hbar g(a^\dagger\sigma_- + a\sigma_+) \tag{1.74}$$

1.6.2 Jaynes-Cumming Model

In early atomic physics experiments were performed on a system with several identical atom-like systems coupled to a high-Q cavity in vacuum. The behavior of this coupled system is described by the Jaynes-Cummings Hamiltonian as derived in the previous section,

$$H_{JC} = \hbar\omega_r(a^\dagger a + 1/2) + \frac{1}{2}\hbar\omega_a\sigma_z + \hbar g(a^\dagger\sigma^- + a\sigma^+)$$

where ω_r is the frequency and the first term represents the energy of the resonator or electromagnetic field . The second term represents the two level system such as a qubit. As described in the previous section, the last term represents the interaction of the coupled system where the qubit can either emit $a^\dagger\sigma^-$or absorb $a\sigma^+$ a photon from the field.

One can find the eigenstates for the Hamiltonian. It is important to introduce the combined occupation number

$$\hat{n}_{com} = \hat{n} + \hat{n}_{atom} = \hat{a}^\dagger\hat{a} + \hat{\sigma}_+\hat{\sigma}_- \tag{1.75}$$

Obviously the occupation number commutes with $\hat{a}^\dagger\hat{a}$ and $\hat{\sigma}_+\hat{\sigma}_-$, such that $[\hat{n}_{com}, \hat{\sigma}_+\hat{\sigma}_-] = [\hat{n}_{com}, \hat{a}^\dagger\hat{a}] = 0$ and then

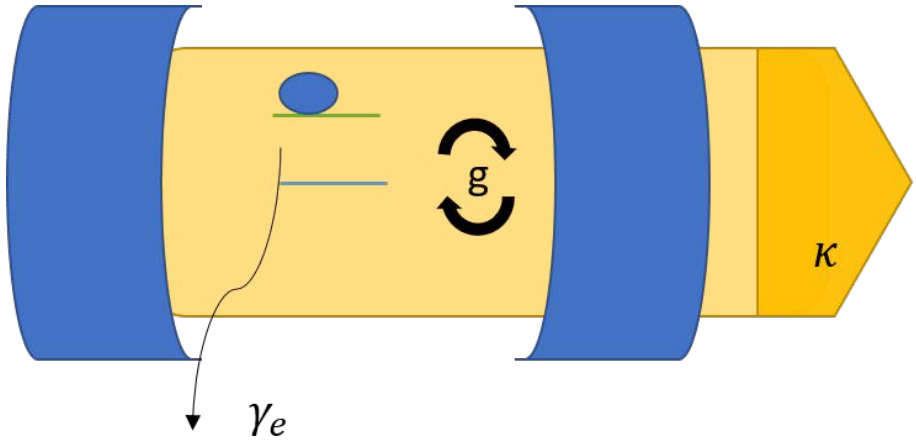

Figure 6: Diagram showing the different channel through which matter and light can interact. The atom-like two level system can lose a photon to the cavity at rate $\gamma_e$or decay with relaxation time T_1. The two level system can couple to the cavity at rate $g/2\pi$. The cavity can lose a photon externally at rate κ or emit a photon to the two level system.

$$[\hat{n}_{com}, \hat{H}_{JC}] = -i\hbar g([\hat{n}_{com}, \hat{a}\hat{\sigma}_+] + [\hat{n}_{com}, \hat{a}^\dagger\hat{\sigma}_-] \tag{1.76}$$

Through simple algebra can then show that

$$[\hat{n}_{com}, \hat{H}_{JC}] = 0 \tag{1.77}$$

This means they share the same set of eigenstates. Furthermore $[\hat{n}, \hat{n}_{atom}] = 0$ since they operate on different subspaces and thus share a common set of eigenstates but have different eigenvalues. Then we can look at a set of basis states for the total Hamiltonian as

$$|n, s\rangle = |n\rangle \otimes |s\rangle = \{|n, g\rangle, |n, e\rangle, n = 0, 1, 2, ...\} \tag{1.78}$$

These are called bare states where the eigenvalue equation holds

$$\hat{n}_{com}|n,s\rangle = (n + n_{atom})|n,s\rangle \tag{1.79}$$

The atom has only two states that contribute to the Hamiltonian. In the bare-state basis this is

$$\hat{H}_{JC} = \sum_{n,n'=0}^{\infty} \sum_{s,s'=e,g} |n,s\rangle\langle n,s|\hat{H}_{JC}|n',s'\rangle\langle n',s'| \tag{1.80}$$

using simple algebra with the annihilation operators and raising and lowering operators,

$$\hat{a}^{\dagger}\hat{\sigma}_{-}|n,e\rangle = \sqrt{n+1}|n+1,g\rangle \tag{1.81}$$

$$\hat{a}\hat{\sigma}_{+}|n+1,e\rangle = \sqrt{n+1}|n,e\rangle \tag{1.82}$$

one finds that since the interaction Hamiltonian only couples pairs of bare states, for $n > 0$ the Hamiltonian decouples into an infinite direct product of 2x2 matrix Hamiltonians with elements

$$\hat{H}_n = \begin{pmatrix} \hbar\omega n + \frac{1}{2}\hbar\omega_0 & \hbar g\sqrt{n+1} \\ \hbar g\sqrt{n+1} & \hbar\omega(n+1) - \frac{1}{2}\hbar\omega_0 \end{pmatrix} \tag{1.83}$$

Diagonalizing the matrix the eigenenergies are

$$E_{\pm} = \hbar\omega(n + 1/2) \pm \frac{1}{2}\hbar\omega_{R,n} \tag{1.84}$$

where the eigenfrequencies $\omega_{\pm} = E_{\pm}/\hbar$ where

$$\omega_{R,n} = \sqrt{\Delta_{\omega}^2 + 4g^2(n+1)} \tag{1.85}$$

This is known as the Rabi frequency as we saw earlier in the simplified equation 1.22 and the detuning $\Delta_{\omega} = \omega - \omega_0$. The eigenstates are

$$|n+1,+\rangle = \sqrt{\frac{\omega_{R,n} + \Delta_{\omega}}{2\omega_{R,n}}}|n+1,e\rangle + \sqrt{\frac{\omega_{R,n} - \Delta_{\omega}}{2\omega_{R,n}}}|n+2,g\rangle \tag{1.86}$$

$$|n+1,-\rangle = -\sqrt{\frac{\omega_{R,n} - \Delta_{\omega}}{2\omega_{R,n}}}|n+1,e\rangle + \sqrt{\frac{\omega_{R,n} + \Delta_{\omega}}{2\omega_{R,n}}}|n+2,g\rangle \tag{1.87}$$

As we saw earlier there is a degeneracy in the states $|n+1,g\rangle$and $|n,e\rangle$ in the case of zero detuning. In the coupled system as shown in the ladder states the uncoupled $|0,e\rangle$and $|1,g\rangle$ are split by the vacuum Rabi frequency $\omega_{R,0}$and the degeneracy is lifted. Additionally the splitting is dependent on the number of photons as you can see in the ladder states in Figure 7.

This is a quantum-mechanical phenomenon this is not expected or can be seen from classical physics.

It is useful to look at the time evolution of the dressed states. If an atom-

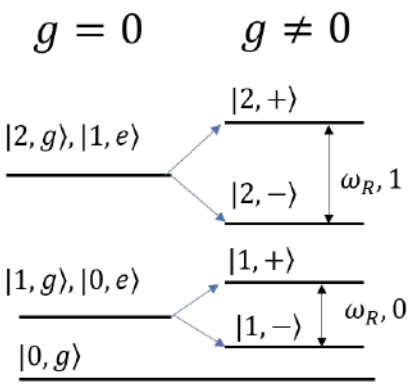

Figure 7: The ladder show the energy levels of the Jaynes-Cummings Hamiltonian at different photon numbers that are available when there is no coupling, g=0 and when there is coupling. It is clear that the coupling breaks the degeneracy of the ground and excited states. Interestingly the gap between the two states now has a dependence on the photon number $\sqrt{n}$

like TLS in the excited state interacts with a single-mode field the system can written as [47]

$$|\psi(t)\rangle = \sum_{n=0}^{\infty} C_e(t) \frac{e^{-|a|^2/2}\alpha^n}{\sqrt{n!}} |n, e\rangle + C_g(t) \frac{e^{-|a|^2/2}\alpha^n}{\sqrt{n!}} |n+1, g\rangle \tag{1.88}$$

where α is the coherent state amplitude and the factor of $e^{-|a|^2/2}\alpha^n/\sqrt{n!}$ comes from the Poisson distribution of photon numbers. $|\alpha|^2 = \bar{n}$ where $\bar{n}$ is the average number of photons in the cavity. From the Schrodinger's equation and using $C_e(0) = 1$ and $C_g(0) = 0$ at resonance

$$C_e(t) = \cos(g\sqrt{n+1}t) \tag{1.89}$$

$$C_g(t) = i\sin(g\sqrt{n+1}t) \tag{1.90}$$

Then the probability of finding the atom in the excited state is

$$P_e(t) = \sum_{m=0}^{\infty} |\langle m, e|\psi(t)\rangle|^2 = e^{-|a|^2} \sum_{n=0}^{\infty} \frac{\alpha^n}{\sqrt{n!}} \cos^2(g\sqrt{n+1}t) \tag{1.91}$$

Figure 8 shows $P_e(t)$ as a function of the scaled gt for an average photon number of 10. This is the fully quantum mechanical approach which has oscillations that undergo a number of collapses and revivals [55], where the semi-classical model has Rabi oscillations that have a constant amplitude.

1.7 Overview of Thesis

So far I have reviewed some of the underlying theory for my research. I have analyzed conduction in superconductors. I have quantized the atom-like two level system which will represent a qubit or TLS defect. And then I quantized the interaction between the two and completed the derivation for the Jaynes-Cummings Hamiltonian. I discussed the different types of resonators that will appear in this thesis and motivated the importance of understanding the energy loss and conductivity in superconductors. Next I will review the theory of the standard tunneling model which describes the two level system defects. These defects plague superconducting qubits and are a major limiter to coherence in qubits. I will discuss the eigenmodes and the energies involved

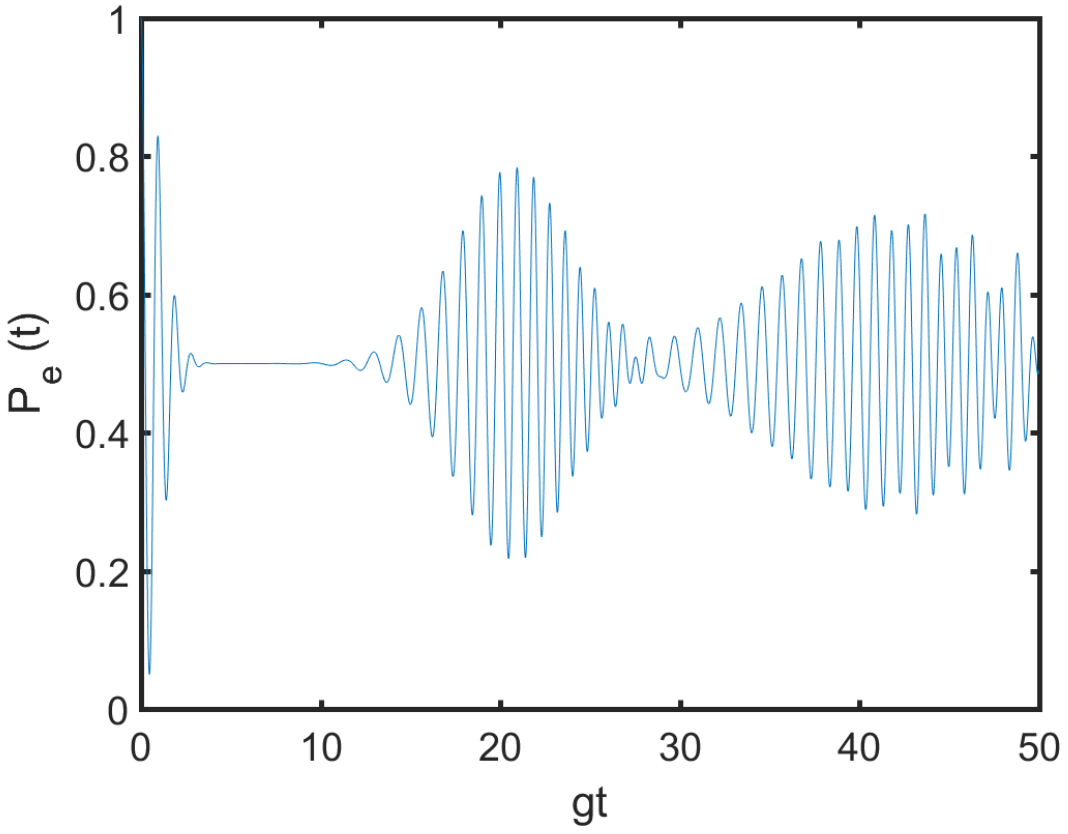

Figure 8: The probability of being in the excited state with $|\alpha|^2 = \tilde{n} = 10$. $P_e(0) = 1$.The graph shows how the oscillations disappear or "collapse" and after a few Rabi cycles one can see them return in so called "revivals".

in the TLS system and how one can tune their energies to learn about their characteristics. Then I will talk about the circuit theory behind measuring a resonator coupled to a transmission line and specifically how to extract the quality factor from the transmission S_{21}. I will then go into detail about the resonators and qubit designs and experimental results. I will discuss one of the first observations of individual surface TLS in a resonator using an on chip voltage bias. Then I will discuss an unexpected loss transition in thin TiN that is observed with a small change in film thickness. I will talk about the significance of each observation and how these results help the overall understanding of the underlying loss mechanisms.

2 Nanoscale Two Level System Defects

In 1970s Zeller and Pohl showed that indeed the thermal properties of amorphous and crystalline materials below 1K act remarkably different[38]. Crystalline insulating materials at the time were easily described by the Debye theory which treated the atomic vibrations as phonons confined in the solid. It predicted a T^3 temperature dependence of the heat capacity,C. Not only did it debunk that crystals and amorphous solids are different at low temperature but it showed a universality among amorphous materials. They showed that whether the material be an oxide glass, or inorganic or organic polymer, the specific heat varied linearly at low temperatures as the thermal conductivity varied as T^2. The specific heat capacity is $c_p = \frac{C}{M}$ where C is the heat capacity in units of Joules/K and M is the mass. This led to significant interest in the conductivity at low temperature of amorphous materials.

Within years several theories had emerged attempting to understand the thermal conductivity and specific heat such as dispersive or damped phonons[39] , or scattering from structural inhomogeneity [40]. Eventually, it was resolved that TLSs can explain the phenomena properly, as described in separate theories by Phillips, and Anderson, Halperin, and Varma [41],[42]. The theory was later accepted and became known as the Standard Tunneling Model. Relevant to the density of these TLSs, the absolute value of thermal conductivity and internal friction was found within an order of magnitude of each other [38]. This became important later in quantum computing when people tried to study TLS as defects in the dielectrics, and change the material type. I

will discuss the results of Dr. Bahman Sarabi who would show cavity QED analyzing TLSs in a Si_3N_4 tri-layer capacitor[32].

2.1 Standard Tunneling Model

The dielectric (or electric-field) loss is the predominant loss mechanism and decoherence source for many superconducting qubits. In contrast, there is often very little loss observed in the inductor (corresponding to a nearly zero resistance in series) far below the critical temperature T_c in conventional superconductors, such as Aluminum. Dielectric loss arises in TLSs, presumed to be atoms or a group of atoms, that reside in amorphous dielectrics. As mentioned earlier, the theory is called the STM. The STM assumes that in disordered solids, certain TLSs have two accessible potential minima. The standard model for the TLS uses a double-well potential, as shown in Figure 9. At millikelvin temperatures, we assume that the relevant TLS coordinate (angle or position)is restricted to the ground states of the two wells (L and R, for left well and right well), and that only the two lowest energy levels are important. The TLSs have a uniform spatial distribution in the bulk of an amorphous dielectric. Also, in the STM, the barrier heights between the wells is assumed to be uniform, and this gives rise to a logarithmic distribution in the tunneling energy, Δ_0

$$d^2n = P_0 d\Delta \frac{d\Delta_0}{\Delta_0} \tag{2.1}$$

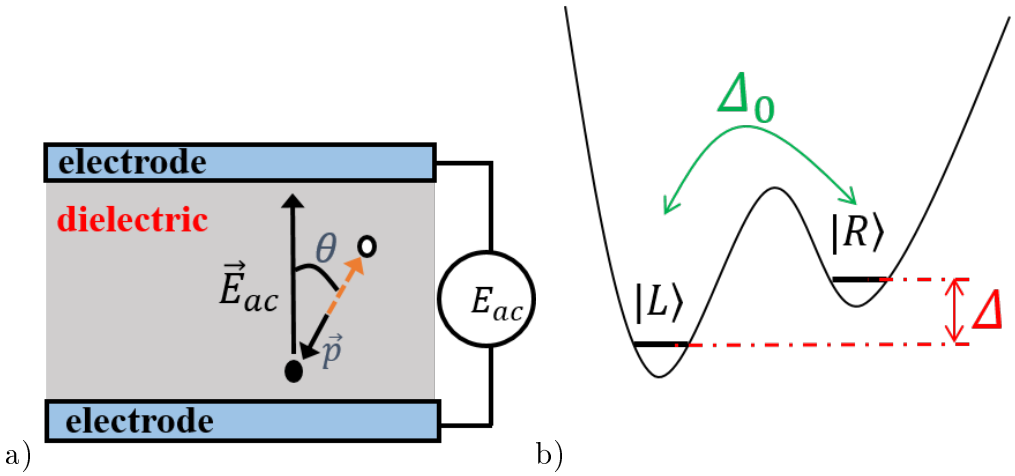

Figure 9: a) Diagram showing a parallel plate capacitor and a defect TLS with dipole moment p with an angle θ between the dipole moment and the electric field $\vec{E_{ac}}$b) is an energy diagram showing the double well potential which describes the ground state of the two wells, left $|L\rangle$ and right $|R\rangle$, that the defect can reside in. The defect TLS has a tunneling energy $\Delta_0$and an asymmetry energy Δ.

Throughout the rest of the thesis I may refer to these nanoscale two level system defects as simply TLSs.

One can write the Hamiltonian of the two level system from the STM as

$$\hat{H} = \hat{H}_L + \hat{H}_R + qV \tag{2.2}$$

where we then had defined $\Delta = (E_L - E_R)/\hbar$ where $E_L$and $E_R$are the energy of the left and right wells. The tunneling matrix element is defined as $\Delta_0 = \frac{1}{\hbar}\langle\psi_L|T|\psi_R\rangle$. This defines the Hamiltonian as

$$\hat{H} = \frac{\hbar}{2}\begin{bmatrix} -\Delta & \Delta_0^* \\ \Delta_0 & \Delta \end{bmatrix}, \tag{2.3}$$

with eigenvalues

$$\omega_{\pm} = \pm\frac{1}{2\hbar}\sqrt{\Delta^2 + \Delta_0^2}. \tag{2.4}$$

Due to the coupling (tunneling) between the wells the degeneracy is lifted, and at $\Delta = 0$, the energy difference$E_{gap} = \hbar\Delta_0$.

Below we consider how adding a drive effects the Hamiltonian.

2.1.1 TLS with interacting field

When we add a perturbation or external field, E for a charged TLS with electric dipole $p = qd/2$ where d is the separation distance between the wells.

$$\hat{H} = \begin{bmatrix} \hbar\omega_1 + W_{11} & W_{12} \\ W_{12}^* & \hbar\omega_2 + W_{22} \end{bmatrix} \tag{2.5}$$

Using $W = 2p \cdot E$ and choosing a new ground state energy

$$E_0 = -\frac{1}{2}(\hbar\omega_1 + W_{11} + \hbar\omega_2 + W_{22}) \tag{2.6}$$

and then introducing a detuning, Δ,which is the energy difference between the perturbed states and Rabi Frequency, Ω,which is the strength of the coupling. We have

$$\Delta = \omega_2 + W_{22}/\hbar - \omega_1 - W_{11}\hbar \tag{2.7}$$

$$\Omega = 2W_{21}/\hbar$$

The Hamiltonian can then be rewritten

$$H^{'} = \frac{\hbar}{2}\begin{bmatrix} -\Delta & \Omega^{*} \\ \Omega & \Delta \end{bmatrix} \tag{2.8}$$

or

$$H^{'} = \frac{e}{2}\begin{bmatrix} D & 2M \\ 2M & -D \end{bmatrix} \tag{2.9}$$

where D represents the energy shift of the relaxing states in the field and the elements 2M describe the TLS coupling strength for the resonant interactions.

This is equivalent to the spin 1/2 particle in a magnetic field B with a perturbing field B_0, $B^{'} = B + B_0$ where $\Delta$is the Zeeman splitting and Ω is the applied magnetic field along the off axis. We can then continue in this basis where the corresponding Hamiltonian is

$$H = -\hbar\gamma(BS) = \hbar\gamma(B_0 S) - \hbar\gamma(B^{'}S) = H_0 + H \tag{2.10}$$

where γ is the gyromagnetic ratio and S is the spin. Using the Pauli matrices

$$\sigma_x = \begin{bmatrix} 0 & 1 \\ 1 & 0 \end{bmatrix} \tag{2.11}$$

,

$$\sigma_y = \begin{bmatrix} 0 & -i \\ i & 0 \end{bmatrix} \tag{2.12}$$

,

$$\sigma_z = \begin{bmatrix} 1 & 0 \\ 0 & -1 \end{bmatrix} \tag{2.13}$$

one can write the effective fields as

$S = \frac{1}{2}\sigma, -\hbar\gamma B_0 = (0, 0, E_t)$, $-\hbar\gamma B' = (\frac{2\Delta_0}{\epsilon} p \cdot E, 0, \frac{2\Delta}{\epsilon} p \cdot E)$

If we assume zero loss and infinite TLS (spin) lifetime the motion can be described by

$$\frac{d}{dt} S(t) = \gamma S \times B \tag{2.14}$$

For a finite lifetime the situation we can think use the Bloch equations developed for nuclear magnetic resonance experiments (NMR)[115]. These differential equations describe the relaxation of a TLS ensemble.

$$\frac{d}{dt}\langle S_x(t)\rangle = \gamma(\langle S_y\rangle B_z - \langle S_z\rangle B_y - T_2^{-1}\langle S_x\rangle \tag{2.15}$$

$$\frac{d}{dt}\langle S_y(t)\rangle = \gamma(\langle S_z\rangle B_z - \langle S_x\rangle B_y - T_2^{-1}\langle S_y\rangle \tag{2.16}$$

$$\frac{d}{dt}\langle S_z(t)\rangle = \gamma(\langle S_x\rangle B_z - \langle S_y\rangle B_y - T_1^{-1}\langle S_x\rangle + T_1^{-1} S_z^l |B_z(t)| \tag{2.17}$$

where $T_1$and T_2 are the longitudinal and transverse relaxation times. The difference in the population of the two levels due to thermal excitations is

$$S_z^l|B_z(t) = \frac{1}{2}\tanh(\hbar\gamma B_z(t)/2k_BT) \tag{2.18}$$

T_1^{-1} is the rate at which a non-equilibrium population relaxes into equilibrium through absorption or emission of phonons or photons. Whether absorption or emission the rate will always pull the system back into equilibrium. For a tunneling TLS it is known [48, 4]that the phonon emission is

$$T_1^{-1} = (\frac{\Delta_0}{\epsilon})^2 T_{1,min}^{-1} \tag{2.19}$$

where

$$T_{1,min}^{-1} = \left[\frac{M_L^2}{v_L^5} + \frac{2M_T^2}{v_T^5}\right]\frac{\epsilon^3}{2\pi\rho\hbar^4}\coth(\epsilon/2k_BT) \tag{2.20}$$

$T_{1,min}$is the minimum T_1 time for a TLS with energy ϵ. M_L and M_T are the longitudinal and transverse phonon deformation potentials. $v_L$and v_T are the longitudinal and transverse velocities, and ρ is the mass density of the material.

T_2 is the coherence time and the quantity $2T_2^{-1}$ in the Bloch equation is the spectral linewidth of an ensemble of TLS that take part in the resonant absorption at a given frequency. Several mechanisms can cause limitations in the coherence time. The most significant are the relaxations of the TLS and any interaction between the TLS which can broaden the spectral linewidth.

Essentially one can categorize the broadening into relaxation processes set by T_1 and phenomena that affect the phase of the precessing TLSs, set by the dephasing time T_ϕ. These are related to T_2 by[41],

$$T_2^{-1} = \frac{1}{2}T_1^{-1} + T_\phi^{-1} \tag{2.21}$$

Using the Bloch equations the attenuation length $l_{res}$is an amorphous solid at acoustic intensity J is

$$l_{res}^{-1} = l_0^{-1}\frac{\tanh(\hbar\omega/2k_BT)}{\sqrt{1+J/J_C}} \tag{2.22}$$

where

$$l_0^{-1} = \pi n_0 M^2 \omega/\rho v^3 \tag{2.23}$$

is the low intensity limit of the attenuation length at zero temperature in terms of the density of states, n_0 of TLS energy splitting where the critical intensity is

$$J_C = \hbar^2\rho v^3/2M^2T_1T_2 \tag{2.24}$$

Similar to acoustic attenuation, the loss tangent of an amorphous dielectric caused by the distribution of randomly oriented TLS dipole coupled to an AC electric field is found to be

$$\tan\delta = \tan\delta_0 \frac{\tanh(\hbar\omega/2k_BT)}{\sqrt{1+\omega_R^2 T_{1,min} T_2}} \tag{2.25}$$

where the low power limit of the loss tangent is

$$\tan\delta_0 = \frac{\pi P_0 p^2}{3\epsilon} \tag{2.26}$$

and the characteristic Rabi frequency of the ensemble is

$$\omega_R = \frac{2pE}{\sqrt{3}\hbar} \tag{2.27}$$

but for an individual TLS it is

$$\omega_R = \frac{\Delta_0}{\epsilon} \frac{2\boldsymbol{p}\cdot\boldsymbol{E}}{\hbar} \tag{2.28}$$

There is additionally a critical electric field amplitude E_C

$$E_C = \frac{\sqrt{3}\hbar}{2p\sqrt{T_{1,min}T_2}} \tag{2.29}$$

We can then combine equations and the loss tangent can be written in terms of the electric field amplitudes as

$$\tan\delta = \tan\delta_0 \frac{\tanh(\hbar\omega/2k_BT)}{\sqrt{1+(E/E_C)^2}} \tag{2.30}$$

At low temperatures and low power the TLSs are generally in the ground state and actively participate in photon absorption and emission processes,

hence causing maximum dielectric loss (tan = $\tan\delta_0$). For increasing drive power, the TLSs with $E \simeq \hbar\omega$ interact most strongly with the field. When the power or field reaches a certain critical threshold (E_C) TLS are excited at the Rabi-frequency that exceeds their loss rate, $\Omega_R >> 1/\sqrt{T_1 T_2}$. This will saturate the TLS, bringing their probability of being excited to 1/2 (equally likely to absorb or emit a photon). This reduces the number of TLSs in the ground state available for additional photon absorption, and the loss tangent decreases. In this high-power limit, $E >> E_C$, loss tangent decreases as E^{-1} . I will often refer to the equation above when I talk about the power dependence of the loss or the internal quality factor Q_i where for full participation $\tan\delta = Q_i^{-1}$.

2.2 Surface Loss Theory

Understanding surface TLS is paramount to improving the coherence in superconducting qubits. It is known that surface TLS significantly hinder the Q_i in resonators and qubits[43, 44, 45]. Most attempts to mitigate loss from TLS through very clean fabrication [54]or making structures larger to reduce the participation ratio.

For an LC resonator on resonance the magnetic energy W_M stored is equal to the electric energy W_E and thus the total energy

$$W_T = 2W_E \tag{2.31}$$

The power loss per unit volume is σE^2,where the conductivity $\sigma = \omega\epsilon \tan\delta_0$ for a dielectric volume with permitivity ϵ and quantum-regime loss tangent $\tan\delta_0$ and frequency ω, and E is the electric field magnitude. The power loss in the volume is

$$P_L = \int d^3r\omega\epsilon\left(r\right)\tan\delta_0\left(r\right)\left|E^2(r)\right| \tag{2.32}$$

The quality factor for a co-planar film is

$$Q = \frac{\omega W_E}{P_L} \tag{2.33}$$

The maximum electric energy stored is

$$W_E = \int d^3r|(E\left(r\right)^2\left|\epsilon\left(r\right)\right. \tag{2.34}$$

therefore the quality factor is

$$Q = \frac{\int d^3r|(E^2(r)|\epsilon\left(r\right)}{\int d^3rtan\delta_0\left(r\right)\left|E^2(r)\right|\epsilon\left(r\right)} \tag{2.35}$$

The volume integrals can be turned into summations to account for different TLS hosts. We can simulate the electrostatic field distribution $|E(r)|$ at different interfaces using the finite element solver COMSOL. We properly model microwave fields electrostatically because we generally look at local fields, which are much smaller than the wavelength. Also, the penetration depth in the superconductor is small relative to the electrode thickness for

Aluminum. The summation can be reduced to 2 dimensions. Assuming the zth dimension is uniform, it can be canceled out of the formula and the quality factor would then become

$$Q = \frac{\sum_i \Delta A |E_i|^2 \epsilon_i}{\sum_i \Delta A |E_i|^2 \tan\delta_i \epsilon_i} \tag{2.36}$$

where i represents the different interfaces where the TLS defects reside and where $\Delta A = \Delta x \Delta y$ where Δx and Δy are the step size. One can then introduce a participation ratio as

$$p_i = \frac{\sum_i \Delta A |E_i|^2 \epsilon_i}{\sum_{tot} \Delta A |E_i|^2 \epsilon_i} \tag{2.37}$$

where $\sum_{tot} \Delta A |E_i|^2 \epsilon_i = \sum_{MS} \Delta A |E_{MS}|^2 \epsilon_{MS} + \sum_{SA} \Delta A |E_{SA}|^2 \epsilon_{SA} + \sum_{MA} \Delta A |E_{MA}|^2 \epsilon_{MA}$ which allows for equation to be rewritten as

$$Q = \sum_i p_i \tan\delta_i \tag{2.38}$$

The lossy surfaces that host TLSs are at the Substrate-Air (SA), Metal-Substrate (MS), and Metal-Air (MA) interfaces. I will discuss these interfaces in following sections and focus on the experiments on loss in chapter 5.

Loss is proportional to $|E|^2$and we can integrate $|E|^2$with respect with distance from the corner to account for surface loss in a representative cross section. We can fit the curve from Figure 10 to obtain an equation of the electric field as a function of distance. From the fit for relevant medium, lengths, we find the power law

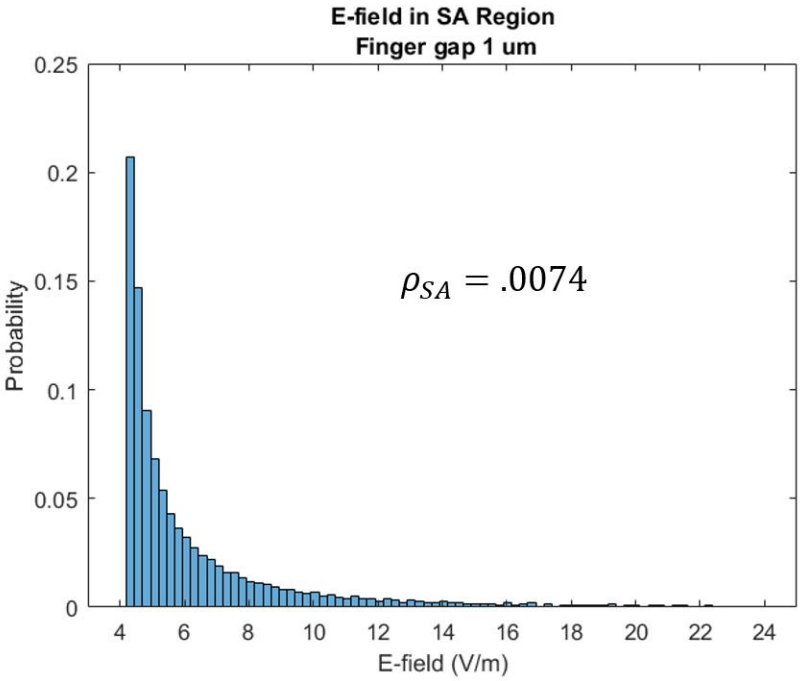

Figure 10: Electric field distribution of the Substrate-Air (SA) interface in a film with LW=LS=1μm. In this work a 3 nm thick dielectric layer at the MS,SA, and MA interface is assumed. The participation ratio for the SA volume is .0074. The complete model will discussed for this in chapter 5.

$$|E|^2 = As^{-1}. \tag{2.39}$$

Within one structure we have a power loss that is approximately

$$P_{l,i} = lt\omega\epsilon \tan\delta_{0,i} \int |E(s)|^2 ds, \tag{2.40}$$

for lossy thickness t and finger length l. It is interesting to numerically integrate in 1D for an estimate of the loss near corners. Here we choose 1nm as a sufficiently small grid, because discrete TLS effects at shorter distances will not model true experimental loss. However, we also integrate in 2D in COMSOL to precisely calculate dielectric variations within a host thickness layer. In order to calculate the loss, the integrals are changed to summations

$$P_l/l = \omega\epsilon \tan\delta_0 \sum_i |E_i|^2 \Delta A, \tag{2.41}$$

where $\Delta A = \Delta x \Delta y$ where Δx and Δy are the step size in the x and y direction in the COMSOL simulation.

Using this method we can then look at all the different TLS interfaces. Additionally we can plot the ratio of the loss as a function of distance from the corner at each interface

Strong coupling will be addressed below. The accumulated loss approaching a corner in at a particular interface i can be written as:

$$\tan\delta_{0,i}(s) = \tan\delta_{0,i} p_i, \tag{2.42}$$

where

$$p_i = \frac{\int_{tls} \epsilon(s) E_i^2(s) ds}{\int_{tot} \epsilon(s) E_{tot}^2(s) ds} \tag{2.43}$$

where the denominator is the total energy in the unit cell.

2.2.1 Standard material of TLS density distribution

In this section I will discuss the TLS density distribution and how we can solve for finding the total number of TLSs in bandwidth of a resonator per bias voltage. This will allow us later to determine the number of strongly coupled TLSs one can expect to find in a particular bias range.

A standard material can have the following TLS density distribution. We can consider it parallel to the field (z).

$$d^2 n = P\left(p_{\|}\right) d\Delta \frac{d\Delta_0}{\Delta_0}, \tag{2.44}$$

We can simplify if we are only interested in the measurement of degenerate wells (hyperbola) picked out a range of delta near $\hbar\omega_r$. More over if the total energy of the TLS $\epsilon = \sqrt{\Delta^2 + \Delta_0^2}$ and if we are only interested in TLS at minimum energy where the asymmetry energy Δ is close to 0 then we can say that $\epsilon = \Delta_0$and

$$\frac{d\Delta_0}{\Delta_0} = \frac{d\hbar\omega_r}{\hbar\omega_r} = \frac{d\omega_r}{\omega_r} = \frac{\kappa}{\omega_r}$$

The measurement focuses on a fractional bandwidth $d\omega = \kappa$ and where

$1/Q_e = \kappa/\omega_r = B/f_r$ about the resonance frequency ω_r. This simplifies the equation to

$$dn = P(p_z)\, d\Delta \frac{B}{f_r}, \tag{2.45}$$

The TLS are biased by one field which makes a given TLS shift in asymmetry energy by

$$\Delta' = \Delta + 2p_z E_{bias}, \tag{2.46}$$

where z is a fixed direction due to a fixed field $\mathbf{E}_{bias} = E_{bias}\hat{z}$.This gives $dn = P(p_z)\, d(\Delta + 2p_z E_{bias}) \frac{B}{f_r}$. The measurement observed the number of TLS per change in E_{bias} for $\Delta' = 0$, which gives

$$dn/dE_{bias} = \frac{2B}{f_r} p_z P(p_z). \tag{2.47}$$

The measured density of TLSs is $\propto p_z P(p_z)$, however a simple division by p_z allows one to get the material distribution from the measured distribution. This derivation will be modified later in chapter 5 to calculate the number of TLS expected from TLS at the different interfaces.

2.3 Background & Previous Studies of Measuring TLS

Two Level System defects are a ubiquitous loss mechanism in superconducting resonators and resonators as well as a source of noise in MKIDs [51]. The

microscopic physical origin of TLS is largely unknown and is thought to be tunneling atoms or a system of atoms that reside and can tunnel in dielectrics [10]. Some have shown that the loss is correlated with the density of OH^-ions [62].These defects can be seen as charged particles with dipoles interacting with an external field. Furthermore these TLS can be pictured to reside in dielectric in a parallel plate manner or in any oxide or nitride region surrounding a metal. These defects can then couple to the system through their dipole moment. Martinis proved that higher quality dielectrics can lead to improved coherence times in phase qubits leading to research in finding lower loss dielectrics[67]. It was Paik and Osborn showed that the loss tangent of SiN_xdepended on the flow rate of the nitrogen during the film deposition[64]. While weakly coupled TLS generally act in an ensemble it is possible to observe individual TLS in the strong coupling regime. Recently, there have been techniques using dc-electric field [32, 33] or strain to modulate TLSs energies in silicon nitride or in alumina respectively.

Dr. Sarabi observed individual TLS in low volume, SiNx tri-layer capacitors as shown in Figure 12[59] [11]. To see TLS a strong coupling between the TLS and resonator is needed as well as a high zero-point fluctuation voltage. The equation for strong coupling in a tri-layer capacitor is

$$g = \frac{\Delta_0}{\epsilon} p \cos\theta \sqrt{\frac{\omega_0}{2\epsilon_r \epsilon_0 \hbar V ol}} \tag{2.48}$$

where Vol is the volume of the capacitor. Thus it can be seen that having a small volume capacitor allows for high couplings in tri-layer capacitors.

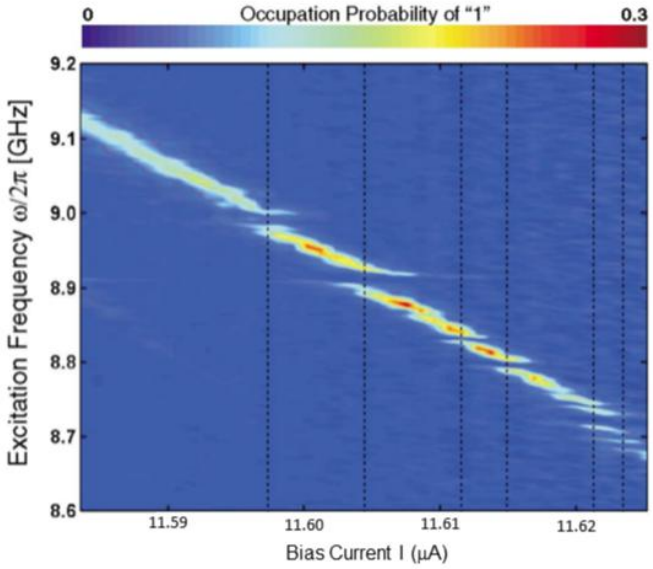

Figure 11: Evidence of defects from splittings, [68]. In later works these were identified as TLS tuned in frequency of the qubit mode from a phase qubit measurement[116]

Additionally the zero point fluctuation voltage is

$$\frac{1}{2}\hbar\omega_0 = CV_{zpf}^2 \tag{2.49}$$

and thus to get a low zero-point fluctuation voltage a low capacitance value is necessary.

I have established the background for measuring TLS in qubits and resonators and described new theory for studying surface TLSs. Next I will discuss the theory behind actually measuring a resonator coupled to a feedline.

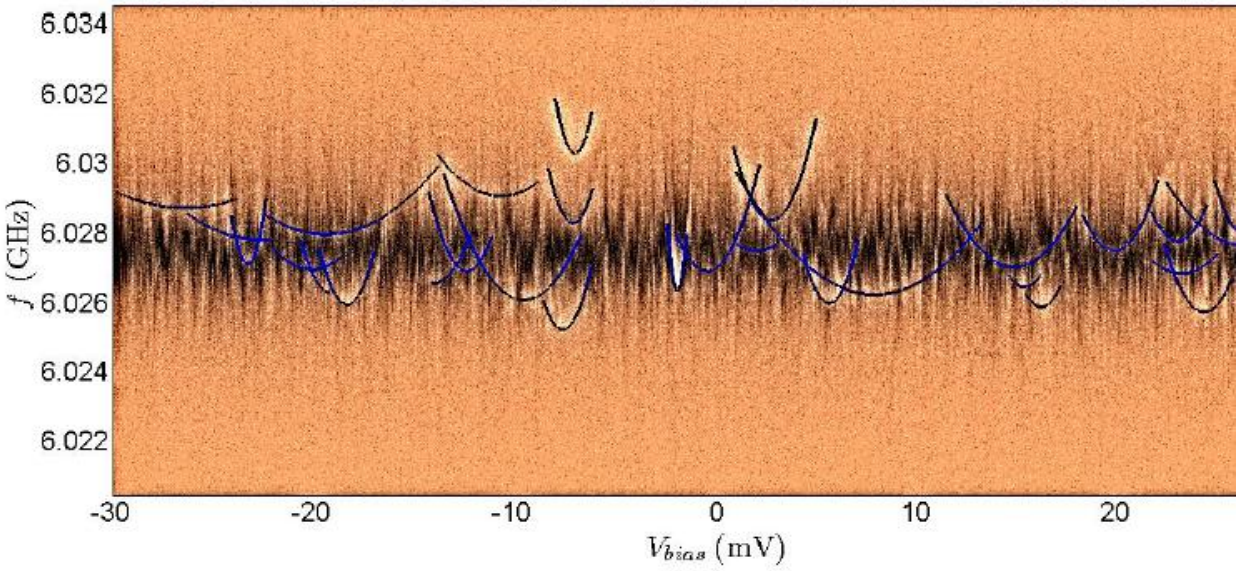

Figure 12: The transmission as a function of frequency and the bias voltage for a biased tri-layer LC resonator[32]. One can see several hyperbola which show how the TLS defects move in energy with bias.

3 Resonance Lineshape & Measurement Theory

As discussed I have designed CPW as well as lumped element resonators to measure the different loss mechanisms that affect the resonators lineshape. The full width half max (FWHM) is often used to determine the internal or external loss of a resonator. This FWHM is a measure of the decay in the resonator. More accurate analysis involves analyzing the transmission, $|S_{21}|$ of a resonator coupled to a transmission line. A circuit model can be used to capture the different impedances, mismatches and couplings involved. I will go through steps using KVL to determine the transmission through a particular circuit. This method will reduce down to equations that are similar to what has been done previously [59].

3.1 Circuit Analysis

For typical resonator measurement a signal is sent through wire bonds onto a transmission line onto the chip and off through wire bonds. A single resonator coupled to this transmission line could be modeled as an impedance from the input side, output side and resonator as shown in Figure 13.

so we can break down this circuit into 2 loops

$$2V_{in} = I_1 Z_1 + I_1 Z_R - I_2 Z_R \tag{3.1}$$

$$-V_{out} = I_2 Z_R + I_2 Z_2 - I_1 Z_R \tag{3.2}$$

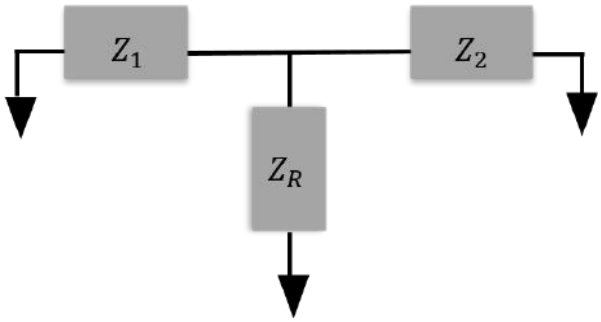

Figure 13: 3 impedance network can be used to represent the circuit of a resonator coupled to a transmission line with an input and output impedance, Z_1, Z_2 and a resonator impedance, Z_R.

We can then put this into the matrix form

$[V] = [I][R]$ or $[R][I] = [V]$

thus

$$\begin{bmatrix} Z_1 + Z_R & -Z_R \\ -Z_R & Z_2 + Z_R \end{bmatrix} \begin{bmatrix} I_1 \\ I_2 \end{bmatrix} = \begin{bmatrix} V_{in} \\ -V_{out} \end{bmatrix} \tag{3.3}$$

The current is the equal to

$$[I] = [R^{-1}][V] \tag{3.4}$$

where

$$[R^{-1}] = |R|^{-1} \begin{bmatrix} Z_2 + Z_R & Z_R \\ Z_R & Z_1 + Z_R \end{bmatrix} \tag{3.5}$$

$$|R| = (Z_2 + Z_R)(Z_1 + Z_R) - Z_R^2 = Z_1 Z_2 + Z_R(Z_1 + Z_2) \tag{3.6}$$

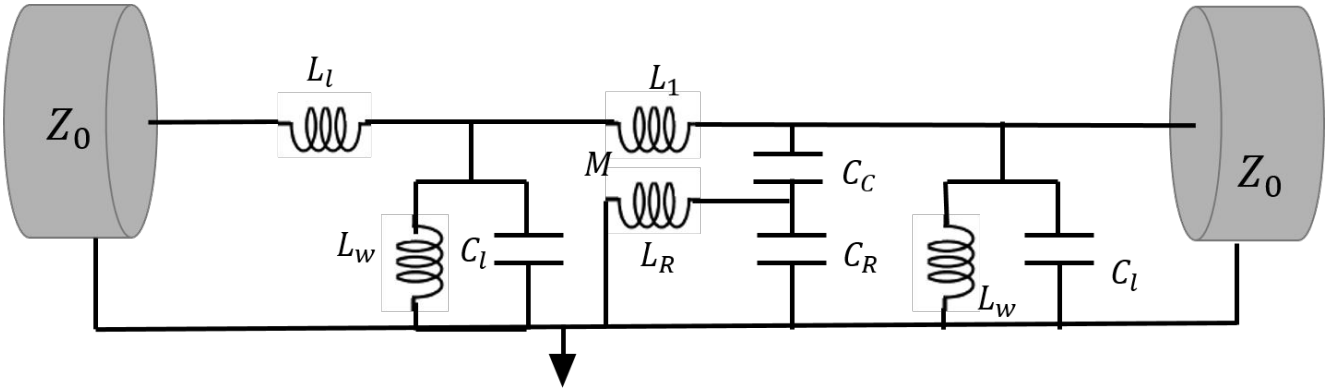

Figure 14: Shows a circuit diagram of a complete circuit showing the wire bonds at the input and output of a resonator coupled to a transmission line.

$$\begin{matrix} I_1 \\ I_2 \end{matrix} = (Z_1 Z_2 + Z_R(Z_1 + Z_2))^{-1} \begin{bmatrix} Z_2 + Z_R & Z_R \\ Z_R & Z_1 + Z_R \end{bmatrix} \begin{bmatrix} V_{in} \\ -V_{out} \end{bmatrix} \tag{3.7}$$

$$I_1 = \frac{V_{in}(Z_2 + Z_R) - V_{out} Z_R}{Z_1 Z_2 + Z_R(Z_1 + Z_2)} \tag{3.8}$$

$$I_2 = \frac{-V_{out}(Z_1 + Z_R) + V_{in} Z_R}{Z_1 Z_2 + Z_R(Z_1 + Z_2)} \tag{3.9}$$

If we look at a more general circuit model including wire bonds we will need 3 loops to solve. We have to reduce the parallel impedance from the wire bond into Z_1 and Z_2.

Loop 1 goes through the input $V_{in}$the characteristic impedance the wire bond, L_1, the output wire bond and the output voltage and again Z_0. For simplicity we will say the wire bond impedance at the input side is $Z_1 =$

$i\omega C_l + (i\omega L_w)^{-1}$ and the output is Z_2.

Loop 1 (input and output)

$$2V_{in} + I_1(Z_0 + 2i\omega L_l + i\omega L_1 - i\omega M) + I_2 i\omega L_1 + V_{out} = 0 \tag{3.10}$$

Loop 2 (input wire bond through resonator)

$$I_2(Z_1 + i\omega L_1 + 1/i\omega C_c + i\omega L_R - i\omega M) + I_1 i\omega L_1 - I_3/i\omega C_c = 0 \tag{3.11}$$

Loop 3 (output side wire bond through resonator)

$$I_3(Z_2 + 1/i\omega C_R + 1/i\omega C_c) - I_2/i\omega C_c \tag{3.12}$$

Combining loop 2 and 3 equations by first solving for I_3in terms of $I_2$from loop 3 equation and then solving for the transmission can be reduced to

$$S_{21} = 1 + I_1\left(\frac{(i\omega L_1)^2}{(Z_1 + i\omega L_1 + 1/i\omega C_c + i\omega L_R - i\omega M - [(i\omega C_c)^2(1/(Z_2 + (i\omega C_c)^{-1} + (i\omega \hat{C_R})^{-1})]^{-1})}\right. \tag{3.13}$$

$$\left. -(Z_0 + i\omega L_T)\right)$$

where $L_T = 2L_1 + L_R + M$

This equation however does not establish a link between the the quality factors and circuit elements. A Norton equivalent circuit which can be made

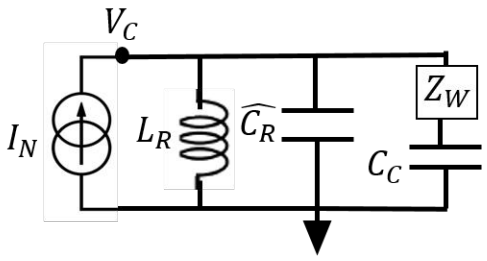

Figure 15: Norton equivalent model helps to simplify the total circuit to elements in parallel with the voltage across the resonator capacitor

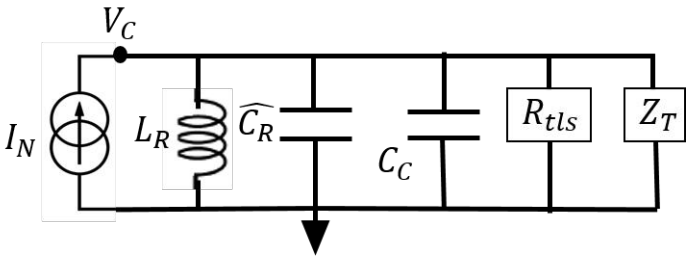

Figure 16: Norton equivalent that includes the loss of the TLS defects in the capacitor of the resonator

from $V_c$and reduces to Figure 14 as discussed in references [59][106]

From the Norton equivalent

$$I_N = V_C G_N \tag{3.14}$$

where $I_N$is equal to I_1above and $Z_W = (Z_0^{-1}/2 + Z_1^{-1}/2)^{-1}$assuming that $Z_1 = Z_2$. The complex capacitance $\hat{C_R}$ can be replaced by an ideal capacitance and a part that is resistive to account for the dielectric loss such that $C = Re(\hat{C})$ and $R = 1/\omega Im(\hat{C})$ additionally $Z_{\hat{C}} = 1/i\omega C_R + R_{tls}$.

We then have

$$Y_{N0} = 1/Z_{th} = \frac{i\omega C_C}{1 + i\omega Z_w C_C} \tag{3.15}$$

where if you let $i\omega C_c << 1$ then

$$\frac{i\omega C_C}{1 + i\omega Z_w C_C} = i\omega C_C + \omega^2 C_C^2 Z_w/2 \tag{3.16}$$

finally

$$G_N = 1i\omega L + i\omega C + G_T \tag{3.17}$$

where

$$G_T = Z_T^{-1} = \frac{i\omega C_C}{i\omega C_C Z_W + 1} + \frac{1}{2Z_W}(\frac{M}{L} + \frac{i\omega C_C Z_W}{i\omega C_C Z_W + 1}) \tag{3.18}$$

Similarly to the complex capacitance we can split the effective admittance $G_T$into

$$R_T = Re(\hat{G_T}) \tag{3.19}$$

$$C_T = 1/\omega Im(\hat{C}) \tag{3.20}$$

$$R_{eff}^{-1} = R_T^{-1} + R^{-1} \tag{3.21}$$

The total quality factor for the parallel LC circuit is then

$$Q = \omega R_{eff}(C + C_T) \tag{3.22}$$

and

$$\omega_0 = \frac{1}{\sqrt{L(C + C_T)}} \tag{3.23}$$

Additionally further algebra

$$R_T^{-1} = \frac{1}{2Z_W}\left[(\frac{M}{L})^2 + \omega^2 C_C^2 Z_W^2\right] \tag{3.24}$$

Near resonance $\omega \simeq \omega_0$ we can then rewrite the transmission equation as

$$S_{21} = \frac{V_{IN}}{V_o} = 1 - \frac{R_{eff}/R_T}{1 + 2iQ(\omega - \omega_0)/\omega_0} \tag{3.25}$$

It can rewritten in another way as [69]

$$S_{21} = 1 - \frac{Q|\hat{Q}_e^{-1}|e^{i\phi}}{1 + 2iQ(\omega - \omega_0)/\omega_0} \tag{3.26}$$

Therefore

$$Q_e = \omega_0 R_T(C + C_T) \tag{3.27}$$

$$Q_i = R\omega_0 C \tag{3.28}$$

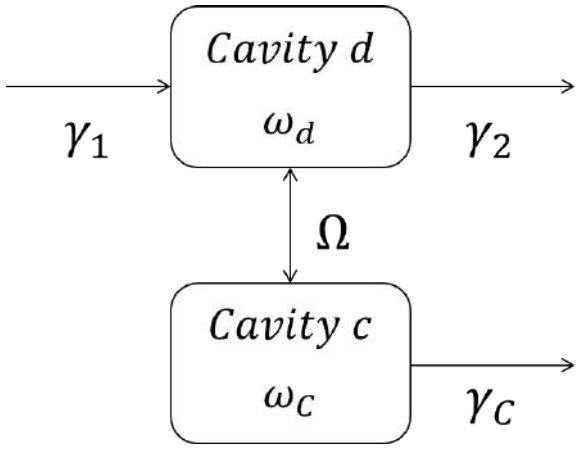

Figure 17: Dual Cavity Model with a low Q cavity d coupled to a high Q cavity c. Typically cavity c is our resonator we are trying to measure.

3.2 Dual Cavity Model

assuming a low-Q mode in cavity d that is coupled to the transmission line halves through 1 and 2. Cavities c and d are coupled to each other with rate .

Ignoring 1, 2, and c, the Hamiltonian for this system is

$$H_{sys} = \hbar\omega_C cc^\dagger + \hbar\omega_d dd^\dagger + \hbar\Omega(cd^\dagger + dc^\dagger) \tag{3.29}$$

where c and d are the photon annihilation operators of the corresponding cavities. Similar to Eq. 1.29,

$$[d, d^\dagger] = [c, c^\dagger] = 1 \tag{3.30}$$

$$[c, d^\dagger d] = [d, c^\dagger c] = 0 \tag{3.31}$$

$$[c, d] = [c, d^\dagger] = [d, c^\dagger] = 0 \tag{3.32}$$

The Heisenberg equations give the solution for lossless coupled light modes as [70]

$$\frac{d}{dt}c = -i\omega c = -\frac{i}{\hbar}[c, H_{sys}] \tag{3.33}$$

$$\frac{d}{dt}d = -i\omega d = -\frac{i}{\hbar}[d, H_{sys}] \tag{3.34}$$

One can find the quantum Langevin equations [71] for the one-sided one-mode cavity c as

$$\frac{d}{dt}c = -i\omega c = -\frac{i}{\hbar}[c, H_{sys}] - \frac{\gamma_C}{2} + \sqrt{\gamma_c}c_{in} \tag{3.35}$$

and the output

$$\frac{d}{dt}c = -i\omega c = -\frac{i}{\hbar}[c, H_{sys}] - \frac{\gamma_C}{2} + \sqrt{\gamma_c}c_{out} \tag{3.36}$$

where γ_c,$c_{in}$and c_{out} are the decay rate, the input field and output field c.$\gamma_c$appears due to a quantum fluctuation dissipation theorem [22]. Cavity d can be thought of in the same way.

The boundary conditions which relate the input and output fields to the annihilation in each cavity is

$$c_{in} + c_{out} = \sqrt{\gamma_c} c \tag{3.37}$$

$$d_{1,in} + d_{1,out} = \sqrt{\gamma_1} d \tag{3.38}$$

and

$$d_{2,in} + d_{2,out} = \sqrt{\gamma_2} d \tag{3.39}$$

We assume only one input field $d_{1,in}$ and set $d_{2,in} = c_{in} = 0$ and we get

$$c = \frac{-2i\Omega d}{\gamma_c - 2i(\omega - \omega_c)} \tag{3.40}$$

$$d = \frac{2\sqrt{\gamma_1} d_{1,in} - 2i\Omega c}{\gamma_1 + \gamma_2 - 2i(\omega - \omega_d)} \tag{3.41}$$

and then

$$d = \frac{2\sqrt{\gamma_1} d - 2\sqrt{\gamma_1} d_{1,in} + 2\sqrt{\gamma_2} d_{2,out} + 2i\Omega c}{\gamma_1 + \gamma_2 + 2i(\omega - \omega_d)} \tag{3.42}$$

Solving for $d_{2,out}$one will get

$$d_{2,out} = \frac{\sqrt{\gamma_1 \gamma_2} d_{1,in}(\gamma_c - 2i(\omega - \omega_c))}{\gamma_c - 2i(\omega - \omega_c)(\gamma_1 + \gamma_2 - 2i(\omega - \omega_d)} \tag{3.43}$$

The transmission is the ratio of the output field to the input field

$$S_{21} = \frac{\langle d_{2,out} \rangle}{\langle d_{1,in} \rangle} \tag{3.44}$$

$$S_{21} = \frac{\sqrt{\gamma_1 \gamma_2}}{\frac{\gamma_1+\gamma_2}{2} + i(\omega - \omega_d) + \frac{\Omega^2}{\gamma_c/2 + i(\omega - \omega_c)}} \tag{3.45}$$

Note that the sign of ω can be determined for convention used. There is now an easy way to map the fit parameters between equation (3.30 and 3.45) where you can solve for the quality factors. The low Q cavity $Q_d = \omega_d/\gamma_d$ is required to be much smaller than $Q_c = \omega_c/\gamma_c$.

Using reference,[73] there are further correlations and help me find the fit parameters, Q_i, Q_e,and ω_0. Namely,

$$Q_i = Q_c = \omega_c/\gamma_c \tag{3.46}$$

$$Q_e = \frac{\gamma_1 + \gamma_2}{4\Omega^2}\omega_c = \frac{\gamma_d \omega_c}{4\Omega^2} \tag{3.47}$$

These equations help to characterize the response of a resonator that is coupled to an ensemble of TLS. The following section discusses the fitting technique and shows grows of how the fitting parameters are found using the Monte Carlo method.

Quantum-Mechanical TLS-Cavity Model

In the previous section (Chapter 2.1) I had shown how to find the transmission of a cavity coupled to a low Q feedline. Here I will show a model for several strongly coupled TLS coupled to a resonator. I will use the spin operator $\hat{S}_i$ to denote the TLS since a TLS is analogous to a spin $\frac{1}{2}$particle. A coherent state approximation is used for photon in the cavity, c, coupled to input fields $\hat{a}_1$,and output ,$\hat{a}_2$. The equation of motion is

$$\frac{d}{dt}\hat{c} = -\frac{i}{\hbar}[\hat{c}, \hat{H}_{sys}] - \frac{1}{2}(\gamma_1 + \gamma_2)\hat{c} + \sqrt{\gamma_1}\hat{a}_1 + \sqrt{\gamma_2}\hat{a}_2 \tag{3.48}$$

where $\hat{H}_{sys}$is the system Hamiltonian, γ_1 and γ_2 are the cavity mode decay rates in the input and output channels.

$$\hat{H}_{sys} = \hbar\omega_c\hat{c}^\dagger\hat{c} - i\hbar\sum_{i=1}^{N} g_i(\hat{S}_i^-\hat{c}^\dagger + \hat{S}_i^+\hat{c}) + \sum_{i=1}^{N}\epsilon_i\hat{S}_i^z \tag{3.49}$$

similar to the Jaynes-Cummings model except that there are N TLSs rather than one. $\hat{S_i^+}$and $\hat{S_i^-}$are the TLS raising and lowering operators. ϵ_i is the TLS energy for the ith TLS with resonator coupling g_i. The cavity c ground state energy is

$$Cv_{rms}^2 = \frac{1}{2}\hbar\omega_c^2 \tag{3.50}$$

where v_{rms} is the rms voltage across the capacitor C. If the input field is present in just channel 1 with frequency ω then one can characterize the time

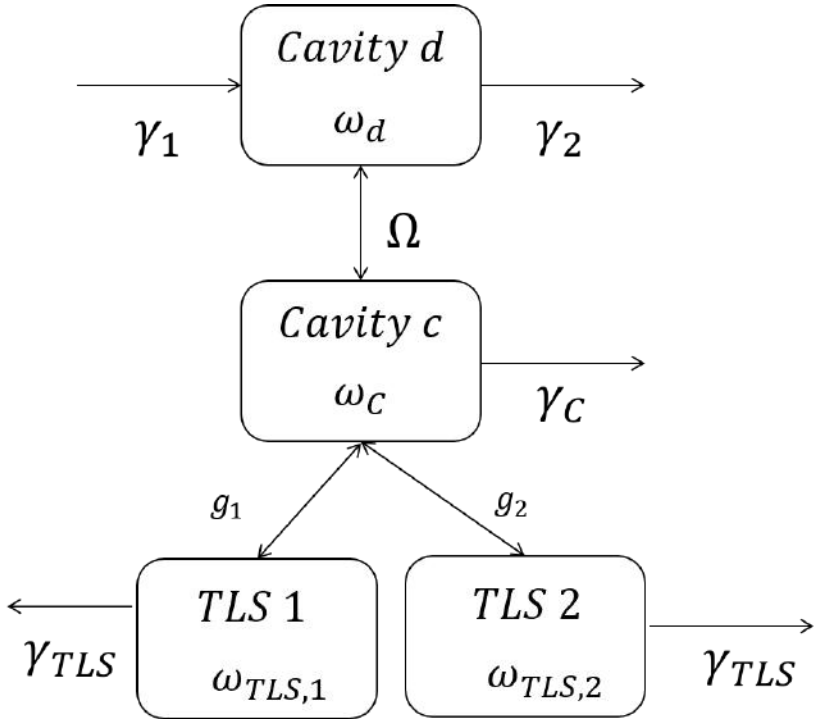

Figure 18: Dual Cavity diagram showing the different decay rates in the cavities and shows how multiple TLS can couple to high Q cavity c.

evolution equation for the cavity operator c as

$$i\omega\hat{c} = -i\omega\hat{c} - \frac{\gamma_c}{2}\hat{c} + \sum_{i=1}^{N} g_i \hat{S}_i^- + \sqrt{\gamma_1}\hat{a}_1 \tag{3.51}$$

where $\gamma_c = \gamma_1 + \gamma_2$ and similar for the time evolution of the TLS operator $\hat{S}_i^-$

$$i\omega\hat{S}_i^- = -i\omega\hat{S}_i^- - \frac{\gamma_{TLS}}{2}\hat{S}_i^- - g_i\hat{S}_i^z\hat{c} \tag{3.52}$$

One can then solve for the TLS operator

$$\hat{S}_i^- = \frac{ig_i c}{i(\omega_{tls,i} - \omega) + \gamma_{tls,i}/2} \tag{3.53}$$

In the high temperature limit ($k_b T \sim \hbar\omega$) one can use the mean field technique replacing the operator with its thermodynamical average value,

$$\langle S_z \rangle = -\frac{1}{2}\tanh(\frac{\hbar\omega}{2k_B T}) = -s \tag{3.54}$$

This technique is consistent with the previous discussion of acoustic absorption by TLSs[74]. I can now substitute for S_i^- to obtain a solution for the cavity c,

$$c = \frac{\sqrt{\gamma_1}a_1}{i(\omega_c - \omega) + \gamma_c/2 + 2s\sum_{i=1}^{N}\frac{g_i^2}{i(\omega_{tls,i}-\omega)+\frac{\gamma_{tls}}{2}}} \tag{3.55}$$

One can then apply the boundary conditions to find the transmission

$$a_1(+\infty) = a_1(-\infty) - \sqrt{\gamma_1}c \tag{3.56}$$

$$a_2(+\infty) = a_2(-\infty) - \sqrt{\gamma_2}c \tag{3.57}$$

Using a single-photon scattering function and the Moller operator to the find the transmission [?]

$$S_{21} = \frac{\sqrt{\gamma_1\gamma_2}}{i(\omega_c - \omega) + \frac{\gamma_1+\gamma_2}{2} + 2s\sum_{i=1}^{N} \frac{g_i^2}{i(\omega_{tls,i}-\omega)+\frac{\gamma_{tls}}{2}}} \tag{3.58}$$

For a more complete model we can introduce the low Q cavity d, and assuming only one input field a_1 and using the mean field technique for S_z operators one finds

$$S_{21} = \frac{\sqrt{\gamma_1\gamma_2}}{i(\omega_d - \omega) + \frac{\gamma_d}{2} + \frac{\Omega^2}{i(\omega_c-\omega)+\frac{\gamma_c}{2}+2s\sum_{i=1}^{N} \frac{g_i^2}{i(\omega_{tls,i}-\omega)+\frac{\gamma_{tls}}{2}}}} \tag{3.59}$$

One can simplify the above equation by considering a single strongly coupled TLS coupled to the cavity c. The equation then becomes

$$S_{21} = \frac{\sqrt{\gamma_1\gamma_2}}{i(\omega_d - \omega) + \frac{\gamma_1+\gamma_2}{2} + \frac{\Omega^2}{i(\omega_c-\omega)+\frac{\gamma_c}{2}+\frac{2g^2\tanh(\hbar\omega/2k_BT)}{i(\omega_{tls}-\omega)+\frac{\gamma_{tls}}{2}}}} \tag{3.60}$$

The average weakly coupled TLS response

$$\gamma_{c,weak} = \langle \sum_i \frac{g_i^2}{i(\omega_{tls,i} - \omega) + \frac{\gamma_{tls,i}}{2}} \rangle = \omega_c \pi P_0 p^2 / 3\epsilon \tag{3.61}$$

where

$$\tan_\delta = 1/Q_c = \gamma_c/\omega_c \tag{3.62}$$

Q_c is the internal quality factor for cavity c

I have derived the dual cavity model which is used to do the transmission fits from the experiment to extract the quality factors of the resonators. To do the fits I use the Monte Carlo fitting algorithm which I will discuss in the next section.

3.2.1 Monte Carlo Fitting Method

The Monte Carlo method is a stochastic model that can help obtain deterministic solutions. I have modified a script written by Dr. Sarabi that I use for most of my resonator fits and it proves very efficient. The idea is after a certain number of iterations using randomly adjusted fitting parameters I will reduce the error every iteration and find the best solution. Every loop I either keep or discard the fitting parameter based on if the error calculated during that loop decreased or increased. The error thus gets lower and lower every turn.

More specifically I begin the fit by making an initial guess of the parameters using the bandwidth of the resonator $Q = \frac{\omega_r}{B}$. This quick fit allows one to

generate the initial fitting parameters, Qi, γ_c,Ω, and ω_0 . Then I perform the Monte Carlo process. Each parameter x, is allowed to change $x = x_0 e^{\zeta\xi}$ each loop. x_0 is the previous value of the parameter, ζ determines the sign, either 1 or -1. ξ determines the range of the parameter. Using these varied parameters we fit equation x over a range of several orders of magnitude in power or average photon number, $\bar{n}$. Then we use the least square method to find the error. Where the error is

$$error_i = y_i - f(x_i) \tag{3.63}$$

The error is then summed and minimized by keeping the parameter if the new error is less than the previous error or finding a new parameters if the error is greater. Additionally we are most interested in fitting the resonance or dip of the $|S_{21}|$. Generally this value is very small and thus one often fit the inverse of $|S_{21}|$. By inverting one is now weighing the error from the resonance more than the error of the background. Below is an example of a fit to resonator.

In some cases I do multiple Monte Carlos if the data ranges over several orders of magnitude to get the best fit. Also in some cases there is a resonance in a box mode which has a distinct slope. I found that subtracting out the slope from the background greatly improved the fitting. This can be an issue especially if the resonator is under coupled.

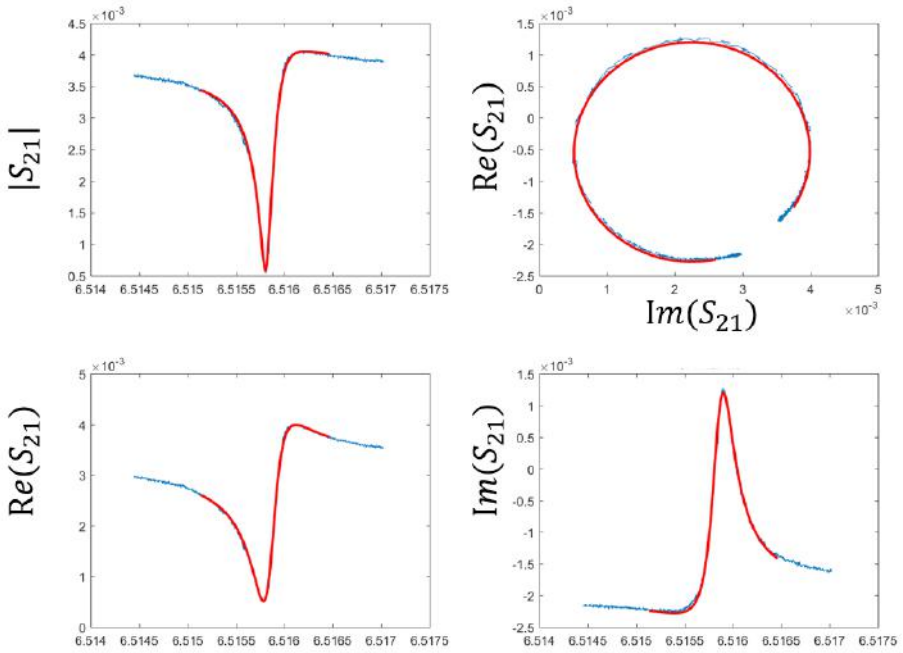

Figure 19: Shows fits to data using the dual cavity model. Plotted in the graphs are the magnitude of the transmission, $|S_{21}|$(top left), real part (bottom left), and imaginary part (top right) versus the frequency in GHz. The imaginary part versus the real part of the transmission, S_{21} is plotted in the top right. At the opposite end of the opening of the circle is the resonator frequency, ω_0.

Resonator critical coupling technique

Generally it is important make the resonators critically coupled where $Q_i = Q_e$. This allows for the most sensitive measurement of the internal quality factor. To set the coupling quality factor I've used either microwave office or Sonnet. These programs are 2.5 dimension EM simulators that are very effective. One can set the substrate loss to zero and set the losstan or the dielectric to be $1/Q_i$. This allows one to get a quick estimate of Q_e. If the resonator is critically coupled ($Q_i = Q_e$) one will measure the transmission with a depth of 6 dB or $|S_{21}| = -6dB$. That is known from the following quick derivation from the transmission formula.

If you look on resonance, $\omega = \omega_0$ the bottom term drops out and taking the real part of the external quality factor $Re(\hat{Q}_e) = Q_e$

$$S_{21} = 1 - Q/Q_e \tag{3.64}$$

$$Q^{-1} = Q_i^{-1} + Q_e^{-1} \tag{3.65}$$

therefore

$$S_{21} = \frac{1}{Q_e}(Q_i^{-1} + Q_e^{-1})^{-1}$$

when critically coupled $Q_i = Q_e$,thus

$$S_{21} = 1/2$$

finally converting to units of dB

$$S_{21} = 20log(.5) = -6dB$$

4 Experimental Setup and Fabrication tools

So far I have gone over the device theory, the circuit model and analysis techniques I use to get my data. In this section I will talk about the experimental setup and the fabrication tools used to physically make the device.

4.1 Experimental Setup & Fabrication tools

All of my measurements were done on a Leiden 650 CF dilution refrigerator at temperatures ranging between 10mK and 80mK.

4.1.1 Leiden 650 CF

Figure 20 shows the Leiden dilution refrigerator with the mu metal can on but the IR shielding cans off. The top middle picture shows the chip of the TiN resonators. The bottom middle shows the copper sample box used for the measurements. Copper is used because it is a good thermal conductor. On the right is a schematic of the attenuation and RF components in our line. Our attenuators are from Midwest Microwave. We use 10 dB attenuators which are thermally anchored on a mounting panel at each stage. The RF lines are made of beryllium copper because they have a low thermal conductivity. I built and programmed a microwave switch box which gives the ability to measure up to 4 samples as the same time. At the output there are two isolators used to prevent reflections. There are two amplifiers used in the output line. A HEMT LNA amplifier is used at the 3Kstage and another amplifier is used at room

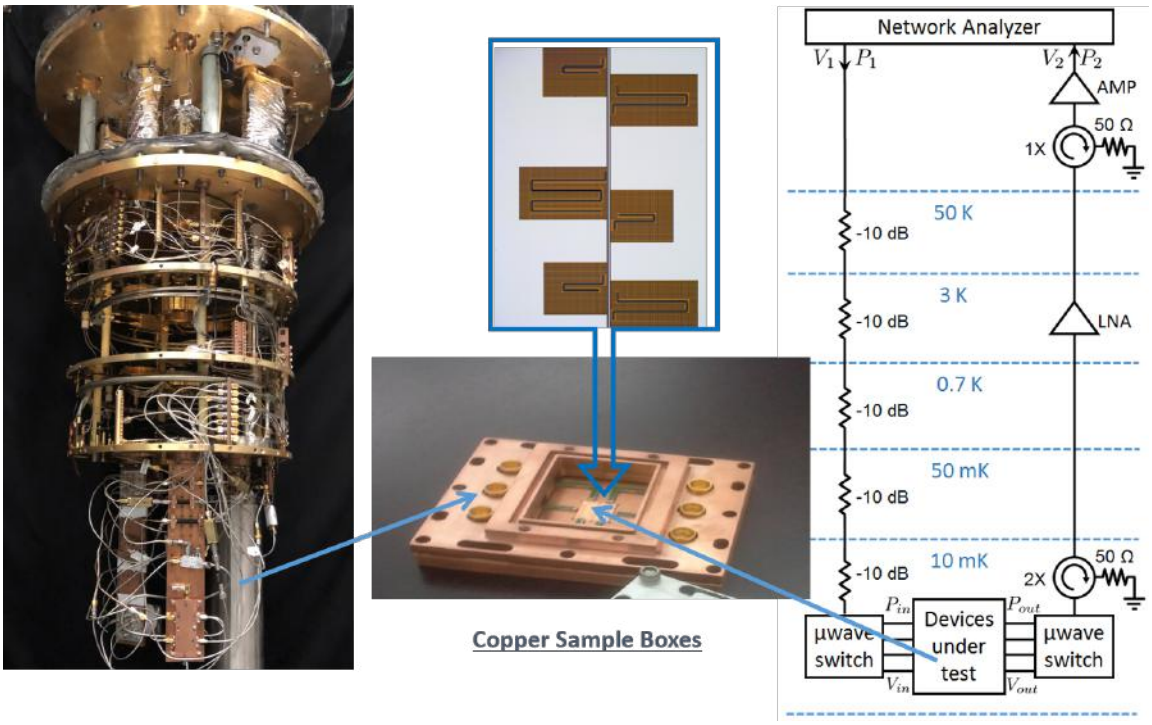

Figure 20: This illustration shows the Leiden dilution refrigerator used to make all the measurements. The top middle picture shows the chip of TiN resonators. The bottom middle shows the copper sample box used for the measurements. Copper is used because it is a good thermal conductor. On the right is a schematic of the attenuation and RF components in our line. We use a microwave switch which gives the ability to measure up to 4 samples as the same time. We use a HEMT LNA at 3K and a RT amp on the output line.

temperature. The sample box is mounted at the lowest temperature stage called the base stage. This stage will reach temperatures as low as 10 mK. The sample box is tightly screwed into the mounting panel which is attached to the base plate. To cool the refrigerator there is a specific process.

My cooldown process involved pumping on the IVC and still, traps, condensing lines for several hours when warm. I added about 10 mbar of He4 exchange gas into the IVC once the OVC and IVC were below a 1mbar. I then pumped down the still until it too reached 10 mbar. I then turned on the pulse tube compressor which would take the system down to 4K-5K. Occasionally I would use the liquid nitrogen precooling line which would speed up the cool down by about 13 hours. When the system reached 4-5K I would release the exchange gas by heating the sorb in the still. This would bring all the stages between 3-4K. I would then start condensing, starting with He3 and then He4. The additional cooling power comes by creating a superfluid by diluting He4 with He3. Since He3 is the lighter atom it sits on top of the He4 superfluid but because of the slight attractive force between some He3 will diffuse into He4. Thus about 6.4% of the superfluid is He3. When we start circulating or pumping on this circuit some He3 leaves the superfluid creating an osmotic pressure in the superfluid. This osmotic pressure causes the ordered vapor He3 to enter the disordered superfluid, absorbing heating. A cold plate that is attached to this stage has the sample box with the device in it mounted on. The sample box will hold the chip in place and allows for other connections to be made to the chip. Aluminum wire bonds will then connect directly from

the launches of the chip to a PCB board that connects to an SMP connector. The SMP connector is then connected to SMA RF cables which allow for RF measurements to be made via an Vector Network Analyzer (VNA). I will discuss the packaging in greater detail in subsequent sections. Additionally many extra steps are taken to protect the chip from the environment. To protect against stray IR the 50 mk the inner can is lined with carbon black silicon carbide crystals to absorb IR so it doesn't reach the sample. IR can be produced at 3K as black body radiation and can break up Cooper pairs in the superconducting circuit. A mu metal shielding can as seen in the above Figure and encloses the sample box. This shield prevents magnetic fields from entering due to its high permeability and will be further discussed below.

Mu Metal Shielding

To protect our qubits and resonators from stray magnetic fields use a μ metal double layer shield. The shield is made of μ metal which has a high permeability $\mu \sim 70,000$ at room temperature. Its performance dues degrade slightly when cooled but in general is expected to reduce the fields getting to the device greatly. One can calculate the reduction from a spherical shield as [56]

$$R = \frac{9\mu_0}{2\mu(1-a^3/b^3)}$$

where a and b are the inner and outer radius of the shield and $\mu = 70k$. With an inner radius of 1.5" and a thickness of .07" I calculated $R = 5.0 \times 10^{-4}$ which equals a factor of 2000 protection from magnetic fields. This number is

an estimate as it is a cylindrical shield and there is a double wall of μ metal inside. We also try to reduce magnetic fields by using brass screws and plates over stainless steel, silver or gold (can have nickel diffused in it).

With all these protections we don't expect the Earth's .5 Gauss magnetic field to cause any flux in our devices. Several of our bias lines and RF lines do penetrate the shield which could cause magnetic fields inside however for CPWs with centerlines around $10\mu m$ the critical field is several Gauss which we do not expect to reach.

Fabrication tools

I fabricated all the devices in the class 10k clean room at the Laboratory of Physical Science building.

4.1.2 Photolithography tools

In this section I will discuss the different tools used to do the photolithography for each device I talk about in this thesis. I will discuss the specific fabrication process for most of the devices I talk about in subsequent chapters and sections.

I often used the Kurt J. Lesker model CMS-18 DC sputtering tool for aluminum or TiN depositions. For the patterning I used the 5X GCA stepper tool which took the masks I designed and exposed light through it as it stepped through a full wafer. Both tools are shown in Figure 21. I used 3 inch wafers either of high resistivity [100] floatzone silicon or sapphire wafers.

a)  b) 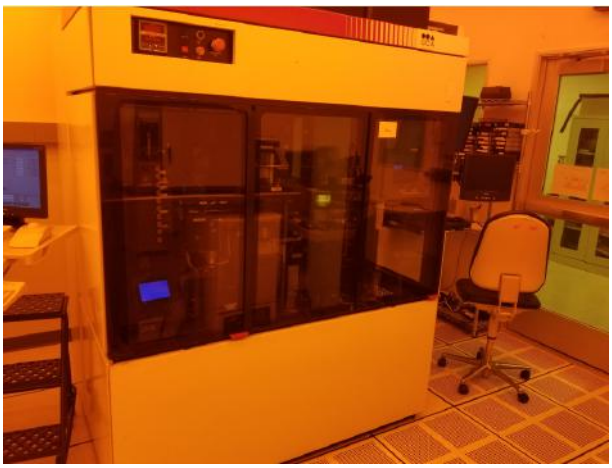

Figure 21: Picture of a) CMS-18 DC sputtering tool and b) 5X GCA stepper tool

a) b)

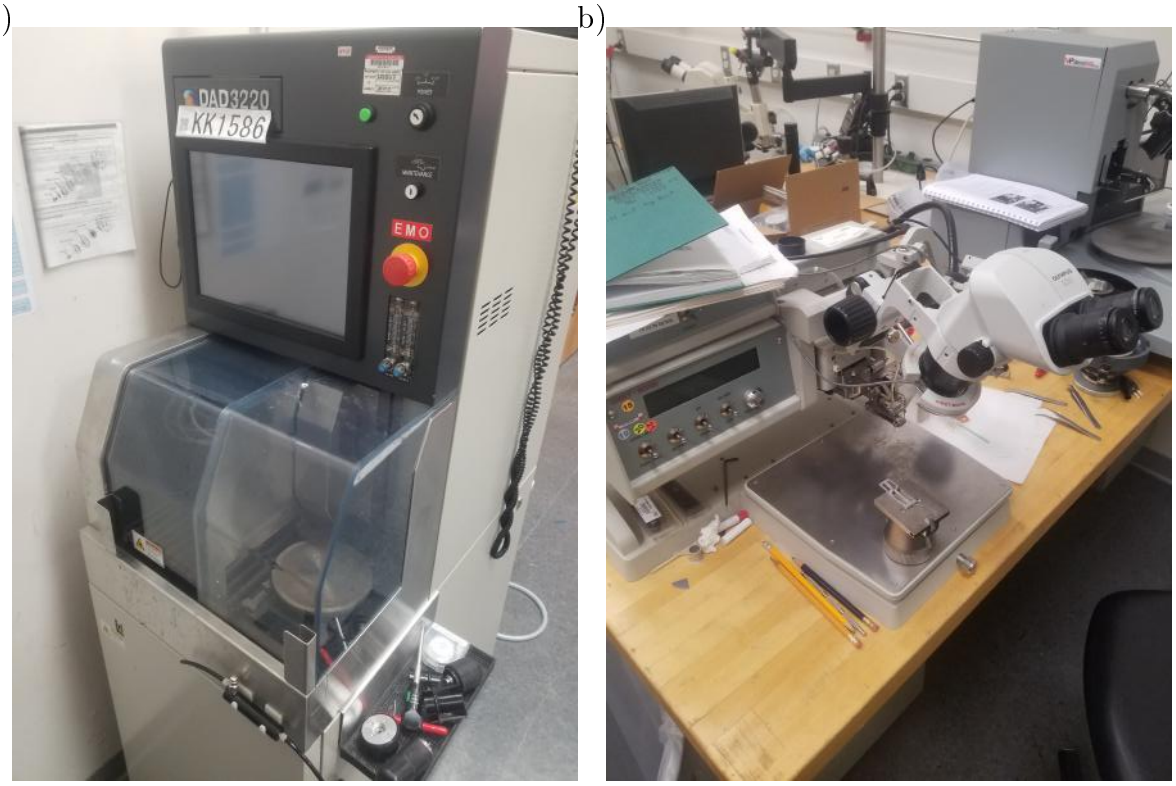

Figure 22: Picture of Disco DAD3220 Dicing tool, Wirebonder, Joel SEM, e-beam evaporator.

Dicing

To dice the wafers after completing the fabrication process I used the DAD3220 series by Disco.

The blades I used to cut silicon were different than the blades for cutting sapphire. To cut silicon I used a Disco ZH05 series blade. I used a ZH05 SD2000-N1-50 - HEEE2028S. This mean the blade had a grit size of 2000, an exposure of .89-1.02 mm, and a kerf width of 37.5 $\pm$2.5 μm.

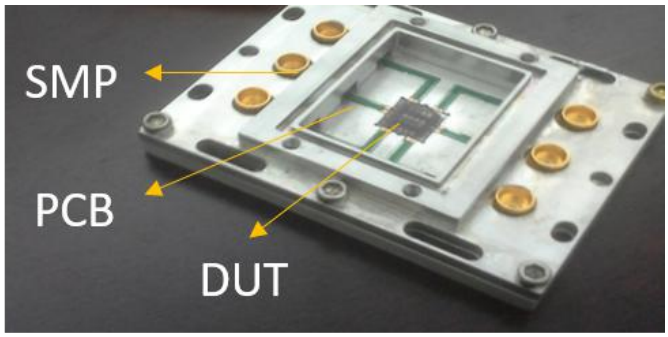

Figure 23: An aluminum sample box with a device held by GE varnish in the center. The device is wire bonded to PCB traces as indicated. The PCB traces are soldered to SMP connectors. The SMP connectors then attach to SMA connectors in the RF input and output lines.

4.1.3 Device Packaging

Sample Box

Packaging a device is an often overlooked crucial aspect of the experimental setup. By packaging I mean the placing of the chip into a sample box and then wiring the chip to the sample box using a wirebonder. The sample box was designed by Dr. Aruna Ramanayaka and tested to have insertion loss better than 60 dB in the frequency range of 4-8 GHz. The sample box has PCB traces that are held in place with small amounts of GE Varnish. The center traces is often used as the RF input and output that connects to a center feedline transmission line. The other traces where you can see the orthogonal bends, in Figure 23, can be used to apply a DC or RF bias.

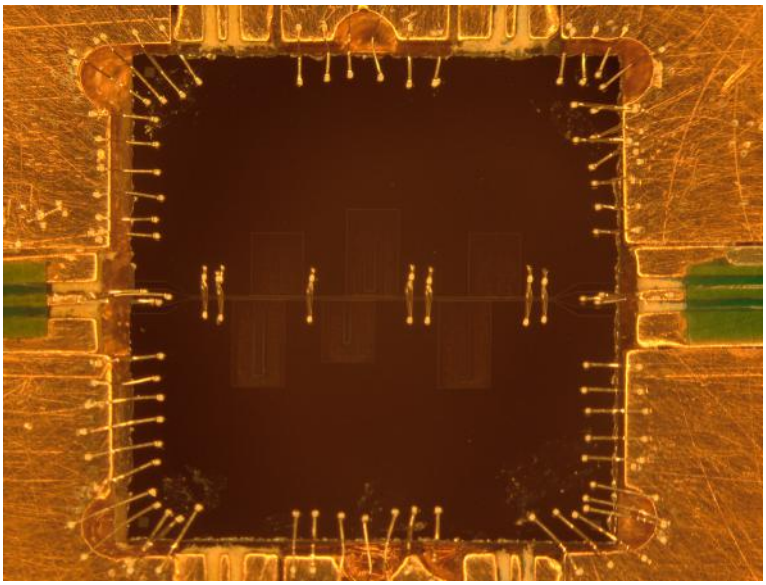

Figure 24: Wirebonding chip to sample box with cross over bonds between ground planes to help prevent slot line modes

Wirebonding

Wirebonding in general has proved to be an underlying source of loss or of unwanted modes in the frequency ranges we care about [37]. Wirebonds act as small impedance mismatches on the 50 Ωinput and output side of a chip. In general they are modeled, as has been discussed in the previous section, as an inductor in series with a parallel capacitance and inductance.

4.2 Calibration of the input line

In general it is paramount to know the total RF attenuation on the input line that enters from the fridge from the VNA to the device under test. This allows you to know the power at the device. This attenuation is a func-

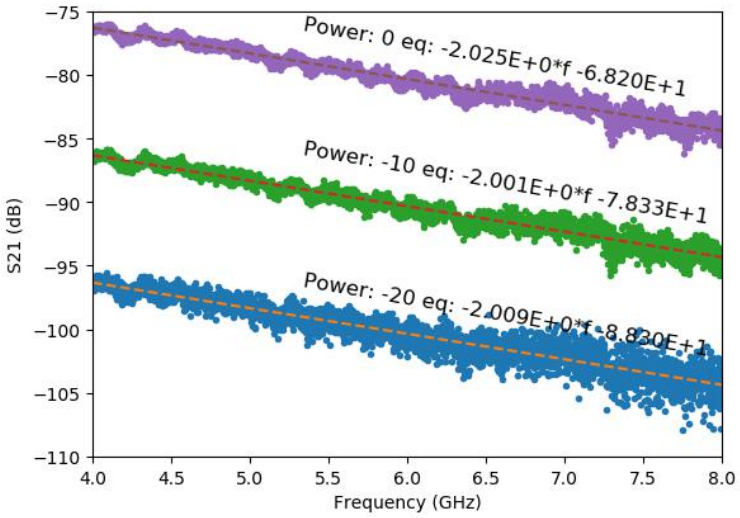

Figure 25: Example input line calibration where data is taken at 3 different powers and then fit to equation 4.2

tion of the source frequency f and source power,P_1. In measuring the loss dependence from power I am able to use this calibration as a way to accurately know the number of photons in the cavity. The calibration is performed by measuring the transmission S_{21} from the network analyzer to the device input in the frequency span one is interested in, which is namely between 4-8 GHz. I first measure the transmission for three different source powers $P_1 = -20dBm, -10dBm, -0dBm$ at room temperature to the device. For the calibrations, the dependence of Pin on frequency was assumed to be log-linear (to 1st order), and Pin for an arbitrary frequency and P_1 interpolation and extrapolated points were used.

The calibration was performed each time the input circuit was altered. Figure 25 shows the input calibration measurement of P_{in} versus f in the 4-8

GHz range for three applied powers. Each measurement of Pin versus f in Fig. 23 was set to a log-linear expression to obtain the slopes,m and the offsets, b ,

$$P_{in} = mf + b \tag{4.1}$$

where all powers are expressed in the log form (dBm) basis 10. The average, m, determines the frequency dependence of P_{in}, the offset is used to help determine the dependence of the power at the device P_{in} from the source power. All the data for different powers is then set to the equation

$$Pin = \bar{m}f + m^{'}P_1 + b^{'} \tag{4.2}$$

where as of February 2021 our calibration equation has $m = -2.02\bar{6}dBm/GHz$,$m^{'} =$ 1.001and $b^{'} = -65.2$dBm.

5 Spectroscopy of Surface TLS

Understanding surface TLSs, at material interfaces, is paramount to improving the coherence in superconducting qubits. It is known that surface TLS significantly hinder the Q_i in resonators and T_1 in qubits [43, 44, 45, 86]. Most attempts to mitigate loss from TLSs are made by using larger structures to reduce the participation ratio of lossy interfaces, or reduced fabrication residue [54]. Avoiding TLSs through material improvements remains the most straight forward approach, controlling them through their energies may lead to even better coherence times. Also, controlling TLSs energies allows for characterization of generally unknown parameters such as the TLS coherence time and TLS's AC & DC coupling, where the DC coupling relates to the dipole moment . In previous tri-layer capacitor experiments TLSs energies have been tuned in and out of bandwidth of a resonator, allowing for dipole moment analysis [29]. Additionally recent results show observation of externally biased surface TLSs in transmon qubits [61, 34, 31]. One of the studies [82] measured TLSs coherence times by observing coherent swap oscillations and was able to extract TLS-qubit couplings from TLS located in the junction and at the interface of the shunting capacitor.

Here we present an on chip electric field tuning technique to study particularly the TLS along the surface of an IDC in a lumped element resonator. I have measured over 50 TLS with direct measurement of the coupling strength by analyzing the anti-crossings from the eigenmodes with an average coupling strength of 100 kHz. These anti-crossings can be fit to the eigenmode equa-

tions and when used in combination with COMSOL simulations we can extract information on the average dipole moment parallel to the field, $p_{\parallel}$, coupling, $g/2\pi$,T_1, as well as information about the physical location of the strongly coupled TLS. Because of the high fields near corners a single photon and to a relatively high quality factor of 30k we observe only on average about 2% of surface TLS crossing the resonator frequency per 100mV in the bandwidth of the resonator. These are actually anti-crossings between the TLS and the resonator. Surface TLS have been observed before in qubits with external biases[82], a measurement of substrantial TLS-resonator couplings at surfaces of a thin film resonator has not been made using an on chip dc-electric field bias to our knowledge.

5.1 Simulating surface TLSs

Significant work has been done to understand the participation ratios, p_i of TLS defects. Particularly simulations using COMSOL have shown that the MS and SA interface have the highest p_i [5]. Furthermore structures have been fabricated to minimize the loss at some interfaces and increase it at others in an attempt to determine the loss tangent at each interface[84]. This study found that although the MA interface has a low participation the loss tangent is significantly higher than previously thought finding, $\tan\delta_{MA} = 3.3\times10^{-3}$. Despite these works there is not a lot of research linking simulation to experiment on individual TLSs. Specifically there are not a lot of studies examining the location of strongly coupled TLS. Strongly coupled TLS in

particular affect coherence in qubits. In this section I will examine first how to find the loss at each interface and then discuss observing strongly coupled TLS defects related to simulations.

To find the participation ratios of TLS at each material interface one first finds the electric field distribution. Each interface has a similar looking graph. Where there is the highest probability of having the lowest electric field which is usually located at the center of the IDC finger in the case of the MA, MS regions. The highest fields will be concentrated near the corners. As you can see in Figure 27e the fields at the corner, $|E| \backsimeq 45V/m$ (3x3 nm area) are indeed about an order of magnitude higher than at any other interface. It is also important to note that for high coupling, $g/2\pi = \frac{\Delta_0}{\epsilon} 2p_{\|} E_{RMS}$, large electric fields, E_{RMS}, are needed. In past, tri-layer capacitor LE resonators, TLS biased experiments [11] electric fields strengths of 20 V/m were present. Below I will show how one can simulate the electric field in a co-planar structure similar to the environment seen by the resonators I have measured.

COMSOL simulations were made to create an environment similar to that of a real IDC or co-planar structure. I created a simulation of several superconducting fingers placed on a substrate. The fingers alternate between high and low potential similar to those in an IDC. Fig 26a shows the mesh. The grid I used extremely fine simulation grid points near the corners and in the TLS region to best capture the electric fields at those regions. TLS are considered to reside at 3 different interfaces; the Metal-Substrate (MS) , the Substrate-Air (SA), and the Metal-Air (MA). However from my analysis I argue that it is

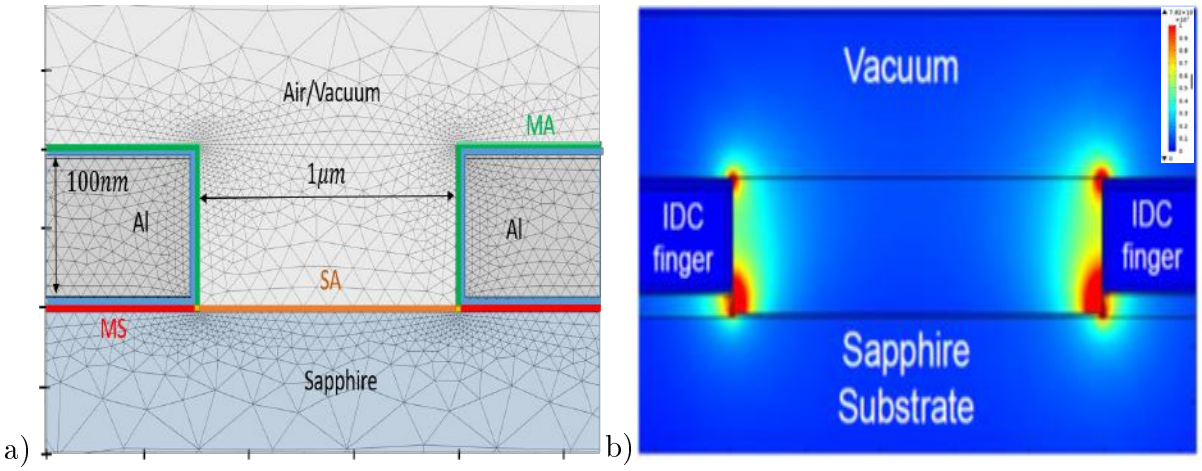

Figure 26: a) Shows the mesh from the COMSOL simulation for two 100 nm thick aluminum films. The simulations has seven such electrodes and counter electrodes alternating between high potential and ground. The red region is the Metal-Substrate interface, the green is the Metal-Air, the orange is the Substrate-Air. As is common in the field, a 3nm TLS host thickness is assumed [5]. The blue outlines the metal finger and the yellow is the corner of the film where the electric fields are highest. b) Shows the electric field density acquired from COMSOL. We can see that the energy density and energy is especially high near the corner of the metal finger next to the substrate.

better to expand this to at least 4 or 5 interfaces of interest with the other two areas being the SideWall (SW) and the corners. The device is under vacuum at low temperature, thus the air near zero absolute pressure. The metal fingers are separated by a distance of $1\mu m$ and have a height of 100 nm. The substrate is 400 μm thick and the TLS host-layer thickness is assumed to be 3 nm which is considered to be the native thickness of aluminum oxide[5]. Furthermore when calculating the participation ratios I assume $\epsilon_{MS} = \epsilon_{MA} = 10\epsilon_0$ and $\epsilon_{si} = 11.9\epsilon_0$ for silicon substrate. Also the following assumptions were used based of inhomogeneous electric fields in co-planar structures.

$$p_{MS} = p_{MS,\perp} >> p_{MS,\parallel}$$

$$p_{MA} = p_{MA,\perp} >> p_{MA,\parallel}$$

$$p_{SA} = p_{SA,\parallel} >> p_{SA,\perp}$$

We can simulate the electrostatic field distribution $|E(r)|$ at different interfaces using the finite element solver COMSOL. These fields properly model the fields at microwave frequencies, because we generally look at local fields, which are much smaller than the wavelength. Also, the penetration depth in the Al superconductor is small relative to the electrode thickness. From the COMSOL simulation as shown in Fig 27. we can generate electric field vectors at certain areas within the model with a certain step or grid size. The grid

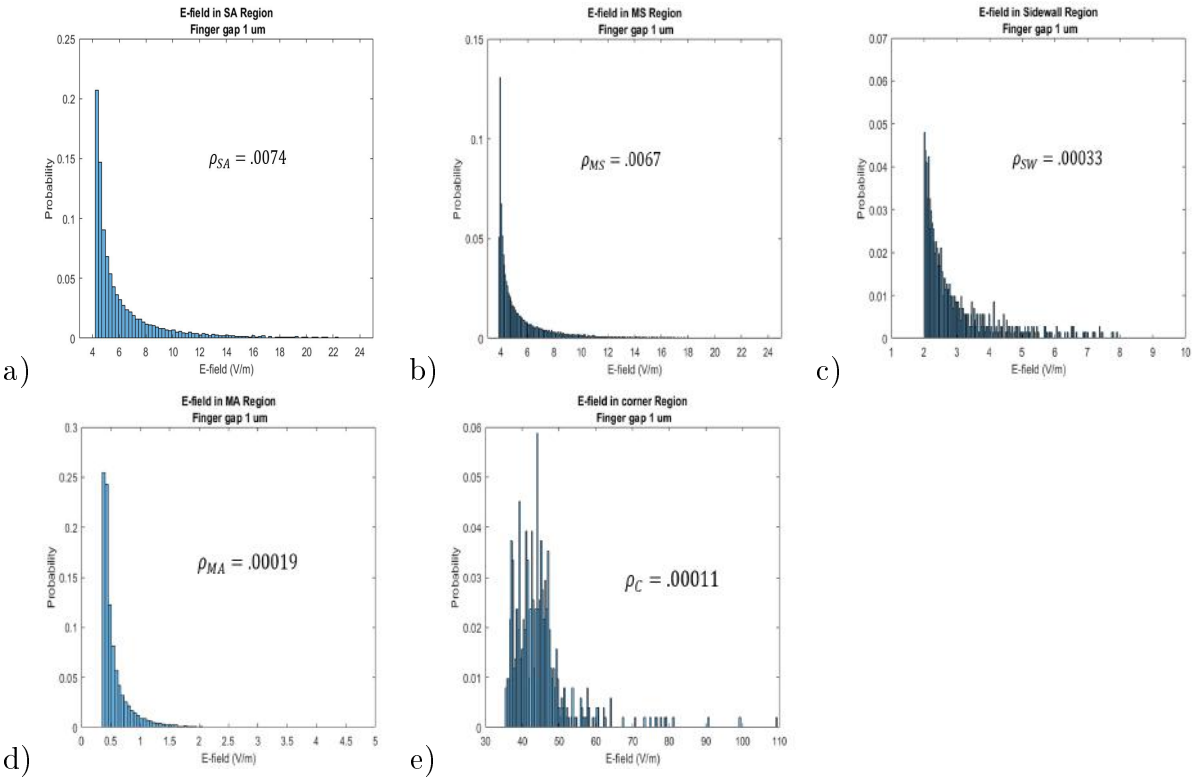

Figure 27: Electric field distribution of the 5 interfaces (a-e) of interest in a base film with LW=LS=1μm and a 3 nm of dielectric layer at the MS,SA, and MA interface is assumed. The fields at the corner e) are about an order of magnitude higher than in the bulk regions of the other interfaces.

size decreases to close to 0.1 nm near the corners, but also the actual corners are not expected to be sharper than 1nm in experiment.

Specifically one can examine the dependence of the field as a function from the highest field corner. I will define the high field corner as the intersection of the MS and SA regions. The fields are highest in this area as seen in Figure 27e.

When integrating over a half micron from the high-field corner (half micron is chosen because the conductor width is 1μm and the fields are symmetric about

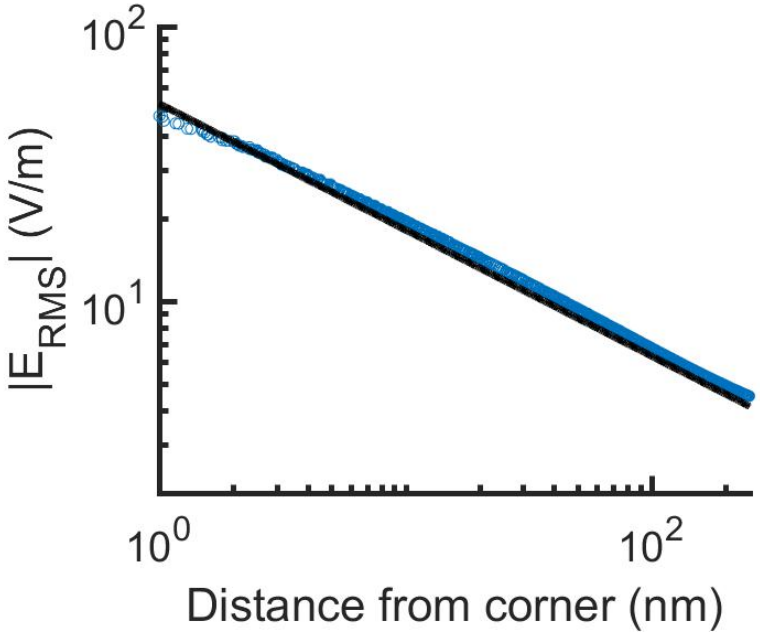

Figure 28: Electric field strength, assuming a zero-point fluctuation (zpf) voltage of $7\mu V$, versus distance from the highest field corner. This field is along the MS interface (under the metal). The corner was chosen because the field generally decreases away from that point. The field scales as $r^{-.5}$. In actual fabrication there is not a perfectly sharp corner but fields should be similar at a sufficient distance (e.g. 10 nm).

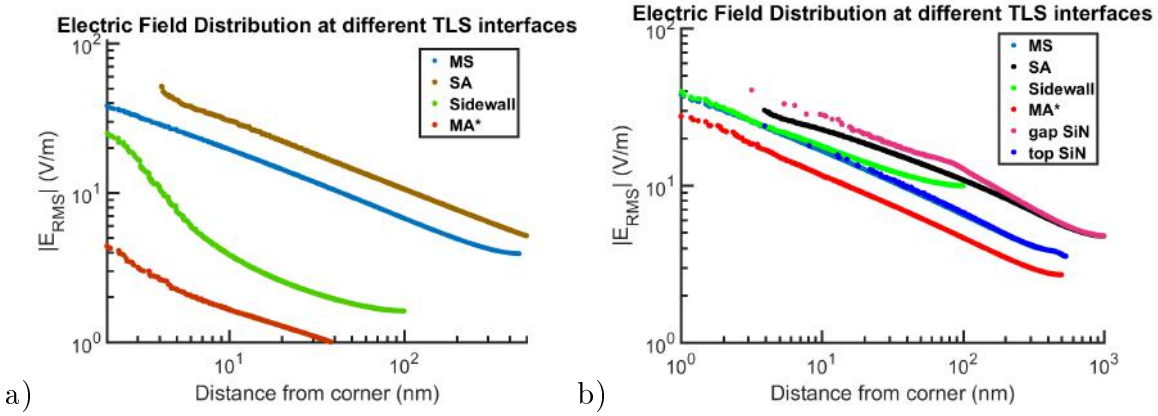

Figure 29: a) Scatter plot of the simulated electric field (at $V_{zpf} = 7\mu V$)from COMSOL as a function of distance from the high-field corner at 4 different interfaces; Metal-Substrate (MS-blue), the Substrate-Air (SA-brown), the Sidewall (yellow) , and the Metal-Air (MA-red) interace. b) shows scatter plot of device with SiNx deposited on top. The SiN that exists in the gap between the electrodes is plotted in pink. *The MA interface shown is the distance from the weak-field corner, which is the top corner of the sidewall. The Sidewall also has influence from the weak field corner which is why the slope isn't as linear as the others in a)

the center of the conductor), starting at 1 nm. We are interested in knowing the distances which contains the majority of the loss. One obtains the ratio $P_{l,tls}/P_{l,tot} = 45\%$ within 40 nm of the highest field corner and 80% within 200nm meaning that the TLS within 40 nm of the corner produce almost half of the loss from the MS region.

TLSs have a statistical density, but in small volumes the discreteness and randomness of individual TLSs become apparent in resonators [32, 82]. This can also lead to Strong-coupling cQED effects of those discrete TLSs. This is especially relevant to TLSs near corners, such as those with small s in Figure 29. Additionally we can separate the loss such that $\tan\delta_{tot} = \tan\delta_{discrete} + \tan\delta_{bulk}$. If we examine the region 40 nm away from the MS/SA corner we find that only 20% of those TLS will have strong enough coupling to be in the strong coupling regime. Furthermore since we know that almost half the loss is due to TLS in this region we can then estimate that about 10% of the total loss is from discrete TLS.

TLS Coupling to resonator

While the TLS related loss from a resonator is generally from weakly coupled bath of TLSs, when the single photon electric field strength become high enough the TLSs can appear discrete. This resonator will have capacitance C and ensemble-limited quality Q_i . A TLS is in the strong coupled limit if $g > g_{min} \equiv \min(\kappa_{eff})$ where $\kappa_{eff} = \sqrt{\gamma_{TLS}(\kappa_\perp + \kappa_\parallel)}$ $\kappa_\perp = \omega_c/Q_i$ where Q_i is the internal loss to due weakly coupled TLS, $\kappa_\parallel = \omega_c/Q_e$and γ_{TLS} is the

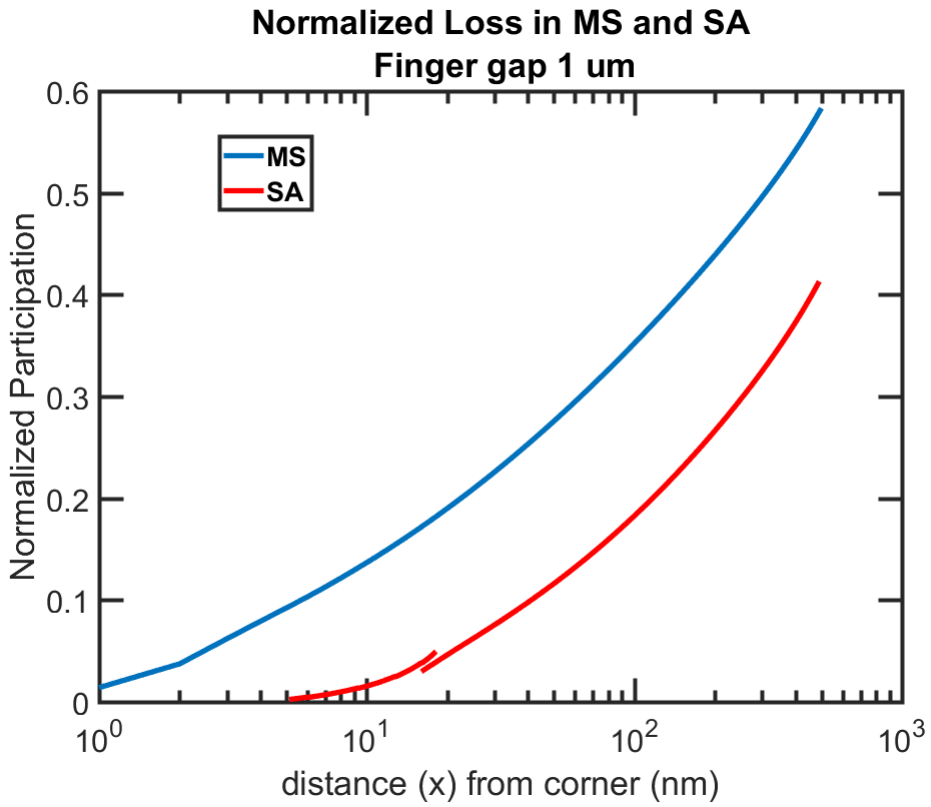

Figure 30: Shows the cumulative normalized loss as a function of distance away from the corner of the film. The blue represents the MS interface and the orange the SA interface

decay rate of the TLS. Suppose we only consider transition dipole moments of value $p_{tr} = p_{real}\Delta_0/\sqrt{3}\epsilon$, where the square root of 3 comes from considering a representative angle found by the effective average from random orientation

$$g = \frac{\Delta_0}{\epsilon} 2 p_{tr} E_{RMS}/\hbar \tag{5.1}$$

. We can then calculate the zero-point fluctuation voltage, $V_{RMS} = \sqrt{\frac{\hbar\omega}{2C}} = 6\mu V$ for a capacitance of $54fF$ and $\omega = 6GHz$.

For example if we assume $Q = 30k$ for base and $6k$ for SiNx film at the single photon regime and if we assume that the decay of our TLS, $T_{1,SiNx} = 3.2\mu S$ [11], $T_{1,AlOx} = 500nS$ [83], $T_2 = 2T_1$(assuming no dephasing) $\gamma_{TLS} = 1/T_2 = .15$ MHz, and $\gamma_{AlOx} = .9$MHz then we get an effective decay rate $\kappa = 350kHz$ in the base film and $\kappa = 400kHz$ in the film with SiNx deposited. The values can be used as a general threshold for the strong coupling regime. However, it has been seen that TLSs on the same order or less as the decay can still be observed [32]. From the electric field distribution we can find the coupling as a function of distance from the highest field corner.

There exists two categories of TLSs in our simulations. TLS which have strong enough coupling to be in the discrete regime and TLS which have weak coupling and act as a bulk ensemble. We can estimate the minimum single photon electric field to be in the strong coupling regime $E_{min}$of a resonator. If we assume the TLS energy is approximately equal to the tunneling energy, $\Delta_0 = \epsilon$ and $p_{tr} = 4$ Debye (= 0.86 eÅ) then $E_{min} = 16$V/m from the distri-

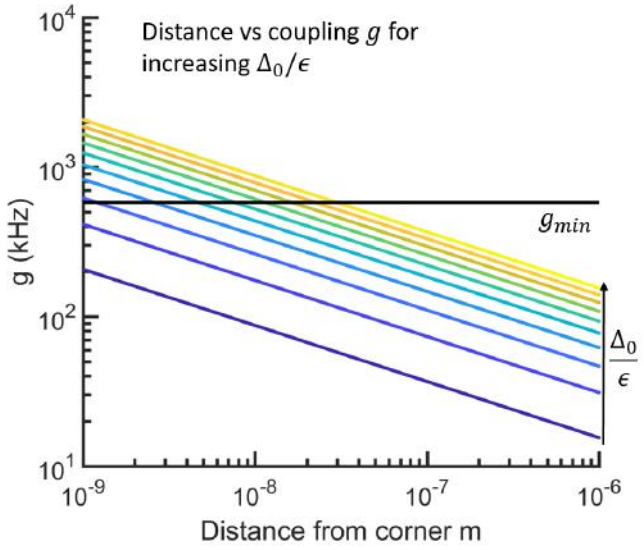

Figure 31: Simulated coupling $g/2\pi$ for TLS which reside in a 3nm thickness area for a given resonator with an IDC of LW=LS=1μm assuming $p_{\parallel} = 4D$. Purple to yellow is for increasing ratio of Δ_0/ϵ from .1 to 1. $g_{min}$is a property related to the quality factor of the resonator and is assumed here to be 350kHz.

bution of the electric field plots I calculate that about $\sim 2\%$ of the total TLS at all interfaces are at a high enough electric field to be in the this regime. Estimating the coupling of the TLS and resonator allows us to estimate the number of strongly coupled TLS that we reside in the bandwidth of the resonator that can be observed. The coupling depends not only on the dipole moment and RMS electric field but in the ratio of the tunneling energy and the total energy of the TLS. Thus I have plotted the expected couplings at the MS interface for the assumed parameters given earlier for varying ratios of Δ_0/ϵ. The graph shows that TLS within the first 50 nm (assuming a maximum $p_{\|}$) can have a strong enough coupling to be considered in the strong coupling regime. The number of strongly coupled of TLS will be estimated in the next section.

Estimating Number of TLS

We can then look at the coupling of the TLS defects to the resonator. We find that within the first 50 nm the TLS have a high enough coupling to be in the strong coupling regime. We can determine the number of TLS expected inside that volume within the bandwidth of the resonator using equation for the distribution of TLS

$$d^3N = P_o dV d\Delta d\Delta_0/\Delta_0 \tag{5.2}$$

This can then be transformed into polar coordinates using $E = \sqrt{\Delta^2 + \Delta_0^2}$

and $\phi = arctan(\Delta/\Delta_0)$ $P_o = \frac{3\epsilon tan\delta_0}{\pi p^2} = 2.4 \times 10^{44} J^{-1} m^{-3}$assuming AlOx TLS with $tan\delta_0 = 2\times10^{-3}, \epsilon = 10\epsilon_0$ and $p = 4$ Debye as used in the previous section we find that for a bandwidth of $300kHz$ we can expect .1 strongly coupled TLS in bandwidth of our resonator. This calculation assumes 100% participation ratios. However for surface TLS which are affected by an inhomogenous field this is not the case. Thus further theoretical derivations are necessary to estimate the number of surface TLS to be seen in bandwidth.

5.1.1 Feasibility Study

Consider that TLSs from surfaces that are defined by the lines $\mathbf{s} = s\hat{s}$ in a cross section of the IDC. The field created by electrodes produces its own direction for coupling to TLSs, where $\mathbf{E_{Bias}}(\mathbf{r}) = \mathrm{E_{bias}}(\mathbf{r})\hat{z'}(\mathbf{r})$. Consider that the surface is represented by a uniform coordinate y, representing the distance along an IDC finger. Then there are only a locus of points in (x,z) representing the surface. For a particular material surface i, this can be made into a function along the distance of this curve $\overrightarrow{E}_{bias} = \mathrm{E_{bias}(s)}\hat{z'}(\mathrm{s})$. Surfaces have a material distribution and we will sample it with the field direction z', and the constituent dipoles with moments along this local field $p_{z'}$. (while I am using z symbol here I am really talking about the dipole moment that is parallel with the electric field). The distribution is still $P\left(p_{z'}\right)$, giving the equation

$$dn = P\left(p_{z'}\right) d\Delta \frac{B}{f_r}, \tag{5.3}$$

Previous work in the group, [Hung, Osborn "Probing hundreds of individ-

ual two-level defects in polycrystalline and amorphous alumina", unpublished, 2021], finds that p_z can be centered on a single value of p_z where the mean is equal to the width. Assuming a single p_z, we find we can use the inverse length l to find the bias field from $V_{ZPF,RMS}$ where

$$l^{-1}(r) = E_{ZPF,RMS}(r)/V_{ZPF,RMS} \tag{5.4}$$

and then

$$E_{bias}(r) = V_{bias}/l(r) \tag{5.5}$$

$$\Delta'(\mathbf{r}) = \Delta + 2p_z E_{bias}(\mathbf{r}) = \Delta + 2p_z(V_{bias}/V_{ZPF,RMS})E_{ZPF,RMS}(\mathbf{r}) \tag{5.6}$$

Once again we find that the dependence is

$$dn/dV_{bias} = \frac{B}{f_r} 2p_{z'} P\left(p_{z'}\right) E_{ZPF,RMS}(\mathbf{r})/V_{ZPF,RMS}, \tag{5.7}$$

Using $g = 2p_z^{'} E_{RMS}/\hbar$ the expression reduces to

$$dn/dV_{bias} = \frac{B\hbar}{f_r V_{ZPF,RMS}} g\left(p_{z'}, r\right) P\left(p_{z'}\right), \tag{5.8}$$

where we again recognize that we can parameterize the position along a surface using a distance s. The resonator properties set a minimum $g(p_z, s)$ to observe .We define a minimum $g = g_{min}$ that is observable, and from this define $p_{zmin}(s)$ (which also allows a definition of $s_{max}(p_{z'})$) the maximum distance from highest field corner. Finally we integrate over the range of s for

the material, at each $p_{z'}$.

$$dn/(dV_{bias}) = \frac{B\hbar}{f_r V_{ZPF,RMS}} g\left(p_{z'}, s\right) P\left(p_{z'}\right), \tag{5.9}$$

We can then write the differential for the total number of TLS N as $dN = dnds\, tl_{tot}$ where t is the thickness and $l_{tot} = 2n_{finger}l_{finger}$ is related to the number (length) of fingers n_{finger} (l_{finger}) as

$$dN/dV_{bias} = \int \frac{B\hbar t l_{tot}}{f_r V_{ZPF,RMS}} g\left(p_{z'}, s\right) ds P\left(p_{z'}\right) \tag{5.10}$$

Then we can take each $p_{z'}$ and integrate $g\left(p_{z'}, s\right) ds$ from 1nm up to an s_{max} since only TLS within s_{max}will have strong enough coupling. This integral can be solved numerically or using a fit from the simulated COMSOL electric field.

$$\int_{1nm}^{s_{max}} g\left(p_{z'}, s\right) ds \tag{5.11}$$

From doing a fit from the COMSOL data we find an that the electric field varies as $E = E_0/s^{\alpha}$, which allows us to make a theoretical g that can be integrated. To determine the upper bound of the integral we can use g_{min} to find s_{max} since the minimum g required to be in the strong coupling regime is related to s_{max} through

$$s_{max} = \left(p_{z'} E_0/(\hbar g_{min})\right)^{1/\alpha} \tag{5.12}$$

TLS Study	T_1	V_{tls}	*Bandwidth*	$\bar{g}$	$\bar{N_b}$	$N_{tls}/100mV$
Surface TLS Device	500 nS	$12\mu m^3$	270 kHz	100 kHz	.1	2.7
Tri-Layer SiN [10]	3.2 μS	$80\mu m^3$	1.1 MHz	1 MHz	1	112

Figure 32: Table shows the difference in the parameters for the tri-layer resonator and the surface TLS design. These parameters were used to calculate the number of strongly coupled TLS expected on average in the bandwidth, $\bar{N_b}$ as well as the number of strong TLS expected for a 100mV range of bias, $N_{tls}/100mV$.

where we have used $g = p_z^{'} E_{RMS}/\hbar$ and E_0 is a fitting parameter along with α .Additionally, the criteria to be in the strong coupling regime is $g > \kappa_{eff}$ where $\kappa_{eff} = \sqrt{\gamma_{tls}(\kappa_i + \kappa_e)}$ and $\kappa_i = f_r/Q_i$ and $\kappa_e = f_r/Q_e$and $\gamma_{tls} = 1/\sqrt{T_1 T_2}$ thus $g_{min} = \kappa_{eff}$

These are equations are helpful in establishing the feasibility of observing individual surface TLS. Below is the figure estimating the number of TLS in the strong coupling regime assuming a $T_1 = 500ns$, p_z = 1Debye, Q_i=30k, Q_e=30k and assuming a TLS volume of $12\mu m^3$ compared to previous tri-layer devices [11, 59]. Additionally we can find the minimum RMS electric field required for a TLS to be in the strong coupling regime assuming a dipole moment and T_1time.

5.2 Device Design and Experimental Setup

Identifying the dominant interfaces could allow for a more targeted research to minimize the TLS loss. Some studies have used COMSOL as a way to estimate participation ratios and showed the MS and SA interfaces to have the most significant contribution to the loss [5]. A Lincoln Laboratory study fabricated

and altered different CPW structures attempting to isolate the regions of loss at different interfaces and showed that actually the MA interface, while having a lower participation ratio, actually has a significantly higher loss tangent that previously thought [84]. Thus there is still need to better understanding TLS loss at the interface. To model the loss due to surface TLS it is common to look at the participation ratio associated with the different interfaces where the TLSs reside, most commonly the Metal-Substrate (MS), Substrate-Air (SA), and Metal-Air (MA) interfaces. It is documented in [5]that as the LW and gap of a finger decreases the participation of the interfaces (which host TLSs) increases as expected, however they all increase at the same rate and thus it is hard to experimentally verify which interface is more dominant than any other. Below we present a study where specific interfaces are examined by the addition of a Si_3N_4 layer. The addition of a Si_3N_4 layer on top of the metal electrodes will change the participation ratio and thus also the internal loss of the device. I hypothesize it would elucidate which interfaces are most dominant in the loss of common high-coherence superconducting circuits.

This design was meant to examine two largely misunderstood concepts for surface TLS. The first challenge is understanding the loss tangent at the different interfaces. The second is being able to see individual surface TLS in such a way as to extract meaningful information about their coherence times and dipole moments. To understand the interface loss we examined two different TLS laden dielectrics, AlOx and deposited Si_3N_4. These dielectrics reside near the superconducting co-planar capacitor. Two films were fabricated

one was a base film where AlO_x TLS primarily reside around the capacitor electrode and in the gaps between electrodes. The other was film with 250 nm of Si_3N_4 deposited on top of the capacitor electrodes. By first establishing a baseline loss from the first film we can understand the added loss from the deposited layer. This technique can be applied to other dielectrics and film types.

The resonator inductively couples to the transmission line so that 2-port microwave transmission measurements can be carried out. The applied dc bias voltage from room temperature is filtered by an RC filter, 3dB attenuator and a copper powder filter. It thus generates an dc-field E_{ex} across each capacitor. The maximum V_{ex} is $100mV$ at which we observe no fridge heating, thus no significant leakage current. Two base resonators were fabricated per chip with nominally the same capacitors, but different value inductors, giving resonance frequencies of approximately 5.75 GHz and 5.6 GHz. The resonators were measured at or below 50 mK. A probing photon number $\bar{n}$ less than one is used for all the reported data, to allow observation of TLSs near their ground state.

To study the surface TLS a lumped element LC resonator is designed which is coupled to a transmission line. A schematic of the design is shown below in Fig.34. There are 4 equal interdigitated capacitors which are individually equal to the total capacitance C of 54 fF. They are arranged in an electrical bridge to create points of equipotential to isolate the bias line from an RF mode and line. The RF line is probed through the transmission S_{21} and can

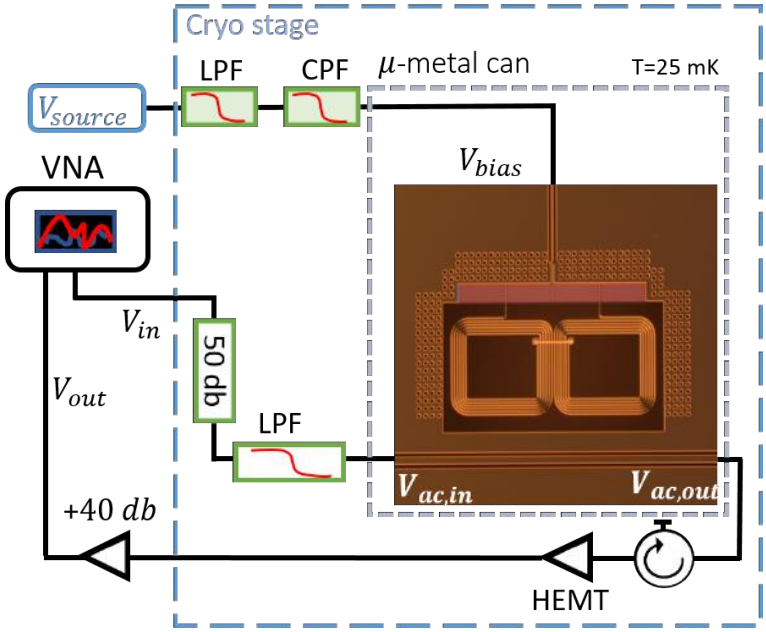

Figure 33: A diagram of the experimental setup. A lumped element resonator is coupled to a transmission line. $|S_{21}|$ is fit to extract the quality factors of the resonator. The fabricated image of one of the resonators measured is pictured. A zoomed image of the device is shown in Figure 38.

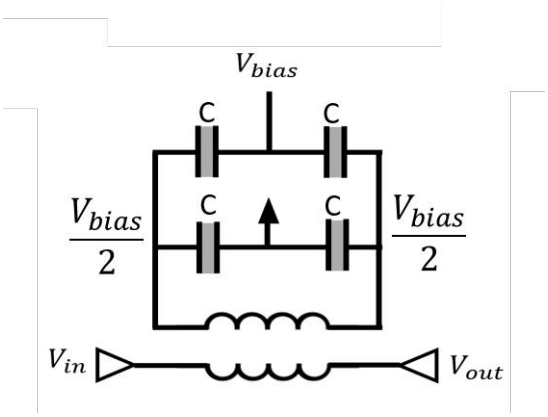

Figure 34: Schematic of the lumped element resonator. A four-capacitor bridge isolates the bias line from the ac-mode of the resonance and the(RF) readout line.

be measured and fit using equations discussed earlier in chapter 3.

The resonator was designed with a 54fF IDC capacitance in a bridge configuration. The four capacitors in the bridge are equal allowing us to separate the DC bias from the RF by biasing at a virtual ground. A double spiral inductor was designed to achieve an inductance of 15 nH. The low capacitance is important to achieve a high zero point fluctuation rms voltage which in turn determines the coupling strength according to $V_{zpf} = \sqrt{\frac{\hbar\omega}{2C}}$.

5.3 Fabrication Process for Coplanar Surface TLS study

We are interested in studying two-level-system defects that reside at the different material interfaces of an aluminum film with a crystalline silicon or sapphire substrate. Typically these TLS will reside in the amorphous oxide regions, SiO_2 or Al_2O_3, between the film, substrate, and vacuum. Half the

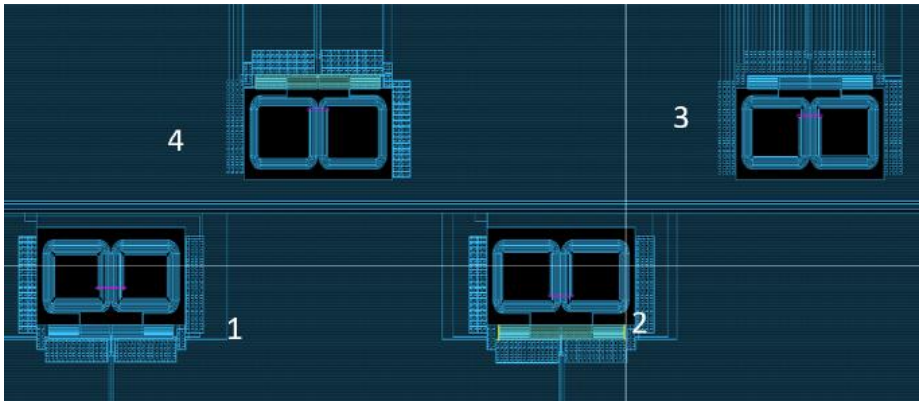

Figure 35: Layout of the 4 lumped element resonators. The resonators consist of an IDC capacitor with a capacitance =54 fF and a large double spiral inductor. A double spiral inductor was necessary to maintain the symmetry of the device and also to obtain a large inductance, L=12 nH. Resonators 2 & 4 have Si_3N_4deposited on top of the IDC. Resonators 1 & 3 are base.

resonators had a silicon nitride dielectric deposited over the IDC. $Si_3N_4$is a common dielectric in quantum computing, where the TLS dipole moment and coherence time have been measured[64, 11, 32].

Photolithography

Typically, fabrication starts with a sapphire or high resistivity ($\rho > 20$k) silicon wafer. The wafer is placed in a sputtering chamber for deposition at 100c and a constant pressure of 5mTorr of Argon . Close to100 nm thick of aluminum is deposited. After metal deposition the wafer is ready for the photolithography process. We use a GCA autostep 200 i-line 5x stepper. This exposes the aluminum film into the designed pattern. First, HMDS is spun at 3000 rpm for 60s, followed by the spinning the 906-10 OIR Photoresist (PR), and then followed by a pre-bake at $90°C$ for 1 minute before exposure. The HMDS is

a crucial intermediate layer. It provides a better surface for the PR to adhere to, which is important when patterning small linewidths and line spacings. I am typically using 1μm linewidths of PR or less to create the mask. After the resist is on, the wafer is then placed in the stepper and exposed for .35 seconds per chip. On this 3 inch wafer we fabricate 78 6.35mm (0.25 in.) chips. After exposure the wafer is then post baked for 1 minute at 120 Celsius. The resonator is then developed in OPD 4264 which will chemically remove the exposed resist, revealing the aluminum that is underneath. Fig.35 shows examples of a similarly fabricated resonator consisting of a large spiral inductor and interdigitated capacitor.

Etching Processes

After the development, the film is ready to be etched. Our first option for an etch is a wet etch with an aluminum etchant which etches at 61 nm/min isotropically (as much laterally as vertically). The other option is a plasma etch with BCl_3, that etches vertically and thus produces sharper corners. However the ICP etch will harden the existing resist to the point that it can be difficult to remove even if an oxygen ash is performed. Thus, typically a wet etch is performed to create a cleaner wafer and reduce resist remains. The process continues with the deposition of Si_3N_4 on top of the film using a plasmatherm PECVD tool. We have the tool deposit the Si_3N_4 for 9 minutes at $300°C$. This produces a thickness of approximately 250 nm, and afterwards a profilometer is used to get a more accurate thickness. After the Si_3N_4 deposition, a resist layer

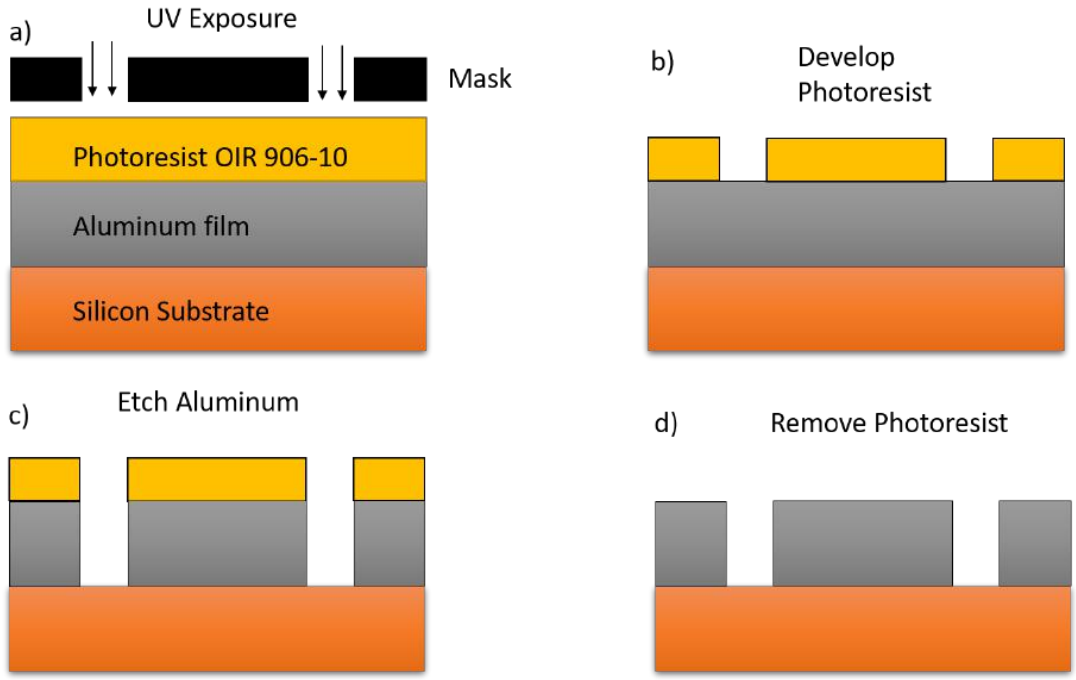

Figure 36: Typical photolithography process. OIR 906-10 photoresist is spun on the wafer and preheated. a) the wafer is exposed in the stepper to UV for .35 seconds. b) The resist is developed removing any PR that was exposed. c) Removing the PR allows one to etch the Al underneath. Typically a wet etch is performed with an etch rate of 60nm/min. d) Finally the PR is removed with an acetone spray, bath and sonication. It is also helpful to heat microposit at 80 C to completely remove any PR. Removing the PR is an extremely important step especially if one has multiple layers and exposures as one doesn't want excess PR to reduce the quality of the films.

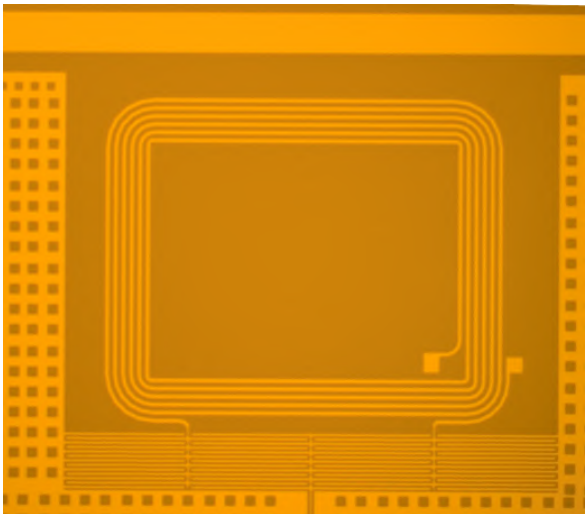

Figure 37: Image of design 2 LC resonator in fabrication, after the aluminum etch.

is spun on again with a prior HMDS layer in preparation for the VIA layer. This wafer is prebaked again and placed in the stepper for exposure. After a postbake the wafer is developed in OPD 4262. Once the layer is developed and an image is taken to confirm that the resist has been developed, exposing the Si_3N_4 underneath. The wafer is then placed in the plasmatherm 790 for an RIE etch to create the VIA. A plasma created from 20 ccm of SF_6 and 5 ccm of oxygen is then created to etch the exposed Si_3N_4 for 3 minutes. The etch rate is typically 90 nm/minute.

Figure 37 shows the first layer of the design for studying surface TLS, named design 2. The resonator is a large spiral inductor and a small interdigitated capacitor with linewidths near $1\mu m$ and line spacings $< 1\mu m$.

After the VIA layer is made the resist is removed in acetone using a 10

second spray and then letting it bath in acetone for 5 minutes. The wafer is then blown dry after a rinse in IPA/Methanol. The wafer is then placed inside the AXXIS sputtering system. To remove any native oxides that have developed inside the VIA, an ion mill is used. In-situ we then immediately follow the ion mill with a deposition of the top layer of aluminum. It is 250nm thick. After deposition, another photoresist layer is prepared with development. Next a wet etch is performed. Afterwards, the photoresist is removed with acetone. Finally the Si_3N_4 layer can then be removed. The last layer is removing all the Si_3N_4 except in certain resonators where we purposefully leave SiN on top of the interdigitated capacitors to increase the TLS density. Again a PR layer is spun on, baked, exposed, and developed. The wafer is then ready for the Si_3N_4 etch using the same RIE process to make the VIA layer previously stated. After the Si_3N_4 etch the remaining PR is removed with acetone, methanol, and IPA. The processing of the wafer is now complete. To prepare the wafer for dicing a layer of FSC photoresist is spun on at 3000 rpm for 60 seconds and then baked at 120 $^{\circ}C$ for 5 minutes. This layer helps to protect the top of the wafer from any debris from the blade and dicing process. Figure 38 shows a completed resonator before the final FSC PR is spun on.

Dicing and Packaging

After the wafer has been diced, individual chips can be extracted. The PR resist layer of a chip is removed with acetone before being placed inside of a

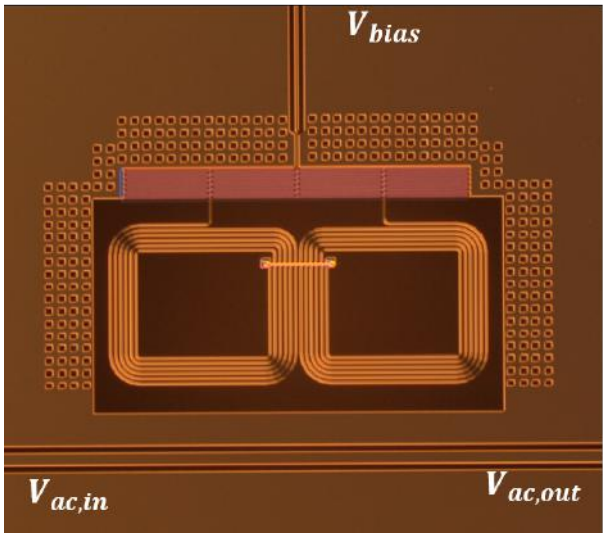

Figure 38: Optical image of finished fabrication of design of STLS, showing the ac ports and the bias port.

sample box, shown in Figure 23.

GE Varnish on the backside of the corners of the chip is used to adhere the chip to the sample box. Wirebonds are then used to connect the CPW transmission lines on the PCB of the sample box to the launch of the chip. Additional bonds are placed all around the GND of the chip to the sample and additionally placed across the center transmission line to reduce slotline modes. These bonds are made of gold and typically less than 1 mm in length as shown in the Figure 24 . Our sample box has been designed to reduce box modes in our operating frequency range between 4-8 GHz. These sample boxes were designed and analyzed by Aruna Ramasuna and made by myself.

The sample box is sealed by small brass screws. Brass has a low amount of magnetic fields. The sample box is placed on a cold block at the mixing

chamber or the lowest level of our Leiden dilution refrigerator. Our refrigerator reaches a base temperature near 20mK. Additionally a mu metal shield is used to reduce any stray magnetic fields from the earth as discussed earlier. The inside of the 50 mK can is coated with Carbon black to reduce IR radiation even further.

5.4 Power Saturation of Loss Tangent

In this section I will focus on the analysis of the loss due to surface TLSs. While TLSs within deposited dielectrics are fairly well understood, e.g., have an expected ac-field, and dc-field dependence, $tan(\delta) = tan(\delta_0)/(\sqrt{1+(V/V_C)^2}$ surface TLS defects do not seem to follow the same theory. Their power dependence is much weaker and the TLSs have not been individually measured. Surface TLS defects reside in one of many possible interfaces at a dielectric surface oxide or dielectric interface. The complications of measuring an individual TLS there may be related to the way the electric field is inhomogeneously distributed in Coplanar Waveguide (CPW) or Interdigitated Capacitor (IDC) structures. When the field is inhomogeneous the strength of the field that the TLSs feel will vary in space.

As discussed earlier,one can find the total loss tangent will be equal to the sum of the product of the participation ratio of each TLS interface with the loss tangent associated with the dielectric.

$$1/Q_i = \sum p_i tan\delta_i \tag{5.13}$$

For example AlOx has been measured [83] as having a loss tangent of 2×10^{-3}while our low stress Si_3N_4 has a loss tangent measured in the past [64, 11] as 2×10^{-4}. And we can say for a base resonator that the MA and MS interface are AlOx since we are sputtering Aluminum and the other regions will also become oxides and thus the total loss becomes

$$tan\delta = p_{MS}tan\delta_{SiO_2} + p_{SA}tan\delta_{SiO_2} + p_{MA}tan\delta_{AlOx} \tag{5.14}$$

COMSOL is used to simulate the CPW and IDC structures and obtains the electric field vectors $E_{j.}$. The probability P_j of having an electric field, E_j,can be found by creating a histogram of all the electric field vectors in the TLS host area. The loss in terms of the electric field is then equal to the sum over all electric field values in the TLS host area.

$$\tan_\delta = \sum_j p_o P_j(E_j) \tan_{\delta_i} / \sqrt{1 + (E_j/E_C)^2} \tag{5.15}$$

where $p_o$is the participation ratio of the interface and. $E_C$is the critical field which occurs at the quantum limit $n = 1$ and $\tan_{\delta_i}$is the low power loss tangent at a particular interface. Additionally it is necessary to account for the changing of the voltage in actual experiment versus in the simulation which is only for a single simulated voltage. This can be accounted for by adding the ratio V/V_{sim}

a)

Base Film

LW/LS = $1\mu m/1\mu m$	Participation Ratio
MA	1.4×10^{-4}
Side Wall	5.1×10^{-4}
Corner	3.5×10^{-4}
MS	6.7×10^{-3}
SA	7.4×10^{-3}

b)

Si_3N_4Deposited Film

LW/LS = $1\mu m/1\mu m$	Participation Ratio
MA+SW	1.3×10^{-2}
MS	7.1×10^{-3}
SA	1.2×10^{-2}
MA (Si_3N_4)	.23
$Si_3N_4 - gap$	.38

Figure 39: shows the expected participation ratios for a) a base film b) Si_3N_4deposited film each has100 nm thick Al with 3 nm assumed TLS thickness at the MS, SA, and MA interfaces. Seven $1\mu m$ LW fingers or electrodes were spaced $1\mu m$ apart with a $400\mu m$ substrate.

$$\tan_\delta = \sum_j p_o P_j(E_j) \tan_{\delta_i} / \sqrt{1 + (\frac{V}{V_{sim\,j}} \frac{E_J}{E_C})^{2-\alpha}} \tag{5.16}$$

From simulation the expected participation ratios at the different interfaces are shown in the below figure. I assume 3 nm of a crud layer, likely either organics or $AlOx$ at the MS and SA interface as well as 3 nm thickness of AlO_xat the MA interface for both films. 250 nm of $Si_3N_4$is deposited on the second type of resonator.

From these expected participation ratios I can calculate the expected loss in each film at low power. For the base film

$$\tan\delta_{base} = (p_{MS} + p_{SA} + p_{Corner} + p_{MA} + p_{SW}) \tan\delta_{AlOx} = 33k$$

For the film with silicon nitride deposited

$$\tan\delta_{SiN} = (p_{MS} + p_{SA} + p_{MA} + p_{SW})\tan\delta_{AlOx}$$

$$+p_{SiN}\tan\delta_{Si_3N_4} = 5.4k$$

The results are presented in the next section.

5.4.1 Measurement of power saturation of base andSi_3N_4 deposited resonators

The power dependence of the inverse quality factor of the resonator will illuminate the TLS losses that exist in the film. In the base film SiO_2 at the MS and SA interface will play a large role where participation ratios are expected to be higher. While AlO_x will be present at the MA interface which one would expect to play a smaller role due to a lower participation.

Figure 40 shows the power dependence of the inverse $Q_i^{-1}$of the base film and Si_3N_4deposited film. At low powers the base resonators measured an average $1/Q_i = 5.8 \times 10^{-5}$ while as expected from the COMSOL simulations there is less loss in the base film due to a lower TLS density. The Si_3N_4fills the gap between the electrode and counter electrodes in the IDC in the other film and I measured an average $1/Q_i = 1.5 \times 10^{-4}$.

Using equation (5.16) I can fit the loss tangent using the fitting parameters of $p_i\tan_{\delta_i}, 1/Q_{hp}, \alpha$,and E_C . I assumed a relative permitivity of Si_3N_4 of 6.5

and a permitivity of 10 and AlO_x as done in other studies [5]. I am able to use the participation ratios simulated from COMSOL as a good initial guess for my Monte Carlo method fit. The base fitting equation is

$$\tan\delta_{base} = (p_{MS}+p_{SA}+p_{Corner}+p_{MA}+p_{SW})\tan\delta_{AlOx}\sum_j P(E_j)/\sqrt{1+(\frac{V}{V_{sim\,j}}\frac{E_J}{E_C})^{2-\alpha}} \tag{5.17}$$

For the film with silicon nitride deposited

$$\tan\delta_{SiN} = (p_{MS}+p_{SA}+p_{Corner}+p_{MA}+p_{SW})\tan\delta_{AlOx}\sum_j p_o P_j(E_j)\tan_\delta/\sqrt{1+(\frac{V}{V_{sim\,j}}\frac{E_J}{E_C})^{2-\alpha}} \tag{5.18}$$

$$++\,p_{SiN}\tan\delta_{Si_3N_4}\sum_j p_o P_j(E_j)/\sqrt{1+(\frac{V}{V_{sim\,j}}\frac{E_J}{E_C})^{2-\alpha}}$$

I get very good agreement however can interesting fitting parameters. From the fit I extract an inverse high power quality factor, $1/Q_{hp} = 1.7\times10^{-5}$. At high power there is likely quasiparticle loss that is dominant. Radiation loss should be low since the geometry is small[94]. I found $\alpha = .12$ and $p_i\tan_{\delta_{AlOx}} = 1.32\times10^{-5}$. I was expecting $p_i\tan_{\delta_{AlOx}} = 2.8\times10^{-5}$this mean that the assumptions I made for the participation ratio or AlOx loss tangent in reality is lower. I suspect that the participation ratio in reality is lower than in my simulation. Since it is very possible that the actual thickness of the TLS host region is thinner than I assumed at 3nm. Additionally it is likely

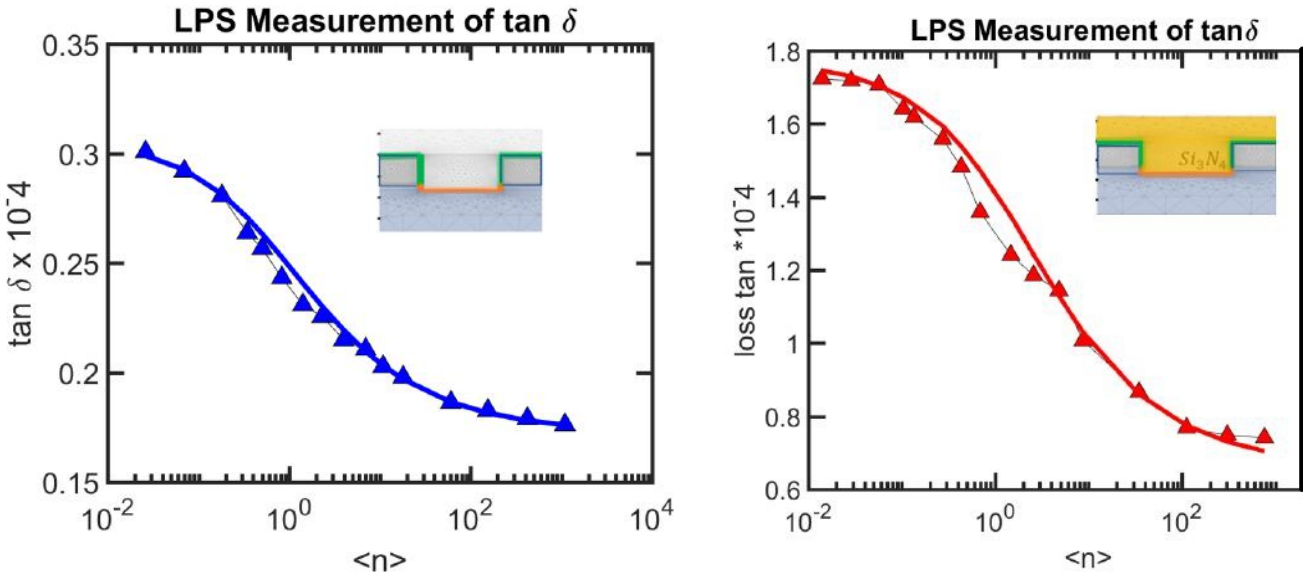

Figure 40: Graph of the inverse Q_i of the resonators measured. The low power loss is lower in the base film as expected. The base film measured 33k at low power while the silicon nitride film Qi measured 5.7k.

that at the MS interface there is more organic crud than AlOx. Some groups claim to greatly reduce loss in sapphire substrate at the MS and SA region by ion milling in-situ before they deposit[54] . The fit for the critical field $E_C = 1.1V/m$. Using equations (2.29-2.30) and assuming that the ensemble $p_z = 7.9D$ for AlO_x one can obtain a T_1relaxation time of $2.2\mu S$. This value for the ensemble TLS is much higher than expected since AlOx T_1times are generally 100ns-1μS [83]. This is another indication that the TLS host are likely organics or OH- ions.

Slight deviation in the base fit in the middle powers could be due to different interfaces saturating at different power values. While we know all the dielectric crud layer is $AlOx$ it is possible the $\tan\delta$ is different at the different interfaces. Furthermore the fit gives us an idea of the physical TLS host thickness at each interface and the coherence of the ensemble of TLS.

To fit the film with silicon nitride deposited we can add the loss from the surface oxides

$$\tan_{\delta base} = \sum_j p_o P_j(E_j) \tan_{\delta_{AlOx}} / \sqrt{1 + (\frac{V}{V_{sim\,j}} \frac{E_J}{E_C})^2} \tag{5.19}$$

to the loss tangent for the silicon nitride

$$\tan_{\delta total} = \sum_j p_o P_j(E_j) \tan_{\delta Si_3N_4} / \sqrt{1 + (\frac{V}{V_{sim\,j}} \frac{E_J}{E_C})^2} \tag{5.20}$$

$$+\sum_k p_o P_k(E_k)\tan_{\delta AlO_x} / \sqrt{1+(\frac{V}{V_{sim\,k}}\frac{E_k}{E_C})^2}$$

It is important to consider that the participation ratios of the MS,SA, and MA interfaces of the $AlOx$ have changed as shown in the table in Figure 39. The ratios have changed because of the added silicon nitride which has a relative permitivity of 6.5 which replaces the permitivity of the vacuum ($\epsilon_r = 1$). This in turn reduces the participation ratio of the field in the substrate from 52% to 37% and increases the field in the gap between the fingers from 6% to 27% . Although more than 60% of the field is in the regions filled by the silicon nitride because the intrinsic loss tangent, $\tan_{\delta_{Si_3N_4}}$, is an order of magnitude lower than in the $AlOx$ layers the silicon nitride region is expected to contribute to 66% of the loss while the AlOx regions are significantly smaller in size they are an order of magnitude lossier and thus still are responsible for 33% of the loss.

Focusing back on the results for the silicon nitride deposited film I also obtained good agreement again in the fits as seen in b) of Figure 40. From the fit I extract an inverse high power quality factor, $1/Q_{hp} = 6.3 \times 10^{-5}$. At high power there is likely quasiparticle loss that is dominant. I found $\alpha = .02$. This is interesting in that is was a factor of 6 less than the base film and is very close to the exponential dependence in STM. This is likely because although we have a co-planar device we have deposited a dielectric that dominates the loss with a participation ratio of 66% close to the participation in an traditional trilayer

capacitor. Thus as you get closer to the full 100% participation it would make sense that α would get reduced. The critical field fit $E_C = .7V/m$ and if we assume $p_z = 7.9D$ then we get a $T_1 = 3.4\mu S$ which is very close to the value of $3.2\mu S$ obtained is previous studies of Si_3N_4[32]. I extracted a participation ratio of SiNx of .61, close to the expected .66. I also extracted a losstangent of $1.7 \times 10^{-4}$for Si_3N_4 which is in the range I was expecting. Slight misfits in the middle of the power dependence is likely due to the two types of TLS saturating at different powers.

Conclusions

From the good agreement in the fits for the data of the base film and comparing it to the film with SiNx deposited I've shown that COMSOL can be used very effectively to help obtain losstangents of dielectric films. This technique could be used to find the losstangent of unknown dielectric films without having to create a tri-layer device. This extra simplicity makes the technique very appealing. Additionally we found that as the participation ratio of the TLS host area gets closer to 1 the electric field parameter α gets closer to 0 as expected from STM. We found the losstangent of SiNx to be 1.7×10^{-4}we also found a losstangent of the crud layer of a sapphire film to be 2.5×10^{-3}.

5.5 Observing Individual surface TLS

In the previous section I analyzed the TLS loss at different interfaces. I will now focus on the observation of individual surface TLS. While individual TLS

have been observed in previous experiments[32], those TLS are exposed to a homogeneous electric, surface TLS see an inhomogeneous field. This difference along with the fact that surface TLS see low fields on average make direct observation of TLS-resonator crossings difficult to see. The goal is to characterize the TLS-Resonator couplings, $g/2\pi$, and understand the location of where these strongly coupled TLS exist. I will show how we can extend the dual cavity model below to account for strongly coupled TLS.

5.5.1 Surface TLS at low power

Characterizing TLS is paramount to understanding the interaction between TLS and qubits. To observe individual TLS the film was purposefully designed to have a micron LW = LS =1μm. This smaller line spacing and gap allows for high electric fields as seen in simulation. This geometry also increases the TLS-Resonator coupling because it is proportional to electric field. Thus at low temperatures and low powers and if the coupling is on the order of the decay individual TLS can be observed.

The goal is to characterize surface TLS coherence times, couplings and dipole moments which are largely unknown. In this section I will discuss the results of measuring the resonator at low temperatures and at low powers in the single photon regime without any bias.

Data was collected in over 13 separate cooldowns. It is important to warm up the fridge past 4K to observe new TLS and allowing the TLS to have enough energy to overcome the potential barrier. In one specific cooldown I

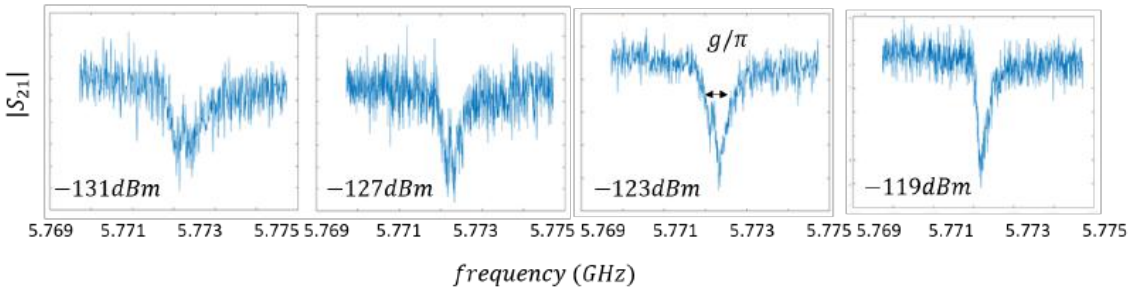

Figure 41: Transmission of a TLS coupled to the resonator as the power increases from left to right, -131 dBm, -127 dBm, -123 dBm, and -119 dBm (input power at device). At the right most power the TLS-Resonator system becomes decoupled as the power has become too high and the critical photon number has been reached.

was able to observe a strongly coupled TLS in the bandwidth of my resonator. Due to the relatively high Q_i, (Q_i=30k) and thus the small bandwidth, and low electric fields (compared to others [32][82]) I had calculated the average number of TLS to observe in bandwidth of the resonator as 2%. Figure 41 shows the magnitude of the transmission , $|S_{21}|$ versus the frequency. When the power at the device is lower than -119 dBm I could observe the coupled TLS-Resonator system and measured a splitting of 220 kHz. By fitting this to equation (3.60) I could also extract a T_1 time . As I increased the power, the system becomes decoupled and the bare cavity resonance is found, $\omega_0 = 5.7722$ GHz. Below is a color plot showing the transition of the TLS-resonator as a coupled system to an uncoupled system at higher powers.

Additionally I can fit this TLS according to equation (3.43). I find that $\omega_{tls} = 5.77217$GHz , $g/2\pi = 120kHz$, and the relaxation time $T_1 = 380ns$. The fitted coupling has 5kHz or 2% difference compared to the coupling measured directly from the graph.

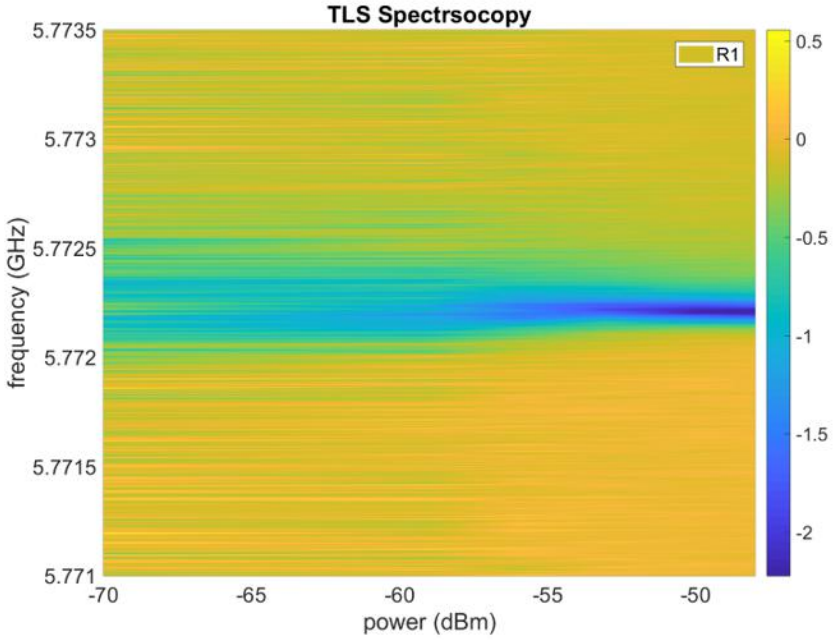

Figure 42: Shows the transmission of a strongly coupled TLS coupled to the resonator as a function of source power. At low powers there are two distinct peaks one is more resonator-like the other more TLS-like. As power is increased the TLS-Resonator system becomes decoupled at the critical photon field, n_c, and the bare cavity resonant frequency is restored. The splitting was measured to be, $f_g = 2g/2\pi = 235kHz$

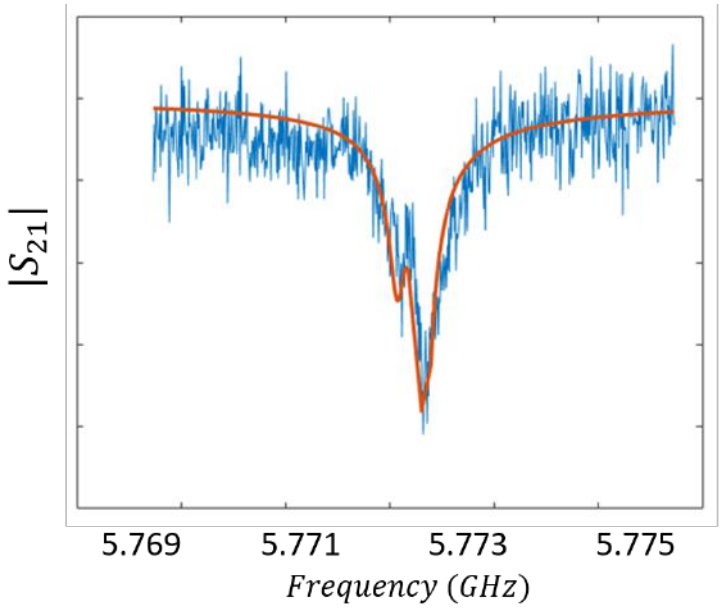

Figure 43: Normalized transmission of single strongly coupled TLS to a resonator. The raw data is in blue and the fit is in red. From the fit I extract a coupling of $g/2\pi = 120kHz$, and a coherence time of $T_1 = 380nS$

5.5.2 TLS Bias Results

Characterizing and observing surface TLS is crucial to the continued improvement in superconducting quantum devices where STLS remain the predominant loss mechanism in high Q_i resonators and decoherence in qubits. In the previous sections I showed experimental observation of TLS-Resonator coupling at low power and the geometry of the design. In this section I will discuss the results of applying a bias on chip through a 3rd port.

The main distinguishing feature from my design and others is that besides the observation of surface is the use of an on chip bridge bias scheme as described earlier in section 5.4. In order for the tuning of the TLS to be

observable, the noise on the voltage line must be much less than the amount of voltage that moves a TLS across the bandwidth of the resonator.

$$V_{noise} << hBl(r)/2p_z, \tag{5.21}$$

I will calculate this is the following section. Ideally the noise voltage amplitude from 0 to a few GHZ should not exceed a few millivolts. If the noise has a white spectrum, this implies a power spectral density of 200 pV/ p Hz. The setup I used is shown in Fig. 44. The DC voltage source was connected to a SR560 preamplier that had an integrated tunable LPF which I set to DC. I operated the preamp using its internal battery for better isolation from 60-Hz noise. The gain was set to 1. The output of the preamplier goes to first a RT low-pass RC filter with a cutoff frequency around 100 Hz and then the in the fridge at the 3K plate I used another low-pass RC filter with a cutoff frequency of 30 Hz to reduce the Johnson noise. Then the bias line goes through a 10 dB microwave attenuator installed at the still plate (.7 K) to thermalize the center conductor carrying the voltage and reduce thermal noise from higher temperature stages. Lastly, a copper powder low-pass filter with a cutoff frequency of 100 kHz was used at the base plate to filter noise from higher-temperature stages.

In this setup the voltage across the capacitor on the devices has a large attenuation. For the setup of Fig. 44 I found $V_b = .0051V_{source}$. It is important to know that if$V_{noise} > hBl(r)/2p_z$ some TLS features will not appear clearly in the S_{21} bias measurement.

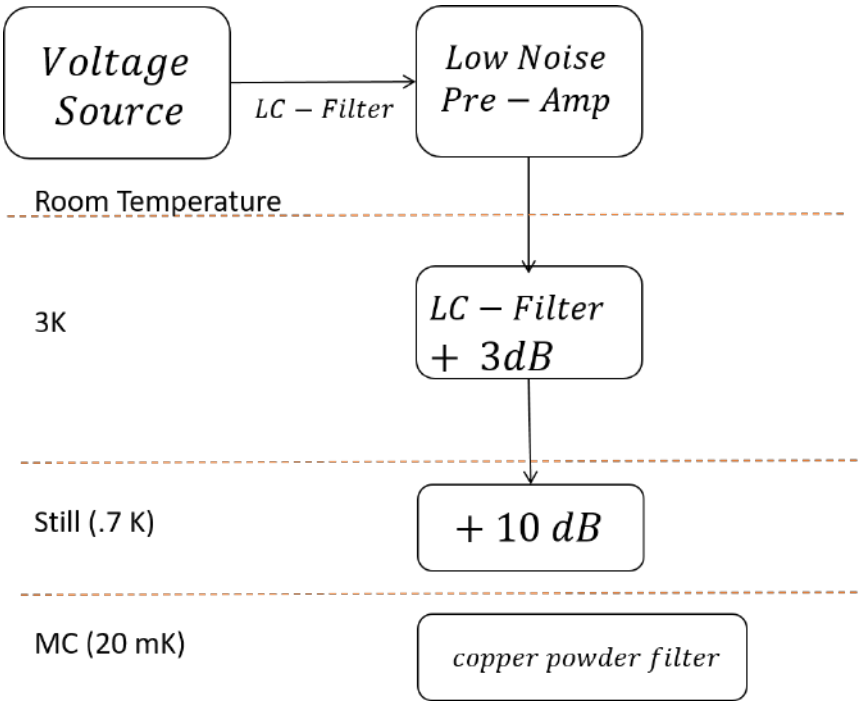

Figure 44: Diagram of RF components at the bias line at the different temperature stages. At room temperature I used a Yogokawa GS200 voltage source and used 2 cascaded RT LC filters with a cutoff frequency below a 1 MHz. At room temperature I also used a Stanford Research SR560 set to DC filter mode with a gain of 1. I then used another LC filter at 3K and had a total of 15dB of attenuation on the bias line which in addition to reduce noise helps to thermalize the center conductor. At the low stage I used a copper powder filter.

Fitting TLS energy eigenmodes

As derived in chapter 2 when a TLS is coupled to a resonator the degeneracy is broken and an avoided level crossing is created. While in previous biased TLS measurements direct observation of these avoided crossings was not clearly seen I will show data where these crossing are clearly seen and can be fit to extract the coupling, g, and the individual coherence time T_1. While the coupling and T_1 can be directly extracted the TLS energies Δ, and Δ_0 and dipole moment, p_z can also be extracted in the fits if we assume a particular electric field for a given voltage bias. Recall that the field at the TLS interfaces are inhomogeneous and thus is it difficult to know the physical location of the TLS being observed. However from the data we can make conclusions about the maximum distance that strongly coupled TLS can exist and be calculate a minimum and maximum p_z by using the measured couplings.

As described earlier we observe the coupled eigenmodes

$$E_{\pm} = \frac{1}{2}\hbar(\omega_r + \omega_{tls}) \pm \hbar\sqrt{g^2 + (\frac{\Delta_w}{2})^2} \tag{5.22}$$

subtracting the two modes gives

$$E_+ - E_- = 2\hbar\sqrt{g^2 + (\Delta\omega/2)^2} \tag{5.23}$$

and if one looks on resonance, $\Delta_\omega = 0$, then the minimum frequency difference between the two modes is $2g\hbar$. By fitting the frequency of the resonator versus the bias voltage one can extract the eigenmodes around the forbidden

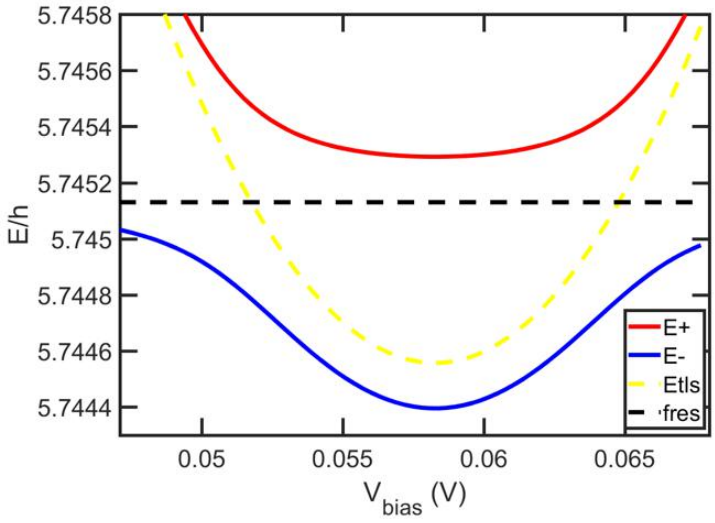

Figure 45: The eigenmodes of the coupled TLS-Resonator system. The blue and red show the $E_{-}$and E_{+}eigenmodes of the coupled system. The dotted yellow and black lines show the uncoupled TLS energies and the resonator energy as a function of voltage biased.

crossing and measure the coupling g. Below shows the data and fit for one of the strongly coupled TLS which has a $g/2\pi = 275kHz$. I found I can easily obtain this coupling by plotting the frequency of the minimum of the magnitude of the transmission, $|S_{21}|$ I can find the eigenmodes as seen in Fig 47.

Below shows the results of one of 20 cooldowns of bias measurements compared to a time measurement with no bias. I scanned over 1 MHz and swept the bias over 400mV measuring the transmission, S_{21} through the feedline. The spectroscopy shows several crossings as well as a single hyperbola in the scan. From this measurement I can then fit the eigenmodes and extract the TLS energies, dipole moment and coupling, $\Delta, \Delta_0, g/2\pi$. The assumptions I make for these fits are: I assume a distance of 20nm from the highest field

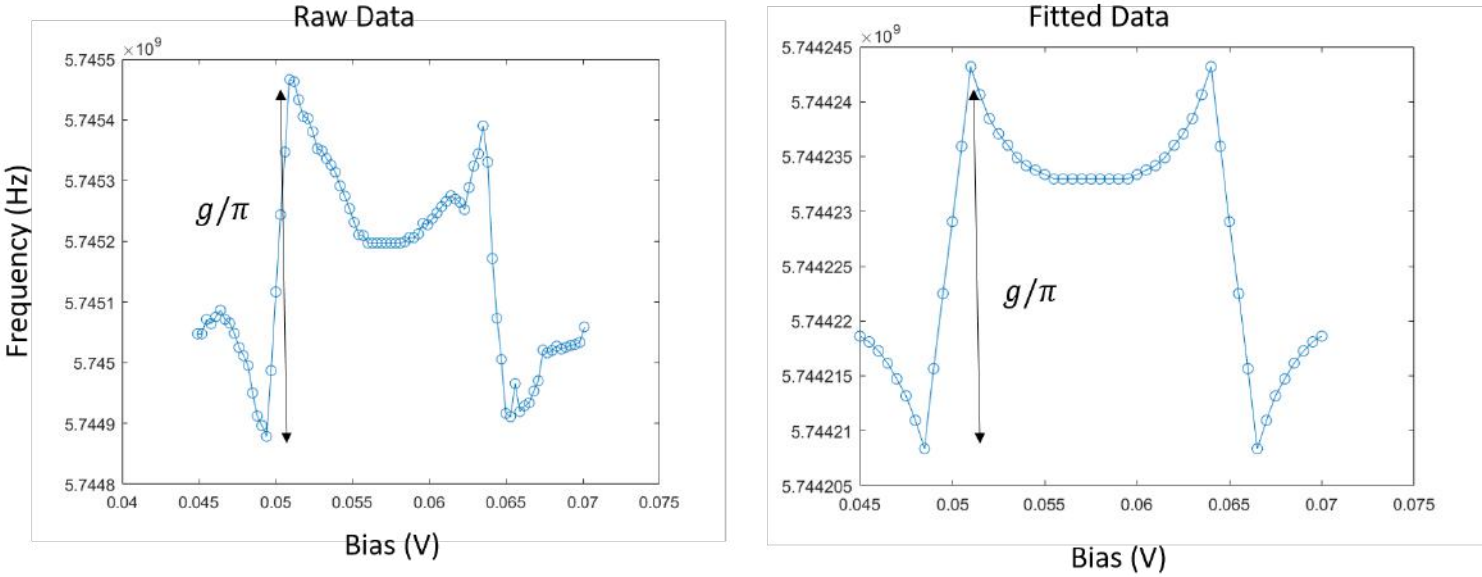

Figure 46: a) Experimental data and b) fitted data of a single crossing from a particular data set. The y axis is the frequency of the minimum of the magnitude of the transmission $|S_{21}|$, while the x is the bias voltage at the source. I can extract the coupling $g/2\pi$ by subtracting the maximum frequency from the one eigenmode from the lowest frequency of the other eigenmode.

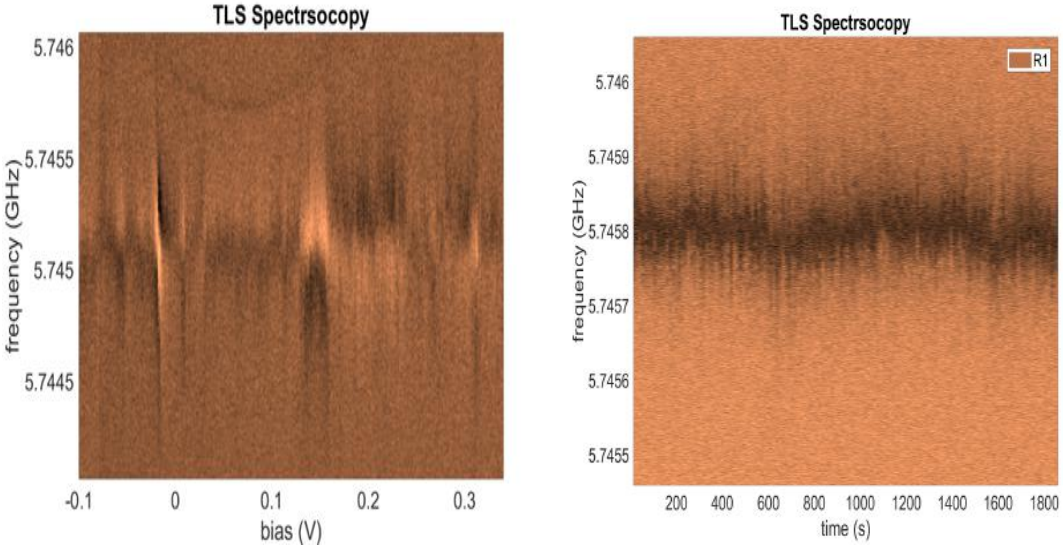

Figure 47: a) TLS Spectroscopy showing the transmission, $|S_{21}|$(color) where the darker is a lower transmission plotted versus for different bias voltages. Multiple TLS-Resonator forbidden crossings and a hyperbola can be observed. The background has been substrated to enhancce the TLS features. b) Spectroscopy showing transmission over time with no bias and thus no crossings are seen.

corner, this allows me to calculate reasonable the electric field values for a given bias voltage (from COMSOL simulations). Additionally I assume a loss tangent of 2×10^{-3}, I use the Qi and Qe measured previously of Qi=30k, and Qe=75k. I also assumed a $T_1$of 500 ns also.

For TLS with asymmetry energy Δ'near 0 one will see the bottom of a hyperbola. If the asymmetry is not near 0 then one will see an anti-crossing of the TLS-Resonator coupled system. Some crossing are less visible than others. The clarity of these crossings is largely determined by the bandwidth since that determines the noise threshold our bias line needs to be above. From (5.15) I calculated .15mV which is largely due to the low bandwidth of

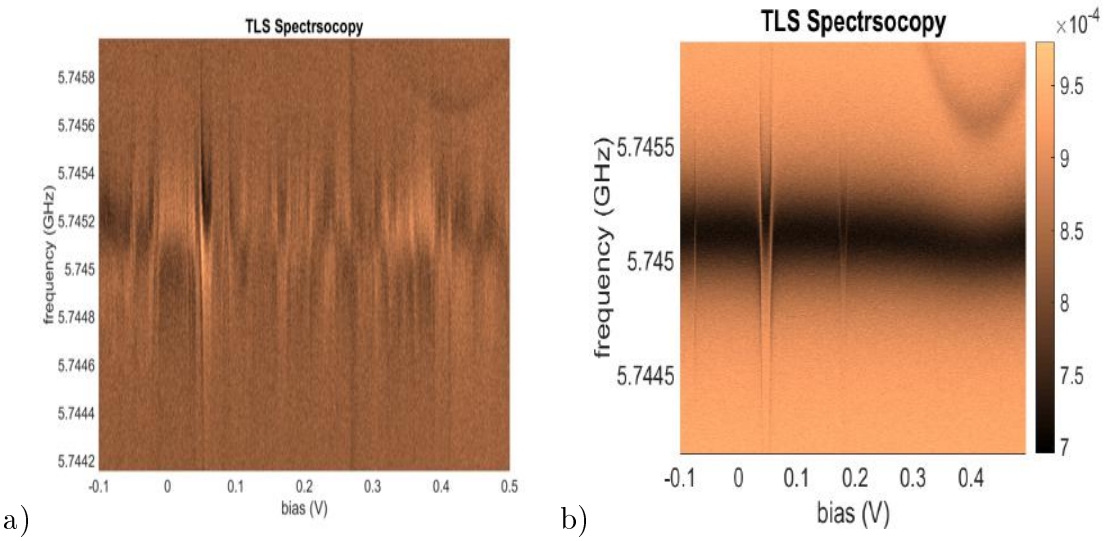

a) b)

Figure 48: Shows the frequency and the transmission, $|S_{21}|$,as a function of bias (separate cooldown from Figure 47). a) I have subtracted the background to highlight the crossing features as well. One can see several crossings and a hyperbola showing in the upper right.b) Shows a fit to the eigenmode equations of the experimental data highlighting some of the predominant TLS features. These results show the energy eigenstates of surface TLS defects coupled to the resonator.

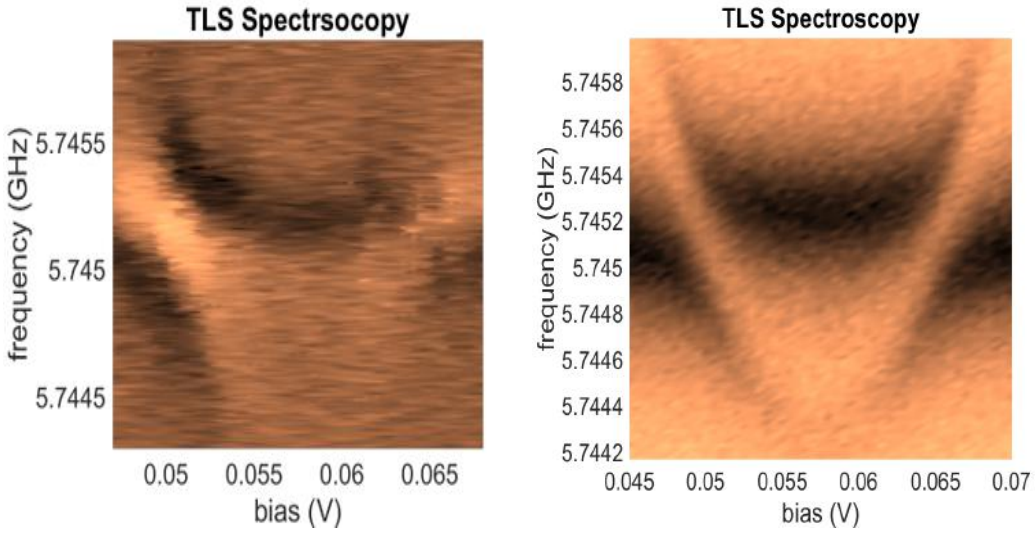

Figure 49: Comparison of the a) experimental data b) a fit of a single strongly coupled TLS.

235kHz measured from the transmission. Using a spectrum analyzer I measured $V_{noise} = .3mV$at the GHz frequencies that we operate in. Thus the measured noise is on the order of magnitude of the threshold which mean some TLS features may be difficult to observe. In the below table I summarized the extracted parameters from 20 of the 52 TLS measured. I found an average $p_z(20nm)$of 1.8 Debye, an average tunneling energy,$\Delta_0 = 23.79\mu eV$ and an average $\Delta(0) = 1.2\mu eV$.

As shown in Figure 47, I can measure the coupling, $g/2\pi$ of the TLS-resonator system directly from the eigenmodes. By analyzing over 50 TLS from over ten cooldowns I can summarize the measured coupling data with a histogram, Figure 50. The data suggest there are two peaks and was fit to a double Gaussian with averages $\mu_{1,}\mu_2$ and standard deviations, $\sigma_1\sigma_2$.From

TLS number	Cooldown Date	p_z (20nm)	$g/2\pi$ kHz	Asymmetry Energy, $\Delta(\mu eV)$	Tunneling Energy, $\Delta_0(\mu eV)$
$TLS1$	8/02	3.1	135	0.120344	23.78829
$TLS2$	7/19	2.7	275	2.959164	23.80336
$TLS3$	7/19	2.1	98	0.953443	23.78829
$TLS4$	8/02	1.1	137	1.402146	23.78549
$TLS5$	8/06	1.3	159	1.147733	23.7815
$TLS6$	7/22	.80	186	1.652219	23.77558
$TLS7$	7/16	1.6	151	0.972549	23.79158
$TLS8$	7/16	1.2	139	0.095344	23.78204
$TLS9$	7/22	1.9	177	1.355945	23.77678
$TLS10$	7/25	2.5	65	0.220219	23.78829
$TLS11$	7/25	1.0	61	2.056149	23.77856
$TLS12$	7/25	1.2	147	2.911481	23.77006
$TLS13$	7/25	.95	56	1.652219	23.85478
$TLS14$	7/25	2.1	51	0.82796	23.78539
$TLS15$	7/25	1.5	64	2.889662	23.78256
$TLS16$	8/1	.95	73	0.157847	23.80702
$TLS17$	8/1	1.9	48	0.363971	23.78846
$TLS18$	8/1	3.3	82	0.220283	23.79265
$TLS19$	8/1	2.2	90	1.015978	23.79077
$TLS20$	8/1	2.6	110	1.080993	23.79171

Table 1: Tables shows extracted parameters such as dipole moment assuming 20 nm, $p_z(20nm)$,the coupling $g/2\pi$, the tunneling energy, Δ_0 and the asymmetry energy at zero bias, $\Delta(0)$ for 20 surface TLS during different cooldowns.

the fit I found $\mu_1 = 80kHz$ with a standard deviation of, $\sigma_1 = 18kHz$. The second Gaussian has an average of $\mu_2 = 140kHz$ and a standard deviation of $\sigma_2 = 25kHz$. The two peaks in the data is suggestive that there exists possibly

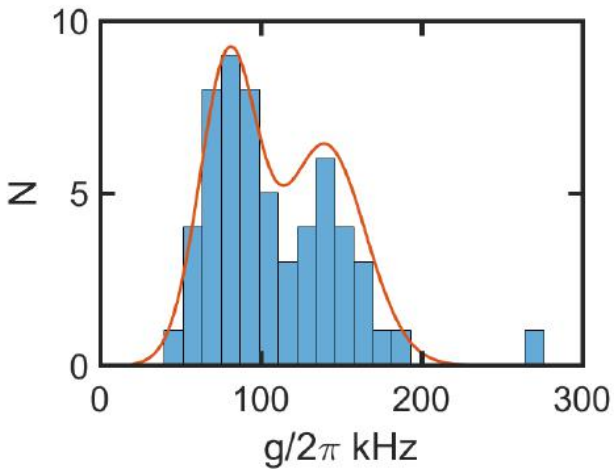

Figure 50: Histogram of the coupling, $g/2\pi$ of 52 TLS defects. The histogram fits to a double Gaussian with the first Gaussian having an average, $\mu_1 = 80kHz$ and a standard deviation of, $\sigma_1 = 18kHz$. The second guassian has an average of $\mu_2 = 140kHz$ and a standard deviation of $\sigma_2 = 25kHz$.

two dipole moments from an AlOx layer and a crud layer such as some organic, or photoresist that was stuck in the gaps. Additionally the two peaks could be due TLS at different interfaces. One peak could from the TLS at the MS interface and the other at the SA or sidewall. In figure 29 one can see the different of the MS & SA interface is about a factor of 2 at 17.5 nm distance from the corner. That factor of 2 could be the reasoning behind the factor of 2 in the average coupling data. Additionally there is a factor in the field between the sidwall and MS near 5nm.

5.5.3 Dipole Moment Characterization

The dipole moment of the TLS is an important parameter that directly affects the relaxation time T_1as well as the coupling of the TLS to other systems. While I can not determine the exact p_z from the data due to to the inhomogeneity of the electric field. I can determine $p_{z,min}$ and a $p_{z,max}$. Additionally if I assume the TLS location from the highest field corner I can find a p_z at a certain distance which is shown in Table I. To find $p_{z,min}$ I can use the experimental smallest coupling value measured and the highest rms electric field magnitude expected. For the max dipole moment one can use the opposite. For these I obtain

$$p_{z,min} = \frac{\epsilon}{2\Delta_0}\hbar g_{min} E_{RMS,max}$$

and

$$p_{z,max} = \frac{\epsilon}{2\Delta_0}\hbar g_{max} E_{RMS,min}$$

From the data the smallest ϵ/Δ_0 ratio is ~.99, $g_{min} = 48$kHz, and $E_{RMS,max}$ $p_{z,max} = 4.5$D and $p_{z,min} = .7$D.

Fitting equation (3.60) I can extract a $T_1$for the individual strongly coupled TLS. Some TLS data was too noisy or did not have a good fit and thus for fitting equation 3.60 I extracted $T_1$for 22 of the 52 TLS measured. I found an average $T_1 = 650ns$. The fits appear as in Figure 51 where the y axis the is magnitude of $|S_{21}|$ and the x axis is the frequency.

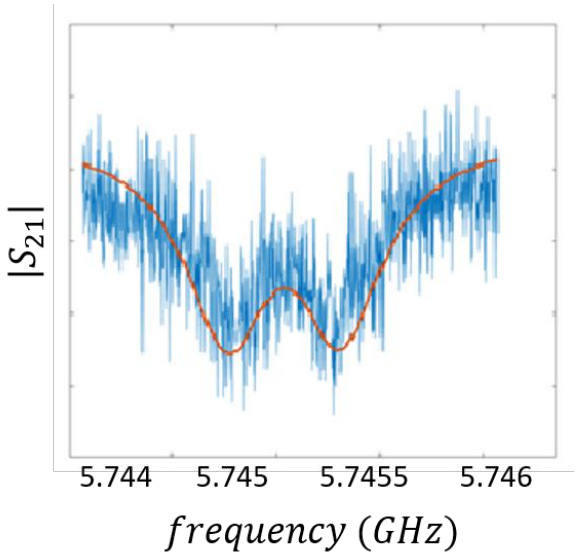

Figure 51: Shows the fit of a single strongly coupled TLS-Resonator system using equation (3.60). This TLS in particular was one of the highest T_1 times of 2.4 μS and one of the strongest couplings, $g/2\pi = 275$kHz.

5.5.4 Comparing Experimental Results to Simulations

Using the standard tunneling model one can simulate the transmission of a resonator coupled to a transmission line that has a bath of weakly coupled surface TLS and a few strongly coupled TLS. To do this I use the distribution of TLS mentioned earlier,

$$d^2n = P_0 d\Delta \frac{d\Delta_0}{\Delta_0}, \tag{5.24}$$

making several reasonable assumptions. I will discuss in this section simulations done post measurement so I could use actual values obtained experimentally in my Monte Carlo method fit.

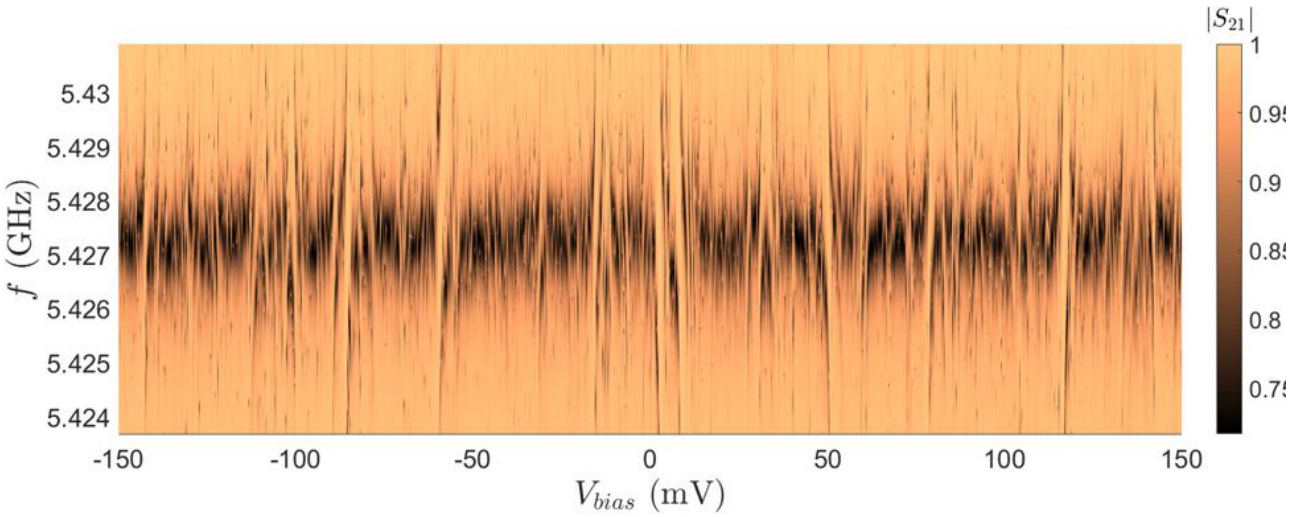

Figure 52: Simulation of surface TLS from COMSOL for the inhomogeneous electric field at MS interface. Assuming a Qi=Qe=30k and a $T_{1,tls} = 400nS$.

From experimental measurements I expect a standard calculated dipole moment to be between .7 D and 4.5 D, and I assume the dipole moment of 2 Debye for the fit and simulation. I used equation (5.15) to distribute the TLS energies, Δ, Δ_0. I calculated the energy density $P_0$from the experimental loss fitting results where I found the loss tangent of aluminum oxide to $\tan_{\delta AlOx} = 1.7 \times 10^{-3}$this lend to $P_0 = 3.8 \times 10^{45} J^{-1} m^{-3}$ from equation 2.26 where I assumed a $p_z = 2D$ from the average dipole moment in the data at 20 nm from the highest field corner. The calculated the TLS volume is $V_{tls} = 12\mu m^3$.

Due to the lower electric field strengths present in the IDC fewer TLS have strong enough coupling to be seen compared to previous trilayer designs. The benefit of this is that the TLS anti crossings with the resonator can be seen. Additionally in my simulation I can find the position of these strongly coupled TLS that are in the bandwidth of the resonator.

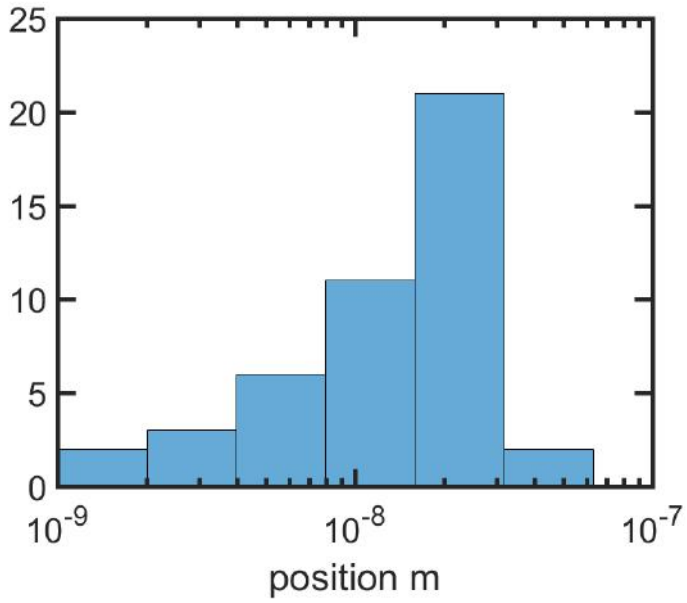

Figure 53: Histogram shows the position relative to the highest field corner in the MS interface of the TLS in the strong coupling regime. The simulation shows that 80% of the strongly coupled TLS reside between 5 nm and 30 nm from the highest field corner.

These simulation show that 80% of the TLS in the strong coupling regime are between 5 and 30 nm of the highest field corner. One potential way to apply this is to create supporting structures underneath the film from the corners of the film up to 30 nm away. This would suggest that most of the TLS at the MS interface would be in the strong coupling regime and thus could be biased out of the resonator or qubit bandwidth. Additionally it has been shown [84] that deep etching at the SA interface can reduce TLS contribution in that region allowing for the loss to be dominated by tuneable TLS.

5.6 Conclusions

Superconducting qubits will continue to thrive in the coming years ahead as more and more research helps to propel the technology. Understanding how to manipulate surface TLS is incredibly important to its success. Surface TLS are ubiquitous and cannot easily be removed through fabrication or design. Controlling TLS energies through biasing may lead to great improvement in coherence times. While others have showed bias tuned TLS in qubits through external bias[11, 82] which are mainly in the JJ barrier, I have shown an on chip bias technique in resonators that has helped elucidate the couplings between the surface TLS and resonator with an average $T_1 = 575ns$, an average coupling, $\bar{g}/2\pi = 103kHz$ and a standard deviation of 12 kHz. This is comparable to couplings found in previous measurements on qubits[82, 61] which found a range of couplings from 30-400kHz. I found that on average less than 2% of TLS will reside in the bandwidth of a resonator and from using exper-

imental data in simulation found that 80% of these TLS reside within 50nm of the highest field corner. Additionally my data on TLS couplings as a histogram fits a double Gaussian and suggests that either 1) two dipole moments exist corresponding to two types of TLS [93] or 2) there are two material interfaces where strong coupled TLS can exist. The two peaks in the data is suggestive that there exists possibly two dipole moments from an AlOx layer and a crud layer such as some organic, or photoresist that was stuck in the gaps. Additionally the two peaks could be due TLS at different interfaces. One peak could exist from the TLS at the MS interface and the other at the SA or sidewall. In figure 29 one can see the different of the MS & SA interface is about a factor of 2 in electric field strength at 17.5 nm distance from the corner. That factor of 2 could be the reasoning behind the factor of 2 difference in the average coupling data. Additionally there is a factor of 2 in the field between the sidwall and MS near 5nm.

Characterizing and observing surface TLS is crucial to the continued improvement in superconducting quantum devices where TLS remain the most prevalent recognized loss mechanism in high-Q resonators and coherent qubits.

6 TiN Films Sputtered on a Substrate Prepared with Oxygen Plasma Functionalization

TiN resonators are used in quantum computing, where high quality factors give long coherence times [92][91]. In addition thin TiN films with high kinetic inductance from high resistivity films are useful for MKIDs[51]. Despite the success of TiN, its loss mechanism in superconducting co-planar waveguides are not well understood. There has been a lot of research studying how growth conditions such as chamber pressure and the gas flow rate, etc. effect the TiN film[3, 7]. Changes in growth conditions effect the resistivity, crystal orientations, stress and loss of the film. $Q_i s$ over a million have been achieved in both the [100] and [111] growths directions with vastly different growth conditions [7, 3][109][110]. High concentrations of oxygen are also known to infiltrate the films[3]. In spite of the high percent of oxygen, high Q_i's can still be achieved [3]. In this study we show how TiN is even more sensitive than previously seen. Simply by changing the film thickness I observe multiple sharp changes in the TiN film. The most notable shift is an order of magnitude increase in loss, as well as a change in film growth direction, grain size, and film stress. A complex impedance study has been performed including the temperature dependence of the complex impedance, which deviates from Mattis Bardeen theory at low temperatures. The data suggests there is imhomogenity in the superconducting order associated with varying sized grains in the films, verified by STM. The increased loss is due to an increase in non-equilibrium quasiparticles in the

thinner film being trapped where the current is concentrated. The increased non-equilibrium quasiparticle concentration is found in the data with using a two fluid model where an increased kinetic inductance factor is found, and by extracting shorter quasiparticle lifetimes using a modified Mattis-Bardeen model. A two gap quasiparticle trapping model is proposed to apply where quasiparticles in larger gapped grains become trapped in lower gapped grains after interacting with phonons. These results show an interesting loss regime in TiN and helps elucidate how parameters such as thickness and substrate preparation greatly impact not only the growth of the film but the underlying superconductivity & loss in the film.

In this section I am going to discuss the loss associated with TiN films grown with and without oxygen prepared substrates at various film thicknesses. In particular we were interested in modifying the MS interface and observing the changes in loss of the resonator. The metal-substrate and substrate-air are understood to have the highest participation ratios and to contribute the most loss[5]. Thus our experiment was meant to modify this region in the fabrication process and see how the loss changes. While we tried many different plasma functionalizations with collaborators[63], I am going to focus on the results from the oxygen plasma treatment. This treatment gave the most consistent and intriguing results.

6.1 Fabrication

A high resistivity silicon substrate with a resistivity of 20 kΩ-cm, was prepared in two different ways to study the effect of the loss due the purposeful introduction of oxygen to the substrate. The first group of prepared wafers are called the base samples. These Si wafers were prepared by etching in 49% hydrofluoric acid (HF) for 30 seconds to remove the native oxide. In the 2nd type, the Si wafers were also HF dipped but were then placed in an oxygen ICP at 50V to generate an oxide layer before TiN was deposited as shown in a TEM image in Figure 1c(c). Both types of TiN films were sputter deposited at 500 C with a surface direct current (DC) self bias of -250 V. The pressure was held constant at 5 mTorr with argon (Ar) and nitrogen (N2) flow rates of 15 sccm and 10 sccm, respectively. Once cooled to below 100° C, a 50 nm layer of aluminum (Al) was deposited in-situ as a capping layer over the TiN feedline for impedance matching. A chlorine-based BCl3:Cl2 etch at 5:1 was used to etch the TiN. These resonators were fabricated with the help of Dr. Peng Xu and Dr. Yaniv Rosen.

6.2 Quality Factor Measurements

In this section I am going to talk about the results from measuring the TiN λ/4 resonators which are shown in Figure 8. The resonator has a center conductor width, w, equal to 3 um and a spacing from the center conductor to the ground plane of $12\mu m$.

The fabrication process for these devices is similar to that shown in Figure

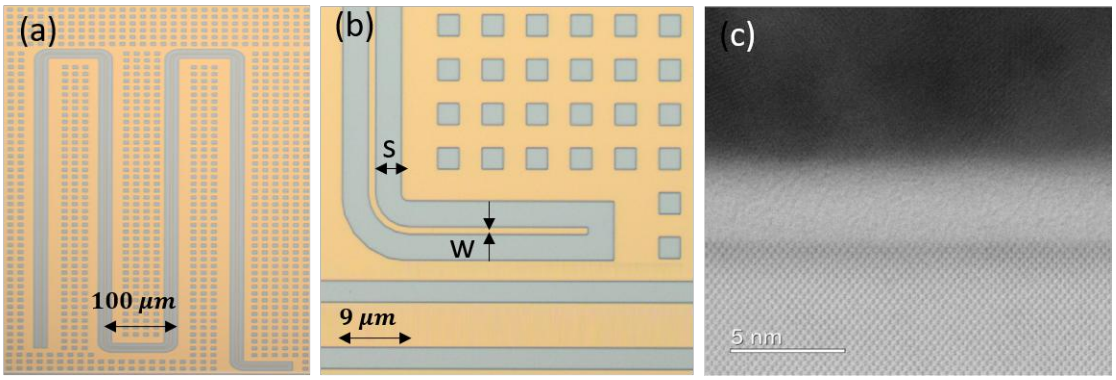

Figure 54: (a)Shows an optical image of the λ/4 co-planar resonator measured (b) shows the coupling of the resonator to a transmission line for readout. The width, w, of the resonator is 12μm while the gap,s, is 3μm. (c) shows a TEM image of a 4 nm amorphous oxide light region between the TiN film (top-dark) and the silicon substrate (bottom-light).

35. We have a single metal layer. In this case we sputter TiN instead of aluminum. However before TiN is sputtered we expose the silicon substrate to an oxygen plasma in an Inductively Coupled Plasma tool (ICP). This effectively creates a 3-4 nm oxide on our substrate before we deposit the TiN. We also have a control group of resonators which I will call base resonators which are not exposed to any oxygen plasma. Of course in these base wafers we do expect a small amount of oxide to grow as we transport the wafers to the sputtering tool within minutes but it may not be consistent, unlike the oxide grown in the ICP (or if we had left it in ambient air for an hour). After the films are grown they are then diced into chips which are placed into a sample box and then mounted into the base stage of a Leiden dilution refrigerator with a base temperature of 10 mK. These packaging steps are further outlined in section 4.1.3. The transmission, S_{21}, of the device is then measured. The results for

the base samples without any plasma functionalization are shown in Figure 11.

The internal quality factor of the films without any plasma functionalization ranged from 110k to 300k at single-photon storage with an average of 155k. The blue data represents TiN films grow up to 50 nm thick while the red represents films grown at 25 nm. It is customary to look at the quality factor at single photon levels since a qubit is typically operated at these low powers. These results establish our baseline. We do not see a significant difference in our base films with thickness. Figure 56 shows the results when the samples are exposed to an oxygen plasma before deposition. It is very evident in this data that there is significant difference in the loss between the two thicknesses. The 25 nm thick films have an order of magnitude lower internal quality factor with an average of 19k at low power. The 50 nm thick films however have an average internal quality factor similar to the base group with an average Qi around 200k.

This result was unexpected. It had been shown in other groups,[3, 7] ,that an increase in oxygen concentration actually decreased the loss seen in the resonator. These films went from $10^4 - 10^6$ when the chamber pressure changed from 2mTorr to 7mTorr which had the effect decreasing the compressive strain from 3800 MPa to 150 MPa and the oxygen content increased from .1% to 8%. The origin of the loss however was not discussed. It has also been seen by NIST Boulder that a 2nm SiN_x layer between films actually improved the internal quality factor while thicker layers of SiN_x reduced the Q_i [7].

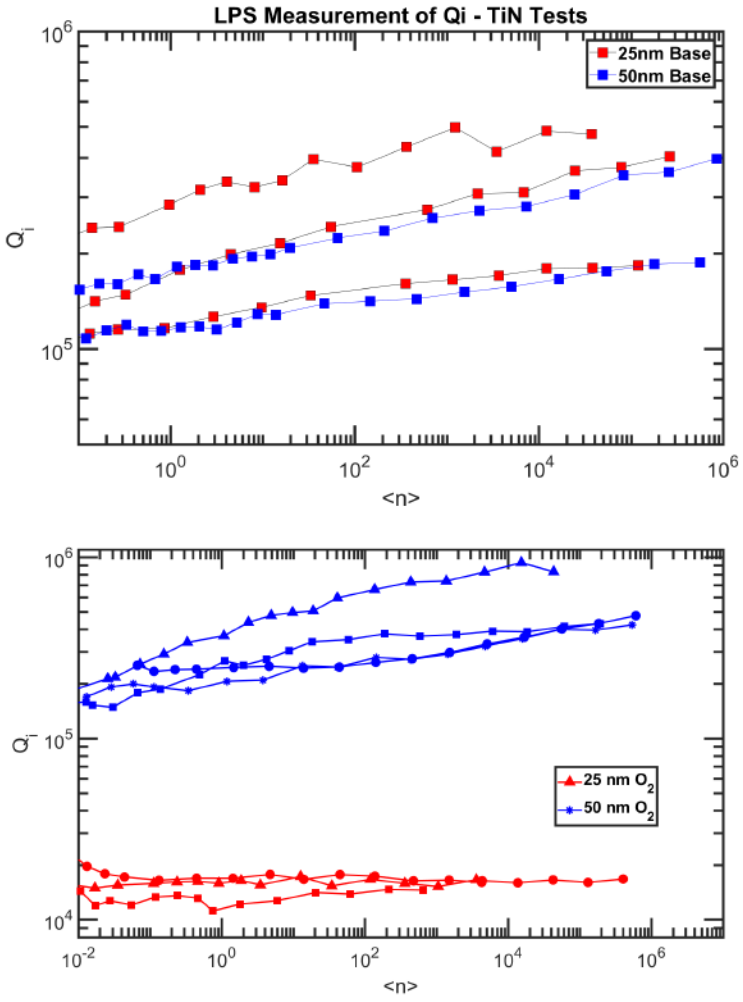

Figure 55: a) This graphs shows the internal quality factors of our base films which have no plasma functionalization b) This shows the order of magnitude decrease in quality factor for films pretreated with oxygen plasma and are 25 nm rather than 50 nm.

Our results show that oxygen prepared substrates induce a loss transition at thicknesses of 25nm and lower. This thickness dependent transition has not been seen before to our knowledge, but it interesting to the community because other unusual phenomena is reported in TiN including superconductor-insulator-transitions[85]and inhomogeneous superconductivity [13] [16].

6.3 Film Stress Measurement and Thermal Stress Calculations

After the loss and growth data it became clear that the oxide layer has changed not only the crystal direction (XRD shown in later section) of the TiN but must have changed other characteristics too. Stress or strain happens in thin films that are deposited on a substrate. Depending on a variety of parameters such as temperature, pressure, etc, the substrate may pull or bend the thin film depending on if it is under tensile or compressive stress. Understanding the stresses on a film can tell a great deal about the growth.

A Toho Technology FLX-2320-S stress measurement system was used to characterize the stress in the thin metal films. The tool determines the film stress by measuring the curvature change of a wafer between pre- and post deposition measurements. The curvature difference of these two measurements is used to calculate stress by from Stoney's equation [14], which relates the stress to the bi-axial modulus of the substrate, the thicknesses of the film and the substrate, and the radius of curvature of pre- and post-deposition wafers. Curvature, $\varkappa$, was measured by directing a laser at the wafer surface

at a known angle. The reflected beam was detected by a position-sensitive photodiode. The deflection was recorded while scanning the surface of the wafer. Stoney's formula for stress is

$$\sigma = (Eh_s^2\kappa)/(6h_f(1-v_s)) \tag{6.1}$$

Where κ is the curvature measured from the deflection, E is the Young's Modulus and v_s , Poisson's number. h_s is the height of the substrate and h_f is the height of the film

The stress measurements showed that there indeed appears to be a transition related to the thickness of the film. As the thickness is raised to 50 nm a large change toward tensile stress is observed as the stress changes in one step from a large compressive value of 4300 MPa to a smaller compressive value 3000 MPa. This large transition towards tensile stress is easily seen in Figure 56. Tensile stress is expected as the film grows as the grains become longer and is dependent on the grain boundaries. As the grains become more connected it becomes energetically favorable to reduce the grain boundaries as the grains become more closely packed [15]. There can indeed be a thickness at which this tensile stress is created. Our base film stress at 50 nm film thickness is consistently equal to approximately 3000 MPa. Thus the thinner oxide film likely has smaller grains with more grain boundaries allowing oxygen to more easily diffuse between the grains. On the other hand the base and the larger oxide films have less stress and have longer, more closely packed grains

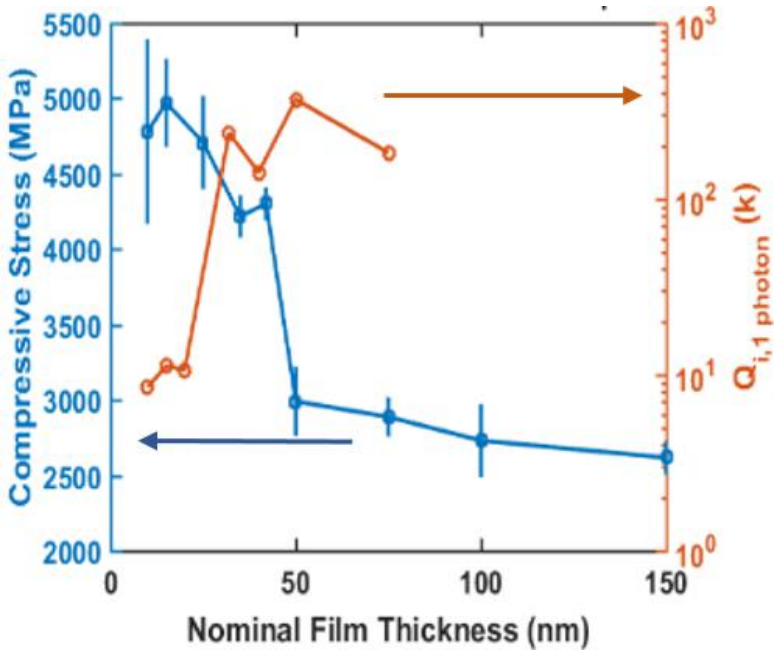

Figure 56: The transition in Qi seems to be related to a change in stress. Where near 50 nm the film transitions to a tensile stress while the Qi increases by an order of magnitude

and fewer grain boundaries. The grains were examined further with TEM and STM images.

6.4 Grains Images from TEM & STM

More data was gathered to verify the grain structure of the films. TEM stands for transmission electron microscopy, where the electrons are sent through the sample. Electrons get refracted by the material, based on scattering in real physical and k-space. While TEM looks at the electrons that have traveled through the sample, it has various imaging modes and detector types. Figure 64 shows the TEM images of the 25nm and 50nm film with oxygen prepared substrates. Over 20 grains were analyzed in each film.

From TEM it was concluded that the average grain size in the thin oxide film is 7.5 nm while the average grain size in the thicker film is 15.5 nm. It was also found that smaller grain tend to exist on the outsides of the film while the center has longer grains.

TiN has been studied in a model with homogeneous gaps [95] and inhomogeneous gaps [97],depending on the disorder in the film and the growth parameters. The homogeneity of the film has a large impact on the complex impedance of the film and the superconducting properties. Scanning tunneling microscopy STM was also performed at the lab here in LPS by Dr. Wan-Ting Liao on our films. She found that in the thinner oxide film there are inhomogenous superconducting gaps that average .42meV. The thicker film also was inhomogeneous and had an average gap of .6meV [57]. The correlation

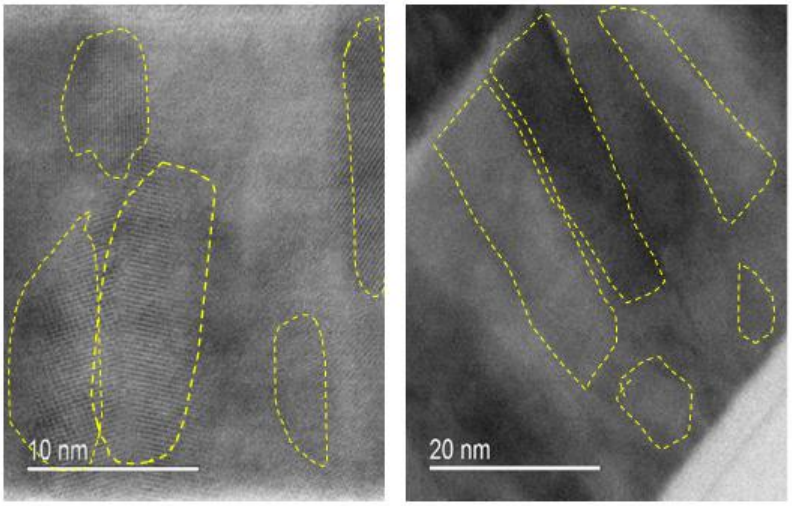

Figure 57: TEM images of the 25nm oxide film (left) and 50nm oxide film (right). The TEM shows how the grain in the thinner film are smaller. Additionally in the thicker film on the right the grains are taller and more column like. The average grain size measured in the thinner film is 7.5 nm while it is 15.5 nm in the thicker film.

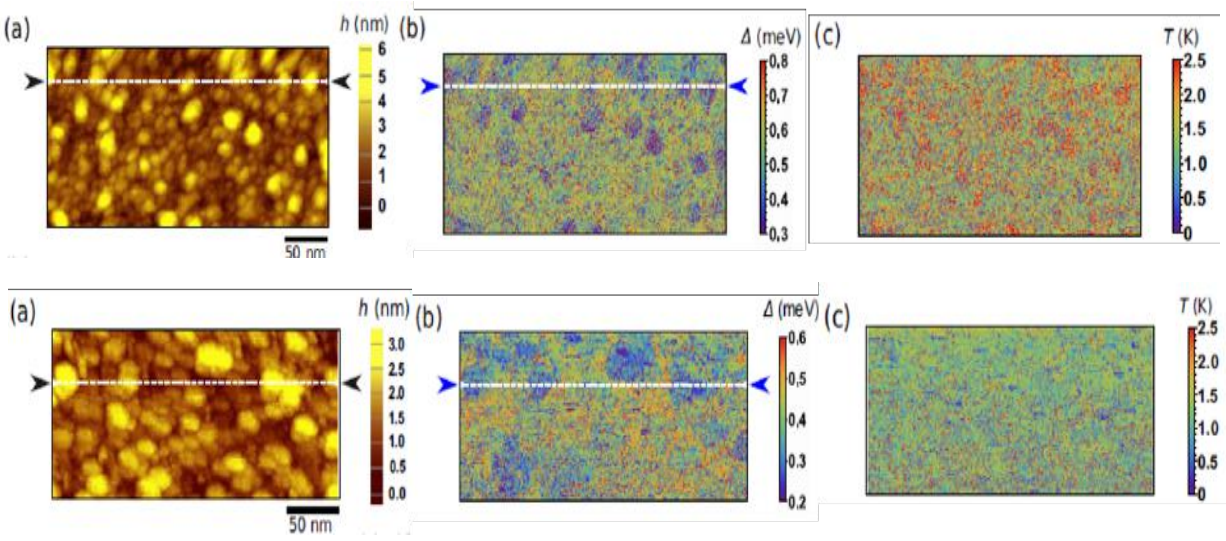

Figure 58: Comparing the temperature, height and gap of the 25 nm thin oxide and 50 nm oxide films. The average gap in the 25 nm film is .42 meV while it is .6 meV in the thicker film. In the thicker film it is notable that some grains have low gap and higher temperatures. This correlation indicates thermal isolation of those grains[57].

between the gaps, grains and temperature were also analyzed. The most striking correlation was in the thicker film where a correlation existed between the gaps and temperatures (Fig 65). The thicker film was showed to have two differences thermally isolated grains as well as larger gaps.

Isolated grains would tend to be more thermally disconnected, it would allow a higher non-equilibrium temperature T when electrical power is dissipated during spectroscopic measurements. Therefore the thicker film could trap quasiparticles in isolated grains better than the thinner film. In contrast, the 25-nm-thick film shows distinct smaller grains in the gap map and topography but relatively featureless variations in temperature. Inhomogeneous gaps and granular films can lead to increased quasiparticle concentrations[13] and in the next section I will examine thermal quasiparticles in the film.

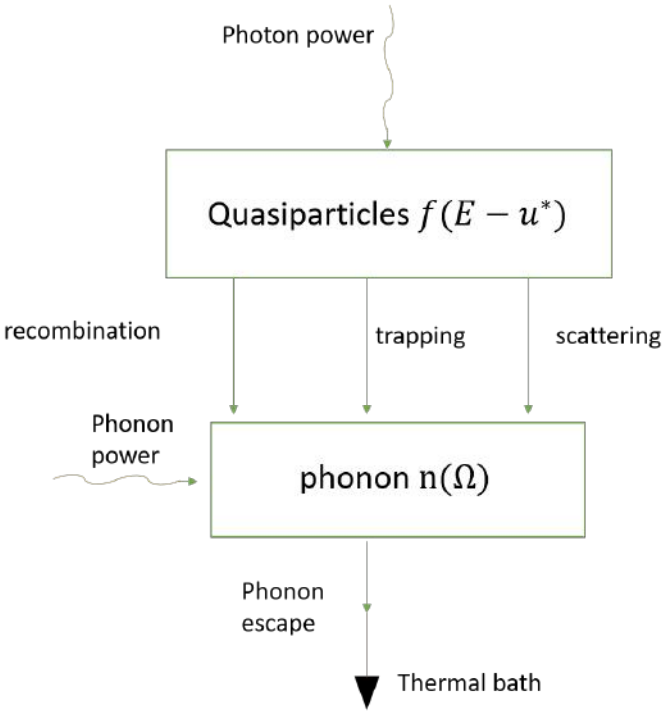

Figure 59: Power exchange model showing the mechanism through which a quasiparticle can be generated, scattered, trapped or recombined The latter processes use phonons to interact.

6.5 Transport Properties of Quasiparticles

Quasiparticles are formed when there is enough energy to break a Cooper pair. The quasiparticle lifetime is $\tau_{qp}^{-1} = \tau_R^{-1} + \tau_{SC}^{-1} + \tau_{trap}^{-1}$ where $\tau_R$is the recombination time, τ_{trap} is the trapping time and τ_{SC} is the scattering time. In general one can use a power flow model to understand how quasiparticles can be generated in Fig 59 below.

The thermal quasiparticle density is

$$n_{qp} = 2N_0\sqrt{2\pi kT\Delta}e^{-\frac{\Delta}{kT}} \tag{6.2}$$

where N_0 is the electron density of states, Δ is the gap energy, and k is the Boltzmann constant. The electron density of states has a number of different values in literature depending on the material and model that is considered. Often the electron density of states is calculated or assumed using the free electron model.

Quasiparticle diffusion

Quasiparticles obey a diffusion equation equation, where the flux of quasiparticles J_{qp} at one instance is

$$J_{qp} = -D\nabla N_{qp} \tag{6.3}$$

where D is the diffusion constant, $D = \frac{1}{3} < v_g l >$, v_g is the group velocity and l is the mean free path. The length a quasiparticle will diffuse until it recombines, l_R depends on the recombination time, τ_R, where $l_R = \sqrt{D\tau_R}$. At low temperatures the length increases as $l_R \sim e^{\Delta/2kT}$. [111]

6.5.1 Transport Properties of our thin TiN films

Some of the transport properties of our films were characterized with the help of our collaborators at LANL, Serena Eley and Leonardo Civale. They used a Hall bar setup to measure the temperature dependence of the resistivity and also measured the upper critical field to extract a coherence length.

The measurements of the temperature dependence of the resistivity, $\rho(T) = \frac{Wd}{L}\frac{V}{I}$, where d is the film thickness, were performed on patterned bridges of

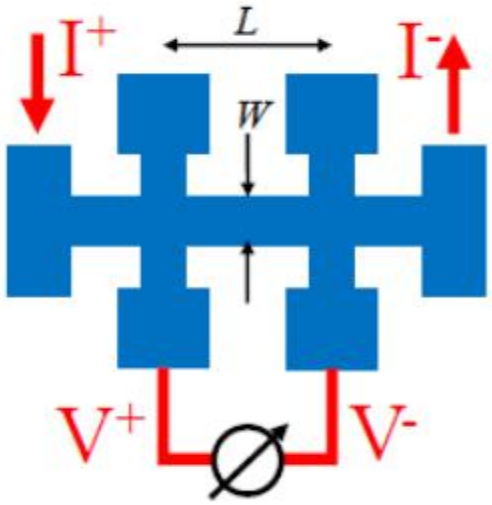

a)

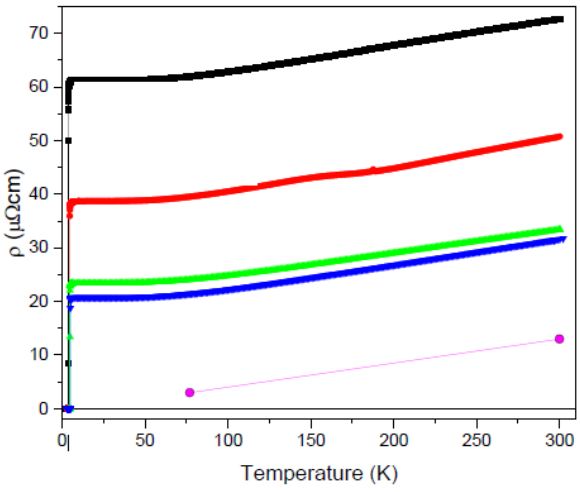

b)

Figure 60: a)Hall bar structure used to determine the resistance up to room temperature. b) Resistivity for different film thickness: black - 25nm oxide, red-25nm base, yellow- 50nm oxide, blue-80nm

width W = 200 m and length L = 1.7 mm using the standard four probe method, as sketched in Fig. 63. They measured temperature for 4 TiN films, as shown in Fig. 60. They used a 17 Hz AC current I = 10 A, which corresponds to current densities J $\backsimeq$ 250 A/cm^2 for the 19.7 nm and 21.5 nm films, $\backsimeq$ 140 A/cm^2 for the 36 nm film and $\backsimeq$ 60 A/cm^2 for the 80.5 nm film. For the 4 films T decreases, until it reaches the residual resistivity ρ_{res} and becomes independent of T below $\backsimeq$ 50K. In a simple model in which the sources of scattering are additive, $\rho(T) = \rho_{res} + \rho_{ph}(T)$, where the temperature independent component p_{res} comes from the elastic scattering with the material crystalline disorder and $\rho_{ph}(T)$ arises from the T-dependent scattering with phonons. ρ_{res} measures the disorder, and is consistent with the coherence length results obtained from the upper critical field (Hc2) measurements, the most disordered film is the thin (25nm) on oxide layer, and the least disordered is the d = 80.5 nm (see Table 2). The origin of resistivity is likely scattering at grain boundaries which may allow JJ coupling to the next grain.

The density of states can also be found from the measured resistivity,ρ of the film and the diffusion constant D, obtained from the critical magnetic field measurements where $D = \frac{4k}{\pi q}(dH_{c2}/dT)^{-1}_{T_c}$ and then $N_0 = 1/q^2\rho D$ where q is the elementary charge. Subsequently using these measured values gives $D = 5.562cm^2/s$ we then calculate the electron density of states, $N_0 = 1.83 \times 10^{10} eV^{-1}\mu m^{-3}$ or $1.148 \times 10^{41} J^{-1}cm^{-3}$.

It is also important to note the length scales of the mean free path compared to the coherence length. In the dirty limit the mean free path is much less than

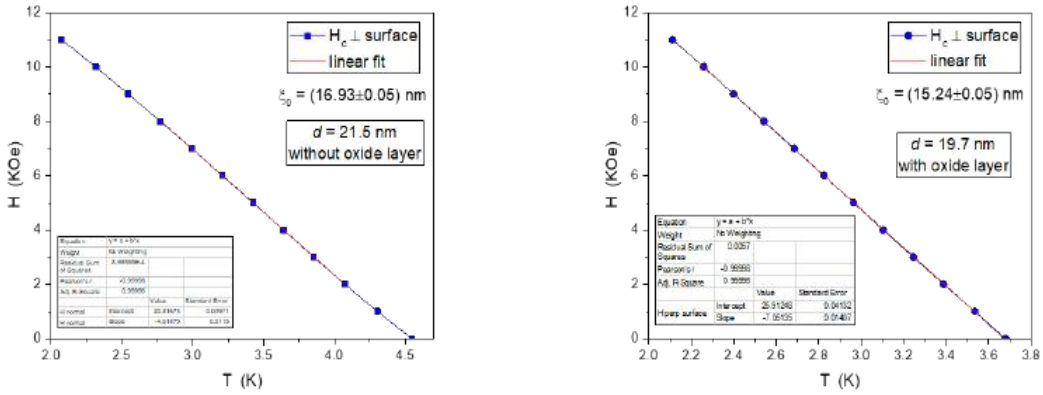

Figure 61: Critical Field measurements for TiN films. Performed by LANL. a) The thin film without oxide prepared substrate shows a coherence length of 17 nm. b) A 20 nm film with oxygen prepared substrate fits to a 15.2 nm coherence length. Smaller coherence length suggests more scattering which is likely in oxidized film due to larger disorder and smaller grain size.

the coherence length $l < \xi$, $(dH_{c2}/dT)^{-1}_{T_c} = -\frac{\Phi_0}{2\pi(.855)\zeta_{BCS}lT_c}$ where $\Phi_0 = h/2e$ and the BCS coherence length ξ_{BCS}. Using the experimental values for the coherence length obtained from Hall bar measurements $l = 1.2nm$ in the free electron model and $\xi = 15.2$ nm. We find that the oxide film at 25nm is in the dirty limit.

6.5.2 Thermal Quasiparticle Concentrations

From the power independent loss and the inhomogeneity of the films quasiparticle loss is suspected. The transport measurements established that our films are weakly disordered superconductors where the thin oxide film has a mean free path under 2 nm. Other TiN disordered films have been shown to have higher quasiparticle concentrations[13]. Thus in this section I will calculate the quasiparticle concentration we expect from thermal quasiparticles and

Films	Tc (K)	ρ $\mu\Omega cm$	$k_f l$	$Q_i(n=0)$	l nm	f_r GHz	α
25 nm base	4.55	51	24	150k	2.2	4.5	.6
25 nm Oxide film	3.65	73	14	10k	1.3	3.8	.75
50 nm Oxide	4.0	34	-	120k	-	4.8	.54
80 nm base	4.9	31	45	130k	3.6	5.5	.3

Table 2: Table shows the key parameters obtain through resistivity and critical field measurements of 4 different types of films measured by LANL. The thin oxide film showed the largest resistivity, highest disorder, lowest quality factor, lowest gap, lowest mean free path and highest kinetic inductance. The other films base and oxide alike have similar quality factors and kinetic inductance ratios that scale as expected with their thickness.

	T	25nm oxide	25 nm Base
D		$5.065cm^2/s$	$3.059cm^2/s$
N_0		$1.015 \times 10^{41} J^{-1}cm^{-3}$	$3.314 \times 10^{41} J^{-1}cm^{-3}$
n_{qp}	Tc/10	$2.78 \times 10^{11} cm^{-3}$	$8.92 \times 10^{11} cm^{-3}$
n_s	Tc/10	$4.50 \times 10^{20} cm^{-3}$	$7.17 \times 10^{20} cm^{-3}$
n_{qp}	Tc/5	$1.84 \times 10^{15} cm^{-3}$	$5.92 \times 10^{15} cm^{-3}$
n_s	Tc/5	$4.49 \times 10^{20} cm^{-3}$	$7.169 \times 10^{20} cm^{-3}$

Table 3: Comparing the thermal quasiparticle density to the superconducting carrier density for the base and oxide 25 nm TiN thin film

then transition to a model for non-equilibrium quasiparticles. Below I calculate the thermal quasiparticle density at different temperatures using equation (6.2). We are most interested in $T_c/10$ which is the temperature where the loss is dominated by a background of quasiparticles. At Tc/10 the thermal quasiparticle density is $n_{qp} = 2.78 \times 10^{11} cm^{-3}$. Below is a table for the base and thin film at 25 nm. In the next section I will show the loss due to these thermal quasiparticle concentrations.

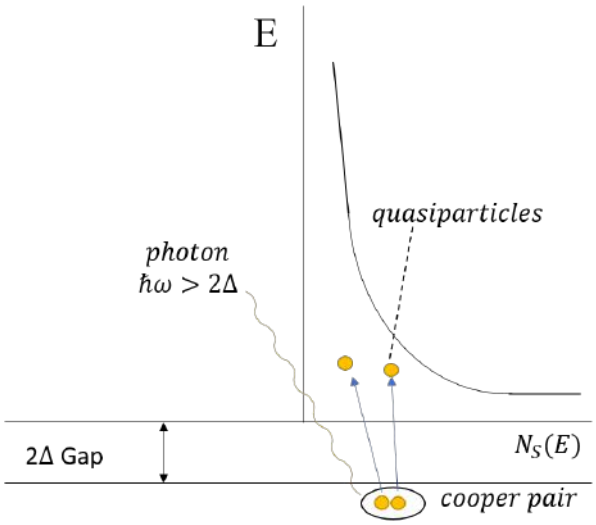

Figure 62: Diagram of the phenomena of a film absorbing an incoming photon. Photons with energy higher than twice the superconducting gap $\hbar\omega > 2\Delta$ will be absorbed by the superconductor and break Cooper pairs, creating quasiparticles. The transmission through the resonator will change. The frequency will decrease and the dip will be shallower due to the increase in KI and the increase in loss from the quasiparticles, respectively.

Calculating loss due to Thermal Quasiparticles

While superconducting carrier density is higher than quasiparticle density at mK temperature, conducting electrons in a two-fluid model is used to describe current paths in our circuits. Quasiparticle loss can be modeled as a resistive element due to the real conductance of the conducting electrons creating a surface resistance.

This model is often used to calculate the loss tangent of a CPW resonator [53] The loss from quasiparticles can be written as,

$$\frac{1}{Q_i} = \frac{\lambda}{s}\frac{g}{g_m}\frac{\gamma\sqrt{2}}{2\pi}(\frac{\Delta}{\hbar\omega})^{1/2}\frac{n_{qp}}{D(Ef)\Delta} \tag{6.4}$$

where g, g_m, γ are all geometric factors expressing the non-uniform current density on the kinetic and magnetic inductance. S is the line width. λ is the penetration depth. I can calculate the number of quasiparticles needed to get the loss in each film assuming a penetration depth of 730 nm[80]. For the thinner oxide film $n_{qp} = 2.2 \times 10^{13} cm^{-3}$ while the thicker film $n_{qp} = .74 \times 10^{13} cm^{-3}$.

The internal quality factor from quasiparticles at $T_c/10$ is closer to 800k and thus thermal quasiparticles do not start dominating the loss until closer to T=Tc/5. Additionally, looking at the thermal quasiparticle concentration calculated earlier ($10^{11} cm^{-3}$) it is clear that thermal quasiparticles alone cannot be responsible for the loss.

Calculating Cooper Pair Density from Kinetic Inductance

From the length of a quarter wave resonator, one can determine the expected frequency of that resonator assuming that there is no kinetic inductance (KI) $\frac{c}{\sqrt{\epsilon_r+1}} = \lambda f_{sim}$where the length of the resonator $l = \lambda/4$ is a quarter of the wavelength. To determine the kinetic inductance you can use the ratio of the simulated frequency without KI and the measured with KI:

$$(f_{sim}/f_{meas})^2 = \frac{L_{tot}}{L_g} = \frac{L_K + L_g}{L_g} \tag{6.5}$$

where $L_g$is the geometric inductance and can be calculated using elliptical integrals of the first kind [4]. The kinetic inductance ratio is defined as $\alpha = L_K/L_{tot}$ and therefore also

$$\alpha = 1 - (\frac{f_{meas}}{f_{sim}})^2 \tag{6.6}$$

and

$$L_K = \frac{L_g \alpha}{1-\alpha} \tag{6.7}$$

The London penetration depth characterizes the length at which the magnetic field penetrates a superconductor and is equal to $\lambda_L = \sqrt{\frac{2m_e}{\mu_0 n_s q^2}}$ where m_e is the mass of an electron, μ_0 is the permeability of free space, $n_s$is the superconducting carrier density and q is the elementary charge. The kinetic inductance is related to the penetration depth by, $L_K = \frac{\mu \lambda_L^2 l}{A}$.

Thus one can solve for the carrier density if the kinetic inductance is known.

$$n_s = \frac{m_e}{2L_K q^2}\frac{l}{A} \tag{6.8}$$

For our thin films of the interest the 25 nm base film measured frequency is 4.56 GHz and the 25 nm oxide film is 4.21 GHz. Using equation 6.6 we can calculate the kinetic inductance fraction of the thin and thick oxide films to be .75 and .6 using the simulated frequency of 7.5 GHz for a film without any kinetic inductance. Furthermore we can calculate the absolute geometric inductance of our quarter wave co-planar waveguide[36][4]

$$L_g = \frac{\mu_0}{4}\frac{K(k')}{K(k)} \tag{6.9}$$

where k is a/b where a is the center conductor width and b is the gap. $K(k)$ is the complete elliptic integral of the first kind

$$K(k) = \int_0^1 \frac{1}{\sqrt{(1-x^2)(1-k^2x^2)}}dx \tag{6.10}$$

$$K(k') = \int_1^{1/k} \frac{1}{\sqrt{(x^2-1)(1-k^2x^2)}}dx \tag{6.11}$$

The geometric inductance is 3.12 nH. From this we can calculate the kinetic inductance in each film and then the superconductivity carrier concentration. For the 20 nm thin film with O_2 pretreated substrate $n_s = 4.49 \times 10^{20} cm^{-3}$ and for the 20 nm thin film base $n_s = 9.02 \times 10^{20} cm^{-3}$. As expected there are fewer carriers in the higher inductance film.

These values are within a factor of 2 of a recent paper to calculate carrier concentration, [60].

6.6 Mattis Bardeen Theory

From the power dependence of the loss data it is clear that the loss is power independent in the thinner film. This suggests quasiparticle or radiation loss. We do no expect the latter due to the geometry of $3/12\mu m$ in LW/LS [94]. From the transport measurements we see that there is a decreased coherence length and decrease mean free path in the thinner film due to an increase in

the disorder. This can increase the quasiparticle - quasiparticles interactions and thus I looked into a model which includes quasiparticle scattering.

In a paper by Argonne a modified Mattis Bardeen theory is proposed. In the original MB theory an inelastic scattering parameter, s, can be set to 0. However it has been shown [16] that by setting s to a finite value one can phonomenologically account for the loss of disordered-superconducting resonators at low temperatures. Essentially a background loss now exists at low temperatures which can be attributed to non-equilibrium quasiparticles. By setting a scattering energy $\gamma = \hbar s$ and using s and Δ as free parameters I made a Monte Carlo fitting code in Matlab to fit the temperature dependence data from the 25 nm thin oxide and 25 nm base films.

Figure 64 shows the ratio of the conductivities as a function of temperature for the two films fitted to a modified Mattis Bardeen equation including inelastic scattering. The red is the thin oxidized film and the blue is the thicker film. The theory fits the data and suggests there is increased scattering in the thinner film. With the addition of the scattering parameter the density of states of the quasiparticles is broadened. This broadening is consistent with the experimental evidence that there is an excess non-equilibrium quasiparticle in the thinner oxide film. As expected the 25 nm oxide films requires a higher scattering energy in order to fit the data at low temperatures. From the fit we were able to extract a quasiparticle scattering time of 1.0 ns of the oxide film and 162 ns for the base film. Qualitatively this suggests that there is more scattering, and higher concentration of non-equilibrium particles, in the 25

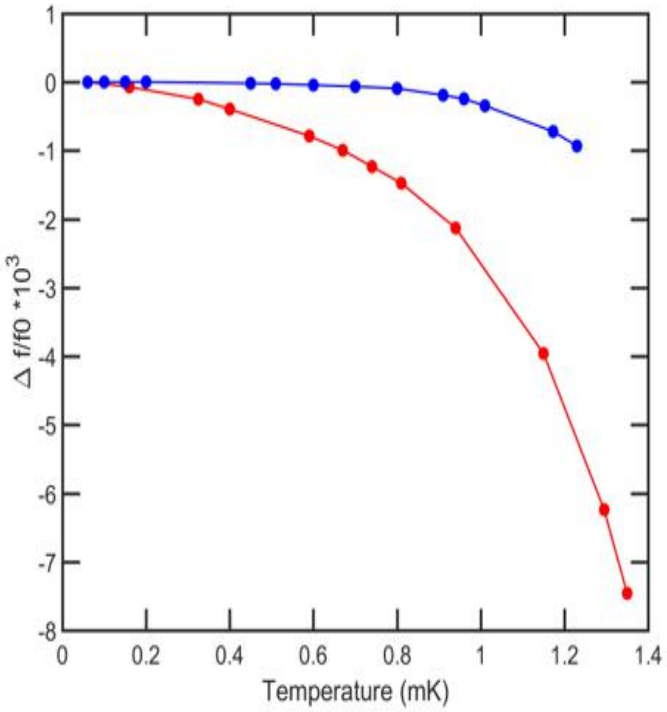

Figure 63: The frequency shift for the thin oxide (red) and the 50nm film (blue)

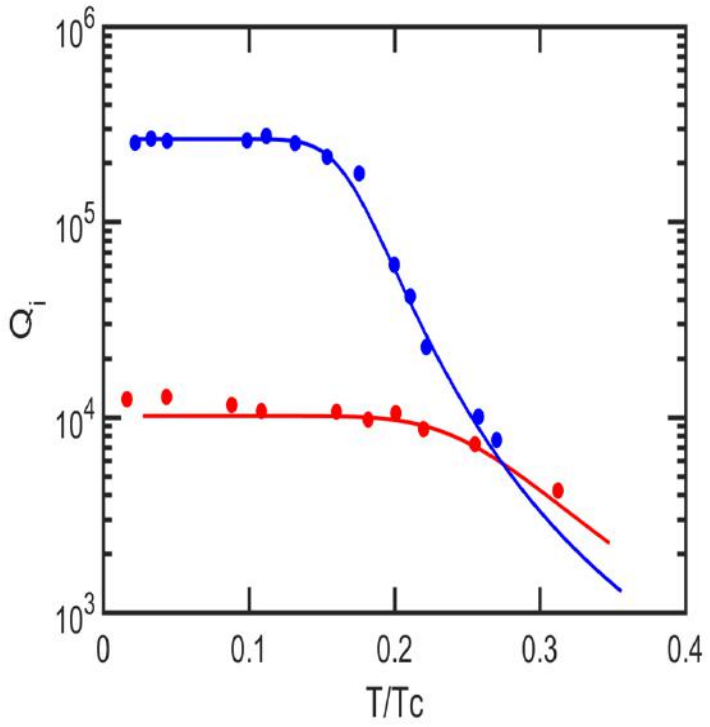

Figure 64: Plot of Q_i vs normalized temperature using a modified Mattis-Bardeen theory with inelastic quasiparticle scattering. The 25 nm thick oxide film (red) shows an order of magnitude more loss than the 50nm oxide film (blue) at low temperatures. At higher temperatures the thermal quasiparticles dominate and the loss is similar.

nm oxide film. While the microscopic origin of this scattering is unclear, the theory of an increased quasiparticle density of states fits the data well showing a large quasiparticle concentration in the thinner film.

We then used a two fluid model approach to extract a total quasiparticle lifetime. Using the two fluid model the total conductivity is $\sigma = \sigma_1 + i\sigma_2$. Q in a thin film is related to the surface impedance $Z_S = R_s + i\omega L_S$where $Q = \omega L_{Tot}/R_{Tot} = \omega L_S/\alpha R_S$

At mK temperatures $\sigma_2 >> \sigma_1$and $L_S = 1/\omega\sigma_2 d$ and $R_S = \sigma_1/\sigma_2^2 d$. Additionally in Tinkham the complex conductivity is given by [88]

$$\sigma = \frac{n_{qp}e^2\tau}{m^*}\frac{1}{1-i\omega\tau} + i\frac{n_s e^2}{m^*\omega} \tag{6.12}$$

where in the limit that $\omega\tau << 1$ one gets

$$\frac{1}{Q} = \frac{\alpha\sigma_1}{\sigma_2} = \alpha\omega\tau_{qp}n_{qp}/n_s \tag{6.13}$$

Introducing the temperature dependence $\delta n_{qp}(T) = n_{qp}$ and $\delta n_{qp}(T)/\delta n_S(T) = -2$ we get

$$\frac{1}{Q}(T) = 8\pi\tau_{qp}\delta n_S(T)/n_S \tag{6.14}$$

We can then substitute for $\delta n_S/n_S$since we know the change in superconducting carrier concentration is related to the change in the surface impedance L_S

$$\frac{\delta n_S}{n_S} = \frac{\delta L_S}{L_S} = \frac{2}{\alpha}\frac{\delta f}{f} \tag{6.15}$$

Then finally we can relate the change in frequency to the loss of the resonator

$$\frac{1}{Q} = -8\pi\tau\delta f \tag{6.16}$$

Using this relationship between the loss and the change in frequency we

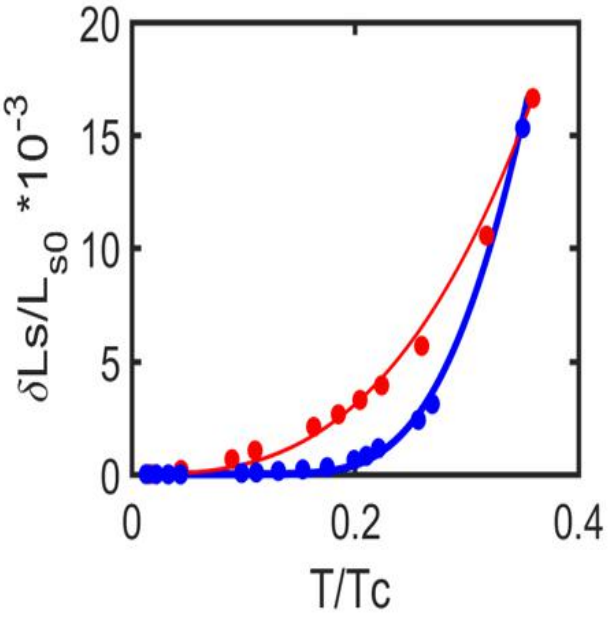

Figure 65: Shows the normalized change in surface inductance obtained from the frequency shift. The large shift in inductance at T/Tc $<$.2 in the thin oxide film (red) indicates breaking of Cooper pairs at unusually low temperatures. This can be due to a large background of non-equilibrium quasiparticles.

see that the lifetime of the quasiparticle is the slope. We can experimentally extract the lifetime of the quasiparticle by plotting the frequency shift with temperature and loss as in the Figure 66 below. It is clear that we see two different slopes further indicating the difference in the quasiparticle density between the two films. Additionally the oxide film sees large changes in the frequency compared to the base indicating a greater change in the quasiparticle density.

From the fit we determine that the quasiparticle lifetime in the oxide film is .32 ps while it is .9 ps in the base. These short lifetimes show that there is a temperature independent scattering rate that is the significant rate in the quasiparticle lifetimes for these films. Quasiparticle lifetimes are expected to be on the order of nanoseconds [98]. Both from the modified Mattis Bardeen theory and from the the two fluid model analysis it is clear that there is a significantly lower quasiparticle lifetime in the thin oxide film. While quantitatively it is hard to determine the significance of this, qualitatively the data shows a higher non-equilibrium quasiparticle concentration in the oxide film. Furthermore we see that there is likely a high quasiparticle concentration that exists at low temperatures it would seem necessary that the lifetime of the quasiparticle be temperature independent until $T = T_c/5$ when the thermal quasiparticles dominate the loss. It is known that quasiparticle trapping can occur in granular films and is thus an area I explored to explain the frequency shifts and loss.

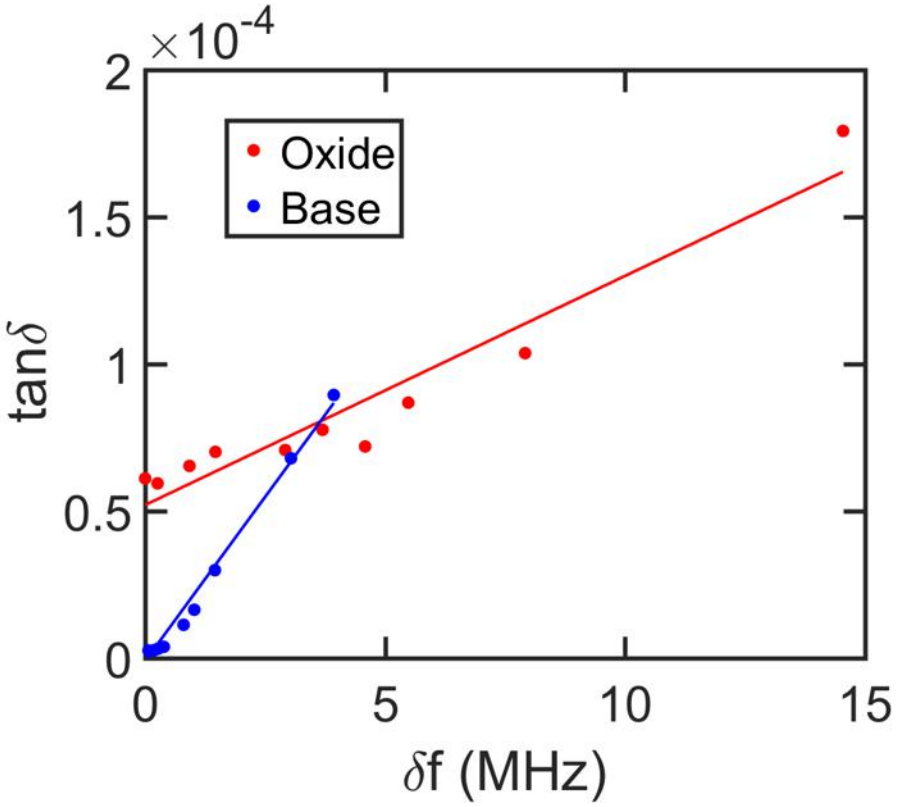

Figure 66: Plot of the loss versus the change in frequency using different sample temperatures. The 25 nm thick with oxide is red while the base film (similar in loss and frequency shift to 50nm oxide film) is blue. These films were fit to a two fluid model where quasiparticle lifetimes could be determined for each film.

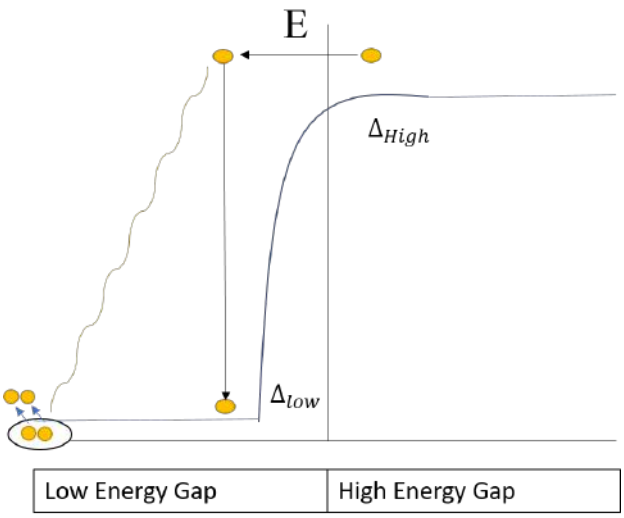

Figure 67: Quasiparticle energy model for trapping quasiparticles in low energy gap in thin oxidized TiN.

6.7 Two Gap Quasiparticles Trapping Model

Our TiN has shown thermally isolated grains at low gap with regions of significantly increased quasiparticle temperature. These areas in turn can trap quasiparticles. While in the thinner film STM revealed the grains were more thermally connected[57]. This suggests that there are more barriers between some grains in the thicker film restricting quasiparticle movement.

A two gap quasiparticle trapping model was developed to characterize the temperature dependence of other TiN films[99]. This model is adopted to fit the anomalous temperature dependence seen in our oxygen prepared films. For this, I propose that a lower gap grain exists in the center, less lossy, portion of the film with gap Δ_1 and a higher gap grain exists near the edges of the film with gap Δ_2. These two different regions may be consistent with TEM

which shows a bigger variation of grain sizes in the thicker films. The edges of the film are known to have a higher current density (in the limit of thickness, $d<<\lambda$) [102]and therefore quasiparticles can cause higher loss in this region. In the thicker film due to the thermal isolation and the presumably large potential barrier between grains, quasiparticles may become trapped in low gapped grains in the center of the film. As the temperature rises there is not enough energy for the quasiparticles to escape from the thermally isolated low gap grains. However in the thinner film no barrier exists. As the temperature rises more quasiparticles now have enough energy to leave the low gapped grains and enter the lossy outer grains. This in turn creates a larger loss in the thin film (with oxygen plasma) since the grains allowed better electrical and thermally conductivity.

Following [99, 112],I can calculate the rate change of the non-equilibrium quasiparticles densities, $n_{qp,1}$and $n_{qp,2}$ in the two regions with different superconducting gaps.

$$\frac{dn_{qp,1}}{dt} = G_{p1} + G_{g1} - G_{tr1}n_{qp,1} - G_r V_1 n_{qp,1}^2 - G_{1,2}An_{qp,1} + G_{2,1}An_{qp,1} \quad (6.17)$$

$$\frac{dn_{qp,2}}{dt} = G_{p2} + G_{g2} - G_{tr2}n_{qp,2} - G_r V_2 n_{qp,2}^2 - G_{1,2}An_{qp,2} + G_{2,1}An_{qp,2} \quad (6.18)$$

where $G_{pj}$is the rate at which the density of non-equilibrium quasiparticles

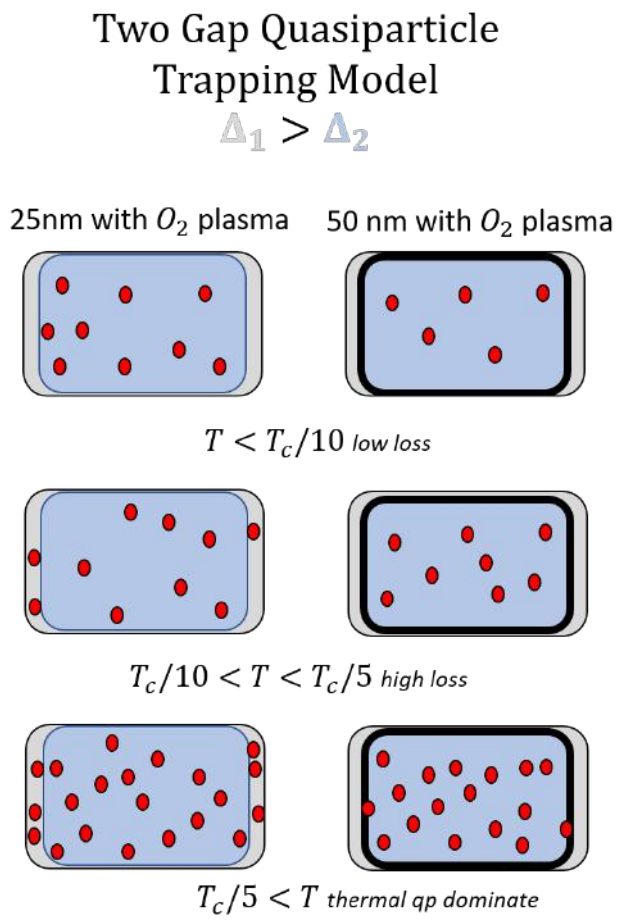

Figure 68: Diagram of the two gap quasiparticle trapping model. Shows how at low temperatures the quasiparticles in the both cases are trapped in the low gapped area in the center where the loss is small. In the thin oxide film as the temperature increases past T/Tc=.1 the quasiparticles have enough energy to escape the low gap center volume to the outer lossy region causing an increase in loss with temperature as more quasiparticle can now be trapped in the lossy outer region. However in the thicker film since the grains are thermally isolated the quasiparticles remain trapped in the center region[57, 99].[112]

are being generated in the region j, $G_{gj}$is the rate that they are being generated thermally, $G_{trj}$is the trapping rate and $G_r$is the temperature dependent rate at which the density of quasiparticles can recombine in a volume V_j, $G_{i,j}$is the rate at which the density of quasiparticles transfers from region i to region j per unit area A. In steady state,

$$\frac{dn_{qp,1}}{dt} = \frac{dn_{qp,2}}{dt} = 0 \tag{6.19}$$

Solving for $n_{qp,1}(T)$

$$n_{qp,1}(T) = \sqrt{\frac{n_{n,1}^2}{1 + \frac{V_2\Delta_2}{V_1\Delta_1} e^{2(\Delta_1 - \Delta_2)/kT}} + n_{th,1}^2} \tag{6.20}$$

which ultimately leads to an inverse quality factor

$$\frac{1}{Q_i} = \frac{2\alpha}{\pi N_0 \sqrt{2\pi k_B}} \left(\frac{\sinh(\xi_1) K_0(\xi_1)}{\sqrt{T_1^*}} \frac{1}{\sqrt{\Delta_1}} P_1 n_{qp,1} + \frac{\sinh(\xi_2) K_0(\xi_2)}{\sqrt{T_2^*}} \frac{1}{\sqrt{\Delta_2}} P_2 n_{qp,2} \right) \tag{6.21}$$

where α is the kinetic inductance fraction, $N_0 = 4.5 \times 10^{10} eV^{-1} \mu m^{-3}$ is the density of states[76], P_1 and P_2 are the fraction of inductive energy in the region. V_1 and V_2 are the volumes. $n_{th,1}$ and $n_{th,2}$ can be considered negligible at T/Tc=.1. We can use the effective temperature T^*used by Parker [75] as a way to account for an elevated effective temperature from non-equilibrium quasiparticles.

The majority of the inductive energy is stored in region 1 which has

a larger superconducting gap at the edges of the film. This means that $P_2 n_{qp,2} << P_1 n_{qp,1}$ so that the loss in region 2 can be neglected. Physically, this is qualitatively consistent with the edges of the TiN resonator (where the RF currents are concentrated [78][79]). In the thinner film as the temperature increases there is a 25% increase in loss as shown in the data from 0 to .8K. This increase in loss in the thin oxide film fits to the two gap trapping model where I fit using the Monte Carlo method to the gap and effective temperature Δ_1, T_1^*. I assume a ratio of the volumes to be $V_1/V_2 = 3.33$, and an initial quasiparticle density to be $n_{qp0} = 160 \mu m^{-3}$. From the fit I find $T_1^* = .1K$, and the $\Delta_1 = .51meV$, 20% different than the value .42meV measured. In the thicker film I set $\Delta_1 = \Delta_2$ due to the fact that there is thermal isolation between the grains and no transfer of quasiparticles. I found $\Delta_1 = \Delta_2 = .81meV$ and $T_1^* = .33K$. The gap value is about 17% different than the measured $.67meV$. From the fit I get good agreement with the data as shown in Figure 69. The good fit suggests the importance for thin TiN films to be careful of the non-equilibrium quasiparticle concentration at low temperatures. Aluminum traps at the shorted end of the CPW may be a good solution to improve the internal quality factor.

Additionally the grain size in the thinner oxide film is approaching the critical grain size where superconductivity is even possible in the grain. As suggested in the references[101] [100] if the average energy level spacing is smaller than the superconducting gap then the grain cannot be superconduct-ing.

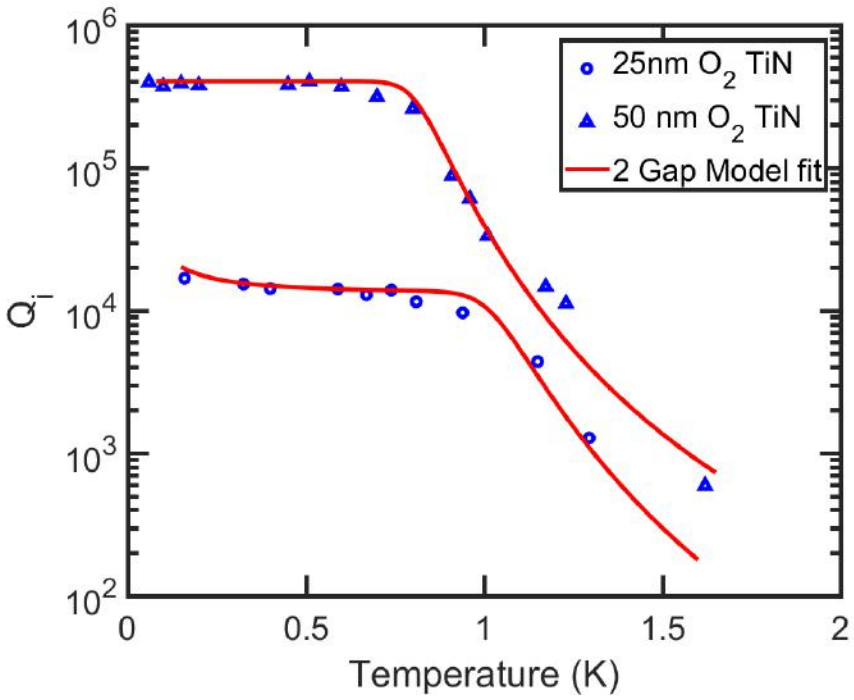

Figure 69: Fit of the 2 film types using the 2 gap quasiparticle trapping model. For the thin oxide film we found good qualitative agreement and quantitative agreement between 20% of fitted values that had been measured separately; namely the gaps for each film, $\Delta_{1,thin} = .57meV, \Delta_{1,thick} = .81meV$.

$$\delta\epsilon = [N(0)b^3]^{-1} < \Delta \tag{6.22}$$

From reference,[77] the density of states for TiN, $N(0)$, is $6{\times}10^{10}eV^{-1}\mu m^{-3}$ and therefore the critical grain size for superconductivity is 6.7 nm which is just 12% off of the 7.5 nm average for the thin oxide film. Thus there are likely grains in the thin film that are no longer superconducting and if these smaller grains are located at the edges then there will be a much higher loss contribution from non-equilibrium quasiparticles in the thinner oxide film.

Additional analysis of TiN thin films

6.8 Structural Changes in thin and thick films

To understand the loss data, information was gathered about the difference in structure between the thin 25nm oxide film and the other films in the study. In particular we are interested in the difference between the 25 nm and 50 nm O_2 prepared films since the quality changes by an order of magnitude even though no thickness dependence is generally expected. Also there is no significant expected difference between the 25 nm films with and without this oxygen preparation, since these films are at the same thickness though one has been prepared with oxygen and could exhibit a slightly higher TLS loss. Thus even though the thin oxide layer is clearly responsible for the increase in loss, only a small difference is expected from simulations (not shown). First it is important to understand the difference in the structure between these

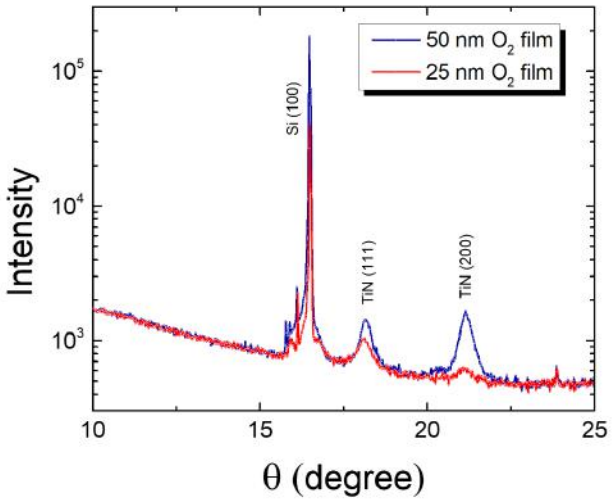

Figure 70: The growth direction is shown for TiN grown on oxide-prepared substrates at 25 and 50nm. The thin oxide film is mainly [111] in growth direction, where the thicker film (and others not shown) are mainly the [200] growth direction. This change was very interesting and can be used to better understand TiN growth.

films. First I will discuss the stress measurements. Below shows the X-Ray Diffraction data for two of the films studied. Surprisingly the crystal growth direction changes. In all the films the [200] growth direction is dominant, except in the 25 nm oxide film the [200] growth is suppressed and the [111] crystal growth direction is now dominant. The change in growth direction is likely related to the stresses involved during deposition, changing as the TiN grows in an attempt to relieve these stresses.

6.9 SIMs Analysis

To determine the elemental composition near the surfaces of the film we sent out our samples to have secondary ion mass spectroscopy (SIMS) performed.

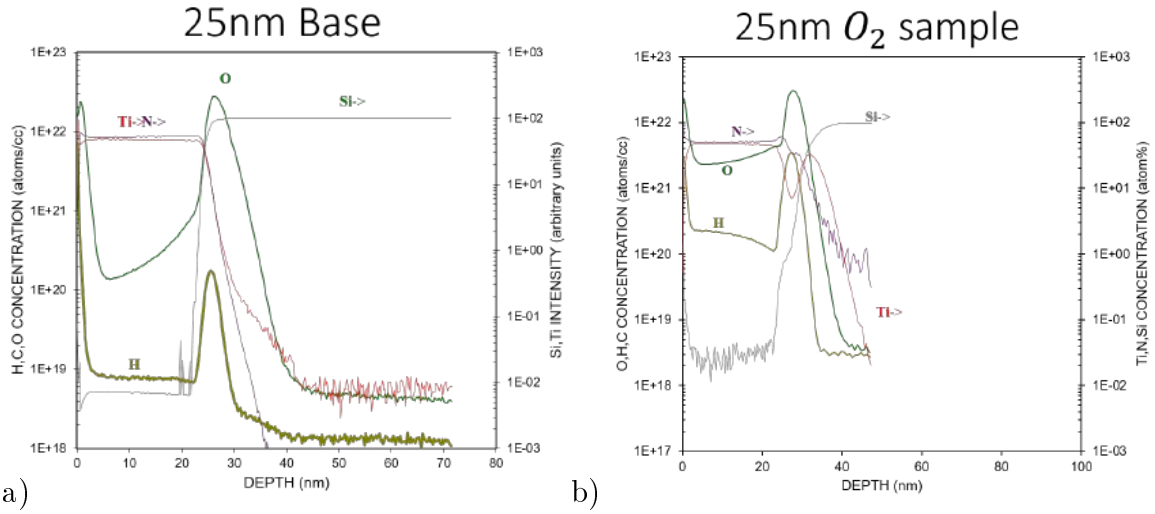

a) b)

Figure 71: a) SIMS results for a 25 nm base film. At the interface there is an oxygen peak while inside the film shows a relatively low oxygen concentration near $2 \times 10^{20} atoms/cc$. b) The oxygen prepared film also shows a large oxygen peak and much higher levels of oxygen and hydrogen in the film.

Data for four samples, 25 nm with oxygen preparation, 25nm base, 50nm with oxygen and 50 nm base, is shown below. The measurements finds the concentration in units of atoms/cc for Hydrogen, Oxygen, Titanium, Silicon and Nitrogen. The depth is the distance from the top of the film through the film and into the substrate.

We found in the thinner 25 nm films a small oxygen peak at the interface and an order of magnitude difference in the oxygen concentration in the film. This is somewhat surprising as both films are expected to be granular and allow oxygen to diffuse into the film.

We sent another 25nm base and 25 nm oxygen prepared film to confirm that the oxygen levels were indeed that high in the film and found 5% smaller

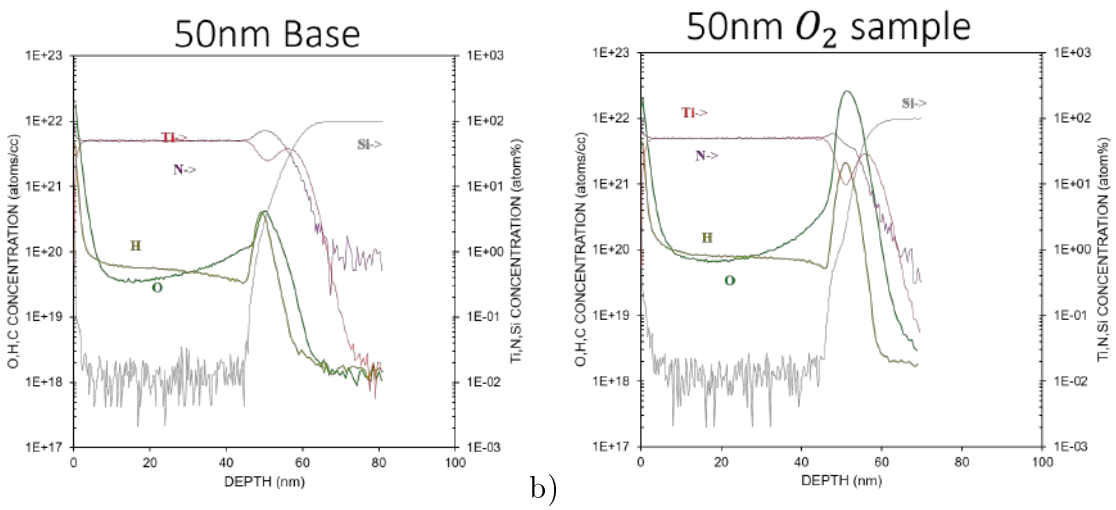

Figure 72: Data shows the SIMs analysis in the thicker films. a) In the base very low levels of oxygen are seen in the film with a small peak at the interface. b) A much larger oxygen peak is seen the 50 nm film as expected but still relatively low levels of oxygen and hydrogen in the film.

levels the 2nd time around for the oxygen prepared film. The results for all the oxygen concentration are plotted in Figure 60 showing the differences between the 4 films. Clearly the 25 nm oxygen has the highest oxygen concentration in the film. The larger oxygen concentration is consistent with the oxygen preparation and a more granular film that oxygen can diffuse between grains, creating surfaces or columns of TiO[58]. It has been shown in previous studies that high oxygen and low stress can lead to high quality factors over 1 million [3]. Those films were deposited at room temperature with no substrate bias while our films were deposited at 500°C with a -250 dc bias. In the past our group has reported on how the crystal direction, stress and bias voltage changes the TiN properties[96]. It found higher DC bias reduced the oxygen

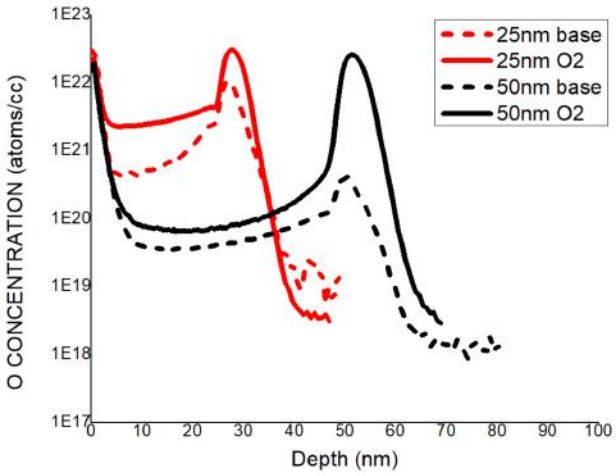

Figure 73: SIMS image showing the oxygen concentration in the film. The thinner films have significantly more oxygen which peak at the interface with the silicon substrate likely due to SiO_2.

concentration.

6.9.1 Thermal Stress

In this subsection I will analyze what happens when a film is cooled down to low temperatures since stress seems to play an important role in the TiN growth and conduction. Upon cooling, substrate and thin films will shrink by some factor given by their thermal expansion coefficient (TEC), α. The strain related to how much the length changes over the initial length $\Delta L/L_0$. It follows that two different materials, film, and substrate with an α_s and an α_f, having the same length L_0 at some T_0 will differ in length at the temperature T by some ΔL(T) or strain, ϵ directly proportional to the mismatch in the thermal expansion coefficient. Thus the strain , $\epsilon = \Delta\alpha\Delta T$.

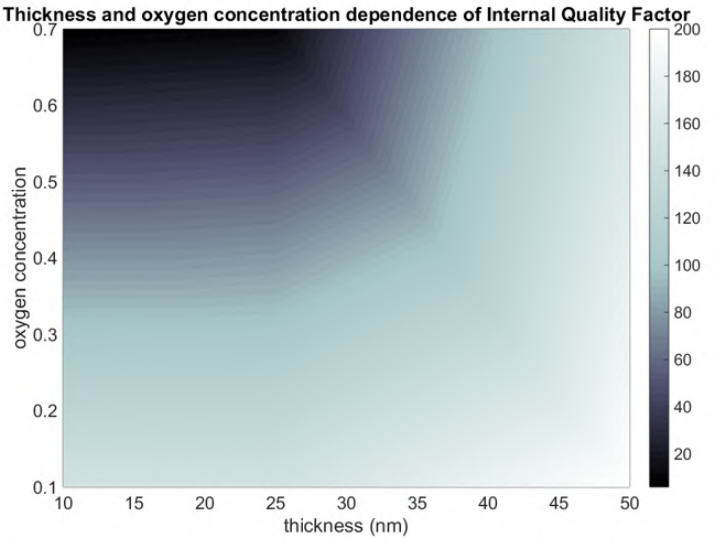

Figure 74: Quality factor of the films measured as a function of the film thickness and percent of oxygen concentration at the interface. The upper left of the graph has thin films with a high oxygen concentration for low Q_i.

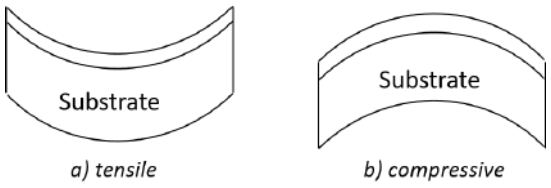

Figure 75: Stress of film if $\alpha_f < \alpha_S$the film is in compression, else if $\alpha_f > \alpha_S$tension

The thermal strain will lead to a thermal stress $\sigma_T = Y\epsilon/(1-v)$ where Y is the Young's modulus and v is Poisson's number.

For silicon $Y_{Si} = 150MPa$ the linear coefficient of thermal expansion from Figure 1a at room temperature $\alpha_{RT} = 2.5 \times 10^{-6}K^{-1}$ at 25K, and $\alpha_{1K} = -.2 \times 10^{-6}K^{-1}$. For TiN, $Y_{TiN} = 640MPa$ the linear coefficient of thermal expansion at room temperature $\alpha_{RT} = 9.35 \times 10^{-6}K^{-1}$

The TiN has not been measured below RT. To approximate at low temperatures we can use the theory model from reference [87]used in Figure 1b.

At 50K

$$\alpha_{1K} \sim .2 \times 10^{-6}K^{-1} + / - .2 \times 10^{-6}K^{-1}$$

Solving for the thermal stress with $v = .3$ and $Y = 640$ for TiN we can get a range for the thermal stress expected

$\sigma_{T_1} = 640 \times (9.35 \times 10^{-6} - .4 \times 10^{-6}) \times 300/.7 = 2.455$ GPa

$\sigma_{T_2} = 640 \times (9.35 \times 10^{-6} - 0) \times 300/.7 = 2.565$ GPa

Meaning given the error of $.2 \times 10^{-6}K^{-1}$in our estimate of the TEC of TiN at low temperature we can expect

$\sigma_T = 2.51GPa \pm .055$ GPa

For silicon

$$\sigma_{T_1} = 150 \times (2.5 \times 10^{-6} + .2 \times 10^{-6}) \times 300/.7 = 174MPa$$

We can sum the in plane thermal stresses $2.51 - .174 = 2.336GPa$

Thus calculating the bi-axial stresses due to the TiN shrinking more than

the Silicon substrate, the film will bow upward as shown in Figure 75a. Overall these stresses are not expected to cause any cracking in the film or changes to the grains when brought down to mK. However this is only an approximation using a polynomial fit from a previous studies,[15][87] which did not go down to mK temperatures.

6.10 Conclusions

In conclusion I measured an order of magnitude loss transition in the TiN films by varying thickness. They were grown with oxygen pretreated silicon substrates or on a silicon substrate with no treatment. While it has been seen that the quality factor of TiN depends on the growth direction and stress,[3] [7], little is known on the loss mechanisms or the transition in parameters at which this loss occurs. We measured and analyzed different characteristics of the films, from stress, to growth direction to the coherence lengths, etc and we found that the thin film grown on oxidized substrate had significant smaller grain sizes, increased oxygen concentration, and a preference for the [111] growth direction and an abrupt transition involving a component of tensile stress when the thickness was increased. Additionally by measuring the critical fields versus temperature we found there was a smaller mean free path, shorter coherence length and more disorder in the thinner oxide film with $k_f l \sim 14$. By analyzing the temperature dependence of the loss and frequency shift a higher number of excess non-equilibrium quasiparticles was determined using a modified Mattis Bardeen model and a two fluid model. From STM we found

both films to have inhomogeneous gaps but the thicker film had thermally isolated grains. Additionally, we found the superconducting gap is lower in the thin film and has smaller grains with an average grain size of 7.5 nm. A 2 gapped quasiparticle trapping model helps further elucidate the difference in the temperature dependence between the films. This model shows how in the thicker film the quasiparticles can be trapped in the low gapped, low loss area. The data supports low conduction of these quasiparticles, that they are not able to leave (not enough energy) due to the thermal isolation in the film found by STM. However in the thin oxide film quasiparticles that are trapped in low gapped low loss area can interact with phonons and escape at higher temperatures and enter the lossier or outside edges of the film causing an increase in loss.

This study identifies a growth and loss transition in thin TiN that had not been previously observed or analyzed. The transition was unexpectedly related to the thickness of the film and how the substrate was prepared. This data helps understand the loss mechanisms in granular TiN as well as the temperature dependent loss from non-equilibrium quasiparticles in an inhomogeneous film.

7 Post Treated TiN - High Q_i Resonators

In this section I discuss results results where we modified the TiN resonators after deposition. Titanium nitride resonators have the ability to achieve high quality factors [91, 3]. However the loss mechanisms in TiN films are not well understood as the film is very sensitive to its growth parameters. Here I will reference my work on a previous publication [63]. We show how depending on the post-treatment of the film, whether through chemical or plasma based treatment, we found quality factors that vary by as much as a factor of 18. We used inductively coupled plasma (ICP) and also reactive ion etching (RIE) for the plasma post-treatment.We found that the microwave resonator quality factor depends on the plasma environment. The plasmas used were oxygen and gas mixtures such as argon/hydrogen Ar/H_2, argon/ octafluorocyclobutane (Ar/C_4F_8), and argon/sulfur hexafluoride (Ar/SF_6). Additionally we varied the plasma chamber conditions, such as treatment time, ICP power, and RIE power. Of the plasma post-treatments, the Ar/SF_6 environments with no or low ICP power showed the highest ability to improve the quality factor . The different processing conditions determined the characteristic of the film and surface such as the roughness of the Si and TiN surfaces, TiN film thickness, and the overall TiN/Si resonator structure including the edge and sidewall. Our results can be used as a guideline for optimizing the microwave resonator performance using post-treatments.

Post-treatment type	Plasma functionalization conditions						Surface analysis					Resonator Frequency	Quality factor
	Flow rate (sccm)	Pressure (mTorr)	Time (sec)	Power RIE (W)	Power ICP (W)	DC bias (V)	Trench depth (nm)	Elemental composition of Si surface C (at. %)	O (at. %)	Si (at. %)	F (at. %)	F_{res} (GHz)	Q_i (n=1) (arb.)
None							102	13.0	37.0	50.0	0	4.58	120 000
None												4.61	170 000
HF only							102	13.8	2.9	82.3	1.0	4.5	510 000
Al etch												4.6	500 000
Ar/H_2	30/10	5	60	80	750	-273	154	4.9	20.5	61.9	0.5	4.9	450 000
Ar/H_2	30/10	20	60	80	750	-275	212	6.4	20.8	69.4	0.8	3.8	290 000
Ar/H_2	30/10	80	60	80	1000	-330	345	0	49.3	49.8	1.0	4.2	50 000
O_2	40	5	60	80	750	-316	125	3.2	60.5	36.3	0	4.3	140 000
Ar/C_4F_8	30/10	5	60	60	750	-339	371	24.2	14.1	40.1	21.6	3.2	125 000
Ar/C_4F_8	30/10	5	60	50	1000	-191	421					3.6	30 000
Ar/SF_6	30/10	80	60	50	1000	-80	650	6.9	26.6	65.4	1.1	3.7	30 000
Ar/SF_6	30/10	80	20	100	800	-242	471	5.1	30	61.5	1.5	3.1	550 000

Figure 76: Plasma functionalization conditions and surface analysis. Strikingly, the HF only treated resonator showed a great improvement likely eliminating oxides on the surface. The best performing resonator was with Ar/SF_6 with 800 W ICP power for 20 seconds. The worst devices had higher power, 1000 W ICP power for 60 seconds.

7.0.1 Resonator Post-treatment conditions

The resonators underwent typical photolithography as discussed in the previous section and were defined using a chlorine-based etch using the BCL_3 plasma. We focused on different plasma functionalizations at different powers and time exposed as shown in the table below

7.1 Q_i measurement for different of plasma functionalization

The Qis had a typical standard deviation of ±30k. The power dependence of Q_i as a function of selected plasma processing conditions is shown in Fig. 77.

As shown in Figure 78, very little power dependence of Q_i was observed

Plasma functionalization conditions							Surface analysis					Resonator Frequency	Quality factor
Exp #	Flow rate	Pressure	Time	Power		DC bias	Trench depth	Elemental composition of Si surface					
				RIE	ICP			C	O	Si	F	F_{res}	Q_i (n=1)
	(sccm)	(mTorr)	(sec)	(W)	(W)	(V)	(nm)	(at. %)	(at. %)	(at. %)	(at. %)	(GHz)	
SF # 1	30/10	80	20	90	0	-214	424	5.9	32.6	59.1	1.0	3.5	810 000
SF # 2	30/10	80	20	90	0	-214	407					3.3	540 000
SF # 3	30/10	80	20	50	0	-35	130	10.9	2.9	83.0	1.8	4.2	180 000
SF # 4	30/10	80	20	70	0	-160	282	8.9	20.9	65.9	1.9	4.5	240 000
SF # 5	30/10	80	20	130	0	-300	477	7.9	29.5	59.3	3.3	4.5	300 000
SF # 6	30/10	80	5	90	0	-214	147	6.8	23.3	65.6	1.9	4.3	180 000
SF # 7	30/10	80	10	90	0	-214	202	7.9	23.7	64.0	2.0	4.0	300 000
SF # 8	30/10	80	30	90	0	-214	465	7.4	24.0	63.9	2.8	4.7	310 000

Figure 77: The plasma functionalization environment such as gas flow rates, pressure, treatment time, ICP and RIE powers and dc self-bias are shown. Note that the plasma exposed resonators were previously exposed to chemical etch with hydrofluoric acid. The surface analyses show TiN/Si trench depth and elemental composition of silicon obtained, respectively by profilometry and XPS analysis. The resonator characteristics were reported in terms of the internal quality factors and resonator frequencies.

as a function of plasma processing characteristics. The Q_i, at single photon, varied as a function of dc bias and treatment time. At low dc bias and short treatment times (Figure 78(c)), Qis were reduced by approximately a factor of 3. Interestingly, as the treatment time increased to 20 seconds and the dc bias increased to -214 V, the Qi recovered and increased to a value close to the HF-treated resonator. However, further treatment time or a high dc bias of -300 V resulted in lowering the internal quality factor . These results suggest that there are plasma treatment conditions for a particular gas environment that can be found to optimize the internal quality factor of the film.

Fig. 79(a) shows the TiN/Si resonator edge without any treatment—the surface on top of the film was noticeably rough. The HF etch cleaned the

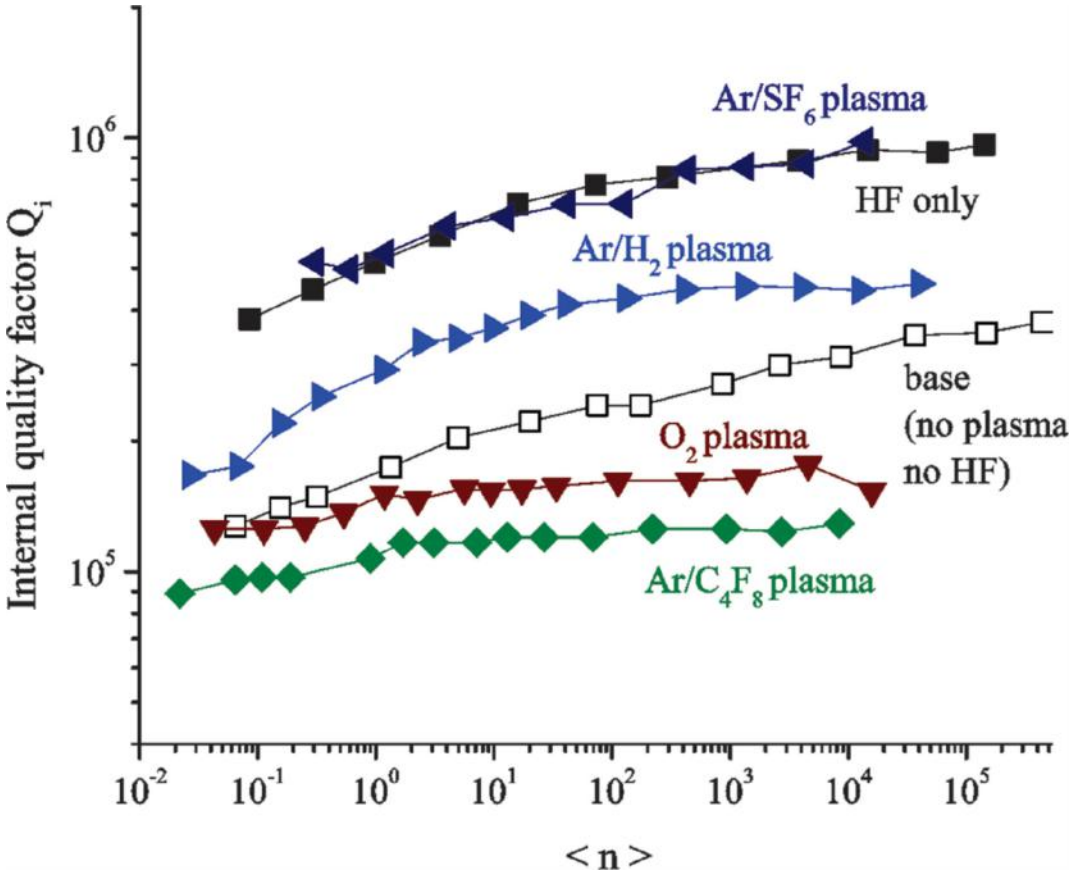

Figure 78: Shows the power dependence of the internal quality factor as a function of average photon number <n> at temperatures near 20 mK.

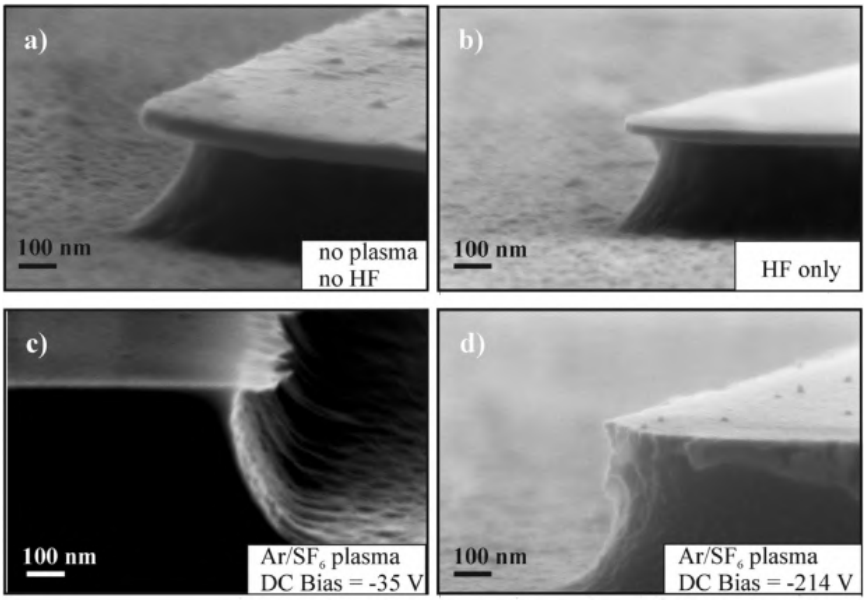

Figure 79: SEM images of the TiN/Si resonator edge in (a) base; (b) HF-only and (c), (d) Ar/SF_6 plasma exposed resonators. (c)and (d) show resonator edges after plasma treatment for 20 s with a dc bias of -35 V and -214 V.

top surfaces as seen in Figure 79(b) and reduced the overall thickness due to Aluminum removal. Fig. 79(c) shows the resonator edge after low RIE power treatment. An overhanging structure over the TiN resonator edge was formed in this film. We attribute the measured low Qi values to the formation of this overhanging structure. Interestingly, when the RIE power was increased to 90 W and a dc bias of -214 V, the edge was cleaned and the overhanging parts were removed. This modification of the surface could explain the increase in Q_i. A further increase in power seemed to cause damage to the TiN films around the resonator edge. Since the edges of the film host the highest currents and corner-like features can radiate energy out and increase quasiparticle loss in the region which could contribute to the lower quality factor values.

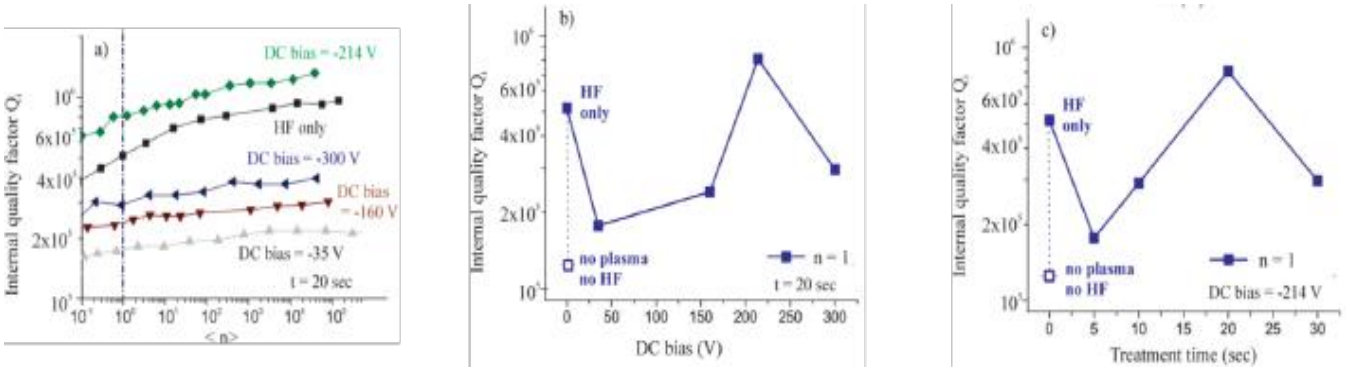

Figure 80: Q_i of base, film treated with HF only, and Ar/SF_6 plasma-treated resonators. The dependence of Q_i on the number of photons is presented in (a) for different bias conditions(b) Dependence of internal quality facotr at one photon as a function of DC bias and treatment time are shown in (b) and in (c), respectively.

7.1.1 Conclusions

Previous attempts to modify the interfaces around a resonator have shown that improvements are possible, whether by etching into the trench or increased cleaning[84, 54]. I showed here how the total loss in a resonator is affected by changing the silicon surface termination, surface TLS and the superconductor edge etch. This work established quantitative structure, property correlations with the measured resonator internal quality factor. We found that the plasma type, the gas environment, and the plasma chamber characteristics lead to unique change of the TiN/Si resonators. A factor of 18 in Q_i was achieved by using ICP/RIE plasma functionalization in oxygen, Ar/H2 , Ar/C4F8 , and Ar/SF_6 gas environments, and different processing conditions. In conclusion the plasma functionalization affects the surface morphology, which affect the resonator internal quality factor. We also found that even when using plasma produced in a single gas environment such as Ar/SF_6 , a particular set of plasma processing conditions is required to optimize resonator quality factor

without destroying the Si/vacuum and TiN/vacuum interfaces, as well as the resonator edges. We varied two processing parameters, in particular, time and power. We showed that at low values of power less than -200 volts, the quality factor are improved, at optimal values, the internal quality factor is improved up to 800k, and at biases larger in magnitude that -250V and times greater than 20 seconds, quality factor decreased again. Our analysis of TiN bulk properties suggest that Ar/SF_6 plasma did not cause significant modification of the superconducting film properties. Thus, microwave resonator performance can be modulated.

8 Biased Qubit Design

In this section I will discuss a qubit design and initial results toward realizing a dc biased transmon qubit. The coherence of superconducting qubits has grown over five orders of magnitude over the last two decades. The current qubits are laid out, over a millimeter in size, on a substrate surface such that they mainly only coupled to two-level defects on the surface. The characteristics of these surface TLS are largely unknown. By studying a qubit or resonator designed with a sub-micron interdigitated shunting capacitor individual TLS residing on the surface may be observable. These TLS can then be biased, changing their energies in such a way as to improve the overall coherence of a qubit. I will start this section by going over the Hamiltonian of the cooper pair box and transmon qubit.

The Transmon is an adaptation of the most basic charge qubit the Cooper pair box. The cooper pair box is the fundamental charge qubit where Cooper Pair number is the main variable of the interaction in the qubit system. Quantum coherent charge oscillations were first experimentally seen by Devoret [18]. A simple circuit representation is shown below with its corresponding Hamiltonian.

A Josephson junction is two superconducting electrodes separated by an insulating barrier. A supercurrent is able to flow through the junction as cooper pairs can tunnel coherently across the barrier. The supercurrent I is

$$I = I_0 sin(\phi(t)) \tag{8.1}$$

Where I_0 is the critical current and ϕ(t) is the time dependent phase difference across the junction. When a voltage V is applied to the junction

$$V = \hbar/2e d\phi/dt \tag{8.2}$$

Then taking the derivative of the supercurrent with time $dI/dt = I_0 cos\phi d\phi/dt$ arriving at

$$dI/dt = (2eVI_0)/\hbar cos\phi \tag{8.3}$$

Recalling the voltage across an inductor as

$$V = -LdI/dt \tag{8.4}$$

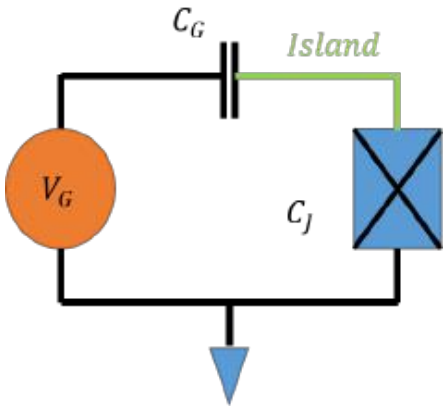

Figure 81: Cooper Pair Box where charge can hop onto the island depending on the voltage levels and energy

We can represent the Josephson junction as having a nonlinear inductance

$$L_J = \Phi_0/(2\pi I_0 cos\phi) \tag{8.5}$$

Where $\Phi_0 = h/e$ is the magnetic flux quantum.

One of the first charge qubits was the Cooper Pair Box. Figure 81 above is a circuit diagram displaying the cooper pair box. A cooper pair is able to tunnel to a superconducting "island", the region between the two capacitors C_G and C_J which represent the gate capacitance and the junction capacitance [18]. The charge can tunnel from the Josephson junction which has a reservoir of Cooper pairs. By raising or lowering the bias voltage, V_G , tunneling one or multiple Cooper pairs from the reservoir becomes energetically favorable or unfavorable. The main degree of freedom then is n, the number of cooper pairs on the island. The charge associated with the island is q= -2en where n is a discrete number. The Hamiltonian can then be described as

$$H = 4E_C(n - n_g) + Ejcos(\phi) \tag{8.6}$$

The charging energy $E_C = (2e)^2/2(C_s)$ And the Josephson energy is equal to $E_J = (I_0\phi)/2\pi$, where C_s is the sum of capacitances; the 2e represents the charge of the Cooper pair. The gate voltage can be re-expressed as a number, $N_g = (C_gV_g)/2e$ (28) Transforming this equation to charge representation

$$H = E_C(N - Ng)^2|N\rangle\langle N| - Ej/2 + \sum N(|N-1\rangle\langle N| + |N\rangle\langle N-1|) \tag{8.7}$$

If you then diagonalize the matrix only looking at the first 3 charge states one finds

$$\begin{pmatrix} E_c(-1 - N_g^2) & -E_j/2 & 0 \\ -E_j/2 & E_cN_g^2 & -E_j/2 \\ 0 & -E_j/2 & E_c(1 - N_g^2) \end{pmatrix}$$

Below, Figure 82, shows the normalized eigen-energies plotted in matlab.

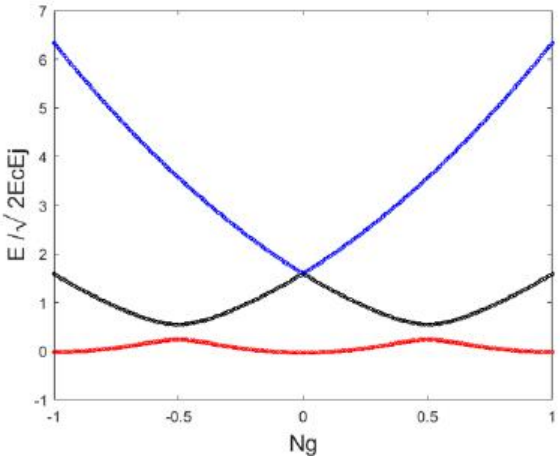

Figure 82: Cooper Pair Box Energy States

The degeneracy between the different charge states in broken due to the Josephson energy E_J. The cooper pair box can be used as a qubit taking the first two energy levels as the qubit $|0\rangle$ and $|1\rangle$ states. As one can see the charge noise changes the energy required to transition between these two states making the CPB not an ideal qubit since charge noise is a common issue[90]. This design however inspired the Transmon qubit which reduces this charge noise by using a larger E_J/E_C ratio.

The transmon qubit is similar to the cooper pair box discussed in the earlier section. The qubit relies on reducing charge noise through shunting capacitors which increases the E_J/E_C ratio such that $E_J >> E_C$ and thus leveling out the energy levels. One can take the Hamiltonian of the cooper pair box a step further to get the transmon using "black box radiation." We can start from

$$H = 4E_C(N - N_g)^2 - E_J \cos\phi \tag{8.8}$$

When we assume $E_J >> E_C$and if we Taylor expand the potential about its minimum we obtain the effective Hamiltonian

$$H_{eff} = 4E_C N^2 + \frac{1}{2}E_J\psi^2 - \frac{1}{4}E_J\psi^4 \tag{8.9}$$

Then one can introduce the bosonic creation and annihilation terms $\alpha^\dagger$and α that diagonalize it

$$H_{eff} = \hbar\omega_0(\alpha^\dagger\alpha + 1/2) - \frac{1}{12}E_C(\alpha + \alpha^\dagger)^4 \tag{8.10}$$

Using the coefficients given by the zero-point fluctuation amplitudes $\psi_{zpdf} = (2E_C/E_J)^{1/4}$and $N_{zpf} = \frac{1}{2}(2E_C/E_J)^{1/4}$ we can then use this to obtain

$$\alpha = \frac{1}{2}(\frac{}{zpf} + i\frac{N}{N_{zpf}}) \tag{8.11}$$

where the harmonic level splitting is $\hbar\omega_0 = \sqrt{8E_J E_C}$

Then applying the RWA as before and using the "black-box quantization" technique [107] we can obtain

$$H = (\hbar\omega - \frac{1}{2}E_c)\alpha^\dagger a - \frac{1}{2}E_C(\alpha^\dagger\alpha)^2 \tag{8.12}$$

8.1 Qubit -Resonator Design Parameters

The resonators are mostly harmonic oscillators whose characteristics are determined by two key parameters: the resonant frequency ω_0 and their bandwidth.

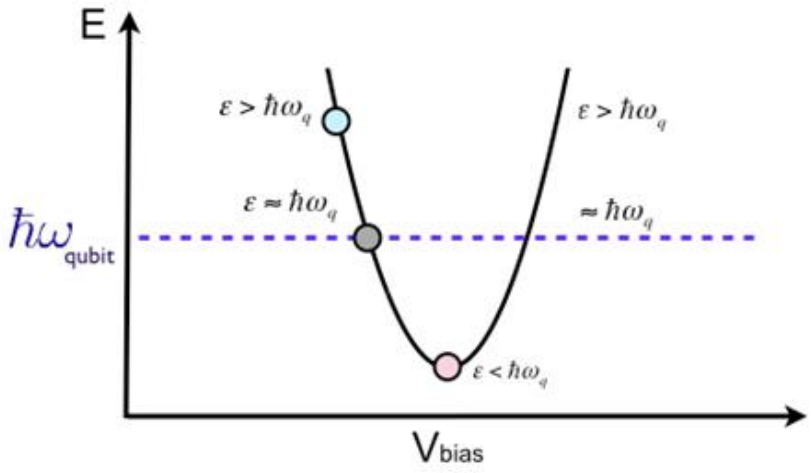

Figure 83: Biasing a single strongly coupled TLS defect out of the bandwidth of the qubit mode. This can reduce the overall loss channels and increase the coherence time of the qubit.

The bandwidth is determined by the full width at half maximum (FWHM) linewidth /2. This bandwidth captures both internal losses in the resonator as well as its coupling to external ports and is related to the internal or external quality factors as discussed earlier. Usually, the readout is designed so that the coupling is much stronger than the internal loss to reduce the amount of measurement signal lost, but much weaker than the resonant frequency, therefore $\kappa << \omega_0$ This will yield a high Q resonator.

The cavity decay rate $\varkappa/2\pi$ is an important parameters for qubit design and is the rate at which photon can leave the cavity. This is generally controlled by the coupling quality factor Qc which can be obtained using KVL, Kirchoff voltage law, in a basic circuit model of a CPW resonator between an input and output capacitor.

We want our output capacitor to be larger than our input capacitor so that the photons leave through the output side and into our amplifiers[108].

C_{out}=10×C_in We choose a Qc near 1000 since we want a $\varkappa$ to be in the MHz range

$$Q_c = Q_{out} = 950$$

$$\kappa/2\pi = f_r/Q_c = 6GHz/950 = 6.3MHz$$

$$1/C_{out} = \sqrt{((2Q_outZ_0^2\omega_0^2)/\pi)} \tag{8.13}$$

This gives an output capacitance of 15 fF and an input around 1.5 fF

$$C_{out} = 15fF$$

$$C_{in} = 1.5fF$$

8.1.1 Finding the coupling capacitance [15]

$$Z = -j[1/\omega C + Z_0 cot(\beta l)] = -j[tan\beta l + Z_0\omega C]/(Z_0\omega C tan\beta l)$$

On Resonance

$$tan\beta l + Z_0\omega C = 0$$

$$C = tan\beta l/(Z_0\omega)$$

If our resonator has a frequency at 6 GHz then our coupling capacitance will be C=20fF

We can then go back and calculate the coupling quality factorQ_c and $\varkappa$ for a given ω_r.

$$Q_c = \pi/(2(Z_0\omega C)^2)$$

$$\kappa/2\pi = f/Q_c$$

8.1.2 Simulating $\varkappa$ and Coupling Capacitance

To simulate the resonator Microwave Office is used as a 2.5 D simulation software package. I can create a $\lambda/2$ resonator in the software and even add the IDCs for the qubit mode. I can then create two ports at the ends. Through these ports I can make a transmission measurement. From theory I can get an estimate of the length and width of the fingers for the IDC which I will use for the input and output capacitors. In the simulation however I can finalize these capacitance values to ensure that I am at the right coupling of the resonator to the transmission line and at the right frequency. The resonator should be critically coupled to the transmission line meaning Qi = Qe. At this coupling there is increased sensitivity to any loss in the system. So from the

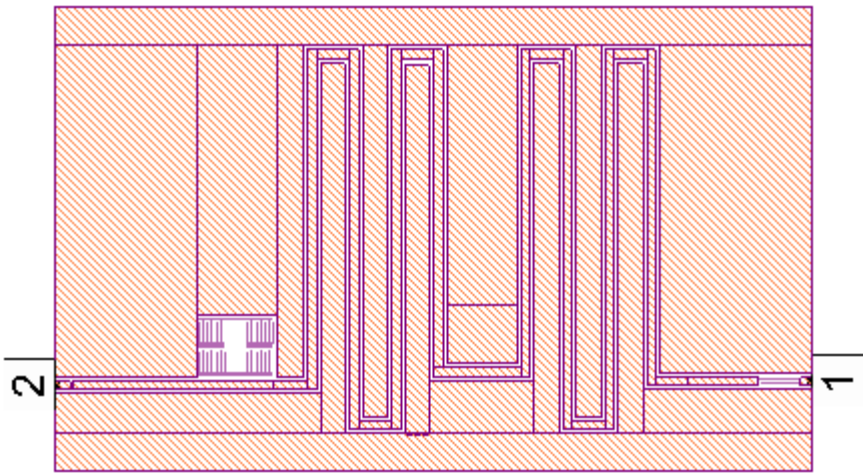

Figure 84: shows the MWO simulation of the λ/2 resonator that is coupled to the transmission line with ports at the input and output.

simulation I can ensure that this coupling is the operating point by looking at the dip in transmission. The transmission; $S_21 = (Q/Qe)/(1 - 2i\Delta\omega Q/\omega)$ where $1/Q = 1/Q_i + 1/Qe$ $\Delta\omega = \omega - \omega_r$ On resonance $\Delta\omega = 0$ and at critical coupling $Qi = Qe, S_{21} = 20log_{10}S_{21} = -6dB$

8.1.3 Estimating the Coupling of Transmon

A linear circuit approach In this section I will discuss the coupling g, between the transmon qubit and the resonator. This coupling is very important to the design as it determines the χ shift in the resonator where $\chi/2\pi = g^2/\Delta$. It is important to note this equation is an approximation if one considers the qubit system as a two level system. In practice there are higher levels excitations where the dispersive shift is better approximated by $\chi/2\pi$ $g^2/\Delta(\alpha/(\Delta + \alpha))$. It is important to be in the dispersive limit so as to perform a quantum non-

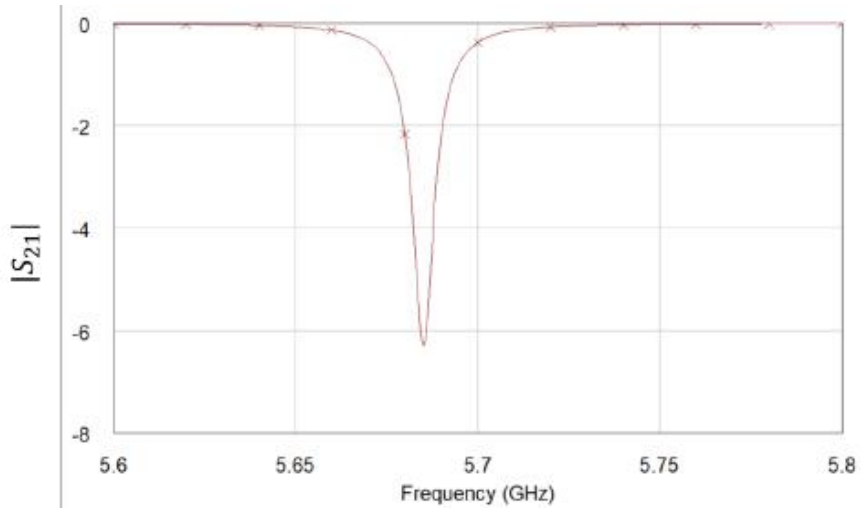

Figure 85: Graph showing the simulated frequency of the resonator. It is important to have the dip at -6db since this is the transmission at critical coupling where Qi = Qe. At critical coupling the system is most sensitive to all sources of internal loss.

demolition measurement. To be in this regime $g \ll \Delta$. Therefore theoretically calculating and simulation this value as best as possible is important. The coupling between the qubit and resonator mode is known to be approximately the same as that for a transmon and a resonator. This value can be determined by looking using Kirchoff Voltage Law and then analyzing the dynamics of the charge in the system.

Loop 1 – Resonator Mode

$$L_R(\ddot{Q_1}) + (Q_1 - Q_3)/C_R = 0 \tag{8.14}$$

Loop 2 – Qubit Mode

$$L_Q(\ddot{Q_2}) + (Q_2 - Q_3)/C_Q = 0 \tag{8.15}$$

Loop 3 – Coupling

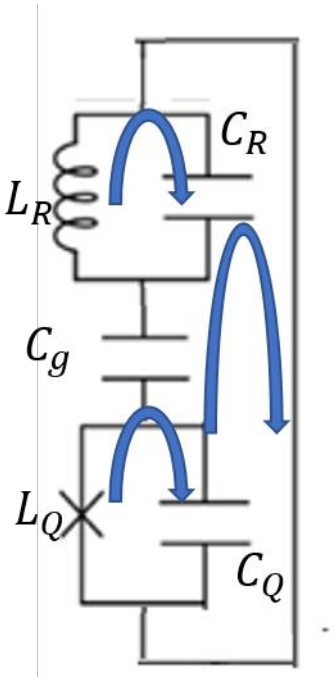

Figure 86: Schematic of the qubit mode coupled to the cavity resonator mode

$$(Q_3 - Q_2)/C_Q + Q_3/C_g + (Q_3 - Q_1)/C_R = 0 \tag{8.16}$$

Rewriting the previous equation

$$Q_3(1/C_Q + 1/C_g + 1/C_R) = Q_2/C_2 + Q_1/C_R \tag{8.17}$$

Plug equation 8.15

$$L_R(\ddot{Q}_1) = Q_3/C_R - Q_1/C_R \tag{8.18}$$

$$= (1/C_Q + 1/C_g + 1/C_R) - 1)1/C_1(Q_2/C_Q + Q_1/C_R) - Q_1/C_R L_R(\ddot{Q}_1) \tag{8.19}$$

$$= Q_1(1/(aC_R^2) - 1/C_R) + Q_2(1/(aC_R C_Q))$$

where $a = (1/C_Q + 1/C_g + 1/C_R)$ Similarly plugging 4 into

$$2L_Q(\ddot{Q}_2) = Q_2(1/(aC_Q^2) - 1/C_Q) + Q_1(1/(aC_R C_Q)) \tag{8.20}$$

Pulling out $Q_1$and Q_2 in and using $\omega_i = \sqrt{1/(L_i C_i)}$

$$(\ddot{Q}_1) = Q_1\omega_R^2(1/(aC_1) - 1) + Q_2\omega_R^2\omega_Q^2(L_Q/a) \tag{8.21}$$

$$(\ddot{Q_2}) = Q_1\omega_R^2\omega_Q^2(L_R/a) + Q_2\omega_Q^2(1/(aC_Q) - 1) \tag{8.22}$$

Which can be rewritten in matrix form as

$$\begin{matrix} \ddot{Q_1} \\ \ddot{Q_2} \end{matrix} = \begin{bmatrix} a_1\omega_R^2 & b_1\omega_R^2\omega_Q^2 \\ a_2\omega_R^2\omega_Q^2 & b_2\omega_Q^2 \end{bmatrix} \begin{matrix} Q_1 \\ Q_2 \end{matrix}$$

We can then understand the dynamics of the charge by finding the eigenvalues for different energies $\hbar\omega_1$ similar to the dynamics of the wave equation

$$\begin{bmatrix} \omega^2 - a_1\omega_1^2 & b_1\omega_1^2\omega_2^2 \\ a_2\omega_1^2\omega_2^2 & \omega^2 - b_2\omega_2^2 \end{bmatrix} = 0$$

Below shows the graphs of the two modes for a changing qubit energy ω_q using matlab to plot the eigenvalues

$$g = 1/4\sqrt{(\omega_R\omega_q)((C_c^2)/(C_3C_4))^{(1/4)}(C_q/C_R)^{(1/4)}}$$

(58) Which is similar to the customary form of the equation

$$g = (e\beta_r j)/\sqrt{\hbar Z_r}$$

$((2E_J)/E_C)^{(1/4)}$ Where B_{rj} is the sum of parallel and series capacitances coupling the qubit and resonator and Z_r is the impedance of the resonator

Above is the plot of linear eigenmodes representing the qubit-resonator

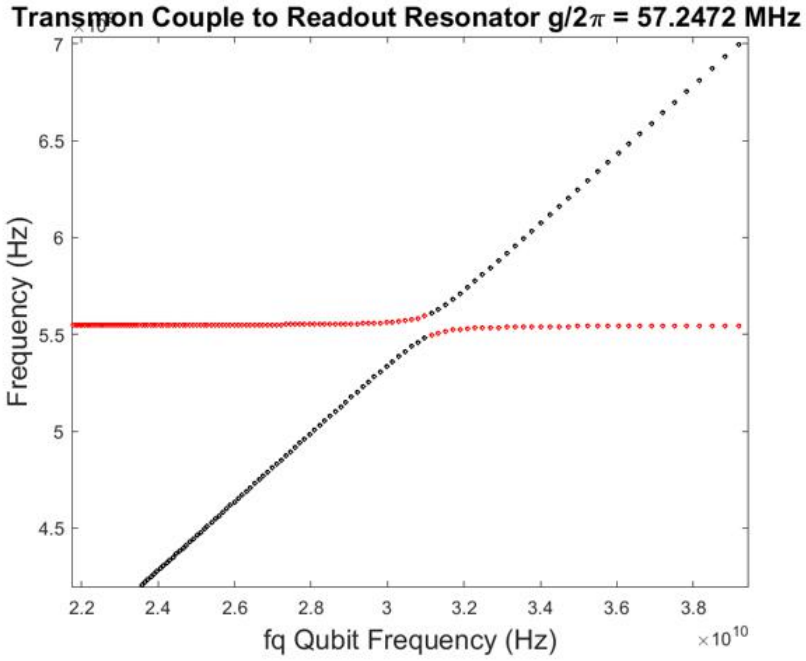

Figure 87: Simulation of coupled qubit-resonator system using circuit analysis

system. The cavity resonance is a constant 5.51 GHz while the qubit frequency is swept by sweeping the value of the inductance associated with the junction. The coupling between the qubit and resonator, $g/2\pi$, breaks the degeneracy and is the coupling rate at which energy is transferred between the two systems. The coupling designed for this qubit is 57 MHz with a qubit shown here of 3.18 GHz and a resonator frequency of 5.5 GHz. These values yield a detuning Δ=2.22 GHz which yields a $\chi/2\pi = g^2/\Delta = 1.5MHz$

8.1.4 Simulating the coupling $g/2\pi$ of the TLS to the qubit

To see a typical TLS with strong-coupling CQED in center of the gap of the IDC , we need the latter's capacitance to be small , assuming a decay rate of the resonator equal to $\kappa/2\pi = 1\times10^{(-4)}tan\delta\omega_c$ When the capacitance becomes <70fF the number of TLS is reduced and they can interact strongly with the cavity and a strong coupling CQED can be achieved where:

$$g = \Delta_0/\epsilon pcos\theta\sqrt{(\omega_0/(2\epsilon_r\epsilon_0\hbar V)}$$

The electric field volume can be calculated by considering the different interfaces that host TLS. One again can assume a 3 nm thickness [5] where TLS may reside. $Vol = n(LW \times t_{tls} \times l)$=(2 um× .003 um×65 um)×20= 8 um^3 Since this volume is much smaller than typical finger widths and lengths, there will be overall less TLS. In fact the number of TLS in a bandwidth BW, $N = 2\pi P_0 V\hbar B \sim .2$ Where $B = \pi/\kappa$

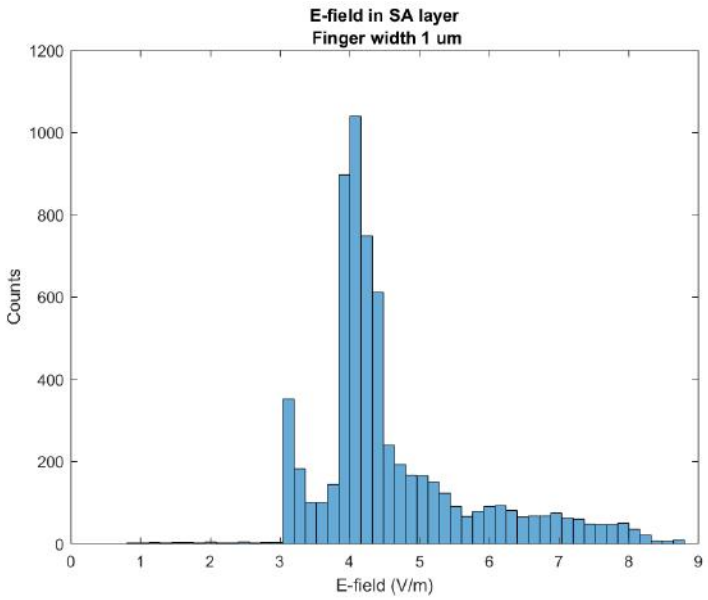

Figure 88: Shows the electric field at $\langle n \rangle$ =1 and the SA interface and the corresponding TLS-Resonator coupling g assuming a dipole moment of 2 Debye

8.2 Simulating T_1

$T_1$is the time associated with the qubit decaying from the excited state back to the ground state. Often $T_1$is the limiting factor in qubit decoherence and optimizing it is of utmost importance. In this section I will show how I can simulate the electrical environment that the qubit sees. I will look at the admittance across the qubit and use the real part of the admittance to help get a value for the T_1time. One can use Y parameters in Microwave office and make use of the voltage controlled voltage source and current controlled voltage sources to evaluate the currents and voltages needed to get the admittance desired. The qubit-environment system is typical modeled as below

As shown in the equations below we need to find the current through the

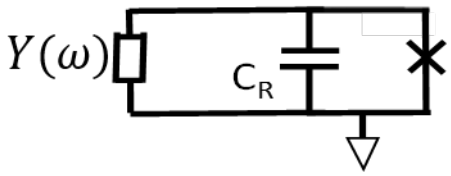

Figure 89: Circuit Schematic of a simplified transmon qubit with a shunting capacitor CR and an admittance from the rest of the circuit, where the real part will contribute to the loss

qubit. To do this we essentially put the current controlled current source in series where the qubit would be. The qubit is taken out of the system since we are interested in the admittance from the qubit perspective. Then the voltage across the qubit is need and to do this a simple voltage controlled voltage source is added in parallel. M is set to 1 and thus

The circuit used in Microwave office is shown below where I even included capacitors to ground to simulate the stray capacitance. Stray capacitance has been simulated as being at much 10% of the nearly IDC and is modeled as such.

The graph can then be made of simply S_{21} as derived in the above equations. The graph is shown below.

In this simulation the resonator frequency is at 7 GHz. As expected you see an increase in the admittance on resonance as the energy is leaving the transmission line. We want to put our qubit at a frequency near 5 GHz. The admittance at 5 GHz as shown is 6×10^{-9}. Using this value we can then calculate the T_1 time. This T_1 is sufficient for our experiment as we will need:

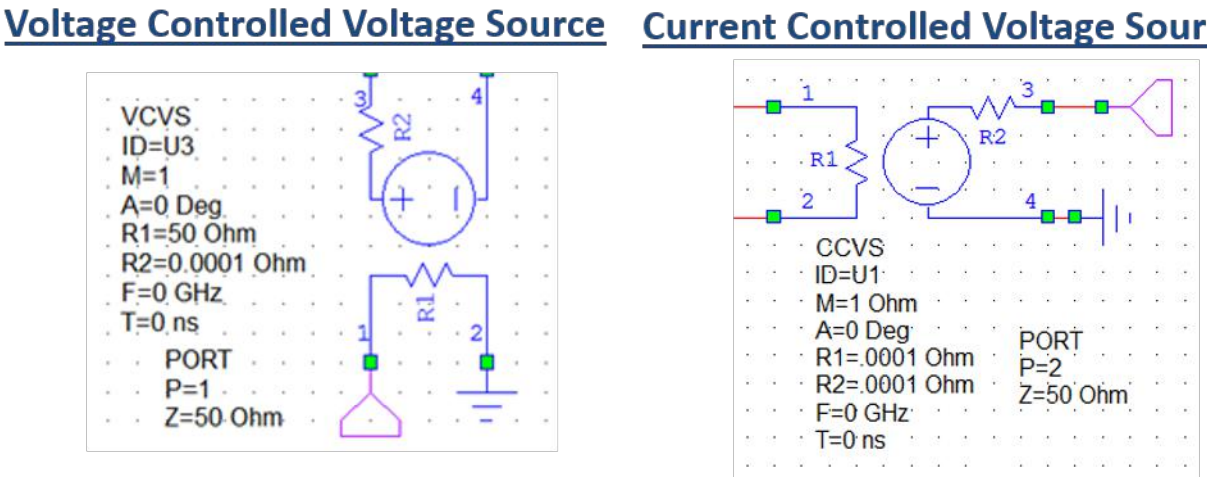

Figure 90: This Figures shows the components used for simulation the admittance across the junction.

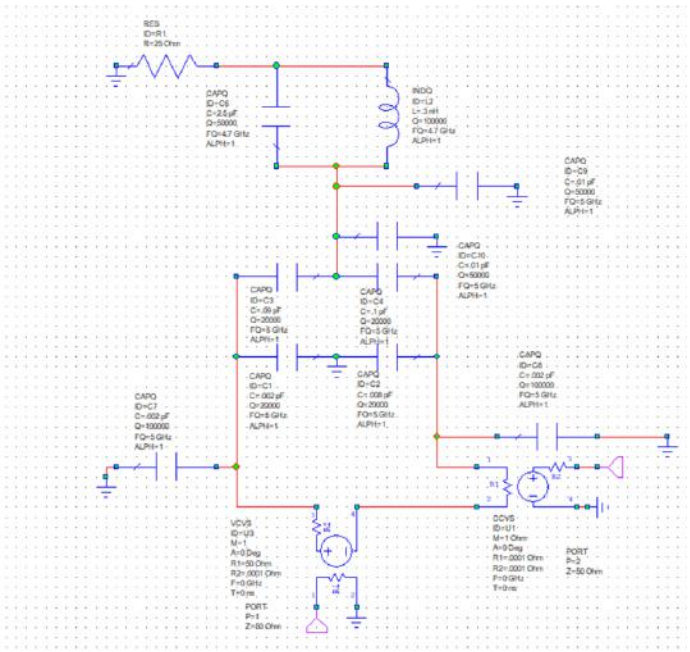

Figure 91: MWO office circuit simulation schematic

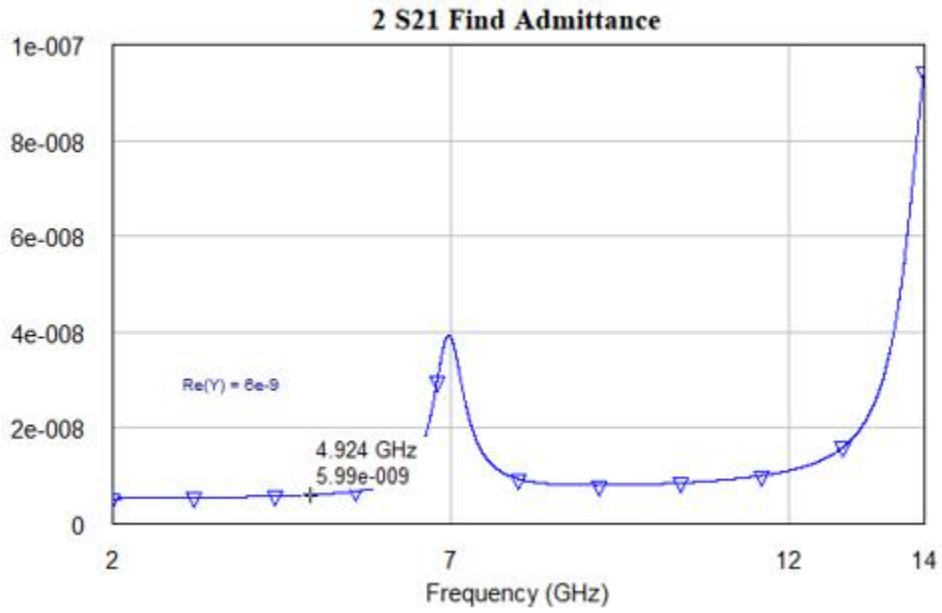

Figure 92: In this simulation the resonator frequency is at 7 GHz. As expected you see an increase in the admittance on resonance as the energy is leaving the transmission line.

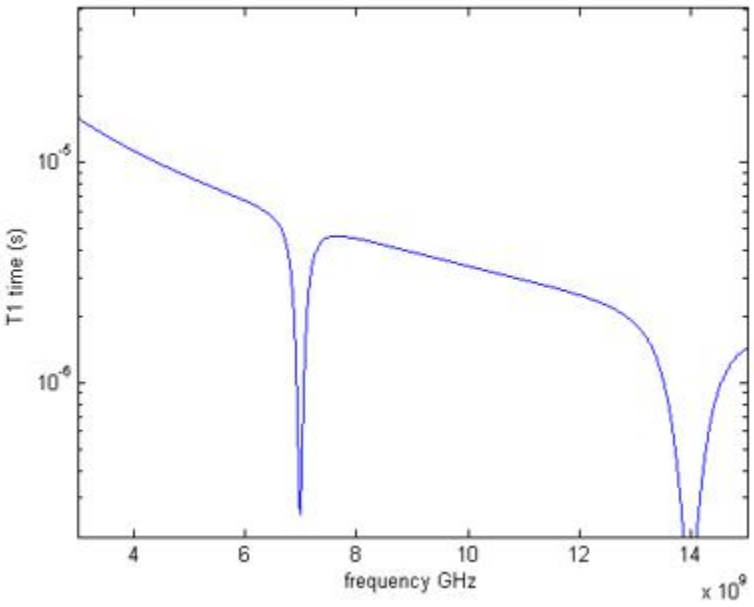

Figure 93: Purcell effect from modes other than the fundamental mode using simulated data

$\chi/2\pi \gg 1/T_1 = 1/10uS = .1MHz$ (63) Where $\chi = g^2/\Delta$ and $\Delta = f_q - f_r$ which is the qubit frequency minus the resonator frequency.

One can also theoretically calculate the admittance using Kirchoff Voltage law. From the calculations you can then plot the T_1 and again as shown in the graph above a T_1 near 10 us is expected for the electrical environment. However the actually T_1 is expected to be lower than $10\mu s$ as we don't expect the electrical environment to be the limiting decoherence source. Other decay mechanisms may reduce this T_1 and be the limiting factor. An additional resonance is near 14 GHz due to the higher order modes of the CPW. Fabrication process and Experimental Setup After the approximate values are known in the schematic, a layout is made in AWR MicroWave Office (MWO),

a two and half dimensional electromagnetic and RF simulator. The resonators are characterized thoroughly in the simulation using scattering parameters to measure the transmission and reflections present in the design. Additionally, the corresponding circuit schematic values can be determined and using special dependent sources, which will be talked about later. For example, one can measure the real part of the admittance across the junction. This admittance is important is understanding the loss that is present in the circuit and can be used to get an estimate for the coherence time, T_1 of the qubit using the equation below where C_s is the capacitance shunting the junction. $T_1 = C_s/Re(Y)$ Designs are then transferred to cadence to complete the layout which will be sent out and made into a mask for the photolithography. For our resonator studies we use 3 inch high-resistivity silicon [100] wafers for low loss substrates. We then sputter TiN onto our substrate and then in-situ Al. A wet etch is performed to remove the Al followed by a dry etch in an RIE system to remove the TiN. Then 1000nm thick blue resist is spun onto the wafer to protect it from the dicing saw. Our wafer is then diced into 6.1mm chips, then wire bonded then placed and glued inside a copper sample box which has SMP connectors that feed the transmission lines on the chip. The sample box is placed and mounted inside the Dilution refrigerator against a copper cold plate for good thermal conductivity. A non-magnetic SMP to SMA cable is then connected to another feed through in the fridge. And finally a SMA to SMA connector connects both sides of the RF line to the Vector Network Analyzer (VNA). Through the VNA we can make transmission (S_{21})

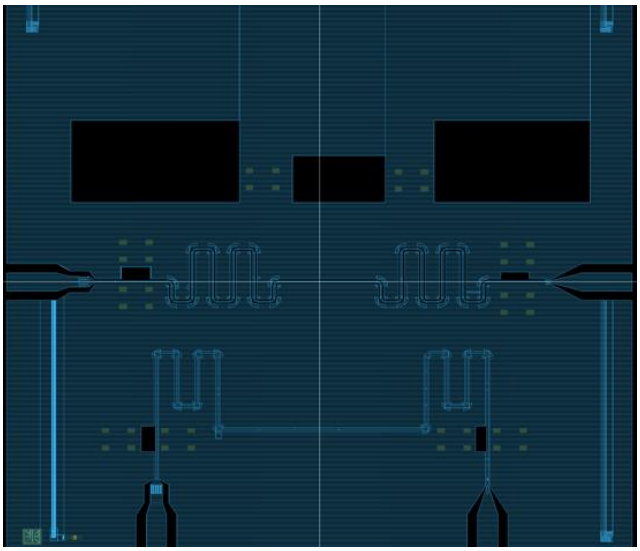

Figure 94: Mask Design of 2 $\lambda/2$ qubit designs

and reflection (S_{11}) measurements.

8.3 Fabrication

Photolithography is the process by which different metals will be patterned onto a wafer. The process involves using a mask to block or allow UV light to the polymer resist layer that is placed on top of the substrate. The resist hit by the UV light will be able to be removed using a particular wet etch. This step is called development. After the resist has been developed metal underneath can then be evaporated or the metal underneath the resist is exposed and a 2nd etch can be done to remove the areas where the metal layer is not wanted. Figure 94 shows the mask for the biased qubit design. This mask was created in cadence as a GDS file and was first simulated in Microwave Office.

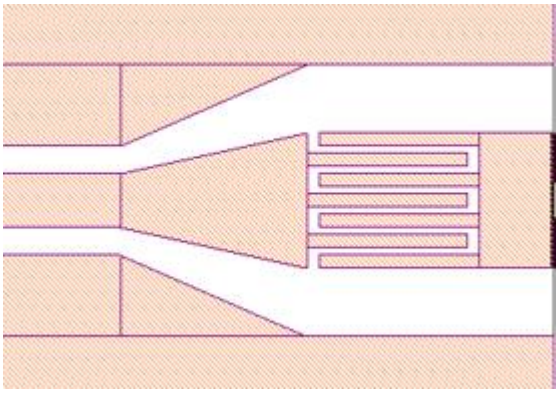

Figure 95: Figure showing the output IDC capacitance from the transmission line to the resonator

The above mask was designed in cadence. The mask is designed to cover a 6.35mm by 6.35mm space representing the size of each chip. This mask enables the fabrication of 2 resonators on a single chip. One transmission line goes across the chip horizontally. The resonator is a half wave CPW with capacitors on the input and output. The input and output capacitors as will be discussed in the follow section in qubit design parameters are asymmetric with the output capacitor being greater than the input to allow photons to prefer to escape through the output where the amplifiers are. The capacitors are interdigitated capacitors where the output capacitor is shown in Figure 94.

The launches on the chip will be wirebonded to a PCB trace and is discussed in the packaging section. There are square alignment marks which surround the location of the qubit near the beginning and ends of each CPW resonator since the fields will be strongest near the ends and allow for more coupling between the half wave resonator and the qubit mode. The large black rectangles are regions where one can place test junctions. Since test

junctions will be under the same conditions during the double angle evaporation, measuring the resistance of these junctions gives one a good idea of what frequencies their qubit will be.

8.4 Photolithography Steps

For our process we used a sapphire substrate for the qubit designs and a silicon substrate for the TiN resonators. For the qubits an aluminum layer is sputtered on top of a sapphire 3inch wafer while TiN is sputtered onto silicon. The resist used is OIR 906-10. The resist is spun onto the wafer at 1000 RPM. Figure 18 shows how a mask is used to expose the resist. The resist is then developed and the aluminum is then etched. Lastly the remaining resist is removed, leaving just the aluminum that is desired. Since our qubits are on a sapphire substrate which have a Z number near that of aluminum (13) thin films grown on sapphire are not easily visible in e-beam lithography. For that reason a gold layer (Z=79) is deposited and used as alignment marks to know where to place our qubit during the e-beam lithography. The gold layer follows the steps in Figure 97 where instead of an etching process a lift off process is used. Here the resist is removed first and then the gold is thermally evaporated on afterwards. A before and after development picture for this gold layer is shown in the Figure below.

Aluminum Deposition – a) First mask allows UV light to expose the underlying resist.

b) The resist is developed, exposing the aluminum.

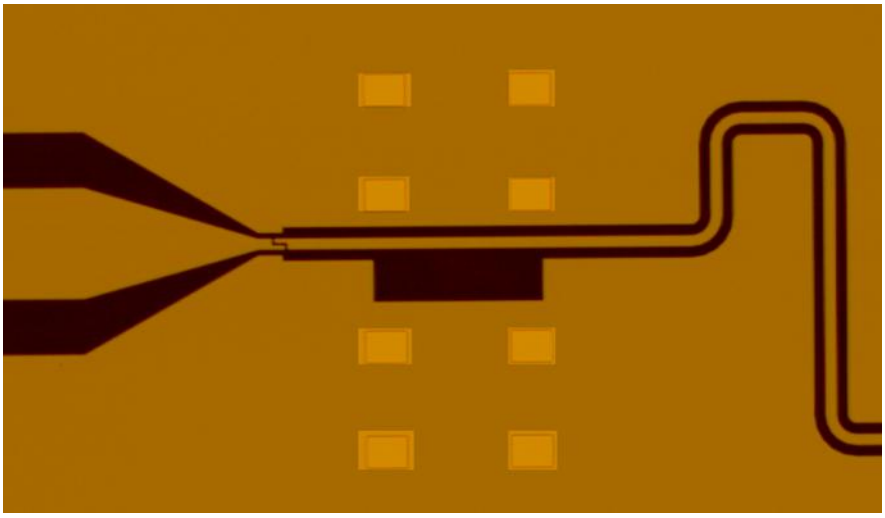

Figure 96: Image of the resonator after the gold layer is evaporated on.

C) The aluminum layer exposed aluminum region is removed using a wet etch.

D) Lastly the remaining photoresist is removed.

a) Mask allows UV light to expose the underlying resist. b) The resist is developed, exposing the substrate. C) Gold Layer Evaporation begins. First a 10nm layer of titanium is deposited to help the gold stick, then 100nm of gold is ebeam evaporated. D) Lastly the remaining photo resist is removed. After the gold has been evaporated and the photoresist has been lifted off, the photolithography is then complete. The sample will then undergo ebeam lithography to pattern the Josephson junction and IDC for the qubit structure.

The gold layer is the lighter false colored yellow. The darker orange is the aluminum layer. Ebeam Lithography After the gold layer is deposited the sample is ready for ebeam lithography. A dual layer of resist will be spun on

top of the wafer. First an MMA layer will be spun at 1000 RPM for 60 seconds created and heated for 5 minutes at 180 degrees C which will create a 900 nm thick resist layer. Next a ZEP 520A resist will be spun at 5000 RPM for 60 seconds and again heated for 5 minutes at 180 degrees C. This will create a 90 nm thick layer of ZEP. The reason for the two different types of resist is very important. The MMA resist polymer is more sensitive to incoming electrons than the ZEP layer and thus during exposure to e-beams the MMA layer will develop an undercut as shown in Figure 98 where the tan color represents the MMA layer. After an additional 20 minutes hard bake of the wafer at 180 degrees C the resist should be sufficiently hardened. An aluminum anti-charging layer is then thermally evaporated. The anti-charging layer needs to be thick enough to prevent enough electron beams from overly exposing the underlying resist but thin enough to allow sufficient electron beams through. A 10 nm layer is evaporated and has worked well. After fabrication, A blue photoresist is then spun on the fabricated wafer to protect it. The next step is to dice the wafer and then 1000nm thick layer of photoresist will protect the wafer from light and the environment. The wafer will be diced using a CA-010-270-080 H dicing blade from Dicing Blade Technology. Once the wafer has been diced, individual chips are ready for e-beam exposure. I used a JOEL SEM tool to perform the e-beam exposure. The steps are outlined in Figure 38. First I will focus on the corner of the chip, and then get a better focus by looking at a scratch I purposely make in the corner. A focus up to 50K magnification can be achieved solely by focusing on the scratch marks.

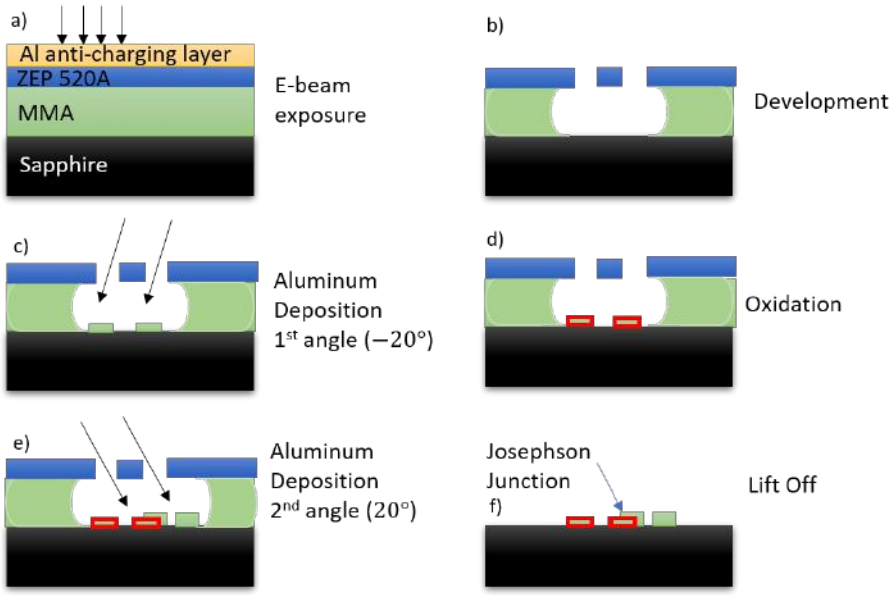

Figure 97: Figure showing the step in the e-beam process including the double angle evaporation.

Then I can get 10-100nm resolution by focusing on a contamination spot. A contamination spot is created leaving the e-beam at max focus, 500K, for 30-60 seconds. If the beam is in good focus a small 10-20 nm dot will be seen. Once good focus has been achieved I move closer to the good alignment marks which are easily seen at magnification greater than 10K. The alignment marks are 40 microns away from the area for my qubit structures. I refocus near my alignment marks and then blank beam and then move onto the area for writing the qubit pattern.

I then load the NPGS and run the file to pattern the qubit structure which is shown in its developed form in Figure 98 corresponding to how it looks in step b in Figure 97. The whitish looking regions are regions showing the

undercut. This image shows good undercut, meaning it is over 200nm which is sufficient to create the bridge but narrow allow the 5um LW of resist to stay in tact. After the area has been exposed. The chip is removed from the SEM and is ready to be developed. First the anti-charging layer is removed using OPD aluminum etchant. The ZEP layer is then developed using Amely Acetate. Then finally the most important step is developing the MMA layer since the undercut for this layer is very crucial for not only Josephson junction structure but also for the IDC in parallel with it. The undercut needs to be large enough such that an opening is created as shown in step b, hence creating a Dolan bridge above the developed resist layer [21]. However the undercut needs to be small enough as to not develop too much of the resist for the IDC layers which need the MMA layer to support a smooth line. This MMA development time has been optimized to 3 minutes and 55 seconds exposure using a mixture of IPA and DI water with a ratio of 5:1. After development is complete a double angle evaporation is performed as shown in steps c,d,e where aluminum is thermally evaporated from an aluminum target. The first layer is 30nm. Then the angle is changed and 330 mTorr of oxygen is allowed inside the chamber and an oxide layer is formed. Then at this 2nd angle a 50nm layer of aluminum is evaporated completing the Josephson junction.

After evaporation the final step is to "lift off" or remove the remaining layers of resist. The chip is placed in NMP for 2 hours at 80 degrees C. After two hours the resist starts to peel off and then the chip is further agitated in the beaker user tweezers. Once all the resist is removed the chip can then

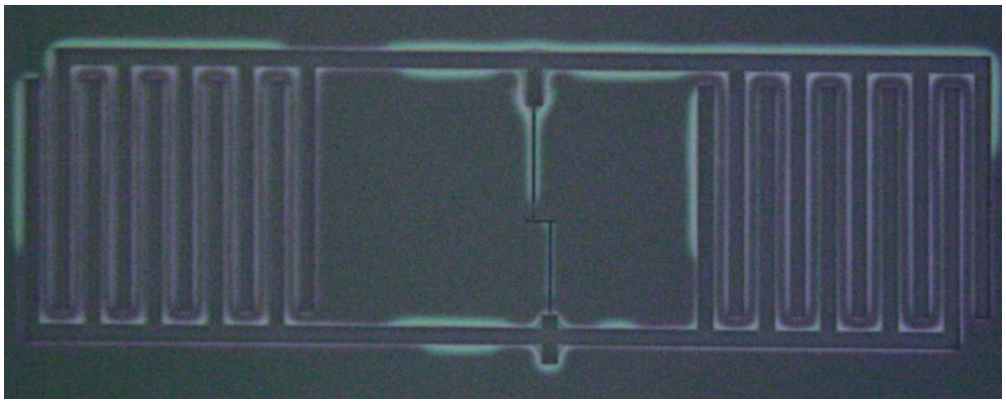

Figure 98: Optical image of a the transmon structure after MMA development

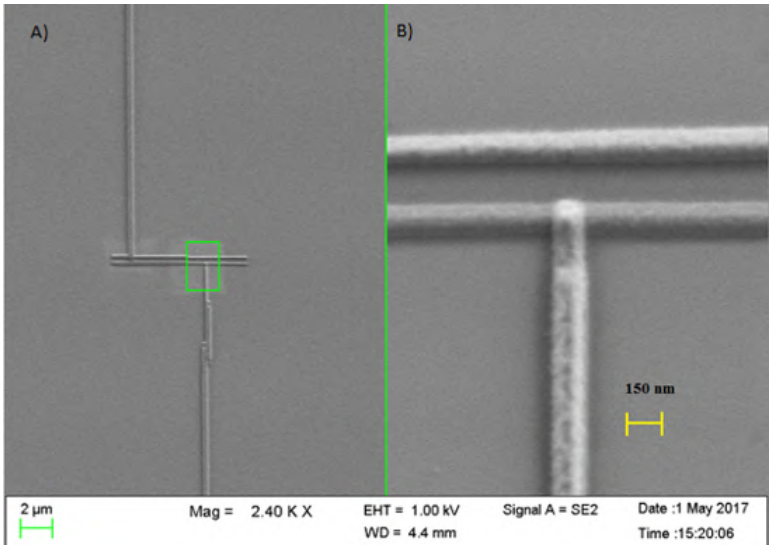

Figure 99: A) Zoomed out image of Josephson junction. B) Zoomed in version of the overlap region of the junction using an SEM microscope.

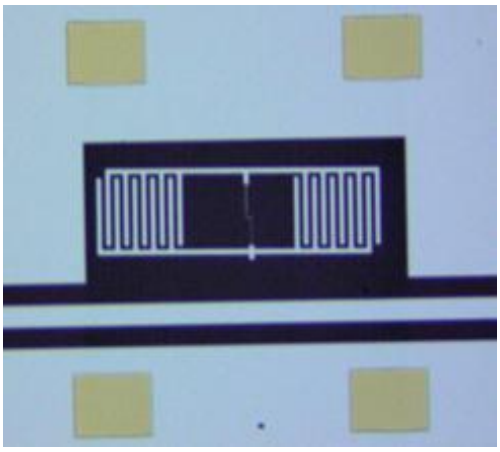

Figure 100: Final Qubit structure after final lift off. Imaged in a Keyence confocal microscope.

be imaged in an SEM as shown in Figure 99 or by a laser Keyence confocal microscope as in Figure 100.

Measurement Setup After the photolithography and e-beam lithography the wafer needs to be packaged and placed inside a dilution refrigerator. The chip are packaged into a copper sample box as shown in Figure 22. This sample box will hold the chip in place and allows for other connections to be made to the chip. Wire bonds will then connect directly from the launches of the chip to a PCB board that connects to an SMP connector. The SMP connector is then connected to SMA RF cables which allow for RF measurements to be made via an Agilent Vector Network Analyzer (VNA).

8.5 High Power Qubit Punchout Measurement

In superconducting qubits, half wave resonators are typically used to read-out the qubit. Coupling a resonator to the qubit mode allows for a way to measure the qubit without perturbing it. Looking at the Jaynes Cummings Hamiltonian

$$H_{JC} = \hbar\omega_r(a^\dagger a + 1/2) + (\hbar\omega_a)/2\sigma_z + \hbar g(a^\dagger\sigma^- + a\sigma^\dagger)$$

This time of nondestructive measurement can be performed if the frequency different or detuning of the two modes is much greater than the coupling strength between them, or $\Delta \gg g$ where $\Delta = f_q - f_r$. This is called dispersive readout. In order to test the qubit, a punchout measurement is first done to get the frequency of the bare cavity resonance. To do this the cavity the power or average photon number in the cavity is increased until it is no longer dependent on the qubit mode. Due to the coupling to the qubit at low powers the frequency will be shifted by a value of χ where ω_r is the shifted cavity resonance. $\omega_r = \omega_r^{'} + \chi$ This can be seen in the Figure below where the low power cavity resonance is displayed in yellow. The power is then increased and the resonant frequencies shifts as shown in the orange curve. At low power the qubit is coupled to the cavity. However once the number of photons in the cavity reaches the critical value, the cavity is no longer coupled to the qubit and is no longer in a dressed state recovering its original resonant frequency.

This shift is more commonly presented as in Figure 101 where the x axis

is the cavity frequency, the y axis is power and the color is related to the S_{22} reflection at the output of the RF signal. χ_{01}/π for this qubit is 4 MHz. Because $\chi_{01}/2\pi = g^2/\Delta = 4MHz$ it is expected to see a 2nd dip related to exciting the qubit from the ground to excited state. We expect this dip to occur about of 2 MHz from the cavity frequency because while χ_{01} relates the frequency shift of the dressed resonator-qubit system to the resonator system $2\chi_{01} = 2\chi + \chi_{12}$. It is important to note that at high power the frequency does not seem to be back in the linear regime. Meaning the $\chi_{01}/2\pi$ might be greater than 4 MHz. While the resonator at that power exhibits 100,000 photons this is not at all enough power to put the aluminum into any nonlinear regime. The cavity frequency was found to be 5.363 GHz. The total quality factor of the cavity was fitted as 10,000, while the external quality factor Qe was fitted to be 700. These values are very encouraging as they are within 5% of the theoretical values from simulation.

The cavity frequency changes at higher power as the qubit-resonator system decouples as the cavity reaches its classical bare frequency. This shift confirms that the qubit is coupled to the resonator. At higher power it appears the shift may be greater than what is possible with the RF in the fridge. A higher power is needed to reach the full bare cavity frequency however the amplifiers in the system begin to saturate at these higher powers. Thus the $\chi/2\pi$ can only be reported as an inequality for now, where

$$\frac{\chi_{01}}{\pi} > 4MHz$$

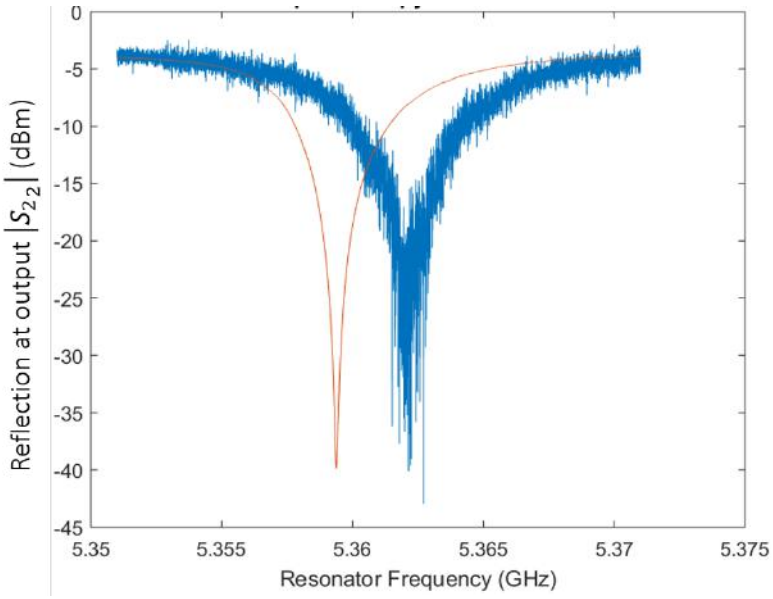

Figure 101: Cavity Punchout Measurement- The x axis is cavity frequency, the y-axis is S_{22}, the reflection at the output port. The cavity frequency changes at higher power as the qubit-resonator system decouples as the cavity reaches its classical bare frequency.

8.6 Conclusions

While this project is still ongoing I have laid the foundation for a transmon design that can be biased to move individual TLS in and out of resonance with the qubit mode. While a few studies,[82] [105],have performed used an external bias or applying strain, an on chip bias in this design makes this study unique. It would help illuminate how much an improvement can be made in the coherence times by tuning the surface TLS in the shunting capacitor.

9 Linewidth & Linespacing Resonator Study

In this mask design I was interested in doing a study where we varied the linespacing, linewidth and external quality factor to better understand the loss mechanisms in thin TiN & aluminum quarterwave resonators. The goal was to get a baseline loss tangent for our titanium nitride and aluminum films and observe how the loss changes for different geometries and couplings. This sort of measurement had been done before where the group saw increased TLS surface loss for smaller geometries[84, 86].

I designed 18 resonators on a single mask. I separated them into 3 groups. The first group I would vary the LW & LS but keep the ratio of LW/LS roughly the same. The second group I kept the LW the same at $15\mu m$ and varied the LS from $3\mu m$ up to $45\mu m$. In the last group I measured a resonator with $LW = 15\mu m$, $LS = 9\mu m$ at 6 different couplings ranging from $50k - 1M$. The complete group set and estimated frequencies are in Figure 102 along with

a)  b)

LW/LS/RES um/um/Ghz	1	2	3	4	5	6	7
Group 1: Vary LW/LS Ratio	6/3/ 5.86	9/6/ 5.936	15/9/ 5.966	21/12 6.007	30/18/ 6.033	51/30/ 6.066	51/30/ 6.1
Group 2: Vary LS	15/3/ 6.59	15/9/ 6.627	15/15/ 6.667	15/30/ 6.713	15/45/ 6.76		
Group 3: Vary Qe	15/9/ 7.3 Q=50k	15/9/ 7.33 Q = 100k	15/9/ 7.36 Q=250k	15/9/ 7.407 Q=500k	15/9/ 7.445 Q=750k	15/9/ 7.491 Q=1M	

Figure 102: a) An SEM image of a few of the quarterwave TiN resonators. One can see the different LWs and LSs resonators that were coupled to a center transmission line. The white streaks and specs are likely artifacts from touching the chip post measurement. b) The different groups measured. I separated the 18 resonators into 7 resonators varying the LW/LS lengths, keeping the ratio the same. The second group I varied just the LS and in the last only the coupling Q_e was varied.

an SEM image of a portion of the fabricated resonators.

Titanium Nitride Resonators

I measured two sets of resonators. Those deposited with Aluminum and those with TiN. I will discuss the latter in this section. TiN is interesting because of its high kinetic inductance as well as its proven to be capable of high Q[109]. To help determine characteristics of the kinetic inductances in the film TiN film I using some of the latest theories [52] . When the film thickness d,is the less than the London penetration depth λ perpendicular magnetic fields can penetrate into the superconductor. In this regime, $d << \lambda$, it is common to refer to the Pearl length $\Lambda = 2\lambda^2/d$.

In MWO I designed the frequencies of the resonators into 3 groups where the frequency is determined by the length of the resonator and the effective permitivity. In experiment however the frequency gets further shifted by the

Resonator Number	Theoretical $\omega_0\ (GHz)$	Experimental $\omega_0\ (GHz)$	$Q_i(\times 10^3)$	LW (um)	LS (um)
1	5.86	3.971	450	6	3
2	5.936	4.458	400	9	6
3	5.966	4.842	90	15	9
4	6.007	4.939	40	21	12
5	6.033	5.06	100	30	18
6	6.066	5.259	100	51	30
7	6.1	5.369	50	51	30
8	6.59	5.435	70	15	3
9	6.627	5.451	35	15	9
10	6.667	5.572	50	15	15
11	6.713	5.732	37	15	30
12	6.76	5.809	50	15	45
13	7.3	5.915	225	15	9
14	7.33	5.931	100	15	9
15	7.36	5.949	60	15	9
16	7.407	6	60	15	9
17	7.445	6.022	50	15	9
18	7.491	6.044	60	15	9

Figure 103: Resonator frequencies and low power internal quality factors for 50 nm TiN films. The measured frequencies were shifted by the kinetic inductance of the TiN. Interestingly the best performing resonators were the ones with the smaller geometry indicating that radiation loss may be a significant loss mechanism.

kinetic inductance. This extra inductance is not accounted for in simulation thus one can consider the difference δf in frequency to be due to the kinetic inductance. Figure 103 shows the frequencies shifts, and internal quality factors for the different geometries for the resonators.

From the TiN results the most interesting aspect of the study was from the frequency shifts. By using reference [52]and by looking at the frequency shift for the different geometries we can fit and find the London penetration depth which is generally an unknown parameter for the resonators measured.

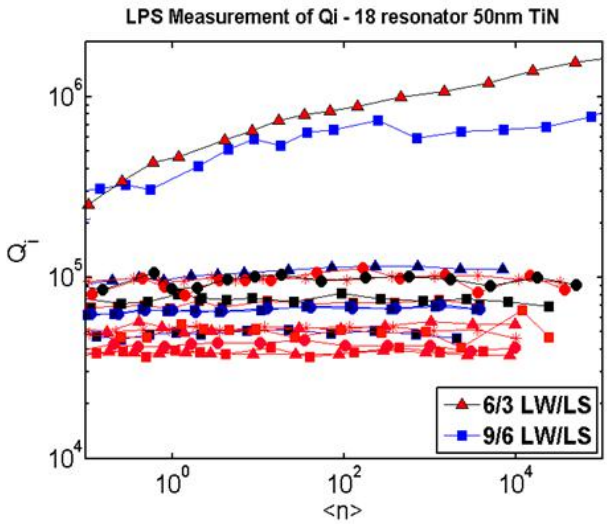

Figure 104: Results of 50nm TiN showing that the two lowest LW, LS resonators performed the best with Qis higher than a million at high power.

By measuring the kinetic inductance and by knowing the geometry of each film I can use the below equation and solve for the pearl length, Λ, which is the slope.

$$L_k^{'} = \frac{\mu_0 \Lambda}{4a} g_{kp}(k,p)$$

$$\Lambda = \frac{\mu_0}{L_k^{'} 4a} g_{kp}(k,p)$$

where

$$g_{kp}(k,p) = \frac{(k+p^2)\tanh^{-1} p - (1+kp^2)\tanh^{-1}(kp)}{p(1-k^2)[\tanh^{-1} p]^2}$$

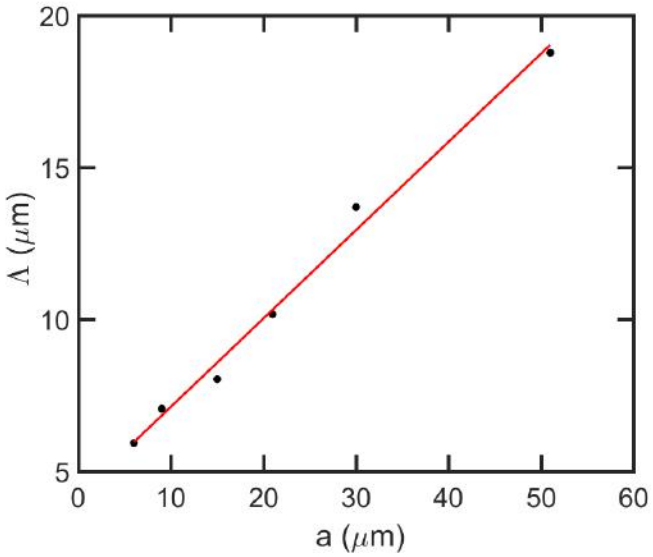

Figure 105: Graph showing the pearl length of the different resonators as a function of their conductor half widths, a

also $k = a/b$ and $p = 1 - \Lambda/a$

recalling

$$L_K = \frac{L_g \alpha}{1 - \alpha} \tag{9.1}$$

and we know the inductance per length L_g/l for a quarterwave resonator. Thus we can solve for the pearl length at different values of a.

9.0.1 Aluminum Resonators

In this section I discuss the results of measuring the same set of resonators deposited with Aluminum. Aluminum has significantly less kinetic inductance and thus the frequencies were largely where I expected them as shown in the Figure below.

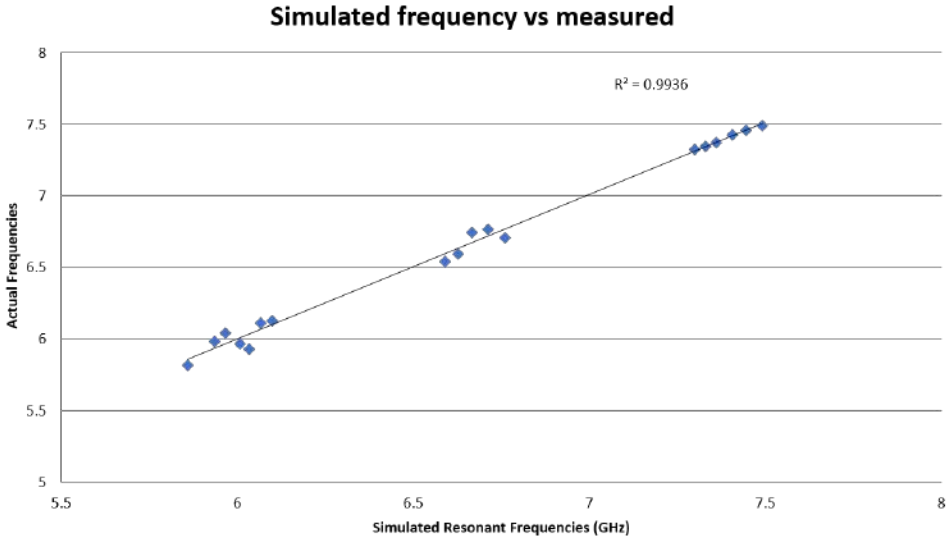

Figure 106: Simulated frequencies versus measured frequencies for Aluminum film

The loss analysis was intriguing. It is expected that for higher LW, LS that the TLS loss will decrease. This is not what occurred. The results from the aluminum resonator study showed that at higher LW, LS there was more loss. This is the opposite effect of dielectric loss where at larger LW,LS the participation ratio is reduced and the dielectric loss is less. This effect is a sign of radiation loss. Therefore there is a trade off between radiation loss and TLS loss. This becomes an important trade off when designing resonators; one needs them thin enough to avoid radiation loss and wide enough to avoid too high of a participation ratio from TLS at the interfaces. The radiation quality factor is,

$$Q_{rad} = \frac{\pi(1+\epsilon)^2\eta_0}{2\epsilon^{5/2}} \frac{1}{I'(\epsilon,n)} \frac{1}{n-1/2} (\frac{l}{s})^2$$

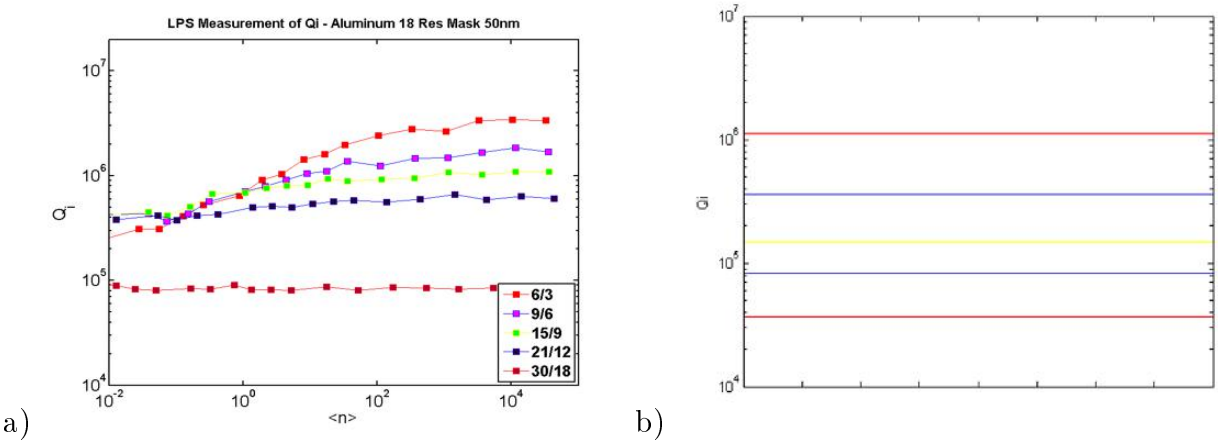

Figure 107: Results looking at the loss dependence on the geometry of the resonator, namely the LW, LS.

where $I^{'}$is the elliptical integral of the first kind, ϵ is the substrate dielectric constant, $\eta_0 = 377\Omega$ the impedance of free space, n is the mode, l is the length of the resonator, s is the width of the center conductor plus the gap, and $Z_0$is the characteristic impedance of the line. As shown in the above Figure 107b I calculated the expected radiation quality factor for the different linewidths and linespacings and got very good agreement qualitatively. The loss of the resonators at high power, where the TLS are saturated, shows a flat power independent loss that matches the calculated radiation quality factor. At low power they all show the same loss due to the TLS except for the largest geometry film. As the LW,LS increase you can see there is less and less power dependence as the radiation loss starts to dominate. Eventually in the largest geometry resonator the loss is completely power independent because the radiation loss is completely dominant.

10 Conclusions

10.1 Summary of Key Results

Superconducting qubits will continue to improve in the coming years as more and more research helps to propel the technology. Understanding how to manipulate surface TLS is incredibly important to its success. Surface TLS are ubiquitous and cannot easily be removed through fabrication or design[84, 86]. My surface TLS research has helped to illuminate ways in which surface TLS can be biased and controlled by identifying characteristic about surface TLS such as the coupling, coherence time and location. While previous experiments on observing individual TLSs were done on tri-layer resonators or in Josephson junctions for qubits[82, 105, 11], my study is one of the first on observing surface TLS in a resonator. Characterizing and observing surface TLS is crucial to the continued improvement in superconducting quantum devices where surface TLS remain the predominant loss mechanism in high Q_i resonators and decoherence in qubits.

By using an on chip dc bias to tune the TLS energies in an IDC of a lumped element resonator, I showed that one can characterize interface TLS systems which continue to plague modern superconducting qubits. We report seeing less than 2% of TLS in the strong coupling regime with an average coupling strength of 102 kHz. The histogram of coupling strengths has the appearance of a double peak and suggests that two dipole moments exist. Our coupling data shows two distinct peaks and fits a double Gaussian. The two

peaks could also be due to AlOx TLS and TLS from photoresist or an organic crud layer that have different dipole moments. The two peaks in the data is suggestive that there exists possibly two dipole moments from an AlOx layer and a crud layer such as some organic, or photoresist that was stuck in the gaps. Additionally, the two peaks could be due to TLS at different interfaces. One peak could from the TLS at the MS interface and the other at the SA or sidewall. In figure 29 one can see the different of the MS & SA interface is about a factor of 2 in electric field strength at 17.5 nm distance from the corner. That factor of 2 could be the reasoning behind the factor of 2 in the average coupling data. Additionally, there is a factor 2 in the field between the sidwall and MS near 5nm. I report that an average dipole moment of 1.2 Debye is found assuming a 20 nm distance from the highest field corner. I found a $p_z min = .7D$ and a $p_z max = 4.6D$. My simulations suggest that 80% of the strong coupled TLS exist at the MS or SA interface due to the electric field distribution close to the corner. My data suggests than all the strongly coupled TLS are within 50 nm from the highest field corner. This technique could ultimately be used in a transmon design to bias strongly coupled TLS out of resonance with the qubit and potentially find a highly coherent, high T_1, sweet spot.

By analyzing the different interfaces associated with the loss between a base film and a film deposited with Si_3N_4I found that the MS, and SA regions dominate the loss as has been shown before. I found that 45% of the loss resides within the first 40 nm from the highest field corner. When fitting

the power dependence using STM I found a factor of 6 less in α, the power dependence fitting parameter,in the SiNx deposited film than the base film. This is likely because although we have a co-planar device which typically has a weak power dependence we have deposited a dielectric that dominates the loss with a participation ratio of 66% close to the participation in an traditional trilayer capacitor. Thus as you get closer to the full 100% participation it would make sense that α would get reduced and almost return to the power dependence expected from STM ($\alpha = 0$). In the SiNx deposited film I found a critical field of $E_C = .7V/m$ and if we assume $p_z = 7.9D$ then we get a $T_1 = 3.4\mu S$ which is very close to the value of $3.2\mu S$ obtained is previous studies of bulk Si_3N_4[32, 59]. I extracted a participation ratio of SiNx of .61, close to the expected .66. I also extracted a loss tangent of $1.7 \times 10^{-4}$for SiNx and $p_i \tan_{\delta_{AlOx}} = 1.32 \times 10^{-5}$ for AlOx. Slight misfits in the middle of the power dependence is likely due to the two types of TLS saturating at different powers. This technique can be used to determine the losstangent of an unknown dielectric in an easy to fabricate 1 layer resonator.

While TiN or closely related NbTiN are becoming important films for superconducting qubit and resonators, their loss mechanisms are not as well understood as aluminum films[95, 3, 7]. The high kinetic inductance for frequency tunability is incredibly important in resonators as well as the tunability in the critical temperature. Furthermore thin TiN and NbTiN are used for ultra high kinetic inductances and is often used in MKID devices [51]. TiN more so than aluminum allows for oxides to diffuse into the material and possibly

allowing for more TLS loss. Therefore it is important to study the different loss mechanisms associated with growing TiN films. This work has shown that preparing a substrate with oxygen at thicknesses lower than 32 nm will induce a transition in growth from [100] to [111] and stress in the film as well. These structural changes to the film lead to an increase in non-equilibrium quasiparticle density and an order of magnitude increase in loss. This can be concluded from fitting the frequency shifts and quality factor with temperature. Non-equilibrium quasiparticles are necessary to fit the deviation from Mattis Bardeen theory at lower temperatures. It is seen from STM [57] the inhomogeneity of the films where the thicker film is more thermally isolated. These observation suggest a quasiparticle trapping model where quasiparticles from higher gapped grains can get trapped in lower gap grains. A 2 gap model is adopted to fit the data and qualitatively describe the results.

10.2 Ongoing Work

10.2.1 Damascene Resonators

In an ongoing collaboration with SUNY Poly we have designed and measured resonators using their CMP process to fabricate lumped element resonators. SUNY Poly has unique capability in their fabrication to use a damascene fabrication technique to etch the silicon substrate, deposit a liner and then deposit the film as in the Figure below. They have demonstrated their fabrication by making very reproducible Josephson junctions[113]. We were excited by this because the resonators will be embedded in the silicon substrate meaning that

a)

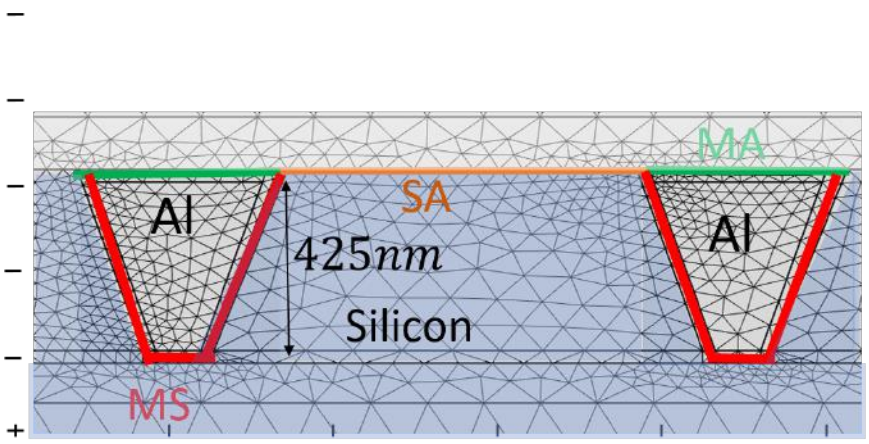

b)

LW/LS = .5μm/1μm	Participation Ratio
MA	2.93×10^{-3}
MS	$\mathbf{1.41 \times 10^{-1}}$
SA	1.23×10^{-2}

Figure 108: a) COMSOL mesh of damascene resonator. b) Participation ratios of the different TLS interface. Due to the film being embedded in the silicon substrate the participation ratio is now dominated by the MS interface.

only 1 TLS interface would dominate the loss, the MS interface between the film and substrate. Figure 108 shows the COMSOL simulations and expected participation ratios for such a structure. As can be seen the MS interface will dominate the loss with a participation ratio, $p_{MS} = .14$. In the simulation we assume a 10nm thick dielectric liner which was made out of TaN. The thickness of the film was 425 nm . The angle of the film from the substrate to the z axis is 70 degrees. I assumed a relative permitivity of the TaN as $\epsilon_r = 10$.

The internal quality factor of the film would be dominated by the loss of the TaN at the MS interface. This would allow an accurate way to measure the loss tangent of TaN. There were three types of resonators on this design intended to investigate different bias techniques and the possible loss through the 3rd bias port.

a) 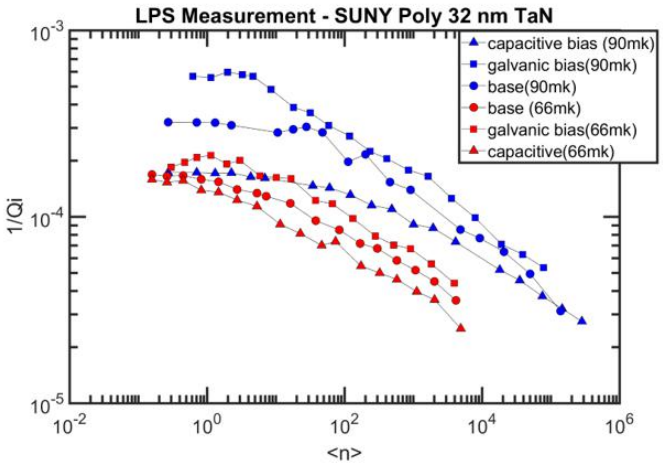

b) 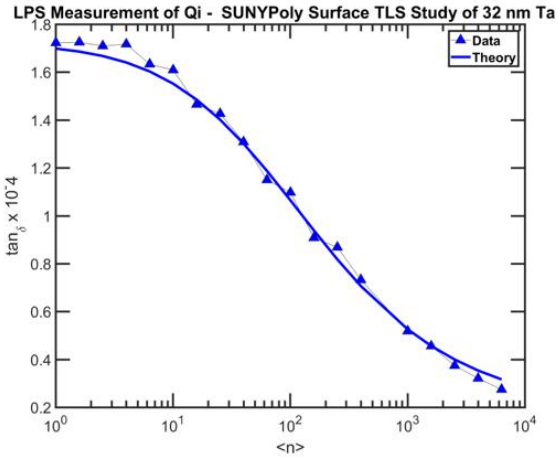

Figure 109: a) Initial power dependence of the inverse Qi of the resonator. b) Fitting to STM model

10.2.2 Fractal Designs

To better tune surface TLS an overcoupled resonator with a higher internal quality factor would allow for more surface TLSs to be observed due to lowering the minimum coupling needed to be in the strong coupling regime. A new quasi-fractal [117] design from has shown the ability to frequency tune the resonance using a current or voltage bias. This would be a very useful design for biasing TLS where one could potentially tune the TLS and the frequency and examine the differences if any of the TLS properties between the two tuning tehcniques.

Initial measurements were made of resonator using a quasi-fractal design. These resonators will have higher Qi than resonators previously used to measure individual TLS and will have a larger TLS volume and can be voltage or current biased. The goal is to measure more individual surface TLS. The

a) 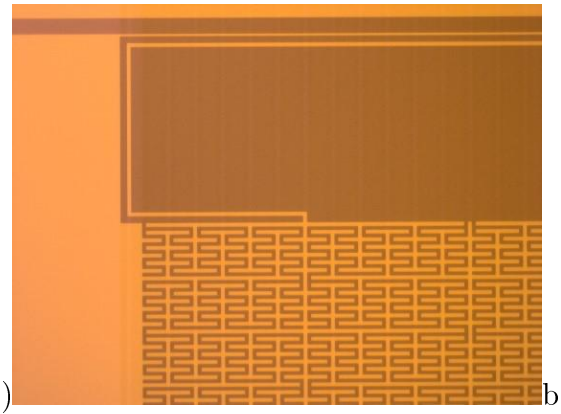 b) 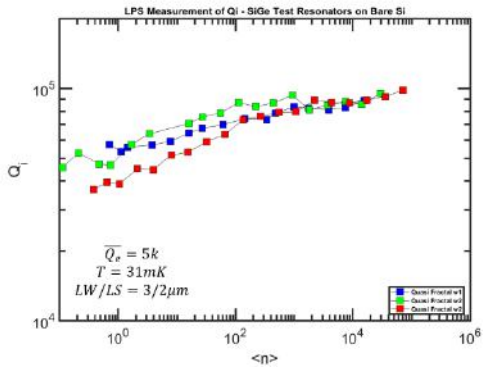

Figure 110: a) Image of a quasi-fractal resonator. b) Power saturation of the quality factor for 3 Quasi-Fractal resonators.

figure below shows an optical image of a fabricated a quasi-fractal resonator coupled to a transmission line. Figure 110c shows the power saturation of 3 quasi-fractal resonators over a single cooldown. The data shows an average Qi of 50k at single photon power and an average Qe of 5k. Thus the system is overcoupled and is not limited in seeing individual TLS by the internal quality factor. This is one advantage of this design.

By examining equation 3.60 one can see that in order to increase the number of TLS per voltage bias. It is important to have a higher bandwidth. However a high bandwidth also will mean a low quality factor which increases the minimum coupling needed for a TLS to be in the strong coupling limit. Therefore this is a trade off that needs to be better understood for observing surface TLS defects.

References

[1] P. P. W. Shor. Algorithms for quantum computation: discrete logarithms and factoring. In Foundations of Computer Science, 35th Annual Symposium on Proceedings, pages 124, 134, Nov 1994.

[2] Morten Kjaergaard, Mollie E. Schwartz, Jochen Braumuller, Philip Krantz, Joel I-J Wang, Simon Gustavsson, and William D. Oliver, Superconducting Qubits: Current State of Play, Annual Reviews Vol. 11:369-395 (2020)

[3] Shinobu Ohya, Ben Chiaro, Anthony Megrant, Charles Neill, Rami Barends, Yu Chen, Julian Kelly, David Low, Josh Mutus, Peter O'Malley, Pedram Roushan, Daniel Sank, Amit Vainsencher, James Wenner, Theodore C. White, Yi Yin, B. D. Schultz, Chris J Palm-strøm, Benjamin A. Mazin, Andrew N. Cleland, John M. Martinis, Sputtered TiN films for superconducting co-planar waveguide resonators, arXiv:1306.2966, (2013)

[4] Gao, Jiansong, The physics of superconducting microwave resonators. Dissertation (Ph.D.), California Institute of Technology. (2008).

[5] S J. Wenner,1 R. Barends,1 R. C. Bialczak,1 Yu Chen,1 J. Kelly,1 Erik Lucero,1 Matteo Mariantoni,1 A. Megrant,1 P. J. J. O'Malley,1 D. Sank,1 A. Vainsencher,1 H. Wang,1, 2 T. C. White,1 Y. Yin,1 J. Zhao,1 A. N. Cleland,1 and John M. Martinis. "Surface loss simulations of superconducting co-planar waveguide resonators" Journal of Applied Physics 109, 063915 (2011); https://doi.org/10.1063/1.3552890 (2011)

[6] J.Bardeen,L.N.Cooper, and J.R.Schrieffer, Phys,Rev.108, 1175 (1957).

[7] Michael R. Vissers, Jiansong Gao, David S. Wisbey, Dustin A. Hite, Chang C. Tsuei, Antonio D. Corcoles, Matthias Steffen, David P. Pappas,Low Loss Superconducting Titanium Nitride Coplanar Waveguide Resonators, Appl. Phys. Lett. 99, 113513 (2011); https://doi.org/10.1063/1.3637047, 2010

[8] A. Wallraff, D. I. Schuster,A. Blais,L. Frunzio, J.Majer,S. M. Girvin,and R. J.Schoelkopf. Approaching unit visibilityfor control of a superconducting qubit with Dispersive readout. PhysicalReview Letters,95:060501, 2005.

[9] David M. Pozar. Microwave Engineering. Wiley, 3 edition, 1990.

[10] Phillips, W. A. Tunneling States in Amorphous Solids. J. Low Temp. Phys. 1972, 7, 351.

[11] Bahman Sarabi, Aruna N Ramanayaka, Alexander L Burin, Frederick CWellstood, and Kevin D Osborn. Projected dipole moments of individual two-level defects extracted using circuit quantum electrodynamics. Physical review letters, 116(16):167002, 2016.

[12] R. BARENDS,N. VERCRUYSSEN,A. ENDO, P. J. DE VISSER,T. ZIJLSTRA,T. M. KLAPWIJK,P. DIENER,S. J. C. YATES,and J. J. A. BASELMANSMinimal resonator loss for circuit quantum electrodynamics. Appl. Phys. Lett., 97: 023508, 2010.

[13] Electrodynamic response and local tunneling spectroscopy of strongly disordered superconducting TiN films, P. C. J. J. Coumou, 1, E. F. C. Driessen, J. Bueno, C. Chapelier, and T. M. Klapwijk, PHYSICAL RE-VIEW B 88, 180505(R) (2013)

[14] G.G. Stoney, The tensions of metallic films deposited by electrolysis, Proc. R. Soc. Land. A82 (1909) 172-175.

[15] Chaudhari, Grain growth and stress relief in thin films, Journal of Vacuum Science and Technology 9, 520 (1972); https://doi.org/10.1116/1.1316674 1971

[16] M. Žemlička, P. Neilinger, M. Trgala, M. Rehák, D. Manca, M. Grajcar, P. Szabó, P. Samuely, Š. Gaži, U. Hübner, V. M. Vinokur, and E. Il'ichev, Finite quasiparticle lifetime in disordered superconductors, Phys. Rev. B 92, 224506 – Published 8 December 2015.

[17] H. Goldstein, "Classical mechanics". 3rd Ed. Addison Wesey (1962).

[18] V. Bouchiat, D. Vion, P. Joyez, D. Esteve, and M. H. Devoret, "Quantum coherence with a single cooper pair," Physica Scripta, vol. 1998, no. T76, p. 165, 1998.

[19] P. Bhartia, Microwave Solid State Circuit Design, 1998

[20] David M. Pozar. Microwave Engineering. Wiley, 3 edition, 1990.

[21] G.J. Dolan, Appl. Phys. Lett. 31, 337 (1977)

[22] M. J. Collett and C. W. Gardiner. Squeezing of intracavity and traveling-wave light fields produced in parametric amplification. Phys. Rev. A, 30:1386–1391, Sep 1984.

[23] Clemens Müller , Lisenfeld, Towards understanding two-level-systems in amorphous solids , Insights from quantum devices, 2019 Rep. Prog. Phys. 82 124501

[24] Y. Nakamura, Y. A. Pashkin and J.S. Tsai, Nature **398**, 786 (1999)

[25] A. Wallraff, D. I. Schuster, A. Blais, L. Frunzio, R.- S. Huang, J. Majer, S. Kumar, S. M. Girvin & R. J. Schoelkopf, Nature **431**, 162 (2004)

[26] M. H. Devoret and R. J. Schoelkopf, Superconducting Circuits for Quantum Information: An Outlook. Science 339, 1169 (2013)

[27] P.W. Anderson, B. I. Halperin, and C. M. Varma, Philos. Mag. **25**, 1 (1972).

[28] W. A. Phillips, J. Low Temp. Phys. **7**, 351 (1972).

[29] J.M. Martinis, K. B. Cooper, R. McDermott, M. Steffen, M. Ansmann, K. D. Osborn, K. Cicak, S. Oh, D. P. Pappas, R.W. Simmonds, and C. C. Yu, Phys. Rev. Lett. **95**, 210503 (2005).

[30] R. W. Simmonds, J. M. Martinis Phys. Rev. Lett. **93**, 077003 (2004)

[31] Y. Shalibo, Y. Rofe, D. Shwa, F. Zeides, M. Neeley, J. M. Martinis, and N. Katz, Phys. Rev. Lett. **105**, 177001 (2010)

[32] B. Sarabi, A. N. Ramanayaka, A. L. Burin, F. C. Wellstood, and K. D. Osborn, Phys. Rev. Lett **116**, 167002 (2016)

[33] B. Sarabi, A. N. Ramanayaka, A. L. Burin, F. C. Wellstood, and K. D. Osborn, Cavity quantum electrodynamics using a near-resonance two-level system: Emergence of the Glauber state. Appl. Phys. Lett. **106**, 172601 (2015)

[34] | J. D. Brehm, A. Bilmes, G. Weiss, A. V. Ustinov, and J. Lisenfeld, Appl. Phys. Lett. **111**, 112601 (2017).

[35] D. Pines and P. Nozieres, The theory of quantum liquids: Volume I, Perseus Books Publishing, L. L. C., 1999.

[36] Gao thesis, The Physics of Superconducting Microwave Resonators, 2008

[37] J Wenner, M Neeley, Radoslaw C Bialczak, M Lenander, Erik Lucero, A D O'Connell, D Sank, H Wang§, M Weidesk, A N Cleland and John M Martinis, Wirebond crosstalk and cavity modes in large chip mounts for superconducting qubits, Supercond. Sci. Technol. 24, 065001 (2011)

[38] R. C. Zeller and R. O. Pohl. Thermal conductivity and specic heat of noncrystalline solids. Phys. Rev. B, 4:2029,2041, Sep 1971.

[39] J. P. Kalejs and H. J. Maris, J. Appl. Phys. 41, 460 (1970).

[40] William H. Carter and Pin-Chin Ho, "Reconstruction of Inhomogeneous Scattering Objects from Holograms," Appl. Opt. 13, 162-172 (1974)

[41] W. A. Phillips. Tunneling states in amorphous solids. Journal of Low Tem- perature Physics, 7(3-4):351{360,1972.

[42] P. W. Anderson, B. I. Halperin, and C. M. Varma. Anomalous lowtemperature thermal properties of glasses and spin glasses. Philosophical Magazine, 25(1):19, 1972.

[43] J. Gao, M. Daal, A. Vayonakis, S. Kumar, J. Zmuidzinas, B. Sadoulet, B. A. Mazin, P. K. Day, and H. G. Leduc, "Experimental evidence for a surface distribution of two-level systems in superconducting lithographed microwave resonators," Appl. Phys. Lett. 92, 152505 (2008)

[44] M. R. Vissers, J. S. Kline, J. Gao, D. S.Wisbey, and D. P. Pappas, "Reduced microwave loss in trenched superconducting co-planar waveguides," Appl. Phys. Lett. 100, 082602 (2012)

[45] K. Geerlings, Z. Leghtas, I. M. Pop, S. Shankar, L. Frunzio, R. J. Schoelkopf, M. Mirrahimi, and M. H. Devoret, "Demonstrating a driven reset protocol for a superconducting qubit," Phys. Rev. Lett. 110, (2013)

[46] E. T. Jaynes and F. W. Cummings. Comparison of quantum and semiclassical radiation theories with application to the beam maser. Proceedings of the IEEE, 51(1):89{109, Jan 1963.

[47] F. W. Cummings. Stimulated emission of radiation in a single mode. Phys. Rev., 140:A1051{A1056, Nov 1965.

[48] S. Hunklinger and W. Arnold. Chapter 3 - Ultrasonic properties of glasses at low temperatures. volume 12 of Physical Acoustics, pages 155 { 215. Academic Press, 1976.

[49] C. A. Blockley, D. F. Walls, and H. Risken. Quantum collapses and revivals in a quantized trap. Europhysics Letters, 17(6):509, 1992.

[50] Z Dridi,B Bouhafs,P Ruterana and H Aourag, First-principles calculations of vacancy effects on structural and electronic properties of TiCx and TiNx J. Phys.: Condens. Matter 14 10237, 2002

[51] Omid Noorzian,Titanium nitride films for ultrasenstivie microresonator detectors, APPLIED PHYSICS LETTERS 97 , 102509 ,2010

[52] John R. Clem, Inductances and attenuation constant for a thin-film superconducting co-planar waveguide resonator, Journal of Applied Physics, October 2012

[53] Vissers, Klapwijk,"Evidence of non-equilibrium distribution of quasiparticles in the microwave response of a superconducting aluminum resonator," 2014

[54] A. Megrant, C. Neill, R. Barends, B. Chiaro,1 Yu Chen,1 L. Feigl,2 J. Kelly,1 Erik Lucero,1 Matteo Mariantoni,1,3 P. J. J. O'Malley,1 D. Sank,1 A. Vainsencher,1 J. Wenner,1 T. C. White, Y. Yin,1 J. Zhao, C. J. Palmstrom John M. Martinis, and A. N. Cleland, Planar superconducting resonators with internal quality factors above one million , APPLIED PHYSICS LETTERS 100, 113510 (2012)

[55] C. A. Blockley, D. F. Walls, and H. Risken. Quantum collapses and revivals in a quantized trap. Europhysics Letters, 17(6):509, 1992.

[56] J. Jackson, Classical Electrodynamics. John Wiley & Sons, 3rd edition ed., 1999.

[57] Wan-Ting Liao , **T. P. Kohler**, K. D. Osborn, R. E. Butera , C. J. Lobb, F. C. Wellstood, and M. Dreyer, 'Scanning tunneling Andreev microscopy of titanium nitride thin films', PHYSICAL REVIEW B 100, 214505 (2019)

[58] N. Kumar, K. Pourrezaei, B. Lee, and E.C. Douglas. Failure mechanisms of TiN thin lm diusion barriers. Thin Solid Films, 164(0):417 ,428, 1988.

[59] Bahman Sarabi,CAVITY QUANTUM ELECTRODYNAMICS OF NANOSCALE TWO-LEVEL SYSTEMS, thesis dissertation. 2014

[60] J. S. Chawla, X. Y. Zhang, and D. Gal, "Effective electron mean free path in TiN(001)", JOURNAL OF APPLIED PHYSICS 113, 063704 (2013)

[61] Bilmes, A., Volosheniuk, S., Brehm, J.D. et al. Quantum sensors for microscopic tunneling systems. npj Quantum Inf 7, 27 (2021). https://doi.org/10.1038/s41534-020-00359-x

[62] M. Von Schickfus and S. Hunklinger. The dielectric coupling of low-energy excitations in vitreous silica to electromagnetic waves. Journal of Physics C: Solid State Physics, 9(16):L439, 1976.

[63] E.H. Lock, P. Xu, T. Kohler, L. Camacho, J. Prestigiacomo, Y. J. Rosen, and K. D. Osborn, IEEE Trans. Appl. Supercond. **29**, 1700108 (2019).

[64] Hanhee Paik and Kevin D. Osborn. Reducing quantum-regime dielectric loss of silicon nitride for superconducting quantum circuits. Applied Physics Letters, 96(7), 2010.

[65] C. S. Owen and D. J. Scalapino, "Superconducting state under the influence of external dynamic pair breaking," Physical Review Letters 28 (1972), no. 24, 1559–1561.

[66] R. Q. Lee and R. N. Simons, "Coplanar Waveguide Aperture-Coupled Microstrip Patch Antenna," IEEE Microwave Guided Wave L ett., Vol. 2, No. 4, pp. 138—139, April 1992.

[67] John M. Martinis, K. B. Cooper, R. McDermott, Matthias Steen, Markus Ansmann, K. D. Osborn, K. Cicak, Seongshik Oh, D. P. Pappas, R. W. Simmonds, and Clare C. Yu. Decoherence in Josephson qubits from dielectric loss. Phys. Rev. Lett., 95:210503, Nov 2005.

[68] R. W. Simmonds, K. M. Lang, D. A. Hite, S. Nam, D. P. Pappas, and John M. Martinis. Decoherence in Josephson phase qubits from junction resonators. Phys. Rev. Lett., 93:077003, Aug 2004.

[69] Moe S. Khalil. A study of two-level system defects in dielectric lms using superconducting resonators. PhD thesis, University of Maryland - College Park, 2013.

[70] H. Haus and W-P Huang. Coupled-mode theory. Proceedings of the IEEE, 79(10):1505{1518, Oct 1991.

[71] H. Haken. Laser Theory. Springer, 1970.

[72] C. W. Gardner. Handbook of stochastic methods for physics, chemistry and the natural sciences, 1983.

[73] Chunqing Deng, Martin Otto, and Adrian Lupascu. An analysis method for transmission measurements of superconducting resonators with applications to quantum-regime dielectric-loss measurements. Journal of Applied Physics, 114(5), 2013.

[74] S. Hunklinger and W. Arnold. Chapter 3 - Ultrasonic properties of glasses at low temperatures. volume 12 of Physical Acoustics, pages 155 , 215. Academic Press, 1976.

[75] Parker, W.H., 1975. Modified heating theory of nonequilibrium superconductors. Physical Review B, 12(9), p.3667.

[76] Khukhareva, I.S., 1963. The superconducting properties of thin aluminum films. Soviet Physics JETP, 16, pp.828-832.

[77] A. Kardakova, M. Finkel, D. Morozov, V. Kovalyuk, P. An, C. Dunscombe, M. Tarkhov, P. Mauskopf, T. M. Klapwijk, and G. Goltsman,"The electron-phonon relaxation time in thin superconducting titanium nitride films", Appl. Phys. Lett. 103, 252602 (2013)

[78] Niepce, D., Burnett, J.J., Latorre, M.G. and Bylander, J., 2020. Geometric scaling of two-level- system loss in superconducting resonators. Superconductor Science and Technology, 33(2), p.025013.

[79] Mattis, D.C. and Bardeen, J., 1958. Theory of the anomalous skin effect in normal and superconducting metals. Physical Review, 111(2), p.412. 1958

[80] Uwe S. Pracht, Marc Scheffler, and Martin Dressel, Direct observation of the superconducting gap in thin film of titanium nitride using terahertz spectroscopy 2012

[81] A. A. Clerk, M. H. Devoret, S. M. Girvin, Florian Marquardt, and R. J. Schoelkopf. Introduction to quantum noise, measurement, and amplication. Reviews of Modern Physics, 82(2):1155, 2010.

[82] Lisenfeld, J., Bilmes, A., Megrant, A. et al. Electric field spectroscopy of material defects in transmon qubits. npj Quantum Inf 5, 105 (2019). https://doi.org/10.1038/s41534-019-0224-1

[83] Shalibo,"Lifetime and Coherence of Two-Level Defects in a Josephson Junction" 10.1103/PhysRevLett.105.177001

[84] Determining interface dielectric losses in superconducting co-planar waveguide resonators W. Woods,1, G. Calusine, A. Melville, A. Sevi, E. Golden,1 D. K. Kim, D. Rosenberg, J. L. Yoder,1 and W. D. Oliver, PhysRevApplied.12.014012

[85] T. I. Baturina, S. V. Postolova, A. Yu. Mironov, A. Glatz, M. R. Baklanov, V. M. Vinokur, Superconducting phase transitions in ultrathin TiN films , arXiv:1109.5270. (2011)

[86] C. Wang, C. Axline, Y. Y. Gao, T. Brecht, Y. Chu, L. Frunzio, M. H. Devoret, and R. J. Schoelkopf, Applied Physics Letters 107, 162601 (2015).

[87] M. Bartosik, D. Holec, D. Apel, M. Klaus, C. Genzel, J. Keckes, M. Arndt, P. Polcik, C.M. Koller, P.H. Mayrhofer, Thermal expansion of Ti-Al-N and Cr-Al-N coatings, Scripta Materialia, Volume 127, 2017, Pages 182-185.

[88] Tinkham, M., 2004. Introduction to superconductivity. Courier Corporation.

[89] Onnes, H.K., 1911. The disappearance of the resistivity of mercury. Comm. Leiden, 122(2).

[90] Schreier, J.A., Houck, A.A., Koch, J., Schuster, D.I., Johnson, B.R., Chow, J.M., Gambetta, J.M., Majer, J., Frunzio, L., Devoret, M.H. and Girvin, S.M., 2008. Suppressing charge noise decoherence in superconducting charge qubits. Physical Review B, 77(18), p.180502.

[91] Chang, J.B., Vissers, M.R., Córcoles, A.D., Sandberg, M., Gao, J., Abraham, D.W., Chow, J.M., Gambetta, J.M., Beth Rothwell, M., Keefe, G.A. and Steffen, M., 2013. Improved superconducting qubit coherence using titanium nitride. Applied Physics Letters, 103(1), p.012602.

[92] Rigetti, C., Gambetta, J.M., Poletto, S., Plourde, B.L.T., Chow, J.M., Córcoles, A.D., Smolin, J.A., Merkel, S.T., Rozen, J.R., Keefe, G.A.

and Rothwell, M.B., 2012. Superconducting qubit in a waveguide cavity with a coherence time approaching 0.1 ms. Physical Review B, 86(10), p.100506.

[93] M. Schechter1 and P. C. E. Stamp,"Inversion symmetric two-level systems and the low-temperature universality in disordered solids."PHYSICAL REVIEW B **88**, 174202 (2013)

[94] B. Mazin, "Microwave Kinetic Inductance Detectors," Ph.D. thesis (California Institute of Technology, 2004).

[95] P. Diener, a), H. Schellevis, and J. J. A. Baselmans,Homogeneous superconducting phase in TiN film: A complex impedance study .Appl. Phys. Lett. 101, 252601 (2012)

[96] H. M. Jaim, J. A. Aguilar, B. Sarabi, Y. J. Rosen, A. N. Ramanayaka, E. H. Lock, C. J. K. Richardson, and K. D. Osborn. Superconducting TiN lms sputtered over a large range of substrate DC bias. IEEE Transactions on Applied Superconductivity, PP(99):1{1, 2014}

[97] W. Escoer, C. Chapelier, N. Hadacek, and J.-C. Ville´gier, Anomalous Proximity Effect in an Inhomogeneous Disordered Super-conductor Physical Review Letters, 93(21). (2004)

[98] Kaplan, Quasiparticle and phonon lifetimes, PRB Volume 14 Number 11, (1976)

[99] Rui Zhang Thesis, LOSS IN SUPERCONDUCTING QUANTUM DEVICES FROM NON-EQUILIBRIUM QUASIPARTICLES AND INHOMOGENEITY IN ENERGY GAP (2020)

[100] Electrodynamics of strongly disordered superconductors, Thesis of Pieter Cornelis Jenze Jan COUMOU, Delft

[101] V. F. Gantmakher and V. T. Dolgopolov, Superconductor-insulator quantum phase transistion, Phys. Usp. 53, 1 (2010).

[102] "Current Distribution in Thin Superconducting Films", E. H. RHODERICK & E. M. WILSON, Nature 194, 1167 (1962)

[103] Reversible Fluxon Logic with optimized CNOT gate components, K.D. Osborn and W. Wustmann. Phys. Rev. B 101, 014516 – Published 31 January (2020)

[104] Ultra-low-power superconductor logic. Quentin P. Herra), Anna Y. Herr, Oliver T. Oberg, and Alexander G. Ioannidis. Journal of Applied Physics 109, 103903 (2011)

[105] Grigorij J. Grabovskij, Torben Peichl, Jürgen Lisenfeld, Georg Weiss, Alexey V. Ustinov, Strain Tuning of Individual Atomic Tunneling Systems Detected by a Superconducting Qubit (2012)

[106] M. S. Khalil, M. J. A. Stoutimore, F. C. Wellstood, and K. D. Osborn. An analysis method for asymmetric resonator transmission applied to superconducting devices. Journal of Applied Physics, 111(5), 2012.

[107] Black-box superconducting circuit quantization Simon E. Nigg, Hanhee Paik, Brian Vlastakis, Gerhard Kirchmair, Shyam Shankar, Luigi Frunzio, Michel Devoret, Robert Schoelkopf, Steven Girvin. Phys. Rev. Lett. 108, 240502 (2012)

[108] Chow Thesis, Yale, Quantum Information Processing with Superconducting Qubits, 2010

[109] Henry G. Leduc, Bruce Bumble, Peter K. Day, Anthony D. Turner, Byeong Ho Eom, Sunil Gol- wala, David C.Moore, Omid Noroozian, Jonas Zmuidzinas, Jiansong Gao, Benjamin A. Mazin, Sean McHugh, Andrew Merrill, arXiv:1003.5584, Submitted to Appl. Phys. Lett. (2009).

[110] G. Calusine, A. Melville, W. Woods, R. Das, C. Stull, V. Bolkhovsky, D. Braje, D. Hover, D. K. Kim, X. Miloshi, D. Rosenberg, A. Sevi, J. L. Yoder, E. Dauler, and W. D. Oliver Analysis and mitigation of interface losses in trenched superconducting co-planar waveguide resonators Cite as: Appl. Phys. Lett. 112, 062601 (2018)

[111] R. Barends, H. L. Hortensius, T. Zijlstra, J. J. A. Baselmans, S. J. C. Yates, J. R. Gao, and T. M. Klapwijk , Noise in NbTiN, Al, and Ta Superconducting Resonators on Silicon and Sapphire Substrates,"IEEE TRANSACTIONS ON APPLIED SUPERCONDUCTIVITY, VOL. 19, NO. 3, JUNE 2009

[112] Discussions with Fred Wellstood (2021)

[113] N. Foroozani, C. Hobbs, C. C. Hung, S. Olson, D. Ashworth, E. Holland, M. Malloy, P. Kearney, B. O'Brien,3 B. Bunday,3 D. DiPaola,3 W. Advocate, T. Murray, P. Hansen,3 S. Novak,3 S. Bennett,3 M. Rodgers,3 B. Baker-O'Neal,3 B. Sapp,3 E. Barth,4 J. Hedrick,3 R. Goldblatt,3 S. S. Papa Rao,3 and K. D. Osborn, Development of transmon qubits solely from optical lithography on 300mm wafers, Quantum Sci. Technol. 4 025012, (2019)

[114] Michael R. Vissers, Robert P. Erickson, Hsiang-Sheng Ku, Leila Vale, Xian Wu, Gene Hilton, David P. Pappas,Low-noise kinetic inductance traveling-wave amplifier using three-wavemixing, Appl. Phys. Lett. 108, 012601 (2016);https://doi.org/10.1063/1.4937922

[115] F. Bloch. Nuclear induction. Phys. Rev., 70:460{474, Oct 1946.

[116] John M. Martinis, K. B. Cooper, R. McDermott, Matthias Steen, Markus Ansmann, K. D. Osborn, K. Cicak, Seongshik Oh, D. P. Pap-pas, R. W. Simmonds, and Clare C. Yu. Decoherence in Josephsonqubits from dielectric loss. Phys. Rev. Lett.,95:210503, Nov 2005.

[117] Sumedh Mahashabde, Ernst Otto , Domenico Montemurro , Sebastiande Graaf, Sergey Kubatkin,and Andrey Danilov, PHYSICALREVIEW APPLIED14, 044040 (2020) Fast Tunable High-Q-Factor Superconduct-ing Microwave Resonators